

In-situ spectroscopic studies of the
mechanism of solid super-acid
catalysed methanol carbonylation

Lee D. Dingwall

Submitted for the degree of Doctor
of Philosophy

University of York
Department of Chemistry

July 2010

Acknowledgements

I would like to thank BP Chemicals and the EPSRC for funding this PhD research. For Supervision and helpful discussions throughout the project, thanks go to Professor Adam Lee, Dr Karen Wilson and Dr Jason Lynam at the University of York and Drs Jon Deeley, Glenn Sunley and David Law (and the rest of my colleagues at BP Chemicals) at the BP Chemicals site in Hull. Thank you to Durham Solid State NMR service, the Swansea Mass Spectrometry Service, MEDAC and Dr Nigel Young for providing some analytical data discussed herein. I would also like to thank The University of York Chemistry workshops for support with construction and maintenance of in-house equipment, as well as Drs Luca Olivi and Andrea Cognigni for their support with XAFS measurements at the Sincrotrone in Trieste. Thank you to the University of York for providing a comfortable and dynamic environment for my personal development, and all of my colleagues and friends (of whom there are too many to mention here, but are written in white ink in the background of this thesis – as promised) who made my time so enjoyable. On the academic side, I would particularly like to thank the York Surface Science and Catalysis group who have recently moved to join the Cardiff Catalysis Institute and the SLUG research group, and wish all current members every success for the future. From my ‘extra curricular activities’ I would like to thank all members of the Chemical *Inter*Actions society, the York Student Cinema and the York Boxing Club as well as the Science Club volunteers team for enriching my life and helping me to refocus my thoughts after becoming ‘over-immersed’ in my research. Special thanks go to Dr Andrew Newman for invaluable discussions and ‘handing over the torch’ for further development of some of the outcomes of his PhD research. Thanks go to James Naughton, Janine Montero and Christine Welby for editing suggestions throughout the thesis. Returning home after a day in the lab was always a pleasure in York thanks to Halifax College flatmates and Dr Jonny Gammon and Alan Burns who have been like brothers and have always provided a warm, friendly and entertaining place to go back to. As for all of my successes, my parents and brother Paul are always deeply rooted at the heart. For my fiancée Anne-Cécile, you’re with me through all of life’s adventures, and on this long and winding path, through blue skies and stormy clouds - I couldn’t have done it without you.

Declaration

I confirm that all work in this doctoral thesis is the soul work of the author unless otherwise stated. Some research reported in this manuscript has been or is in preparation to be published in peer reviewed journal articles referenced below.

1. *A polyoxometallate-tethered Ru complex as a catalyst in solventless terminal alkyne oligomerization*
L. D. Dingwall, C. M. Corcoran, A. F. Lee, L. Olivi, J. M. Lynam and K. Wilson, *Catalysis Communications*, 2008, **10**, 53-56.
2. *Bifunctional organorhodium solid acid catalysts for methanol carbonylation*
L. D. Dingwall, A. F. Lee, J. M. Lynam, K. Wilson, L. Olivi, J. M. S. Deeley, S. Gaemers, G. J. Sunley – *in preparation*.

Table of Contents

Acknowledgements	ii
Declaration	iii
Table of Contents	iv
Table of Figures	viii
Table of Tables.....	xix
Table of Equations	xxi
Table of Schemes	xxii
Abstract	xxiii
Abbreviations	xxv
Chapter 1 - Introduction	1
1.1 - Catalysis.....	2
1.2 - Heterogeneous Catalysis.....	4
1.2.1 - Heterogeneous acid catalysis	5
1.3 - Deactivation in heterogeneous catalysts	7
1.3.1 - Key causes of deactivation	8
1.4 - Catalyst lifetime	9
1.5 - Acetic Acid	10
1.6 - Acetic Acid production from methanol carbonylation	10
1.7 - Multidentate Phosphine ligands in Catalysis	17
1.8 - Polyoxometallates	21
1.8.1 - Chemistries involving the use of polyoxometallates (POMs)	22
1.9 - Heteropolyacids	25
1.9.1 - Structure and Properties.....	25
1.9.2 - Keggin reaction mechanism	27
1.10 - Supported HPA materials	28
1.11 - Synthetic challenges of organic-inorganic hybrid polyoxometallates materials	28
1.12 - Project Aims	29
1.13 - References.....	30
Chapter 2 - Experimental	36

2.1 - Characterisation	36
2.1.1 - Thermogravimetric Analysis TGA and Differential thermal analysis.....	36
2.1.2 - Diffuse Reflectance Infrared Fourier Transform Spectroscopy (DRIFTS)	37
2.1.3 - Raman Spectroscopy.....	39
2.1.4 - Powder X-ray Diffraction	39
2.1.5 - Single Crystal XRD	40
2.1.6 - X-Ray Photoelectron Spectroscopy (XPS).....	40
2.1.7 - X-Ray absorption spectroscopy (XAS)	43
2.1.8 - <i>In-situ</i> XANES.....	46
2.1.9 - Porosimetry	47
2.1.10 - Solution state NMR	48
2.1.11 - Structural MS analysis	49
2.1.12 - Solid state MAS-NMR	49
2.1.13 - ICP-MS and CHN elemental analysis	49
2.1.14 - Pyridine titrations.....	49
2.1.15 - Methanol carbonylation tests	50
2.1.16 - Dimethyl ether carbonylation tests	53
2.1.17 - Ethanol dehydration tests.....	53
2.1.18 - Phenyl acetylene oligomerisation tests.....	53
2.2 - Synthesis of Ru Compounds.....	55
2.2.1 - Synthesis of Ru(Cl)(Cp)(PPh ₃) ₂	55
2.2.2 - Synthesis of RuHPW	56
2.2.3 - Synthesis of [NEt ₃ H] ⁺ ₃ . [PW ₁₂ O ₄₀] ³⁻ (NEt ₃ HPW)	57
2.2.4 - Synthesis of Ru(Cl)(Cp)(dppe).....	57
2.2.5 - Synthesis of ‘RudppeHPW’ compound.....	58
2.3 - Synthesis of Rh compounds.....	59
2.3.1 - Synthesis of Rh(acac)(CO)(xantphos).....	59
2.3.2 - Synthesis of RhXHPW _n :1 (n= 0.5, 1, 2, 3)	59
2.3.3 - Synthesis of RhXHPW _n :1 supported on Davisil 100 silica (n= 0.5, 1, 2, 3)	60
2.3.4 - Synthesis of RhXHPW _n :1 supported on Davisil 100 silica with Cs/Ag dopants	61
2.3.5 - Synthesis of Rh(acac)(CO)(terpyridine).....	61
2.3.6 - Synthesis of RhTHPW1:1	62

2.3.7 - Synthesis of RhTHPW1:1 supported on Davisil 100 silica.....	63
2.3.8 - Synthesis of RhAHPW1:1	63
2.3.9 - Synthesis of RhAHPW1:1 supported on Davisil 100 silica	64
2.4 - Chemicals List	64
2.5 - References.....	66
Chapter 3 - Synthesis, characterisation and catalysis of Ru-polyoxometallates...	67
3.1 - Introduction.....	67
3.2 - Synthesis and characterisation of RuHPW	70
3.3 - CO Binding Studies of RuHPW	87
3.4 - Synthesis and characterisation of RudppeHPW	90
3.5 - CO Binding Studies of RudppeHPW	100
3.6 - RuHPW and RudppeHPW methanol carbonylation tests.....	102
3.7 - RuHPW and RudppeHPW as catalysts in phenyl acetylene oligomerisation	104
3.8 - Conclusions.....	108
3.9 - References.....	110
Chapter 4 - Synthesis, characterisation and catalysis of Rh-polyoxometallates.	114
4.1 - Introduction.....	114
4.2 – [Rh(CO)(Xantphos)]-HPW (RhXHPW) synthesis	117
4.3 - Methanol Carbonylation	128
4.4 - Catalyst deactivation studies.....	132
4.5 - Cs/Ag doped RhXHPW-SiO ₂	139
4.6 - Optimisation of catalyst composition	147
4.7 - DRIFTS study of the mechanism of methanol carbonylation	153
4.8 - Methanol condensation.....	153
4.9 - <i>In-situ</i> DRIFTS study of methanol/HPW interactions.....	154
4.10 - <i>In-situ</i> DRIFTS study of methanol/CO/HPW interactions.....	157
4.11 - Syngas sourced CO for methanol carbonylation	162
4.12 - Conclusions.....	166
4.13 - References.....	167

Chapter 5 - Synthesis, characterisation and catalysis of Rh(Anthraphos)- polyoxometallates	171
5.1 - Introduction.....	171
5.2 - Synthesis and characterisation of Rh(Anthraphos)(CO)HPW (RhAHPW) systems	172
5.3 - Thermal stability of RhAHPW-SiO ₂	181
5.4 - Catalytic application of RhAHPW in methanol carbonylation	184
5.5 - Conclusions.....	186
5.6 - References.....	188
Chapter 6 - Synthesis, characterisation and catalysis of Rh(Terpy)- polyoxometallates	190
6.1 - Introduction.....	190
6.2 - Synthesis and characterisation of Rh(η^2 -acac)(CO) ₂ (terpyridine) and HPW derivative.....	191
6.3 - Catalytic studies of bulk and silica supported RhTHPW	199
6.4 - Conclusions.....	200
6.5 - References.....	201
Conclusions and Future Work.....	203
Appendices.....	207
RhCl(CO)(Xantphos)·1.5THF crystal data.....	CD1

Table of Figures

Figure 1.1.1: Reaction energy profile showing activation energy with and without a catalyst.	2
Figure 1.1.2: General catalyst cycle.....	3
Figure 1.2.1.1: Relative acid strength of solid acids and their catalytic uses, (reproduced from reference 14).	6
Figure 1.3.1.1: Well known deactivation mechanisms: A) coke formation, B) Poisoning, C) sintering of the active metal particles, D) Sintering and solid-solid phase transitions of the washcoat and encapsulation of active metal particles(Reproduced from reference 41).	9
Figure 1.6.1: (a) Schematic of the first proposed mechanism for the Monsanto process (1976) for methanol carbonylation. (b) Currently accepted mechanism for the Monsanto process. Reaction steps are indicated.	11
Figure 1.6.2: Both neutral and anionic pathway hypotheses for the Iridium catalysed CATIVA™ process.	14
Figure 1.6.3: Rh dimer, $[\text{Rh}(\mu\text{-Cl})(\text{CO})_2]_2$ formed at the reactor exhaust from supported RhCl_3 doped HPW catalyst in the presence of 25 % CO / He gas flow.	16
Figure 1.7.1: Wilkinson's hydrogenation catalyst $\text{RhCl}(\text{PPh}_3)_3$	17
Figure 1.7.3: 'Natural bite angle' (β_n) defining 'flexibility range' of a diphosphine transition metal complex.	18
Figure 1.7.4: Transphos bidentate phosphine ligand	20

Figure 1.7.5: Xantphos bidentate phosphine ligand.....	20
Figure 1.7.1.1: General polyoxometallate geometries: (i) Keggin, (ii) Wells–Dawson, (iii) Finke–Droege, (iv) Pope–Jeanin–Preyssier (reproduced from reference 115)	21
Figure 1.8.1.1: Three types of catalysis associated with solid HPA materials: (a) surface type, (b) pseudo-liquid bulk type, (c) bulk type. (taken from reference 109)	23
Figure 1.9.1.1: $PW_{12}O_{40}^{3-}$ Keggin unit.....	25
Figure 1.9.2.1: Proposed schematic for Keggin heteropolyacid catalysed propene hydration (Ku= Keggin unit).	27
Figure 2.1.2.1: (left) <i>in-situ</i> DRIFTS apparatus (right) sample cell showing gas inlet and outlet.....	38
Figure 2.1.6.1: Escape depth curve used to demonstrate the inelastic mean free path of an electron excited by x-ray radiation in XPS.	40
Figure 2.1.6.2: Schematic representation of photoionization.	41
Figure 2.1.7.1: Example of a full EXAFS spectrum.	44
Figure 2.1.8.1: <i>In-situ</i> EXAFS Chamber, (top left) Sample holder and cell for loading sample for in-situ analysis (top right) main chamber for mounting sample cell (bottom left) sample table showing direction of beam entrance and exit (bottom right) inside of main chamber showing mounted cell and gas inlet/outlet.	46
Figure 2.1.15.1: Continuous flow reactor with on-line GC and MS.....	52
Figure 3.2.1: DRIFTS spectra of RuHPW. Comparative spectra are shown for the $Ru(Cl)(Cp)(PPh_3)_2$ (*) and HPW (†) precursors.....	72

Figure 3.2.2: TGA profiles of RuHPW, Ru(Cl)(Cp)(PPh ₃) ₂ and HPW precursors.	74
Figure 3.2.3: Powder X-ray diffractograms of RuHPW and the Ru(Cl)(Cp)(PPh ₃) ₂ and HPW precursors.....	75
Figure 3.2.4: ³¹ P MAS-NMR spectra of RuHPW and the Ru(Cl)(Cp)(PPh ₃) ₂ precursor. Spectral peaks used for integration are encapsulated in dotted lines. Inset shows comparison spectra of the Keggin region for RuHPW, HPW and NEt ₃ HPW.....	78
Figure 3.2.5: Proposed structure and cation in covalently bound RuHPW.....	78
Figure 3.2.6:.. Ru 3p _{3/2} XP spectra of RuHPW. Comparative spectra are shown for Ru(Cl)(Cp)(PPh ₃) ₂ , RuCl ₃ and RuO ₂	79
Figure 3.2.7: Ru K-edge normalised EXAFS of RuHPW, Ru metal, Ru(Cl)(Cp)(PPh ₃) ₂ , RuCl ₃ and RuO ₂	80
Figure 3.2.9: EXAFS chi ² plots, experimental and theory Ru(Cl)(Cp)(PPh ₃) ₂ and RuHPW (with and without HPW coordination)	82
Figure 3.2.8: Fitted radial distribution functions of RuHPW and the Ru(Cl)(Cp)(PPh ₃) ₂ precursor.	83
Figure 3.2.10: Raman spectra of RuHPW and Ru(Cl)(Cp)(PPh ₃) ₂ precursor. * and dotted lines denote the fingerprint bands associated with {Ru(Cp)(PPh ₃) ₂ }. Intense HPW and associated cationic triethylammonium ([NEt ₃ H] ⁺) bands in RuHPW are noted.....	86
Figure 3.3.1: DRIFTS spectra of RuHPW showing CO adsorption as a function of temperature. Inset show mono CO derivative of RuHPW peak intensity (A) as a function of sample temperature. B and C indicate dicarbonyl species.	88

Figure 3.3.2: DRIFTS comparison between RuHPW and treated at 200 °C. Inset: Powder X-ray diffractograms of fresh RuHPW and RuHPW after heating at 200 °C (* denotes common peaks).	89
Figure 3.4.1: Ru(Cl)(Cp)(dppe), used to provide an alternative ligand system to triphenylphosphine (PPh ₃) in RuHPW.	90
Figure 3.4.2: DRIFTS spectra of RudppeHPW. Comparative spectra are shown for the Ru(Cl)(Cp)(dppe) (*) and HPW (†) precursors.....	93
Figure 3.4.3: TGA profiles of RudppeHPW, Ru(Cl)(Cp)(dppe) and HPW precursors.....	94
Figure 3.4.4: Powder X-ray diffractograms of RudppeHPW and HPW and Ru(Cl)(Cp)(dppe) precursors	95
Figure 3.4.5: Ru K-edge normalised EXAFS of RudppeHPW, Ru(Cl)(Cp)(dppe), and RuCl ₃ , RuO ₂ and Ru metal standards.	96
Figure 3.4.6: Ru 3p _{3/2} XP spectra of RudppeHPW and RuHPW. Comparative spectra are shown for Ru(Cl)(Cp)(PPh ₃) ₂ Ru(Cl)(Cp)(dppe), RuCl ₃ and RuO ₂ . ..	97
Figure 3.4.7: EXAFS chi ² plots, experimental and theory Ru(Cl)(Cp)(dppe) and RudppeHPW (with and without HPW coordination).....	98
Figure 3.4.8: Fitted radial distribution functions of RudppeHPW and the Ru(Cl)(Cp)(dppe) precursor.	99
Figure 3.5.1: DRIFTS spectra of RudppeHPW showing CO adsorption as a function of temperature. Inset show mono CO derivative of RudppeHPW peak intensity (A) as a function of sample temperature.	101

Figure: 3.6.1: Methanol % conversion comparison of HPW and the bifunctional RuHPW and RudppeHPW both with 1 equivalent of HPW. Inset: DME production mmol h^{-1}	103
Figure 3.7.1: Heterogeneous and homogeneous <i>E/Z</i> -enyne selectivity profiles in phenyl acetylene oligomerisation over RuHPW and Ru(Cl)(Cp)(PPh ₃) ₂ , respectively. Inset (top right) shows phenyl acetylene conversion profiles.	105
Figure 3.7.2: Heterogeneous and homogeneous <i>E/Z</i> -enyne selectivity profiles in phenyl acetylene oligomerisation over RudppeHPW and Ru(Cl)(Cp)(dppe), respectively. Inset (top left) shows phenyl acetylene conversion profiles.	107
Figure 4.2.1: DRIFTS of RhXantphos precursor and bulk RhXHPW1:1 together with representative Rh standards. Characteristic Xantphos (*), HPW (#) and η^2 -acac bands (θ) are highlighted, together with Rh-CO stretches.....	119
Figure 4.2.2: Normalised Rh K-edge XANES of bulk and silica supported RhXHPW1:1 and representative Rh standards showing HPW materials contain Rh(I).	121
Figure 4.2.3: Comparison of a) Rh 3d XPS and b) W 4f regions for RhXantphos, ion exchanged RhXHPW and bulk HPW.....	122
Figure 4.2.4: χ^2 plots for RhXantphos, RhXHPW1:1 and RhXHPW1:1-SiO ₂	124
Figure 4.2.5: Fitted Rh K-edge EXAFS radial distribution functions of RhXantphos, bulk RhXHPW1:1 and RhXHPW1:1-SiO ₂ . Contributions to the electron density from C, O and P in the first shell are indicated.	125
Figure 4.2.6: Crystal structure of Rh(Cl)(CO)(Xantphos) (image created using ORTEP37)	126
Figure 4.2.7: TGA comparison between 20 and 950 °C of RhXHPW1:1 with HPW and Xantphos ligand	128

Figure 4.3.1: Methanol Conversion profiles of supported and unsupported RhXHPW catalysts compared to pure HPW. (Catalyst amounts: 80 mg HPW, 56 mg RhXHPW1:1, 311 mg RhXHPW1:1-SiO ₂ and 250 mg 50 wt % HPW-SiO ₂ reproduced from ref 17)	130
Figure 4.3.2: Light-off between 100 and 350 °C showing product distributions during methanol carbonylation over RhXHPW1:1-SiO ₂ (Rh : HPW = 1 : 1; HPW 50 %), (where acetyls = methyl acetate and acetic acid).....	131
Figure 4.3.3: DME reaction profile of RhXHPW1:1-SiO ₂ at 200 °C showing conversion to acetyls and acetyl yield over 3.5 hours on stream DME : CO = 1 : 7	132
Figure 4.4.1: Methanol conversion and acetyl selectivity of in methanol carbonylation over RhXHPW1:1-SiO ₂ showing superior stability at 200 °C compared to operation at 250 °C.....	133
Figure 4.4.2: Comparison deactivation of RhXHPW1:1-SiO ₂ at 250 °C during methanol carbonylation with reduction in Rh(I) content as determined by <i>in-situ</i> XANES.....	135
Figure 4.4.3: DSC plots showing thermal evolution of fresh HPW and RhXHPW1:1-SiO ₂ compared with RhXHPW1:1-SiO ₂ ramped to 200 °C under carbonylation condition and cooled under He - 1, (He), 2, (20 % O ₂ /He) and ramped to 200 °C under carbonylation condition, held for 2.5 h and cooled under He - 3 (He) as well as ramped to 350 °C under carbonylation conditions - 4 (He) Showing the effects of time and temperature on catalyst stability.....	136
Figure 4.4.4: Effect of methyl acetate (MeOAc) pre-treatment on acetyl yield of RhXHPW1:1-SiO ₂ showing loss of initial high acetyl yield with a constant 0.55 mmolh ⁻¹ over 2 hours on-stream. Inset: methanol yield during pre-treatment step showing methanol generated from ester hydrolysis of MeOAc.	137

Figure 4.4.5: Effect of co-fed H ₂ O on methanol conversion and acetyl selectivity during carbonylation at 200 °C over RhXHPW1:1-SiO ₂ showing enhanced acetyl yield with the introduction of H ₂ O over 2 hours on stream.....	139
Figure 4.5.2: Powder XRD pattern showing dopant effect on crystallinity; A HPW, B HPW-SiO ₂ , C RhXHPW-SiO ₂ , D Cs/Ag-RhHPW-SiO ₂ , E Cs/Ag-HPW-SiO ₂ *denotes the crystalline HPW phase and § indicates cation-exchanged crystal phase.....	142
Figure 4.5.3: Methanol conversion and MeOAc production over total carbon-oxygenates for Cs/Ag-RhXHPW-SiO ₂ held at 250 °C for 2 hours under methanol carbonylation conditions.	143
Figure 4.5.4: <i>Ex-situ</i> Rh K-edge XANES profiles of fresh bulk and silica supported RhXHPW compared to spent catalysts ramped to 250 °C and 350 °C showing the effect of temperature on oxidation state under methanol carbonylation conditions. Inset: linear combination fit of 1+ and 0 oxidation states showing percentage quantification of reduction to Rh(0).	144
Figure 4.5.5: EXAFS for Rh K-edge χ^2 plots, experimental and theory for fresh and spent (250 °C and 350 °C) Cs/Ag-RhXHPW-SiO ₂	145
Figure 4.5.6: Fourier Transformed Rh K-edge EXAFS spectra of Cs/Ag-RhXHPW-SiO ₂ catalysts showing change of closest neighbouring atomic shells after treatment under methanol carbonylation reaction conditions.....	147
Figure 4.6.1: TGA between 20 and 1000 °C of RhXHPW-SiO ₂ series and HPW reference showing crystalline water loss between 125 and 225 °C and decomposition of Xantphos ligand at ca. 300 – 500 °C.	148
Figure 4.6.2: DRIFTS spectra between 1400 and 1700 cm ⁻¹ of temperature controlled pyridinium dissociation from RhXHPW1:1-SiO ₂ between 25 and 400 °C indicative of Brønsted acidity, (pure HPW is shown for reference). Bands A, B, C and D are characteristic of surface bound pyridinium (see Table 4.6.1).....	150

Figure 4.6.3: Influence of Rh content on DRIFTS-derived pyridinium ion intensity at 1540 cm^{-1} for RhXHPW1:1-SiO ₂ ; pyridinium signals have been normalised relative to the 3 protons expected for the parent H ₃ PW ₁₂ O ₄₀ . Inset shows associated DRIFTS spectra with principal pyridinium ion bands highlighted.	151
Figure 4.6.4: Reaction profiles of RhXHPW-SiO ₂ series with 0 (HPW-SiO ₂), 0.5, 1, 2 Rh's per HPW denoted as 'x : 1', over 5 hours on stream. a, methanol conversion b, selectivity to acetyls where acetyls are (methyl acetate and acetic acid.	152
Figure 4.6.5: Influence of Rh/H ⁺ content on steady state methanol conversion, acetyl selectivity and acetyl yield of RhXHPW-SiO ₂ series during methanol carbonylation at 200 °C. The total amount of Rh was kept constant at 5 mg for each catalyst. Acetyl yield is the average over 5 h on-stream where steady state is achieved.	153
Figure 4.8.1: activated methanol on pendant oxygen of a phosphotungstate anion.	155
Figure 4.9.1: In-situ DRIFTS spectra between 2700 and 3200 cm^{-1} of N ₂ purged bulk HPW after exposure to methanol up to 350 °C showing formation of surface bound methoxy species (C-H bands A and B) A spectrum of DME treated HPW is shown for comparison showing surface bound C-H, A' and B'	156
Figure 4.9.2: DRIFTS spectrum of N ₂ purged RhXHPW1:1-SiO ₂ after exposure to CD ₃ OD at 150 °C showing formation of deuterated methoxy species denoted by * and the formation of a new CO band associated with methylated {Rh ⁺ (CO)(Xantphos)} functionality.	157
Figure 4.10.1: <i>In-situ</i> DRIFTS temperature study of RhXHPW1:1-SiO ₂ exposed to CO/MeOH. bands A, B, C and D correspond to 1 Rh(CO)(Me)(X), 2 Rh(CO) ₂ (X), and 1 Rh(CO)(COMe)(X) respectively. ('X' = xantphos)	159
Figure 4.10.2: Proposed mechanism of RhXHPW methanol carbonylation.	160

Figure 4.10.3: Rh K-edge XANES analysis of RhXHPW1:1-SiO ₂ both fresh and treated under methanol carbonylation conditions at 200 °C for 5 hours, compared to Rh standards of 0, 2 and 3 oxidation states.	161
Figure 4.10.4: Rh 3d XPS analysis of RhXHPW1:1-SiO ₂ treated under methanol carbonylation conditions at 200 °C for 5 hours fitted to Rh(0), Rh(I) and Rh(III).showing partial oxidation to catalytically active species Rh(III) and some reduction Rh(0) under carbonylation conditions	162
Figure 4.11.1: A comparison of activity and selectivity in acetyl synthesis profiles of RhXHPW1:1-SiO ₂ over 5 hours at 200 °C with CO sources of a) pure CO b) 1 : 1 ratio of CO / H ₂ showing retention of activity in methanol conversion but a drop in selectivity in b) suspected to be due to Rh reduction from H ₂ exposure.....	164
Figure 4.11.2 Temperature programmed reduction (TPR) between 20 – 1000 °C in 20 % H ₂ / He gas flow at 20 ml min ⁻¹ showing mass loss profile of RhXHPW1:1-SiO ₂ up to 1000 °C.	166
Figure 4.11.3: Rh 3d XPS of RhXHPW1:1-SiO ₂ exposed to methanol carbonylation conditions with 1 : 1 CO : H ₂ showing three oxidation state environments. Partial reduction of the parent Rh complex Rh(I) to Rh(0) and oxidation to active Rh (III) catalyst species.	166
Figure 5.1.1: Anthraphos PCP ligand showing interaction with a transition metal centre where M = Rh, Ir.	172
Figure 5.2.1: ¹³ C MAS-NMR showing carbon environments associated with the Anthraphos anthracene and phenyl aryl carbons in the Rh-Anthraphos functionality of RhAnthraphos, and RhAHPW and RhAHPW-SiO ₂	174
Figure 5.2.2: DRIFTS spectrum showing bulk bifunctional RhAHPW and supported RhAHPW-SiO ₂ compared with RhAnthraphos and HPW parent species.	175

Figure 5.2.3: Solid state $^{31}\text{P}\{1\text{H}\}$ MAS-NMR spectra of RhAnthraphos, RhAHPW and RhAHPW-SiO ₂ showing loss of Rh bound phosphine signal A, B and C and D on incorporation of HPW (peak E).....	177
Figure 5.2.4: W 4f XP spectra of RhAHPW, RhAHPW-SiO ₂ and bulk HPW showing decrease in binding energy due to impregnation of cationic organorhodium into HPW matrix.	178
Figure 5.2.5: Rh 3d XP spectra of RhAnthraphos, bulk RhAHPW and silica supported RhAHPW-SiO ₂ showing a decrease in Rh(I) and increase in Rh(III) character on incorporation of HPW.	180
Figure 5.3.1: TGA of RhAnthraphos, RhAHPW and RhAHPW-SiO ₂ Showing decomposition of the parent complex > 270 °C and >280 °C in the HPW derivatives.....	181
Figure 5.3.2: In-situ temperature programmed DRIFTS analysis of RhAHPW-SiO ₂ between 25 and 350 °C showing thermal degradation at temperature.	182
Figure 5.4.1: Methanol conversion and acetyl selectivity of RhAHPW-SiO ₂ during continuous operation at 200 °C under standard carbonylation conditions.	184
Figure 5.4.2: DME/Acetyl during methanol light-off over RhAHPW-SiO ₂ showing change in product distribution at 200 °C and 250 °C.	186
Figure 6.1.1: Terpyridine as a multidentate nitrogen donor ligand where M is a transition metal.....	190
Figure 6.2.1: DRIFTS spectrum of Rh-Terpy series with bulk and supported RhTHPW and RhTHPW-SiO ₂ and RhTerpy with rhodium carbonyls denoted by † and η^1 -acac carbonyls denoted by §. Terpyridine and Rh(η^2 -acac)(CO) ₂ precursors for comparison.	193

Figure 6.2.2: DRIFTS infrared spectrum of RhTerpyHPW (*) indicates characteristic bands for terpyridine. The light grey regions show bleaching of characteristic terpyridine bands on incorporation of HPW.	197
Figure 6.2.3: TGA plot show thermal decomposition profile of RhTerpy, RhTHPW and RhTHPW-SiO ₂	198
Figure 6.3.1: Methanol conversion and selectivity to acetyls at 200 °C under CO/MeOH conditions.....	200
Figure 7.1: Comparison of methanol conversion, selectivity to acetyls and acetyl yield in mmolh ⁻¹ gRh ⁻¹ of Rh(L)HPW1:1 –SiO ₂ catalysts in the carbonylation of methanol containing Rh bound to Xantphos, Anthraphos and Terpyridine ligands. All data is quoted for catalysts in steady state at 200 °C with 1 : 1 CO/MeOH feed.	206

Table of Tables

Table 1.3.1.1: Mechanisms of catalyst deactivation	8
Table 1.8.1.1: “Value-adding properties” of polyoxometallates (summarised from reference 129)	24
Table 2.1.6.1: FWHM, peak separation and response factors used for XPS analysis.	43
Table 2.1.15.1: Mass of catalyst used for flow reactor tests.	50
Table 2.3.3.1: Elemental analysis for all RhX : HPW ratio materials studied.	61
Table 3.2.1: Elemental atom % data taken from XPS, CHN and elemental analysis studies. Stoichiometry calculated relative to 12 tungsten atoms.	70
Table 3.2.2: IR bands of DRIFTS spectra for polyoxometallates and organo-Ru framework.....	72
Table 3.2.3: ¹ H NMR assignments for RuHPW in D ₆ -DMSO.....	75
Table 3.2.4: Parameters for EXAFS fitting of Ru(Cl)(Cp)(PPh ₃) ₂ and RuHPW (with and without HPW coordination)	81
Table 3.4.1: XPS Elemental atom % data and calculated stoichiometry for RudppeHPW.....	90
Table 3.4.2: ¹ H NMR assignments for RudppeHPW in D ₆ -DMSO	91
Table 3.4.3: Parameters for EXAFS fitting of Ru(Cl)(Cp)(dppe) and RudppeHPW (with and without HPW coordination)	97

Table 3.7.1: Table comparing heterogeneous and homogeneous initial rate in phenyl acetylene oligomerisation over RuHPW, RudppeHPW, Ru(Cl)(Cp)(PPh ₃) ₂ and Ru(Cl)(Cp)(dppe).....	106
Table 4.2.1: RhXantphos and RhXHPW stoichiometries.....	120
Table 4.2.2: Fitting parameters for EXAFS analysis of RhXantphos, RhXHPW, RhXHPW1:1-SiO ₂	124
Table 4.2.2: Selected bond lengths (Å) and angles (°) for Rh(Cl)(CO)(Xantphos).....	126
Table 4.2.3: Crystallographic details for RhCl(CO)(Xantphos)·1.5THF (full details included on CD1).....	127
Table 4.5.1: Porosimetry analysis of silica supported RhXHPWs	140
Table 4.5.2: Stoichiometry based on XPS atom % of un-doped and Cs/Ag doped RhXHPW-SiO ₂	141
Table 4.5.2: Parameters for Rh K-edge EXAFS fitting of fresh and spent (250 °C and 350 °C) Cs/Ag-RhXHPW-SiO ₂	145
Table 4.6.1: mass % crystalline water (wt % crysH ₂ O) for RhXHPW-SiO ₂ series normalised to H ⁺ per Keggin.	149
Table 4.6.1: Pyridinium absorption IR bands	150
Table 6.2.1: ¹ H NMR chemical environments investigating the effect of Brønsted acidity on the nature of terpyridine.....	196

Table of Equations

Equation 1.9.1: Synthesis of phosphotungstic acid (HPW) in Keggin structure...	25
Equation 2.1.4.1: Equation for Bragg's law indicating the relationship between incident x-ray wavelength on a sample and its lattice spacing and resulting diffraction angle.	39
Equation 2.1.6.1: Binding energy calculated from XPS analysis.....	41
Equation 2.1.9.1: BET equation.....	47
Equation 2.1.9.2: Kelvin equation	48
Equation 2.1.15.1: Calculation for acetyl selectivity in methanol carbonylation experiments.....	51
Equation 3.2.1: Reaction schematic for the synthesis of RuHPW.....	70
Equation 3.6.1: Acid catalysed methanol condensation to dimethyl ether	102

Table of Schemes

Scheme 1.9.1.1: Properties and order of Keggin based heteropolyacids (reproduced from reference 120 and modified to highlight phosphotungstic acid, the heteropolyacid used in this doctoral thesis).	26
Scheme 1.10.1.1: Synthesis of a molecular hybrid containing POM clusters and a transition-metal complex linked by a conducting bridge. (taken from reference 158)	29
Scheme 3.7.1: Schematic of phenyl acetylene oligomerisation using a Ru catalyst.	103
Scheme 4.1.1: Important reaction pathways during methanol carbonylation; (1) direct methanol carbonylation to methyl acetate (2) methanol condensation to dimethyl ether (DME), (3) direct DME carbonylation to methyl acetate, (4) methanol dehydration to higher alkenes, (5) methanol reduction to higher alkanes (MTG chemistry).	114
Scheme 4.2.1: Synthesis and proposed structures of RhXantphos (1) and RhXHPW (2) from $\text{Rh}(\eta^2\text{-acac})(\text{CO})_2$	118
Scheme 4.6.1: pyridine acidic equilibrium with pyridinium ion	149
Scheme 4.8.1: Activation of MeOH on a heteropolyacid Keggin (Keg)	154
Scheme 5.2.1: Synthesis of RhAnthraphos doped HPW, hypothesised by hydride formation of the parent $\text{Rh}(\text{Anthraphos})(\text{CO})$ complex.	176
Scheme 6.2.1: Proposed synthetic route to $\text{Rh}(\eta^1\text{-acac})(\text{CO})_2(\text{terpy})$ and bulk and supported rhodium-terpy doped HPW ‘RhTHPW’.	193

Abstract

Acetic acid is an important industrial chemical, used in paints, plastics and as a solvent for many important reactions including the formation of many household polymers. As a result of this heavy demand, 8 million tonnes of acetic acid is produced annually, of which 80 % of this is produced by methanol carbonylation. Current industrial processes involve rhodium and iridium catalysed homogeneous reactions. Although these processes benefit from high selectivity and activity, they suffer from several drawbacks. Notably, those inherent to all homogeneous processes, including leaching of catalytic materials into the product stream leading to hard purification of products. In addition, current methods involve the use of methyl iodide and hydrogen iodide which are very corrosive and require the reactor vessels to be made from expensive alloys.

The use of heterogeneous catalysts in the synthesis of acetic acid would offer several process advantages, significant ease in product separation, reduced waste and possibilities to operation in a continuous reaction. Previous work by both BP and at the University of York has shown that silica supported $\text{Rh}_2(\text{OAc})_4$ -heteropolyacid systems offer potential as methanol carbonylation catalysts. Heteropolyacids are polyoxometalate inorganic cage structures, which may adopt the Keggin form with the general formula $\text{H}_3\text{MX}_{12}\text{O}_{40}$, where M is the central heteroatom and X the transition metal. Typically M can be either P or Si, and X = W or Mo. Phosphotungstic acid ($\text{H}_3\text{PW}_{12}\text{O}_{40}$, HPW) was selected as this exhibits the highest stability and strongest acidity and would serve to activate MeOH during the carbonylation process.

Following rhodium incorporation, CO binding capacity of the catalyst is increased which facilitates the carbonylation of methanol to acetic acid. However this previous work demonstrated that these catalysts suffer from rapid deactivation resulting from reduction of Rh^{n+} to $\text{Rh}(0)$. This is thought to be due to facile dissociation of the ligands from the complex under the reaction conditions.

The project explores Ru/Rh-HPW systems for catalytic application especially in heterogeneous methanol carbonylation. Alternative silica supported Ru/Rh ligand systems are examined to design a robust bifunctional catalyst, less sensitive to deactivation due to reduction. Particular focus is given to studying catalyst lifetime and both the reaction mechanism and deactivation pathway of the catalyst on-stream.

Novel compounds comprising Ru-tethered polyoxometallate Keggin anions of general formula $[\text{NEt}_3\text{H}]^+[(\text{Ru}\{\eta^5\text{-C}_5\text{H}_5\}\{\text{L}\}_2)_2(\text{PW}_{12}\text{O}_{40})]^-$ have been synthesised where $\text{L} = \text{PPh}_3$ or $1/2$ dppe showing high activity and selectivity in alkyne oligomerisation. Operando CO binding studies were performed to assess the accessibility of the Ru-centre for catalysis. Phenyl acetylene was successfully dimerised under heterogeneous catalytic regime. Selectivity towards the *E*-enyne, not found in the homogeneous $\text{RuCl}(\eta^5\text{-C}_5\text{H}_5)(\text{PPh}_3)_2$ analogue was achieved while retaining high catalytic activity ($\text{TOF } 225 \text{ h}^{-1}$). Although methanol carbonylation was not achieved Ru-POMs showed the proof of principle with catalytic activity while retaining structural integrity.

Robust, bifunctional catalysts comprising $\text{Rh}(\text{CO})(\text{Xantphos})$ exchanged phosphotungstic acids of general formulae $[\text{Rh}(\text{CO})(\text{Xantphos})]_n^+[\text{H}_{3-n}\text{PW}_{12}\text{O}_{40}]^-$ have been synthesised over silica supports which exhibit tuneable activity and selectivity towards direct vapour phase methanol carbonylation. The optimal $\text{Rh}:\text{H}^+(\text{Keggin})$ ratio = 0.5. Higher rhodium concentrations increases the selectivity to methyl acetate over dimethyl ether at the expense of lower acidity and poor activity. On-stream deactivation above $200 \text{ }^\circ\text{C}$ reflects Rh decomplexation and reduction to Rh metal, in conjunction with catalyst dehydration and loss of solid acidity due to undesired methyl acetate hydrolysis, but can be alleviated by water addition and lower temperature operation. A mechanistic insight is provided by a combination of XPS, EXAFS and *in-situ* IR indicating the role of the organoRh and HPW functionalities of activating CO and methanol respectively. The work is extended to include alternative ligand systems, substituting Xantphos for Anthrphos and Terpy respectively. These three systems are compared indicating that no improvement in stability is offered with substitution of the Rh ligand backbone and that the Xantphos system achieved superior catalytic performance at $200 \text{ }^\circ\text{C}$.

Abbreviations

- acac - acetylacetonate
- acacH - acetyl acetonate
- Acetyls - combination of acetic acid and methyl acetate
- AcOH - acetic acid
- Anthrphos - 1,5 diphenylphosphinoanthracene
- Cp - cyclopentadienyl
- Cp* - pentamethyl cyclopentadienyl
- DME - dimethyl ether
- DMSO - dimethyl sulfoxide
- dppe - diphenylphosphinoethane
- DRIFTS - diffuse reflectance infra-red fourier transform spectroscopy
- DSC - differential scanning calorimetry
- DTA - differential thermal analysis
- ESI-MS - electron spray ionisation mass spectrometry
- EXAFS - extended x-ray absorption fine structure
- FID - flame ionisation detector
- FT - Fourier transform
- FWHM - full width half maximum
- GC - gas chromatography
- GHSV - gas hourly space velocity
- HPA - hetropolyacid
- HPW - phosphotungstic acid
- i.d. - internal diameter
- Ku - Keggin Unit
- Keg - Keggin
- LHSV - liquid hourly space velocity
- MALDI-TOF - matrix assisted laser desorption time of flight
- MAS-NMR - magic angle spinning nuclear magnetic resonance
- MeOAc - methyl acetate
- MeOH - methanol
- MS - mass spectrometry
- MTG - methanol to gasoline
- NMR - nuclear magnetic resonance
- PID controller - proportional integral derivative controller
- PPh₃ - triphenyl phosphine
- RhAnthrphos - Rh(carbonyl)(diphenylphosphinoanthracene)
- RhAHPW -
[Rh(carbonyl)(diphenylphosphinoanthracene)(H)]⁺[H₂PW₁₂O₄₀]⁻
- RhAHPW-SiO₂ -
[Rh(carbonyl)(diphenylphosphinoanthracene)(H)]⁺[H₂PW₁₂O₄₀]⁻ supported on silica
- RhHPW - rhodium doped phosphotungstic acid
- RhTerpy - Rh(η²-acac)(carbonyl)₂(terpyridine)
- RhTHPW - [Rh(carbonyl)₂(terpyridine)]⁺[H₂PW₁₂O₄₀]⁻

- RhTHPW-SiO₂ - [Rh(carbonyl)₂(terpyridine)]⁺ [H₂PW₁₂O₄₀]⁻ supported on silica
- RhXantphos - Rh(η²-acac)(carbonyl)(xantphos)
- RhXHPW - [Rh(carbonyl)(xantphos)]⁺ [H₂PW₁₂O₄₀]⁻
- RhXHPW-SiO₂ - [Rh(carbonyl)₂(terpyridine)]⁺ [H₂PW₁₂O₄₀]⁻ supported on silica
- R.P.M. - Revolutions per minute
- RuHPW - [{Ru(η⁵-C₅H₅)(P(C₆H₅)₃)₂ }₂ {PW₁₂O₄₀}]
- RudppeHPW - [{Ru(η⁵-C₅H₅)(C₆H₅)₂P(CH₂)₂P(C₆H₅)₂ }₂ {PW₁₂O₄₀}]
- TCD - thermal conductivity detector
- THF - tetrahydrofuran
- TGA - thermogravimetric analysis
- TOF - turn over frequency
- TON - turn over number
- TPO/R - temperature programmed oxidation/reduction
- XANES - x-ray absorption near edge spectroscopy
- XAS - x-ray absorption spectroscopy
- XPS - x-ray photoelectron spectroscopy
- XRD - x-ray diffraction

Chapter 1 - Introduction

This thesis primarily concerns the synthesis, characterisation and catalyst testing of several solid, bifunctional, metal-doped heteropolyacid systems where the metal is Ru or Rh with an organometallic framework and the heteropolyacid is phosphotungstic acid ($\text{H}_3\text{PW}_{12}\text{O}_{40}\cdot 20\text{H}_2\text{O}$). The main focus for catalytic application is on methanol carbonylation. The organoruthenium/rhodium functionality is studied in terms of its CO binding and activating properties whereas the heteropolyacid component acts as a Brønsted acidic, methanol activating component in a heterogeneous catalytic regime to be employed in a continuous flow system.

To this end, the introduction is structured to consider catalysis, with focus on heterogeneous acid catalyst systems and their benefits over more commonly employed industrial homogeneous species. This leads into the current state of the art in methanol carbonylation catalysis where production utilises relatively simple iodide-based organorhodium/iridium homogeneous catalyst systems. Main concerns are then addressed including (1) the lack of stability of CO-activating organometallic complexes and (2) the use of highly corrosive iodide containing acids for methanol activation in an increasingly environmentally conscious world. The former is engaged by the consideration of more stable multidentate phosphine species and the latter by the use of solid heteropolyacid materials, where a high degree of tunability of the acidic nature is obtainable and the corrosive nature safely contained. The research discussed throughout this thesis demonstrates how the symbiosis of a bifunctional organometallic metal-doped heteropolyacid may be utilised for catalytic application in heterogeneous methanol carbonylation.

1.1 - Catalysis

A catalyst is a substance that accelerates a chemical reaction by providing a route with lower activation energy (**Figure 1.1.1**) but experiencing no net chemical change. This means that in a catalysed chemical reaction the catalyst may undergo several chemical changes forming transition states and/or intermediates but returns to the initial catalyst state in a cyclic mode of action, meaning it is not consumed by the reaction itself (**Figure 1.1.2**). The mechanism for catalyst mode of action is not always simple and some catalysts can have multiple parallel cycles such as the iridium catalysed CATIVATM process for methanol carbonylation discussed in Section 1.6.^{1, 2} In order for a catalytic cycle to be efficient, the intermediates must be short lived. This has the unfortunate consequence that studying these cycles can be difficult. Although a variety of conventional techniques can be employed to characterise isolated intermediates or model compounds such as NMR and IR spectroscopies, for many cycles the mechanism is not firmly established.

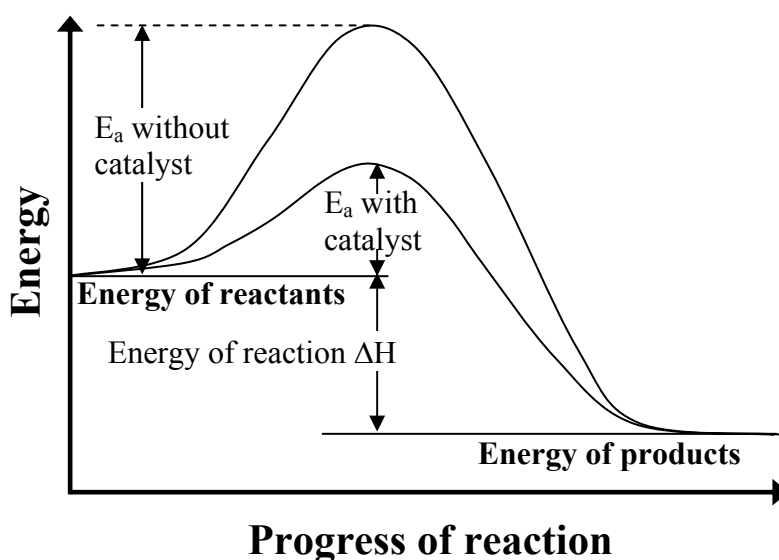


Figure 1.1.1: Reaction energy profile showing activation energy with and without a catalyst.

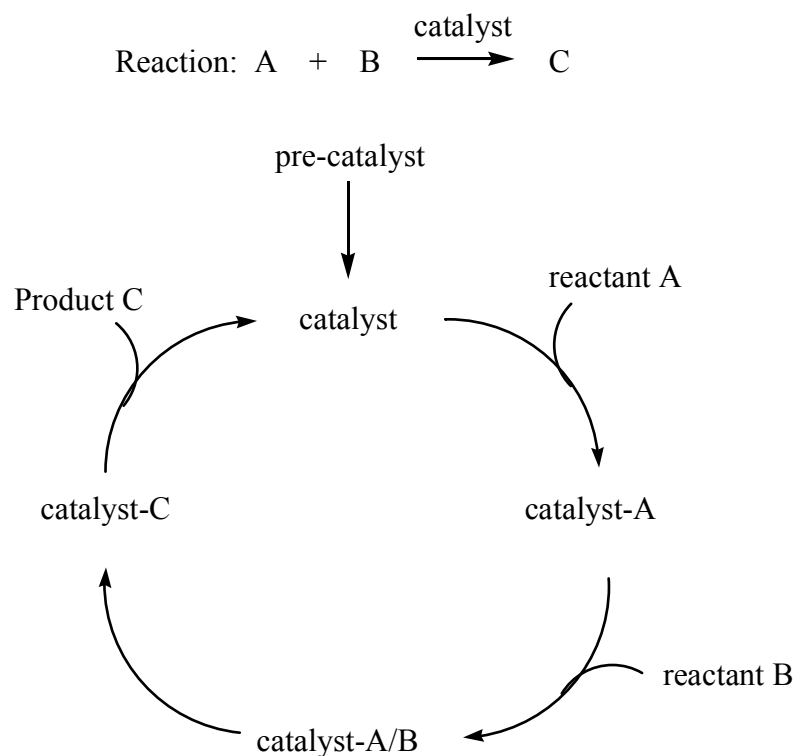


Figure 1.1.2: General catalyst cycle

From a kinetic point of view, catalytic reactions behave like typical chemical reactions, where the reaction rate depends on the frequency of contact of the reactants in the rate-determining step. Catalysts are generally separated into two sub-categories, homogeneous and heterogeneous, although some debate exists concerning the nature of some systems where ambiguity arises.³⁻⁵ Homogeneous catalysts are defined as those operating in the same phase as the components of the reaction whereas heterogeneous catalysts are present in a different phase from the components on which it is acting. As the main theme of this thesis concerns the synthesis and catalytic studies of heterogeneous systems the latter will be discussed in more detail here.

1.2 - Heterogeneous Catalysis

A heterogeneous catalyst was defined in Section 1.1 as being in a different phase to chemical reactants. Generally the catalyst is a solid where the reactants are liquids and/or gases. The main advantage of using a heterogeneous catalyst comparable to their homogeneous counterparts is the relative ease of catalyst separation from the product stream, for example by a simple filtration that aids in the creation of continuous chemical processes. Additionally, heterogeneous catalysts are typically more tolerant of extreme operating conditions than their homogeneous analogues. The former benefit depends upon the active catalyst species remaining a solid and not leaching during liquid phase processes. In this event, more complex separations may be required and periodic regeneration of the catalyst bed is necessary to restore levels of active material in the system. A heterogeneous catalytic reaction involves adsorption of reactants from a fluid phase onto a solid surface, surface reaction of adsorbed species, and desorption of products into the fluid phase. As a result, in heterogeneous catalysis, the diffusion of reagents to the surface and diffusion of products from the surface can be rate determining. Analogous events associated with substrate binding and product dissociation apply to homogeneous catalysts.

Heterogeneous catalyst implementation in industry is already well established for example the use of an iron catalyst in ammonia synthesis using the Haber Bosch process, circa 1909, for which Fritz Haber won the 1918 Nobel prize in chemistry. However studying heterogeneous catalyst systems under real environmental conditions can pose a problem due to the intrinsic nature of the various solid supported and unsupported catalyst materials. To date the most extensive studies have been performed on single crystal or methodically grown clean surfaces with known crystalline faces typically under ultra high vacuum (UHV) conditions. Notably work by Ertl on the mechanism of ammonia synthesis and carbon monoxide oxidation winning the Nobel prize for chemistry in 2008.⁶⁻⁸

1.2.1 - Heterogeneous acid catalysis

Many chemical syntheses proceed through the application of stoichiometric quantities of homogeneous acids, bases or salts. In fact over 15 million tons of sulfuric acid is annually consumed as ‘an unrecyclable catalyst’, which requires costly and inefficient separation of the catalyst from homogeneous reaction mixtures for the production of industrially important chemicals, thus resulting in a huge waste of energy and large quantities of waste products.⁹⁻¹³ This inevitably leads to the generation of large volumes of waste with accompanying treatment and disposal costs. Coupled with increasing legislation on the management of levels of toxic waste, the current trend towards alternative cleaner technologies is understandable, and is an area of significant academic and industrial research. One particular such area of great interest is the use of heterogeneous solid acid catalysts.

Acids are the catalysts which are used the most in industry, including the fields of oil refining, petrochemicals and chemicals. They are responsible for producing more than 1×10^8 million tons per year of products.¹⁴ A number of solid or supported materials are known with high acid/base strength, comparable to their currently employed homogeneous counterparts.¹⁵ The advantages of these over homogeneous analogues include; along with their handling requirements, simplicity and versatility of process engineering, and catalyst regeneration, decreasing reactor and plant corrosion problems, and environmentally safe disposal. Most of the efforts have been directed towards the preparation of a solid thermally stable catalyst in which the acid sites have the required acidity (type and strength) to catalyse a given type of chemical reaction. These solid materials are applicable as green replacements for undesirable reagents, for example Brønsted acids such as HCl and H₂SO₄, and Lewis acids including AlCl₃, ZnCl₂ and BF₃, currently used in stoichiometric amounts. A wide variety of solid acids have replaced stoichiometric acids, a trend growing since the 1940’s and now commercial applications exist for chemistries such as reforming, cracking, isomerisation, alkylation and oligomerisation particularly pertinent to the petrochemical industry (**Figure 1.2.1.1**).

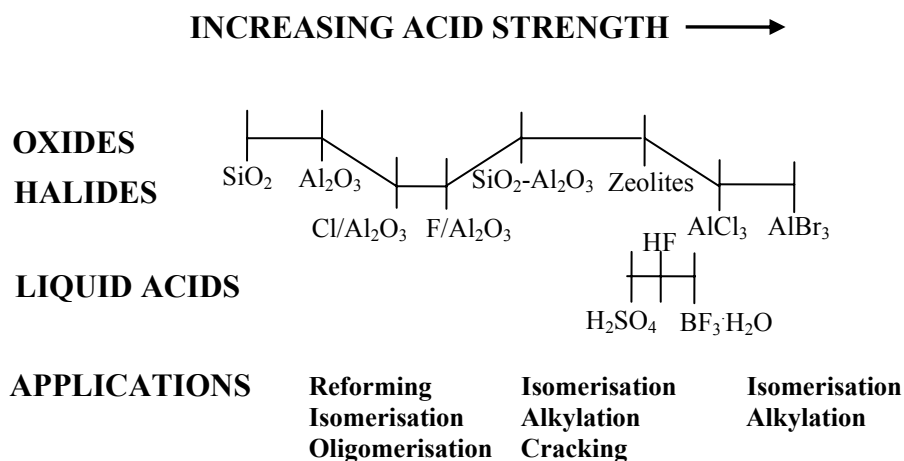


Figure 1.2.1.1: Relative acid strength of solid acids and their catalytic uses, (reproduced from reference 14).

Heterogeneous acid catalysts, as is the case for all heterogeneous catalyst materials are notoriously difficult to study and understand from a mechanistic point of view and indeed produce a consistent data set which can be used to compare against more conventional acids where data is more widely available. However, throughout the heterogeneous catalytic world, benchmarks are becoming more accessible and a deeper understanding of the nature of catalytic action achievable with the use of both calculation and probe molecule experimentation. Llevens *et al.* have described a method, providing a quantitative comparison of the properties of homogeneous and heterogeneous catalyst systems.¹⁶ They explore acidity in terms of the formation of carbenium ions using the surface of zeolites and water molecules in solutions as a model to examine properties such as the formation of the C–surface bond and the projected covalent character of the species. Where it was generally found that, hydrated carbenium ions remain more ionic than those interacting with the surface of silicates or zeolites. This can be extended to encompass other species with consideration of the electronegativity equalisation method (EEM)¹⁷ a fast method for calculating charge using *ab-initio* calculations. Additional experimental spectroscopic methods such as IR, solid state NMR and XPS have proved essential tools in understanding the nature of acid base characteristics in solid acid catalysts¹⁸⁻²⁰ most notable materials such as zeolites,²¹ heteropolyacids²²⁻²⁴ and silica and alumina materials.²⁵⁻²⁸

1.3 - Deactivation in heterogeneous catalysts

The loss of catalyst activity and/or selectivity over its lifetime is referred to as deactivation. Catalyst deactivation is one of the most challenging aspects of catalytic science, and is prevalent in the majority of heterogeneous catalysts. Arguably some of the most widely used heterogeneous catalysts such as iron-based Fischer–Tropsch and zeolitic fluid catalytic cracking catalysts are still closely scrutinised to understand and address their deactivation mechanisms.²⁹⁻³¹

Sustaining catalyst activity is a major concern for both catalyst users and manufacturers. The industrial relevance is that, by reducing catalyst deactivation, relatively small reactors can be used and operation at mild conditions is possible.³² Primarily, if the catalyst has a long life without deactivation, it can reduce the amount of catalyst replacement in a reactor. This in turn would reduce capital costs.

Catalyst selectivity is also an important factor when considering deactivation, either complete deactivation or deactivation towards the required pathway to the desired product. This is also arguably the most important issue, which decides how much of the converted reactant is the sought after product.

Typically, multiphase reactions for the fine and intermediate chemical industry are carried out in batch reactors.³³ This makes it difficult to perform deactivation studies. Reasoning is derived largely due to catalyst recycling procedures, which can cause further deactivation due to loss of catalyst or exposure to air.³⁴ This implies that there are benefits in a less complex procedure for studying deactivation in continuous processes such as those found in the trickle bed or structured catalyst reactors.^{35,36}

In gas phase reactions, ‘accelerated decay procedures’ can be used to study deactivation, *i.e.* running reaction under harsher conditions to prematurely age the catalyst.^{37,38} However, multiphase reactions restrict this kind of analysis as high temperatures are required, which can present safety issues when working at temperatures close to the boiling point. This kind of study must consider the

stability of molecules and secondary reactions, as these factors may have undesired effects on the selectivity.

1.3.1 - Key causes of deactivation

There are numerous reasons for deactivation of heterogeneous catalysts, in particular those with pure or doped metallic surfaces. The key factors are concisely discussed by Gallezot and Besson.³⁹ It is the number of issues, which adds to the complexity of deactivation studies. The potential factors of deactivation are summarised by Bartholomew⁴⁰ into six intrinsic mechanisms: poisoning, fouling, thermal degradation, vapour formation, vapour solid and solid-solid reactions, these are summarised in **Table 1.3.1.1** and a more general diagrammatic representation of typical deactivation mechanisms on the catalyst surface are represented in **Figure 1.3.1.1**⁴¹ Other factors affecting the activity in a liquid phase, catalysed reaction are impurities in solvents and reagents, and the possibility of oligomeric or polymeric by-products formation. These factors affect both activity and selectivity, which can lead to irreproducible results.

Table 1.3.1.1: Mechanisms of catalyst deactivation⁴⁰

Mechanism	Type	Brief Definition and Descriptions
Poisoning	Chemical	Strong chemisorption of species on catalytic sites, thereby blocking sites for catalytic reaction
Fouling	Mechanical	Physical deposition of species from fluid phase onto the catalytic surface and in catalytic pores - also including coke formation
Thermal degradation	Thermal	Thermally induced loss of catalytic surface area, support area, and active phase-support reactions
Vapour formation	Chemical	Reaction of gas with catalyst phase to produce volatile compound
Vapour-solid and solid-solid reactions	Chemical	Reaction of fluid, support, or promoter with catalytic phase to produce inactive phase
Attrition/crushing	Mechanical	Loss of catalytic material due to abrasion Loss of internal surface area due to mechanical induced crushing of the catalyst particle

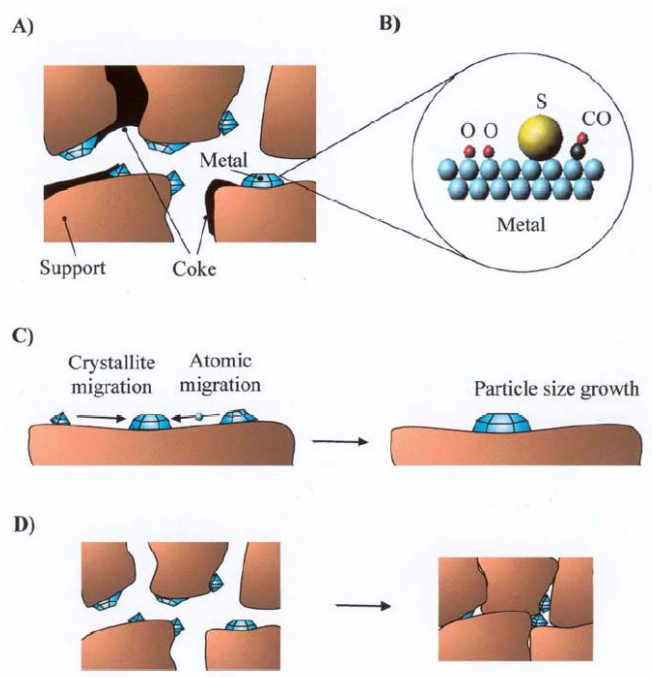


Figure 1.3.1.1: Well known deactivation mechanisms: A) coke formation, B) Poisoning, C) sintering of the active metal particles, D) Sintering and solid-solid phase transitions of the washcoat and encapsulation of active metal particles (Reproduced from reference 41).⁴¹

1.4 - Catalyst lifetime

Ideally, from a user's perspective, a catalyst would not deactivate. However in reality, an assessment of how long the catalyst should survive is often necessary to define a realistic lifetime for a catalyst to be active. The catalyst life cycle can vary enormously, for example, only a few seconds in fluid catalytic cracking (FCC)^{42,43} to the life cycle of several years, as found in iron catalysts for ammonia synthesis.⁴⁴ Ideally, for multiphase continuous systems the catalyst would remain active for many cycles to make the use of continuous processing in fine chemical synthesis more economically viable. Catalyst decay causes increased manufacturing costs, reduced process capacity and increased by-product wastage. This means the payback time for testing on catalyst deactivation and general decay can be very short and therefore justified.⁴⁵

1.5 - Acetic Acid

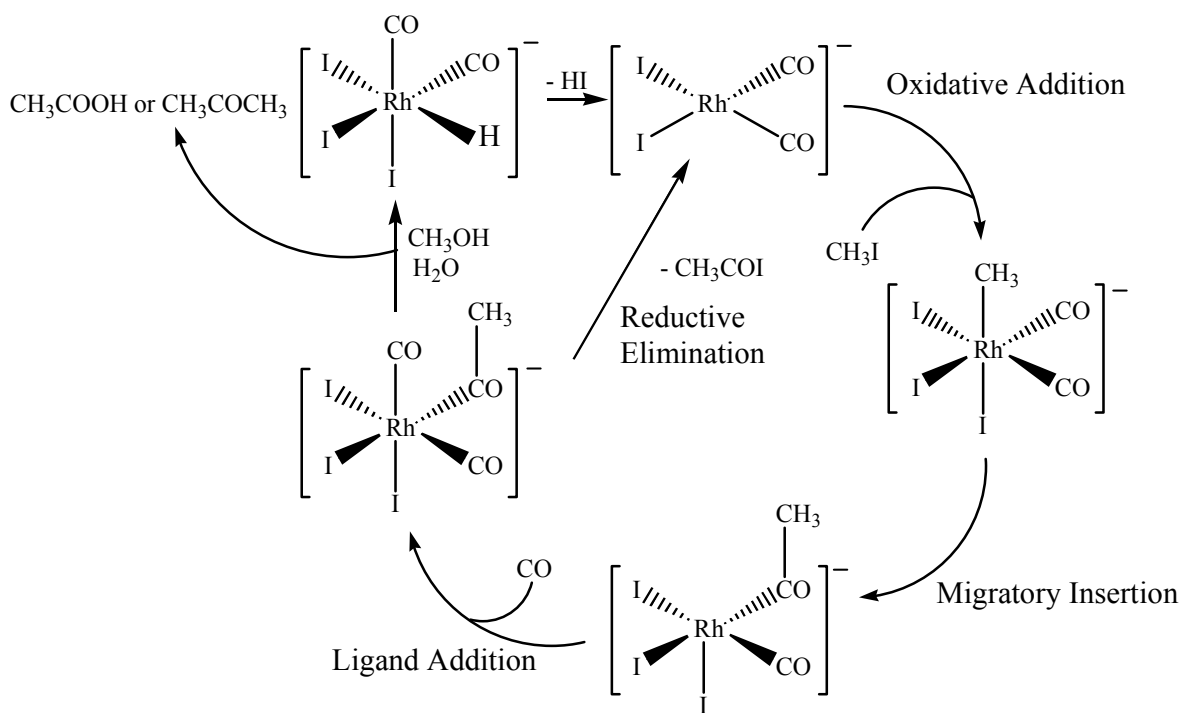
Acetic acid is one of the largest bulk chemicals produced in the world. The global capacity of acetic acid is around 8 million tons per year (Mt/a), with a demand fluctuating between 6.5 and 8 Mt/a⁴⁶ of which approximately 1.5 Mt/a is met by recycling; the remainder is manufactured from petrochemical feedstocks or from biological sources such as fermentation.

Many commercially important chemicals are derived from acetic acid,⁴⁷ including vinyl acetate which is a principal monomer, polymerised finding its use in paints, adhesives and textiles.^{48, 49} Acetic acid plays a key role as a solvent in the production of terephthalic acid, a commodity chemical used as starting chemical for polyesters used in clothing and to make plastic bottles.^{50, 51} As such an important chemical it is imperative to have an efficient economic process which can cope with the vast quantity required annually.

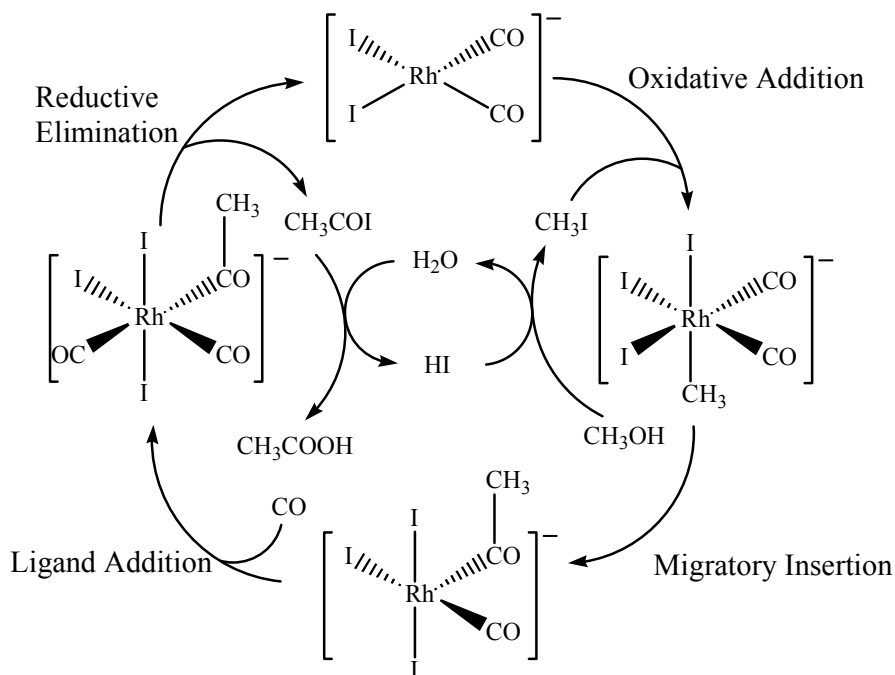
1.6 - Acetic Acid production from methanol carbonylation

Several processes have been used throughout history for the production of acetic acid. The first route was by aerobic fermentation of ethanol. Although this process has become less important, it is still used for the production of malt vinegar. Other processes have been developed which involve methanol only routes or routes from syngas.^{52, 53} However, none have gained so much acclaim as those involving methanol carbonylation.

The major methanol carbonylation processes are homogeneously catalysed by metals such as rhodium (Monsanto), iridium (BP CATIVA), cobalt (BASF) and nickel. The main processes employed are the Monsanto and CATIVA processes. These are outlined in the mechanism diagrams in **Figure 1.2.1** and **1.2.2** respectively. On a historical note, **Figure 1.2.1a** shows one of the original mechanisms proposed for the Monsanto process with the anionic *cis*-[Rh(CO)₂I₂]⁻ as the initially active catalytic species.⁵⁴ **Figure 1.2.1b**⁵⁵ shows the currently accepted mechanism. The starting *cis* Rh(I) complex is the [Rh(CO)₂(I)₂] 16 electron square planar species which undergoes an oxidative addition of MeI,



(a)



(b)

Figure 1.6.1: (a) Schematic of the first proposed mechanism for the Monsanto process (1976) for methanol carbonylation. (b) Currently accepted mechanism for the Monsanto process. Reaction steps are indicated.

generated *in-situ* from HI and MeOH, to form the Rh(III) octahedral species $[\text{Rh}(\text{CO})_2(\text{I})_3(\text{Me})]$. It is here that the ligated methyl group migrates into the Rh–C bond of an adjacent carbonyl group. A vacant co-ordination site accommodates one molecule of CO. The octahedral 18-electron acyl complex $[\text{Rh}(\text{CO})_2(\text{I})_3(\text{COMe})]$ then undergoes a reductive elimination of acetyliodide to regenerate the 16 electron starting complex. Acetyliodide is then hydrolysed to acetic acid regenerating HI for methanol activation. The proposed mechanism has not changed a great deal over the past 30 years except for the elucidation of the final formation of the acetic acid product indicated by the inner reaction cycle. The mechanism has been confirmed by isolation of intermediates and subsequent X-ray crystallography of these species⁵⁶ and by means of high pressure infrared studies.⁵⁷ The process has a selectivity of over 99 % for acetic acid with respect to methanol and over 85 % with respect to carbon monoxide. Typical conditions for the process are in the region of 150 – 200 °C at 30 – 60 bar.⁵⁸

There are several drawbacks associated with the Monsanto process. A major concern from an environmental and cost point of view is the use of corrosive iodide species including MeI and HI. Employing these species means the reactor vessels used are expensive such as zirconium metal or alloys such as Hastelloy.⁵⁹ Although the reaction is very selective, significant capital and operational costs are also incurred by the necessity of operating a large distillation column to remove low levels of high boiling point impurities, with propionic acid being the major component.⁶⁰ Another disadvantage is that the Monsanto catalyst requires a substantial amount of water (14 – 15 wt %) to maintain high activity and good catalyst stability.⁶¹ The Monsanto catalyst also catalyses the water-gas shift reaction which gives rise to the process being strongly dependent on water and hydrogen iodide concentration, this particular point was addressed with the development and implementation of the CATIVATM Ir catalysed process.

The CATIVATM process is a relatively new process having been commercialised in 1996. The process is discussed in the literature⁶²⁻⁶⁴ for its benefits in comparison to the Monsanto process. Although requiring more metal to achieve reaction rates comparable to the Rh system, it benefits from maintaining stability under low water conditions which helps to optimise

methanol carbonylation. There are two catalytic cycles responsible for methanol carbonylation; neutral and anionic (**Figure 1.6.2**). These processes differ by the amount of ligated Γ around the metal centre. The use of third-row transition metals such as Ir in an industrial homogeneous catalytic process is rare; and generally these relatively inert 5d metal complexes exhibit lower activity than their 3d and 4d (in this case Co, Rh) counterparts. Examples where Ir has exhibited desirable traits include the use of $\text{IrCl}(\text{P}(\text{HCy}_2)_3)_3$ as an analogous alternative to the well-established Rh Wilkinson's catalyst. Although this example, as expected shows lower activity (25 % conversion *c.f.* 100 % conversion under the same conditions) in the dehydrocoupling of amine-borane adducts.⁶⁵ The benefits arise from the use of bulky substrates of which Ir can accommodate more easily than metals such as Rh with a smaller atomic radius. Other advantages which are exploited in the CATIVATM process are the stronger Ir-ligand bonds and a preference for higher oxidation states which lead to equally distinct and important differences in behaviour for Ir- and Rh-based methanol carbonylation catalysts. The stronger metal-ligand bonding increases catalyst stability (by reducing susceptibility to CO-loss and precipitation of IrI_3 – the key

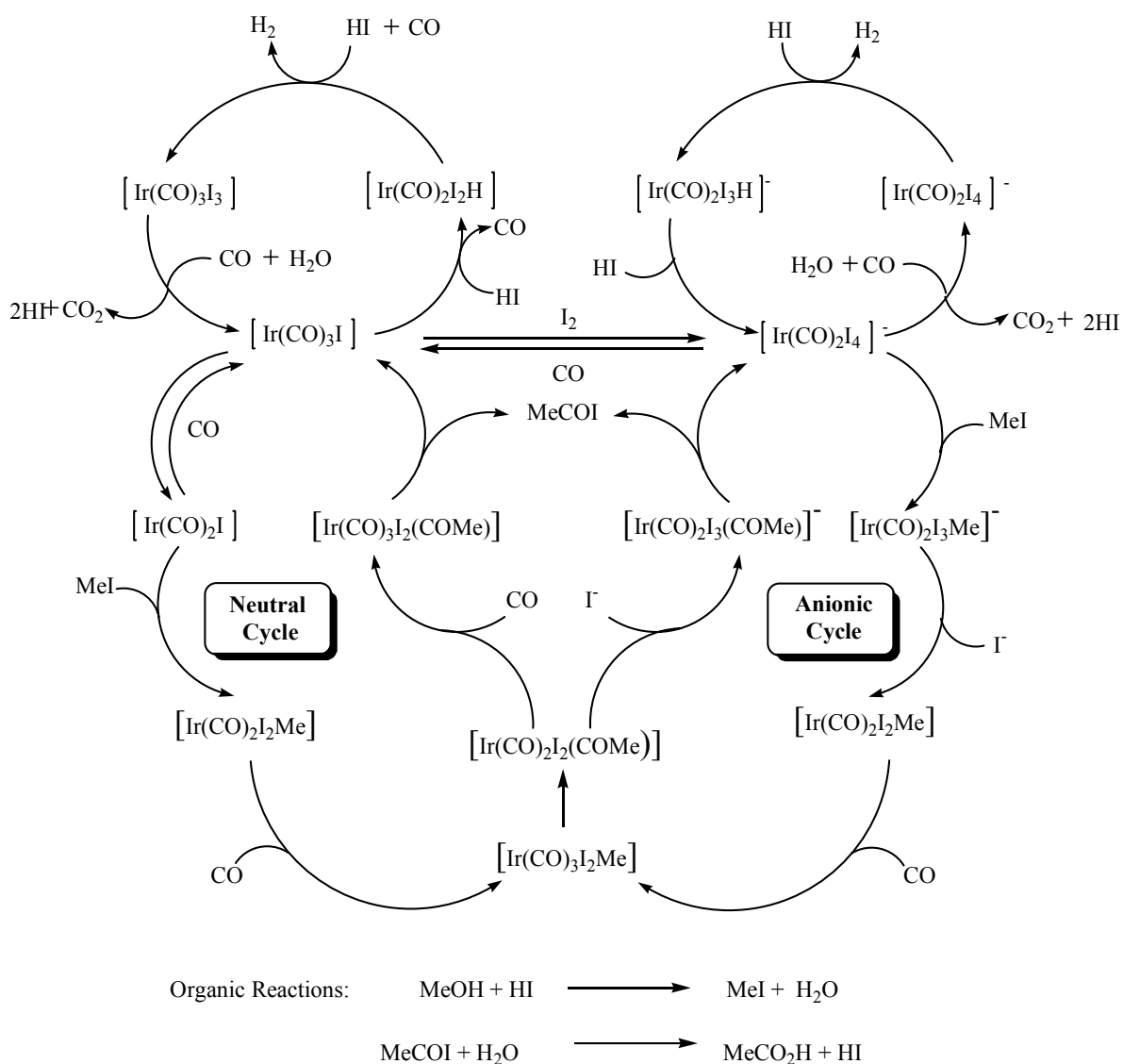


Figure 1.6.2: Both neutral and anionic pathway hypotheses for the Iridium catalysed CATIVATM process.

cause of Monsanto catalyst decomposition to inactive, inorganic Rh salts) but has a dramatic inhibitory effect on the migratory CO insertion step of the catalytic cycle. Thus carbonylation of the Ir(III) resting state methyl complex, $[\text{Ir}(\text{CO})_2\text{I}_3\text{Me}]^-$ becomes rate determining, and commercially advantageous rates are achieved only using promoters such as $[\text{Ru}(\text{CO})_3\text{I}_2]_2$ or InI_3 . These promoters have a dual role, acting as an iodide acceptor to accelerate the stoichiometric carbonylation of $[\text{Ir}(\text{CO})_2\text{I}_3\text{Me}]^-$ to $[\text{Ir}(\text{CO})_3\text{I}_2\text{Me}]$ and catalysing the reaction of $\text{HI}(\text{aq})$ with MeOAc to reduce the concentration of corrosive ionic iodides aiding in the promotion of carbonylation *via* neutral intermediates.

Although these processes benefit from high selectivity and activity they are by no means a panacea to the demands of methanol carbonylation where legislation is tightening on creating a more environmentally 'stream-lined' process, and so suffer from several drawbacks to be addressed. Notably, those inherent to all homogeneous processes, including leaching of catalytic materials into the product stream leading to hard purification of products. In addition, current methods involve the use of MeI and HI which are very corrosive and require the reactor vessels to be made from expensive alloys.⁶⁶ Catalyst systems which do not require a source of highly corrosive HI⁶⁷ or those with less corrosive active methyl intermediates such as chloromethane⁶⁸ are desirable. Halide-free technologies^{69, 70} are greatly sought after and are accessible through a variety heterogeneous solid acid sources such as zeolites⁷¹⁻⁷³ and heteropolyacids (discussed in Section 1.8) which can catalyse the direct protonation of methanol as an activated methyl source.

The use of heterogeneous catalysts in the synthesis of acetic acid would offer several process advantages, notable ease of product separation, reduced waste and possibilities to operation in a continuous reaction. Previous work by both BP and at the University of York has shown that silica supported Rh₂(OAc)₄-heteropolyacid systems offer potential as methanol carbonylation catalysts.⁷⁴

Two systems where the source of rhodium was rhodium acetate and rhodium chloride respectively, were synthesised, characterised and tested for activity in methanol carbonylation catalysis. The rhodium precursors were doped into a silica supported heteropolyacid, in this case heteropolytungstate (HPW) prepared by wet impregnation.⁷⁵ This two component system acts as a bifunctional catalyst where Rh provides a source of activated CO and the heteropolyacid functionality generates a source of Me⁺ in the form of {MeOH₂}⁺.

In the case of the latter RhCl₃ doped system, it was found that the known volatile rhodium carbonyl chloride dimer [Rh(μ-Cl)(CO)₂]₂ (**Figure 1.6.3**) is generated *in-situ*, which is possibly not surprising as it is generally used as a source for chemical vapour deposition of rhodium.^{76, 77} Reactor studies on RhCl₃/SiO₂ under 25 % flow of CO in He showed total loss of rhodium along

with crystallisation of $(\text{Rh}(\text{CO})_2\text{Cl})_2$ at the reactor outlet where exhaust gases cool to $<100\text{ }^\circ\text{C}$.

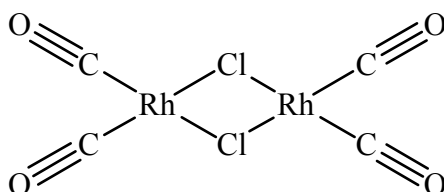


Figure 1.6.3: Rh dimer, $[\text{Rh}(\mu\text{-Cl})(\text{CO})_2]_2$ formed at the reactor exhaust from supported RhCl_3 doped HPW catalyst in the presence of 25 % CO / He gas flow.

A more successful candidate was the rhodium acetate-doped HPW which showed the formation of acetic acid due to catalysts between $\sim 200\text{ }^\circ\text{C}$ and $350\text{ }^\circ\text{C}$. Maximum acetyls were observed for the silica-supported sample (where order of impregnation had no effect on catalysis) with composition 6.0 wt % Rh / 40.9 wt % HPW / SiO_2 , whilst on a per rhodium basis, the best performing material was 0.97 wt % Rh / 17.7 wt % HPW / SiO_2 , with a turnover number of ~ 70 . Again the difficulty with such a system is reduction of the active rhodium species from Rh(II) to metallic Rh(0) due to ligand loss, on stream. In this case it can be clearly noted from reactor studies where stoichiometric acetyl formation $> 300\text{ }^\circ\text{C}$ under a vapour phase flow of methanol and CO in He is observed. This was also confirmed by XPS and EXAFS. Such a system shows promise as a viable carbonylation catalyst, because apart from the formation of dimethyl ether, an intermediate in the formation of acetyls, the catalyst is totally selective to acetyl species (acetic acid and methyl acetate) between ca. $200\text{ }^\circ\text{C}$ and $290\text{ }^\circ\text{C}$. At higher temperatures, light alkanes begin to form from methanol to gasoline (MTG) chemistry on the heteropolyacid. A possible method of stabilising such CO-activating transition metal species is the introduction of more robust organo-ligand systems capable of enhancing chemical and thermal stability in the organorhodium functionality.

1.7 - Multidentate Phosphine ligands in Catalysis

The use of ligands to form complexes with transition metals is well established and still remains a key focus in research topics spanning coordination and organometallic chemistry as well as in homogeneous catalysis. Notably, the study of their effect on the structure and reactivity of catalytic materials is of crucial importance in understanding their impact at promoting chemical reactions. The importance of phosphine ligands was first indicated by the discovery of the Wilkinson hydrogenation catalyst, $\text{RhCl}(\text{PPh}_3)_3$ (**Figure 1.7.1**).⁷⁸ Substitution at the aromatic ring of the ligand revealed an electronic effect on the reaction rate. This clearly illustrated the distinct ligand effect on the reactivity of a transition metal complex. Following from this seminal work a vast catalogue of phosphine ligands have been synthesised⁷⁹⁻⁸³ and have been applied in a vast number of catalytic reactions some notable examples include C-H activation,⁸⁴⁻⁸⁶ cross-coupling^{87, 88} and carbonylation.⁸⁹⁻⁹¹ It became clear that over the spectrum of reactions utilising phosphine ligands that the steric and electronic properties have a considerable influence on the reactivity of metal complexes.

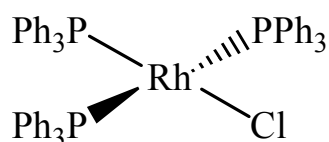


Figure 1.7.1: Wilkinson's hydrogenation catalyst $\text{RhCl}(\text{PPh}_3)_3$

As a result of the importance of these compounds as ligands several important fundamental works have become established 'tools' for the organometallic chemist in studying phosphine ligands in catalysis. It was shown by Strohmeier that the electronic properties of metal complexes can be quantified by the IR carbonyl frequencies of metal complexes.⁹² Tolman introduced a systematic approach to describe steric and electronic ligand effects.⁹³ For phosphorus ligands the cone angle θ (**Figure 1.7.2**) is defined as the apex angle of a cylindrical cone, centred 2.28 Å from the centre of the P atom, which touches the outermost atoms of the model. The electronic parameter χ is based on the difference in the IR frequencies of $\text{Ni}(\text{CO})_3\text{L}$ and the reference compound $\text{Ni}(\text{CO})_3(\text{P-}i\text{-tert-Bu}_3)$.

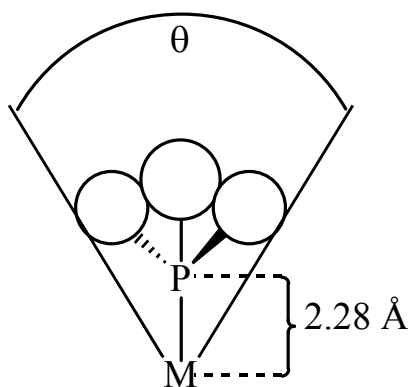


Figure 1.7.2: Tolman cone angle θ .⁹³

Although monodentate phosphines are well established and provide the majority of early examples of successful catalysis, multidentate phosphines which chelate around the central metal have shown considerable influence on increasing the stability and regioselectivity of transition metal complexes in catalysis.^{79, 94, 95} Chelational preferences of bidentate ligands are discussed by Casey and Whiteker.⁹⁶ It was in this work that concepts of the ‘natural bite angle’ and the ‘flexibility range’ for diphosphine ligands were introduced. The natural bite angle (β_n) (**Figure 1.7.3**), is defined as the preferred chelation angle determined by ligand backbone only and not by metal valence angles. The flexibility range refers to the accessible range of bite angles within less than 3 kcal mol⁻¹ excess strain energy from the calculated natural bite angle.

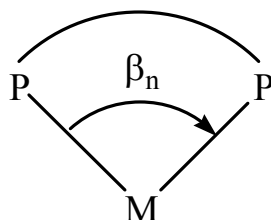


Figure 1.7.3: ‘Natural bite angle’ (β_n) defining ‘flexibility range’ of a diphosphine transition metal complex.⁹⁶

Diphosphines have shown considerable influence on the reactivity and selectivity of catalyst species. The contribution of steric and electronic effects of these ligands in catalysis has stimulated continuous study.^{97, 98} A notable study on the effect of geometrical constraints on the reactivity of metal complexes is presented by Thorn and Hoffmann.⁹⁹ An interesting observation from theoretical calculation is that during migration a phosphine ligand would have a tendency to widen the P–M–P angle in the process to move toward the migrating group. On enforcing an enlarged P–M–P angle, the transition metal complex would have the tendency to resemble the transition state and so accelerate migration reactions. This was supported by experimental observations by Dekker *et al.*, which show increasing migration rates with larger bite angles of palladium diphosphine complexes.¹⁰⁰ Following this it is generally found that rigid backbones employed in the chelation of multidentate phosphines can actually enforce a constrained geometry on the complex which indicates that a certain coordination mode can influence a reaction step of a catalytic cycle in several ways: *i.e.*, stabilisation or destabilisation of the initial, transition, or final state.¹⁰¹

One of the first successful examples of a rationally designed bidentate ligand, intended to enforce a certain conformation, is Venanzi's Transphos **Figure 1.7.4**.¹⁰² This ligand contains a rigid polyaromatic backbone, forcing the formation of *trans*-chelates. The flexibility of the ligand, however, was larger than expected; bite angles as low as 104 ° were also observed.¹⁰³ A considerable contribution to the literature by van Leeuwen *et al.*^{83, 104-106} has identified Xantphos (**Figure 1.7.5**) and derivatives as providing particularly beneficial effects in hydroformylation catalysis both conventional homogeneous and more elaborate silica supported heterogenised analogues, generating more active catalysts with greater selectivity.

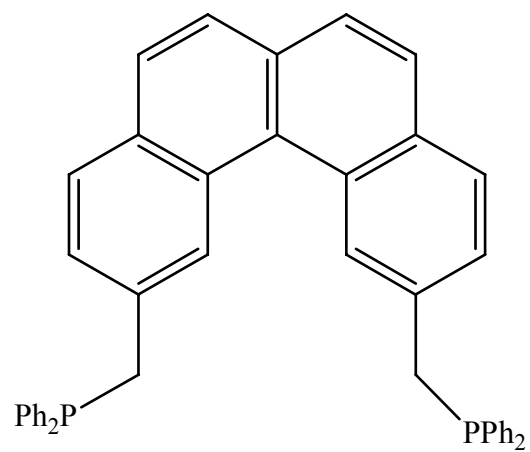


Figure 1.7.4: Transphos bidentate phosphine ligand

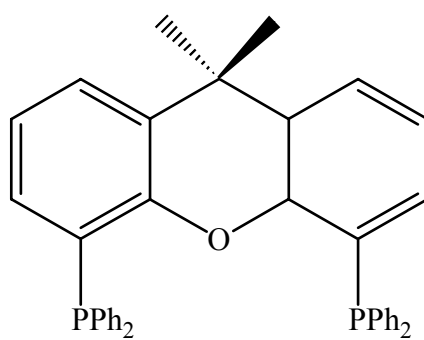


Figure 1.7.5: Xantphos bidentate phosphine ligand

1.8 - Polyoxometallates

Polyoxometallates (POMs) are a general class of inorganic oxide cage structures of which the Keggin form with general formula $H_3MX_{12}O_{40}$, where M is the central atom and X the heteroatom, is the most widely used. Typically M can be either P or Si, and X = W or Mo. Other forms of HPA exist (**Figure 1.7.1.1**), however of these only the Wells–Dawson have been studied to any level of significance,¹⁰⁷ from a catalytic perspective where a modest number of publications exists for chemistries such as esterification and oxidation where the redox properties of these species are exploited.¹⁰⁸⁻¹¹⁴ The Keggin structure

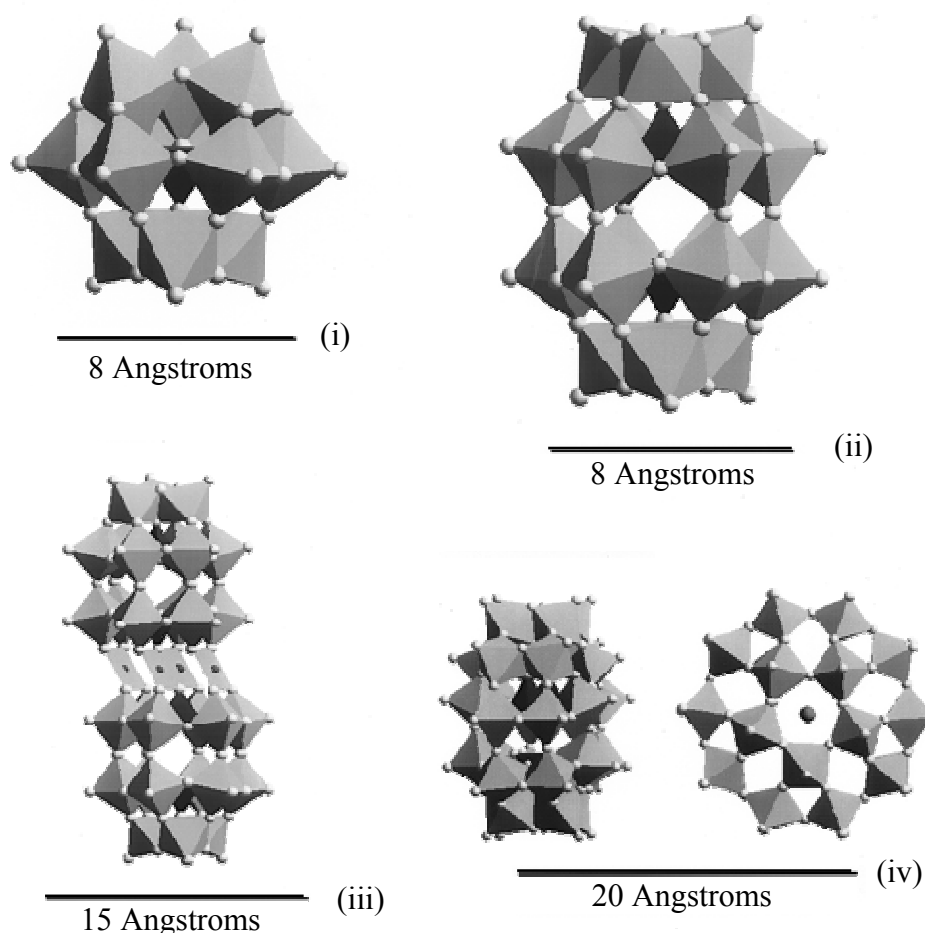


Figure 1.7.1.1: General polyoxometallate geometries: (i) Keggin, (ii) Wells–Dawson, (iii) Finke–Droege, (iv) Pope–Jeanin–Preyssier (reproduced from reference 115)

predominates due to its comparative simplicity of preparation and higher thermal stability.¹¹⁶⁻¹¹⁸ Acidity and structural accessibility factors also favour this form. Several review articles on the general properties and chemistry of Keggin and other polyoxometalate materials are available.¹¹⁹⁻¹²³

The stability combined with the extensively alterable molecular properties of POMs, including heteropolyacids (HPAs), makes them attractive as catalysts. The ease of controlling acidity, reduction potential, solubility and most key factors in catalytic turnover has led to the widespread use of POMs in both homogeneous and heterogeneous catalysis.

The highly acidic character (comparable to that of concentrated mineral acids) and oxidising potential has given them valuable attributes which have been developed to commercial acclaim. The formation of these clusters is relatively easy and they are capable of excellent interactions with solvents and supports, however, characterisation of these materials still leaves a lot of scope with some interesting avenues for mechanistic study.

1.8.1 - Chemistries involving the use of polyoxometallates (POMs)

POMs have a diverse range of applications in many fields such as catalysis, medicine, magnetochemistry, materials, surface chemistry, photochromism and electrochromism owing to the so-called “value-adding properties”.¹¹⁹

These cluster molecules have an impressive stability over a wide range of conditions as well as electron donating/accepting abilities,¹²⁴ This makes them both environmentally and economically attractive in catalysis of a myriad of organic reactions.¹²⁵⁻¹²⁷ POMs including that of the dodecatungsto (or molybdo)-phosphate anion (discussed in context with HPAs) are good at activating molecular oxygen and hydrogen peroxide giving them potential as green reagents in selective oxidation chemistry.¹²⁸ Their acidic properties give them potential in acid catalysed reactions. These two properties will be the focal points considered here.

These cluster compounds have the added interesting feature of being able to control molecular interactions. POM's can be considered as having surface structure and bulk structure. This gives rise to three different modes of catalysis. These modes are surface type, pseudo-liquid bulk type and bulk type. The surface type mode, as pictured in **Figure 1.8.1.1**, illustrates a normal heterogeneous catalytic process which occurs on the solid surface. The second two processes involve bulk interactions. POMs have a flexible solid structure which allows diffusion into the lattice, between individual anion oxidic cages. When diffusion is faster than catalysis, a pseudo-liquid phase builds up and catalysis can occur in the bulk. Acid sites are found in the bulk which gives high catalytically active bulk modes. In the pseudo-liquid bulk type mode the bulk looks like a solid but acts like a liquid. Bulk activity gives rise to selective catalytic processes.¹²²

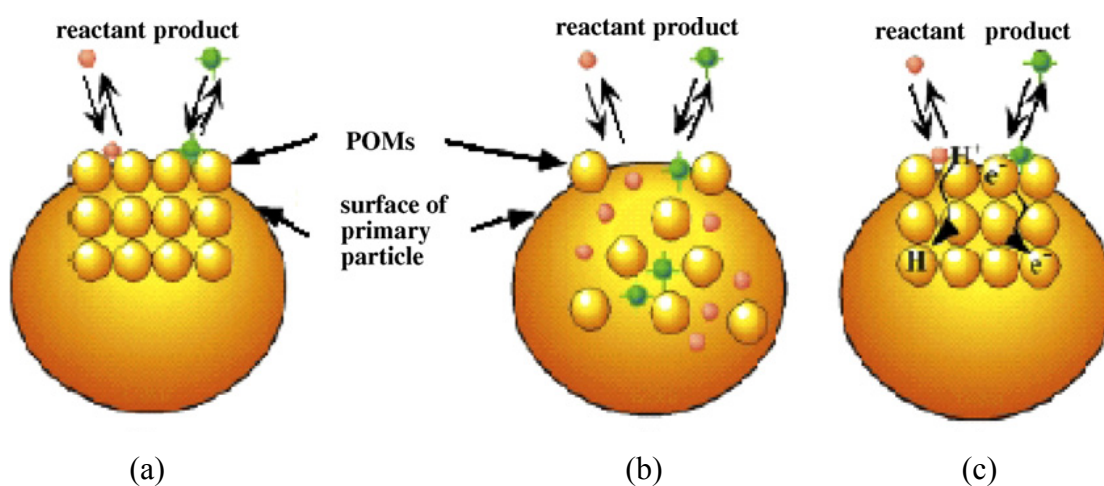


Figure 1.8.1.1: Three types of catalysis associated with solid HPA materials: (a) surface type, (b) pseudo-liquid bulk type, (c) bulk type. (taken from reference 109)

Figure 1.8.1.1 illustrates how several catalytic pathways may operate at once. These three dimensional structural properties derived from the primary through to tertiary structure of polyoxometallates.¹⁰⁹ provides many “value-adding properties” over traditional metal oxides,¹²⁹ outlined in **Table 1.8.1.1**. These often give rise to unconventional acid-base catalytic observations, several of which have been reported in the literature.^{109, 130-132} The number of polyoxometallates available is continuously growing generating an enormous library of structured

Table 1.8.1.1: “Value-adding properties” of polyoxometallates (summarised from reference 129)

Value-adding properties
large size (diameter, 6 – 25 Å)
high molecular mass (10^3 - 10^4)
High ionic charge (anion charge from -3 to -14)
Discrete size/discrete structure compared with the metallic oxides (confined geometric factors)
Strong electrolyte
Easy solubility and stability of acid forms in water and other oxygen-carrying solvents (ether, alcohols, ketones etc.)
Arrhenius acids ($pK_a < 0$)
Incorporate >70 elements - form vast number of structures: <i>processing advantage</i>
Also soluble or transferable into nonpolar solvents: <i>processing advantage</i>
Hydrolysable to form deficient structures: <i>processing advantage</i>

systems for catalytic application.¹³³ For the work explored in this thesis the acidic properties of heteropolyacids based on the polyoxometallates adopting the Keggin geometry are utilised and are therefore discussed in more detail here.

1.9 - Heteropolyacids

1.9.1 - Structure and Properties

Heteropolyacid (HPA) materials are structurally very interesting. A typical HPA of 12-tungstophosphoric acid is formed from a simple acidic condensation of phosphate ions and tungstate ions¹³⁴ (**Equation 1.9.1**).



Equation 1.9.1: Synthesis of phosphotungstic acid (HPW) in Keggin structure.

There are several structures known which are generated from mixing oxide anions of heteroatoms such as phosphorus, arsenic and silicon, with metal oxide anions of tungsten or molybdenum. The most well known structures for these HPA materials are the Keggin,¹³⁵ Keggin lacunary, and Wells–Dawson structured materials.¹³⁶ The most stable is the Keggin structure which has been demonstrated to be a closed cage of octahedral metal oxides with a central singular heteroatom (**Figure 1.9.1.1**).¹³⁷

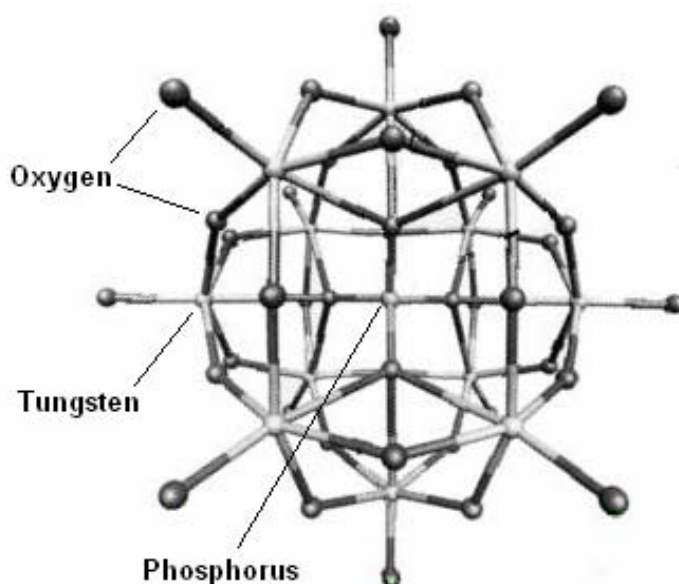
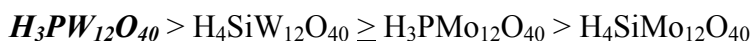


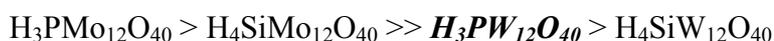
Figure 1.9.1.1: $\text{PW}_{12}\text{O}_{40}^{3-}$ Keggin unit.

The relative activity of Keggin HPAs primarily depends on their acid strength. Other properties such as the oxidation potential, which determines the reducibility of HPA by reaction medium, as well as the thermal and hydrolytic stability, are also important. These properties for the most common HPAs, which are also all part of the Keggin geometry family, are summarised in **Scheme 1.9.1.1**.

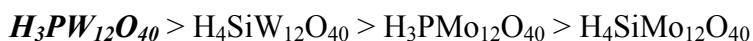
Acid strength



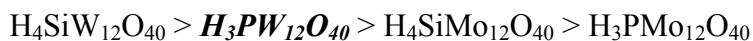
Oxidation potential



Thermal stability



Hydrolytic stability



Scheme 1.9.1.1: Properties and order of Keggin based heteropolyacids (reproduced from reference ¹²⁰ and modified to highlight phosphotungstic acid, the heteropolyacid used in this doctoral thesis).

Tungsten HPAs are generally the catalysts of choice because of their stronger acidity, higher thermal stability, and lower oxidation potential compared to molybdenum HPAs.¹²⁰ Generally, if the reaction rate is controlled by the catalyst acid strength, $H_3PW_{12}O_{40}$ shows the highest catalytic activity in the Keggin series. In light of this an extensive body of literature on bulk and supported heterogeneous as well as homogeneous catalytic processes exists for chemistries such as alkylation, isomerisation and fine chemical synthesis.^{130, 138-140} However, in the case of less demanding reactions as well as in reactions at higher temperatures (*ca.* $> \sim 300$ °C) in the presence of water, $H_4SiW_{12}O_{40}$, having lower oxidation potential and higher hydrolytic stability, can be superior to $H_3PW_{12}O_{40}$ ¹⁴¹ and is utilised in large scale commercialised technologies such as BPs AVADA® process.^{142, 143}

1.9.2 - Keggin reaction mechanism

There are many reactions where Keggin superacids have found a use as catalysts whether it be in an oxidation capacity,¹⁴⁴ or as an electron acceptor in a number of roles,¹²¹ However, although a multitude of reactions are known which involve these Keggin-based materials, mechanistic properties are seldom discussed.

An example of a reaction where the catalytic schematic was proposed is in the hydration of propene to propan-2-ol.¹⁴⁵ The Keggin crystal structure is well documented (Section 1.9.1).¹¹⁶ The $[\text{H}_5\text{O}_2]^+$ unit holding the Keggins together has developed a lot speculation about the pseudo-liquid phase which is considered to give rise to one of several catalytic pathways associated with the bulk. It is hypothesised that the crystalline water provides an environment for stable polar intermediates to be formed (**Figure 1.9.2.1**).

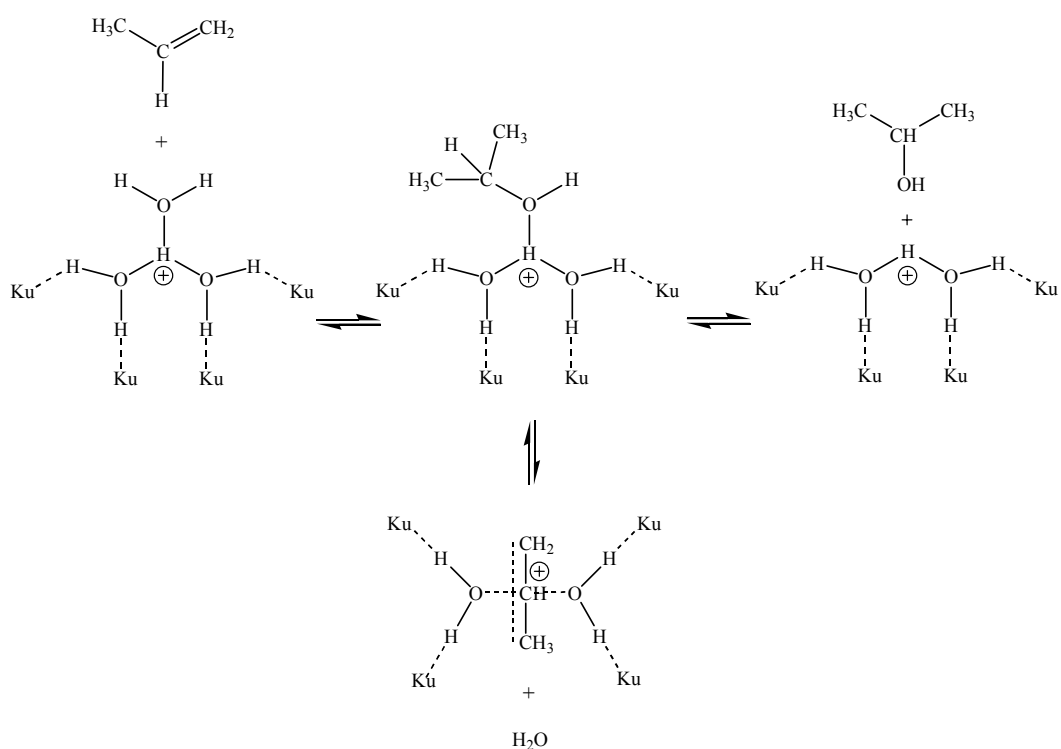


Figure 1.9.2.1: Proposed schematic for Keggin heteropolyacid catalysed propene hydration (Ku= Keggin unit).¹⁴⁵

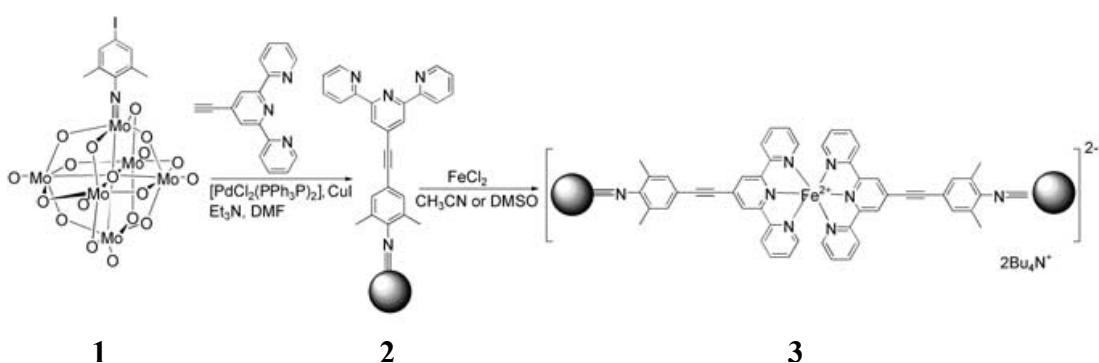
1.10 - Supported HPA materials

The mechanism discussed in the previous section is based on fundamental observations in supported HPAs where a maximum activity is observed when loading onto support materials such as SiO₂, zirconia or titania.¹⁴⁶ In heterogeneous catalysis it is generally found that supporting a catalytic material increases the surface area and therefore increasing the number of catalytic sites available for the substrate therefore improving catalytic turnover. However, in several reactions it is found that highly disperse HPAs do not exhibit the improved activity normally associated in these cases. This is where the pseudo-liquid and bulk phase hypotheses (discussed in Section 1.3.3.) become more readily accepted to explain unusual physical behaviour.

1.11 - Synthetic challenges of organic-inorganic hybrid polyoxometallates materials

Incorporation of additional functionality to Keggin polyoxometalates has been studied over several decades initially to generate simple alkyl or alkoxy groups on pendent oxygen atoms of the Keggin cage to examine possible intermediates in chemistries such as alkylation and isomerisation. These studies normally involved ³¹P or ²⁹Si (where HPAs were silica supported) solid state MAS-NMR^{147, 148} Incorporation of transition metals such as Ru with simple ligands such as DMSO are established but these are generally discussed in terms of their synthetic challenge and not with any specific application in mind.¹⁴⁹⁻¹⁵¹ Interestingly, the development of more complex tethered polyoxoanion structures have been generated where *N*-heteroaromatic species are tethered the pendant oxygen's on the polyoxometallate cage by an *N,N'*-dicyclohexylcarbodiimide dehydration,¹⁵² a technique well established for coupling amino acids in artificial peptide synthesis. Important discoveries where organoimido species with a formal Mo–N imide bond is synthesised with a substantial degree of Mo≡N triple bond character.¹⁵³ A variety of examples of these systems are documented in the literature¹⁵⁴⁻¹⁵⁷ such as the {Mo₆O₁₈} {NC₅H₄(CH₃)₂(I)} species **1** shown in **Scheme 1.10.1.1**.¹⁵⁸ These types of species provide a valuable platform for the incorporation of transition metal functionalities such as compound **3** where a functionalised bi-terpyridine

iron(II) complex is directly tethered to a polyoxometallate via polyoxometalate-functionalised tridentate terpyridine ligand **2**.



Scheme 1.10.1.1: Synthesis of a molecular hybrid containing POM clusters and a transition-metal complex linked by a conducting bridge. (taken from reference 158)

From a functional catalyst point of view these bifunctional systems are in their infancy and definitely require optimisation of synthetic procedures and an understanding of tolerance in realistic catalytic conditions. However in principle the synthesis of these organometallic-inorganic hybrid materials are a promising avenue for future study and catalytic application.

1.12 - Project Aims

The primary goal of the project is to develop a heterogeneous system for methanol carbonylation. This would offer the beneficial possibility of changing from a batch to continuous process. Previous work performed at this institution and funded by the sponsor of this work has shown that $\text{Rh}(\text{OAc})_2$ -exchanged $\text{H}_3\text{PW}_{12}\text{O}_{40}$ are promising bi-functional catalyst systems for the carbonylation of methanol to generate acetyl species. However, these systems suffer from poor stability of the rhodium complex and deactivation by reduction of the metal centre. This issue will be addressed with focus on development of a new robust ligand structure to generate a bifunctional catalytic system which is more resistant towards reduction while achieving comparable or superior activity toward methanol carbonylation.

1.13 - References

1. A. Haynes, P. M. Maitlis, G. E. Morris, G. J. Sunley, H. Adams, P. W. Badger, C. M. Bowers, D. B. Cook, P. I. P. Elliott, T. Ghaffar, H. Green, T. R. Griffin, M. Payne, J. M. Pearson, M. J. Taylor, P. W. Vickers and R. J. Watt, *Journal of the American Chemical Society*, 2004, **126**, 2847-2861.
2. P. M. Maitlis, A. Haynes, B. R. James, M. Catellani and G. P. Chiusoli, *Journal of the Chemical Society-Dalton Transactions*, 2004, 3409-3419.
3. C. Coperet, M. Chabanas, R. P. Saint-Arroman and J. M. Basset, *Angewandte Chemie-International Edition*, 2003, **42**, 156-181.
4. J. A. Widegren and R. G. Finke, *Journal of Molecular Catalysis A: Chemical*, 2003, **198**, 317-341.
5. M. Boudart, *Journal of Molecular Catalysis A: Chemical*, 1997, **120**, 271-280.
6. M. Grunze, F. Bozso, G. Ertl and M. Weiss, *Applied Surface Science*, 1978, **1**, 241-265.
7. G. Ertl, *Catalysis Reviews-Science and Engineering*, 1980, **21**, 201-223.
8. G. Ertl, *Journal of Vacuum Science & Technology A: Vacuum Surfaces and Films*, 1983, **1**, 1247-1253.
9. J. H. Clark, *Accounts of Chemical Research*, 2002, **35**, 791-797.
10. G. A. Olah, G. K. Suryaprakash and J. Sommer, *Science*, 1979, **206**, 13-20.
11. P. T. Anastas and M. M. Kirchhoff, *Accounts of Chemical Research*, 2002, **35**, 686-694.
12. P. T. Anastas and J. B. Zimmerman, *Environmental Science & Technology*, 2003, **37**, 94A-101A.
13. X. Z. Liang, S. Gao, G. Z. Gong, Y. F. Wang and J. G. Yang, *Catalysis Letters*, 2008, **124**, 352-356.
14. A. Corma, *Current Opinion in Solid State and Materials Science*, 1997, **2**, 63-75.
15. A. Corma, *Chemical Reviews*, 1995, **95**, 559-614.
16. V. B. Kazansky, W. J. Mortier, B. G. Baekelandt and J. L. Lievens, *Journal of Molecular Catalysis*, 1993, **83**, 135-143.
17. C. S. Wang, S. M. Li and Z. Z. Yang, *Theochem-Journal of Molecular Structure*, 1998, **430**, 191-199.
18. W. N. Delgass, G. L. Haller, R. Kellermann and J. H. Lunsford, *Spectroscopy in Heterogeneous catalysis*, Academic Press, inc., 1979.
19. L. Dixit and T. Rao, *Applied Spectroscopy Reviews*, 1996, **31**, 369-472.
20. J. P. O. a. R. S. Drago, *Journal of Catalysis*, 1999, **182**, 1-4.
21. V. B. Kazansky, *Catalysis Today*, 1999, **51**, 419-434.
22. E. M. S. a. C. P. Grey, *Colloids and Surfaces*, 1990, **45**, 69-82.
23. G. I. Kapustin, T. R. Brueva, A. L. Klyachko, M. N. Timofeeva, S. M. Kulikov and I. V. Kozhevnikov, *Kinetics and Catalysis*, 1990, **31**, 896-898.
24. J. A. Dias, J. P. Osegovic, R. S. Drago, *Journal of Catalysis*, 1999, **183**, 83-90.
25. A. Corma, *Chemical Reviews*, 1995, **95**, 559-614.
26. Á. Kukovecz, Z. Kónya and I. Kiricsi, *Journal of Molecular Structure*, 2001, **563-564**, 409-412.

27. C. Flego, A. Carati and C. Perego, *Microporous and Mesoporous Materials*, 2001, **44**, 733-744.
28. H. C. E. Péré, O. Cairon, M. Simon and S. Lacombe, *Vibrational Spectroscopy*, 2001, **25**, 163-175.
29. E. de Smit and B. M. Weckhuysen, *Chemical Society Reviews*, 2008, **37**, 2758-2781.
30. S. Vasireddy, A. Campos, E. Miamee, A. Adeyiga, R. Armstrong, J. D. Allison and J. J. Spivey, *Appl. Catal. A: Gen.*, **372**, 184-190.
31. H. S. Cerqueira, G. Caeiro, L. Costa and F. R. Ribeiro, *Journal of Molecular Catalysis A: Chemical*, 2008, **292**, 1-13.
32. J. A. Moulijn, A. E. van Diepen and F. Kapteijn, *Applied Catalysis A: General*, 2001, **212**, 3-16.
33. B. Chen, U. Dingerdissen, J. G. E. Krauter, H. Rotgerink, K. Mobus, D. J. Ostgard, P. Panster, T. H. Riermeier, S. Seebald, T. Tacke and H. Trauthwein, *Applied Catalysis. A: General*, 2005, **280**, 17-46.
34. P. Chin, W. S. Barney and B. A. Pindzola, *Current Opinions in Drug Discovery Development*, 2009, **12**, 848-861.
35. T. A. Nijhuis, F. M. Dautzenberg and J. A. Moulijn, *Chemical Engineering Science*, 2003, **58**, 1113-1124.
36. K. D. Deeng, A. R. Mohamed and S. Bhatia, *Chem. Eng. J.*, 2004, **103**, 147-157.
37. J. J. Birtill, in *Catalyst Deactivation*, eds. B. Delmon and G. F. Froment, Editon edn., 1999, vol. 126, pp. 43-62.
38. J. J. Birtill, *Catalysis Today*, 2003, **81**, 531-545.
39. M. Besson and P. Gallezot, *Catalysis Today*, 2003, **81**, 547-559.
40. C. H. Bartholomew, *Applied Catalysis A: General*, 2001, **212**, 17-60.
41. U. Lassi, thesis, University of Oulu, 2003.
42. X. Dupain, M. Makkee and J. A. Moulijn, *Applied Catalysis A: General*, 2006, **297**, 198-219.
43. R. H. Harding, A. W. Peters and J. R. D. Nee, *Applied Catalysis A: General*, 2001, **221**, 389-396.
44. W. Rarog-Pilecka, A. Jedynak-Koczuk, J. Petryk, E. Miskiewicz, S. Jodzis, Z. Kaszkur and Z. Kowalczyk, *Applied Catalysis A: General*, 2006, **300**, 181-185.
45. J. J. Birtill, *Focus on Catalysts*, 2004, **11**, 1-2.
46. *2010 Report on China's Acetic Acid (AA) Market*, 2010.
47. Y. H. Wang, D. H. He and B. Q. Xu, *Progress in Chemistry*, 2003, **15**, 215-221.
48. *US Pat.*, 5,347,046, 1994.
49. *US Pat.*, 5,332,710, 1994.
50. *US Pat.*, 5,563,293, 1996.
51. G. P. Karayannidis and D. S. Achilias, *Macromolecular Materials Engineering*, 2007, **292**, 128-146.
52. A. Takeuchi and J. R. Katzer, *Journal of Physical Chemistry*, 1981, **85**, 937-939.
53. S. D. Jackson, B. J. Brandreth and D. Winstanley, *Journal of Catalysis*, 1987, **106**, 464-470.
54. D. Forster, *Journal of the American Chemical Society*, 1976, **98**, 846-848.
55. M. C. Thomas, PhD thesis, 2002.
56. F. E. Paulik and J. F. Roth, *Chemical Communications*, 1968, 1578-1579.

57. A. Haynes, B. E. Mann, D. J. Gulliver, G. E. Morris and P. M. Maitlis, *Journal of the American Chemical Society*, 1991, **113**, 8567-8569.
58. M. J. Howard, M. D. Jones, M. S. Roberts and S. A. Taylor, *Catalysis Today*, 1993, **18**, 325-354.
59. S. Zhang, Q. Qian and G. Yuan, *Catalysis Communications*, 2006, **7**, 885-888.
60. J. H. Jones, *Platinum Metals Review*, 2000, **44**, 94-105.
61. A. Haynes, B. E. Mann, G. E. Morris and P. M. Maitlis, *Journal of the American Chemical Society*, 1993, **115**, 4093-4100.
62. *EU Pat.*, 0786447, 1997.
63. *EU Pat.*, 0643034, 1994.
64. *EU Pat.*, 0752406, 1995.
65. M. E. Sloan, T. J. Clark and I. Manners, *Inorganic Chemistry*, 2009, **48**, 2429-2435.
66. H. Jiang, Z. Y. Liu, P. L. Pan and G. Q. Yuan, *Journal of Molecular Catalysis A: Chemical*, 1999, **148**, 215-225.
67. Q. L. Qian, S. F. Zhang and G. Q. Yuan, *Catalysis Communications*, 2007, **8**, 483-487.
68. D. R. Fernandes, N. Rosenbach and C. J. A. Mota, *Applied Catalysis A: General*, 2009, **367**, 108-112.
69. G. G. Volkova, L. M. Plyasova, A. N. Salanov, G. N. Kustova, T. M. Yurieva and V. A. Likholobov, *Catalysis. Letters*, 2002, **80**, 175-179.
70. G. G. Volkova, L. M. Plyasova, L. N. Shkuratova, A. A. Budneva, E. A. Paukshtis, M. N. Timofeeva and V. A. Likholobov, in *Natural Gas Conversion VII*, Editon edn., 2004, vol. 147, pp. 403-408.
71. D. G. H. -E. Maneck, I. Burkhardt, B. Luecke, H. Miessner and U. Wolf, *Catalysis Today*, 1988, **3**, 421-429.
72. Y. J. Jiang, M. Hunger and W. Wang, *Journal of the American Chemical Society*, 2006, **128**, 11679-11692.
73. W. Wang, M. Seiler and M. Hunger, *Journal of Physical Chemistry B*, 2001, **105**, 12553-12558.
74. A. D. Newman, PhD Thesis, York, 2007.
75. A. D. Newman, D. R. Brown, P. Siril, A. F. Lee and K. Wilson, *Physical Chemistry Chemical Physics*, 2006, **8**, 2893-2902.
76. P. S. Jean-Cyrille Hierso, Roselyne Feurer, Philippe Kalck, *Applied Organometallic Chemistry*, 1998, **12**, 161-172.
77. R. F. a. P. K. Jean-Cyrille Hierso, *Coordination Chemistry Reviews*, 1998, **178-180**, 1811-1834.
78. J. F. Young, J. A. Osborn, F. A. Jardine and G. Wilkinson, *J. Chem Soc Chem Comm*, 1965, 131-132.
79. B. Breit, *Angewandte Chemie-International Edition*, 2005, **44**, 6816-6825.
80. D. Aguila, E. Escribano, S. Speed, D. Talancon, L. Yerman and S. Alvarez, *Journal of the Chemical Society-Dalton Transactions*, 2009, 6610-6625.
81. W. M. Dai, Y. N. Li, Y. Zhang, C. Y. Yue and J. L. Wu, *Chemistry-A European Journal*, 2008, **14**, 5538-5554.
82. P. C. J. Kamer, P. W. N. van Leeuwen and J. N. H. Reek, *Accounts of Chemical Research*, 2001, **34**, 895-904.
83. L. A. van der Veen, P. K. Keeven, P. C. J. Kamer and P. van Leeuwen, *Journal of the Chemical Society-Dalton Transactions*, 2000, 2105-2112.

84. W. Baratta, M. Ballico, A. Del Zotto, E. Zangrando and P. Rigo, *Chemistry-a European Journal*, 2007, **13**, 6701-6709.
85. M. L. Deem, *Coordination Chemistry Reviews*, 1986, **74**, 101-125.
86. A. D. Ryabov, *Chemical Reviews*, 1990, **90**, 403-424.
87. M. N. Birkholz, Z. Freixa and P. van Leeuwen, *Chemical Society Reviews*, 2009, **38**, 1099-1118.
88. Z. Freixa and P. van Leeuwen, *Coordination Chemistry Reviews*, 2008, **252**, 1755-1786.
89. C. M. Thomas and G. Suss-Fink, *Coordination Chemistry Reviews*, 2003, **243**, 125-142.
90. S. F. Zhang, C. Y. Guo, Q. Qian and G. Q. Yuan, *Catalysis Communications*, 2008, **9**, 853-858.
91. S. F. Zhang, Q. L. Qian, C. Y. Guo and G. Q. Yuan, *Acta Chimica Sinica*, 2009, **67**, 59-64.
92. Strohmei.W and F. J. Muller, *Chem. Ber.-Recl.*, 1967, **100**, 2812-2821.
93. C. A. Tolman, *Chem. Rev.*, 1977, **77**, 313-348.
94. C. A. Bessel, P. Aggarwal, A. C. Marschilok and K. J. Takeuchi, *Chemical Reviews*, 2001, **101**, 1031-1066.
95. M. Kranenburg, Y. E. M. Vanderburgt, P. C. J. Kamer, P. Vanleeuwen, K. Goubitz and J. Fraanje, *Organometallics*, 1995, **14**, 3081-3089.
96. C. P. Casey and G. T. Whiteker, *Israel Journal of Chemistry*, 1990, **30**, 299-304.
97. P. Dierkes and P. van Leeuwen, *Journal of the Chemical Society-Dalton Transactions*, 1999, 1519-1529.
98. Z. Freixa and P. van Leeuwen, *Journal of the Chemical Society-Dalton Transactions*, 2003, 1890-1901.
99. D. L. Thorn and R. Hoffmann, *Journal of the American Chemical Society*, 1978, **100**, 2079-2090.
100. G. Dekker, C. J. Elsevier, K. Vrieze, P. Vanleeuwen and C. F. Roobeek, *J. Organomet. Chem.*, 1992, **430**, 357-372.
101. J. A. Gillespie, D. L. Dodds and P. C. J. Kamer, *Journal of the Chemical Society-Dalton Transactions*, **39**, 2751-2764.
102. N. J. Destanfo, D. K. Johnson and D. K. Venanzi, *Angewandte Chemie-International Edition*, 1974, **86**, 133
103. G. Bracher, D. M. Grove, L. M. Venanzi, F. Bachechi, P. Mura and L. Zambonelli, *Helv. Chim. Acta*, 1980, **63**, 2519-2530.
104. L. A. van der Veen, P. H. Keeven, G. C. Schoemaker, J. N. H. Reek, P. C. J. Kamer, P. van Leeuwen, M. Lutz and A. L. Spek, *Organometallics*, 2000, **19**, 872-883.
105. L. A. van der Veen, M. D. K. Boele, F. R. Bregman, P. C. J. Kamer, P. van Leeuwen, K. Goubitz, J. Fraanje, H. Schenk and C. Bo, *Journal of the American Chemical Society*, 1998, **120**, 11616-11626.
106. L. A. van der Veen, P. C. J. Kamer and P. van Leeuwen, *Angewandte Chemie-International Edition*, 1999, **38**, 336-338.
107. H. T. a. C. A. Q. G. Baronetti, *Applied Catalysis A: General*, 2001, **217**, 131-141.
108. G. Busca, *Chemical Reviews*, 2007, **107**, 5366-5410.
109. G. X. Li, Y. Ding, J. M. Wang, X. L. Wang and J. S. Suo, *Journal of Molecular Catalysis A: Chemical*, 2007, **262**, 67-76.
110. K. Okumura, S. Ito, M. Yonekawa, A. Nakashima and M. Niwa, *Topics in Catalysis*, 2009, **52**, 649-656.

111. A. Tarlani, A. Riahi, M. Abedini, M. M. Amini and J. Muzart, *Journal of Molecular Catalysis A: Chemical*, 2006, **260**, 187-189.
112. A. X. Tian, Z. G. Han, J. Peng, J. L. Zhai, B. X. Dong and J. Q. Sha, *Journal of Coordination Chemistry*, 2007, **60**, 1645-1654.
113. D. R. Park, S. Park, Y. Bang and I. K. Song, *Applied Catalysis A: General*, 2010, **373**, 201-207.
114. D. R. Park, S. Park, J. H. Choi and I. K. Song, *Catalysis Letters*, 2010, **135**, 269-274.
115. I. K. S. Mahmoud S. Kaba, Dean C. Duncan, Craig L. Hill, and Mark A. Barteau, *Inorganic Chemistry*, 1998, **37**, 398-406.
116. G. M. Brown, M. R. Noe-Spirlet, W. R. Busing and H. A. Levy, *Acta Crystallographica, Section B-Structural Crystallography and Crystal Chemistry*, 1977, **33**, 1038-1046.
117. B. K. Hodnett and J. B. Moffat, *Journal of Catalysis*, 1985, **91**, 93-103.
118. B. W. L. Southward, J. S. Vaughan and C. T. Oconnor, *Journal of Catalysis*, 1995, **153**, 293-303.
119. I. V. Kozhevnikov, *Catal. Rev. Sci. Eng.*, 1995, **37**, 311-352.
120. I. V. Kozhevnikov, *Chemical Reviews*, 1998, **98**, 171-197.
121. N. Mizuno and M. Misono, *Chemistry Review*, 1998, **98**, 199-218.
122. T. Okuhara, N. Mizuno and M. Misono, *Advances in Catalysis*, 1996, **41**, 113-252.
123. T. Okuhara, N. Mizuno and M. Misono, *Applied Catalysis A: General*, 2001, **222**, 63-77.
124. I. V. Kozhevnikov, *Chemical Reviews*, 1998, **98**, 171-198.
125. Y. Liu, K. Murata and M. Inaba, *Catalysis Communications*, 2005, **6**, 679-683.
126. M. Misono, *Catalysis Today*, 2005, **100**, 95-100.
127. J. Pozniczek, A. Micek-Ilnicka, A. Lubanska and A. Bielanski, *Applied Catalysis A: General*, 2005, **286**, 52-60.
128. J. M. Bregeault, M. Vennat, L. Salles, J. Y. Piquemal, Y. Mahha, E. Briot, P. C. Bakala, A. Atlamsani and R. Thouvenot, *Journal of Molecular Catalysis A: Chemical*, 2006, **250**, 177-189.
129. D. E. Katsoulis, *Chemical Reviews*, 1998, **98**, 359-387.
130. A. D. Newman, A. F. Lee, K. Wilson and N. A. Young, *Catalysis. Letters*, 2005, **102**, 45-50.
131. M. J. Janik, R. J. Davis and M. Neurock, *Catalysis Today*, 2005, **105**, 134-143.
132. K. A. da Silva Rocha, I. V. Kozhevnikov and E. V. Gusevskaya, *Applied Catalysis A: General*, 2005, **294**, 106-110.
133. W. G. Klemperer and C. G. Wall, *Chemical Reviews*, 1998, **98**, 297-306.
134. R. Contant and G. Herve, *Reviews in Inorganic Chemistry*, 2002, **22**, 63-111.
135. J. F. Keggin, *Nature*, 1933, **131**, 908-909.
136. L. E. Briand, G. T. Baronetti and H. J. Thomas, *Applied Catalysis A: General*, 2003, **256**, 37-50.
137. J. F. Keggin, *Proceedings of the Royal Society: A* 1934, **144**, 75-100.
138. B. B. Bardin and R. J. Davis, *Applied Catalysis A: General*, 2000, **200**, 219-231.
139. S. Kumar, *Journal of Molecular Catalysis A: Chemical*, 2006, **260**, 49-55.
140. C. Yuan, F. Zhang, J. Wang and X. Ren, *Catalysis Communications*, 2005, **6**, 721-724.

141. M. N. Timofeeva, *Applied Catalysis A: General*, 2003, **256**, 19-35.
142. M. P. Atkins, *Topics in Catalysis.*, 2003, **24**, 185-186.
143. B. Harrison, *Platinum metals review*, 2001, **45**, 12.
144. R. Neumann and H. Miller, *Journal of the Chemical Society Chemical Communications*, 1995, **22**, 2277-2278.
145. A. V. Ivanov, E. Zausa, Y. B. Taarit and N. Essayem, *Applied Catalysis A: General*, 2003, **256**, 225-242.
146. Y. Izumi, R. Hasebe and K. Urabe, *Journal of Catalysis*, 1983, **84**, 402-409.
147. W. H. Knoth and R. L. Harlow, *Journal of the American Chemical Society*, 1981, **103**, 4265-4266.
148. W. H. Knoth and R. D. Farlee, *Inorganic Chemistry*, 1984, **23**, 4765-4766.
149. L. H. Bi, F. Hussain, U. Kortz, M. Sadakane and M. H. Dickman, *Chemical Communications*, 2004, 1420-1421.
150. L. H. Bi, U. Kortz, B. Keita and L. Nadjo, *Journal of the Chemical Society-Dalton Transactions*, 2004, 3184-3190.
151. L. H. Bi, M. H. Dickman, U. Kortz and I. Dix, *Chemical Communications*, 2005, 3962-3964.
152. L. Zhu, Y. L. Zhu, X. G. Meng, J. Hao, Q. Li, Y. G. Wei and Y. B. Lin, *Chemistry-a European Journal*, 2008, **14**, 10923-10927.
153. Q. Li, P. Wu, Y. Xia, Y. Wei and H. Guo, *Journal of Organometallic Chemistry*, 2006, **691**, 1223-1228.
154. Y. G. Wei, B. B. Xu, C. L. Barnes and Z. H. Peng, *Journal of the American Chemical Society*, 2001, **123**, 4083-4084.
155. Q. Li, P. F. Wu, Y. Xia, Y. G. Wei and H. Y. Guo, *Journal of Organometallic Chemistry*, 2006, **691**, 1223-1228.
156. Z. C. Xiao, Y. Zhu, Y. G. Wei and Y. Wang, *Inorganic Chemistry Communications*, 2006, **9**, 400-402.
157. Q. Li, L. Zhu, X. G. Meng, Y. L. Zhu, J. Hao and Y. G. Wei, *Inorganica Chimica Acta*, 2007, **360**, 2558-2564.
158. J. Kang, B. B. Xu, Z. H. Peng, X. D. Zhu, Y. G. Wei and D. R. Powell, *Angewandte Chemie-International Edition*, 2005, **44**, 6902-6905.

Chapter 2 - Experimental

2.1 - Characterisation

2.1.1 - Thermogravimetric Analysis TGA and Differential thermal analysis

Thermogravimetric analysis (TGA) temperature programmed oxidation (TPO) and temperature programmed reduction (TPR) measurements were performed on a Stanton Redcroft STA-780 series thermal analyser. All samples were analysed in an alumina sample cup with a mass of *ca.* 15 mg. An identical alumina cup with 15 mg of alumina powder was used to help stabilise the sample holder balance and as a reference cup. For TGA the sample was exposed to an inert atmosphere using a gas flow of 20 ml min⁻¹ He. TPO and TPR analysis employed a gas composition of 16 ml min⁻¹ He and 4 ml min⁻¹ O₂ or H₂ respectively. A temperature ramp was programmed for 20 °C min⁻¹ up to 1000 °C. Differential Thermal Analysis (DTA) data and mass loss (from TGA/TPO/TPR) data was collected using PICOscope data logging software.¹ TGA measures changes in weight of a sample with increasing temperature. Water content and presence of volatile species can be determined with this technique. DTA measures the difference in temperature between a sample and a thermally inert reference (Al₂O₃) as the temperature is raised. This technique employs differential scanning calorimetry (DSC) to measure the heat flow (heat energy / time) within the material. A change in heat flow is indicative of a thermal process typically indicative of a phase change within the sample. The plot of this differential provides information on exothermic and endothermic processes taking place in the sample. Temperatures for phase transitions, melting points and changes in crystallinity can be determined using this data. Endothermic processes with mass losses below 200 °C are generally associated with loss of solvent or crystalline water from heteropolyacid species. Dissociation of ligands from Ru/Rh centres such as triphenylphosphine or Xantphos and subsequent decomposition tend to provide exothermic processes between *ca.* 250 °C and 500 °C. Exothermic decomposition above 600 °C are due to decomposition of the heteropolyacid

phosphotungstate cage.² TPO and TPR analysis of spent catalysts were used to clean the surface of the catalyst where some remaining product/starting material is retained. Methanol and acetyl species such as methyl acetate and acetic acid can be oxidised in the presence of a dilute flow of oxygen in the gas feed to CO₂ which is lost with an observed exothermic evolution. Conversely, reduction under a dilute flow of H₂ in He affords alkanes at temperatures greater than 200 °C.³ This is also useful for the removal of any coke formation which is prevalent from MTG chemistry catalysed by heteropolyacid catalysts at temperatures greater than 300 °C.^{4, 5}

2.1.2 - Diffuse Reflectance Infrared Fourier Transform Spectroscopy (DRIFTS)

DRIFTS analysis was performed using a Thermo electron corporation Nicolet Avatar 370 spectrometer with KBr beam splitter and windows. An MCT detector was used with smart collector accessory for DRIFTS analysis. Data was collected using OMNIC analytical software. The resolution of spectra was 2 cm⁻¹ over a scan range of 650 – 4000 cm⁻¹ with a signal gain of 1 for *ex-situ* experiments and 8 for *in-situ* (due to the reduction in exposed sample surface). Closed IR cell measurements were performed in a thermo scientific environmental chamber with Zinc selenide windows (**Figure 2.1.2.1**) (C). Gasses (D) were controlled using an MKS instruments MK5059 mass flow controller and Edwards MFC controller unit with CHELL calibration. Typical gas flows were between 5 – 20 ml min⁻¹. Temperature controlled experiments were performed using a 3200 series Eurotherm PID controller (A). Water cooling (B) was integrated into the sample chamber to stabilise temperature during data collection.

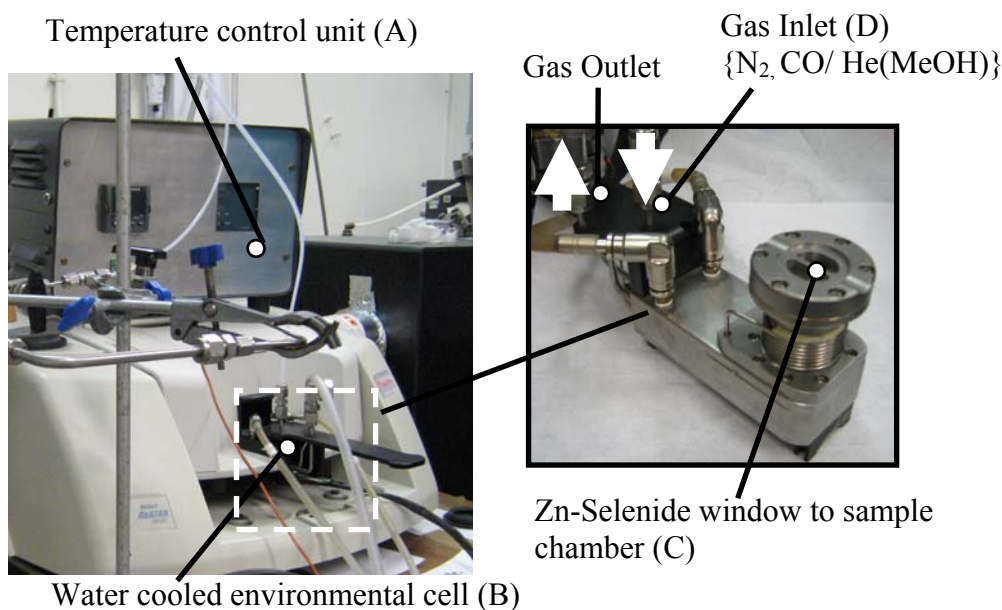


Figure 2.1.2.1: (left) *in-situ* DRIFTS apparatus (right) sample cell showing gas inlet and outlet.

For thermal experimental studies, the sample was typically purged with N₂ at 20 ml min⁻¹ at 25 °C for 5 minutes where a spectrum was collected with 128 scans. The sample was then heated to 50 °C at 10 °C min⁻¹ under a flow of N₂ at 20 ml min⁻¹ where a second spectrum was recorded after a dwell time of 5 minutes. This process was then repeated with 50 °C intervals up to 350 °C. For measurements under CO, samples were heated in the same way under a flow of nitrogen with the flow switched to a premixed 5 % CO in He gas mixture at 20 ml min⁻¹ for 5 minutes. A spectrum was taken to confirm the presence of CO in the sample cell with a band at 2120 cm⁻¹ for gaseous CO and a broad band at 2180 cm⁻¹ indicative of weakly surface bound physisorbed CO.^{6, 7} This was followed by a 5 minute purge under nitrogen. A spectrum of the purged sample was collected with further measurements following the same protocol performed in 50 °C intervals up to 350 °C where the sample was cooled under nitrogen. Where CO and MeOH were dosed on to the sample the 5 % CO / He gas mixture was bubbled through a methanol or D₄-methanol reservoir allowing methanol vapour and CO to be passed over the sample simultaneously.

2.1.3 - Raman Spectroscopy

Raman spectroscopy was performed by Dr Nigel Young at Hull University. Raman spectra were collected in 180° scattering geometry from neat samples using a Bruker FRA 106/S Raman module mounted on a Bruker Equinox 55 FTIR bench with a cw Nd-YAG 1064 nm laser operating at 100-400 mW, a CaF_2 beam splitter and liquid nitrogen cooled Ge detector.

2.1.4 - Powder X-ray Diffraction

Powder X-ray Diffraction (XRD) patterns were recorded using a Bruker AXS D8 diffractometer with a Cu K_α X-ray source. This was equipped with a PSD Lynx eye detector running with 40 kV and 40 mA. Scans typically took ~ 7 minutes and scanned between 2θ , $5 - 80^\circ$ in reflection mode with a step size of 0.02° and 0.1 seconds dwell time per step. Specific angle ranges were chosen where peaks were visible.

The X-ray source fires photons ($\lambda = 1.54 \text{ \AA}$) at a homogeneous (i.e. powdered) solid. Although in a powdered material particles will be randomly orientated, a certain fraction of these will be orientated so that the crystalline material has a crystal plane at the correct angle for constructive interference.⁸ Lattice spacings for various planes are characteristic for different solids giving diffraction patterns according to Bragg's law (**Equation 2.1.4.1**). For further discussion on powder XRD see reference.⁹

Equation 2.1.4.1: Equation for Bragg's law indicating the relationship between incident x-ray wavelength on a sample and its lattice spacing and resulting diffraction angle.

$$n\lambda = 2d \sin \theta$$

n = order of interference (integer), **λ** = incident wavelength, **d** = lattice spacing,
 θ = diffraction angle

2.1.5 - Single Crystal XRD

Single crystal XRD analysis was performed by Dr Adrian Whitwood in the University of York Small Molecule X-ray Crystallography service. A Bruker Smart Apex instrument was employed equipped with a 3-circle goniometer, 2 kW Mo X-ray source and SMART CCD detector. The sample was run at 110 K using a liquid nitrogen cooling system.

2.1.6 - X-Ray Photoelectron Spectroscopy (XPS)

X-ray photoelectron spectroscopy (XPS) allows surface elemental analysis and characterisation of differing chemical environments in catalysts, therefore allowing characterisation of active and decomposed species on the surface. XPS, works by firing monochromatic X-rays at the sample surface, synchrotron radiation is not necessarily required (unlike techniques such as XAFS).¹⁰ The X-ray photons excite and emit electrons from atoms at and below the catalyst surface layers, however XPS is only surface sensitive as the electrons from the upper most layers (0.5 – 3 nm)¹¹ can escape without losing energy. Escape depth curves like

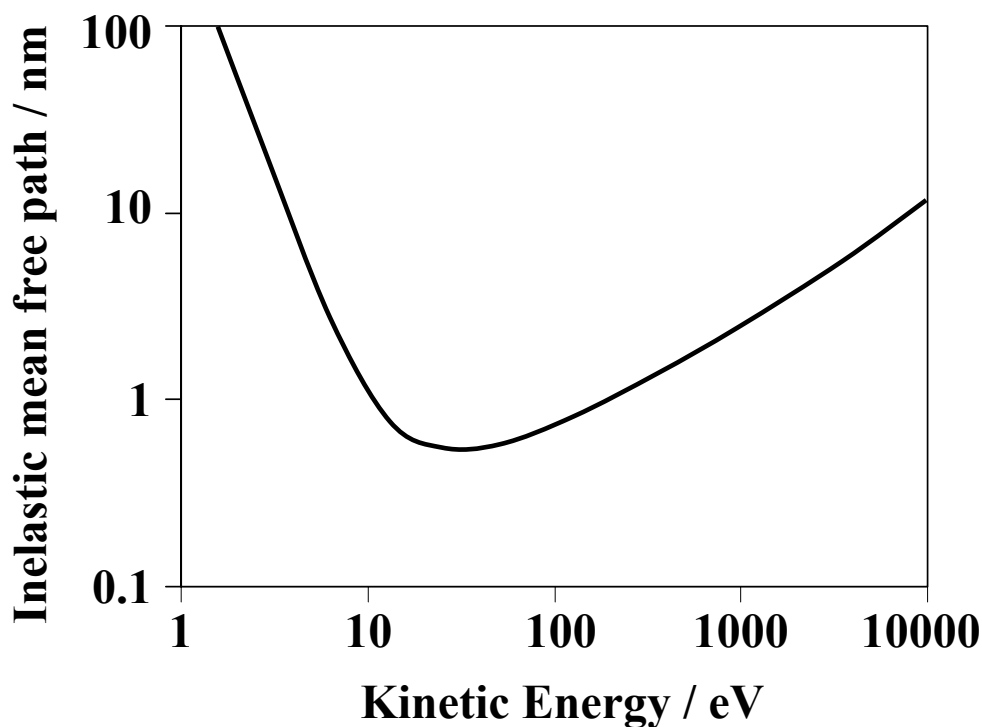


Figure 2.1.6.1: Escape depth curve used to demonstrate the inelastic mean free path of an electron excited by x-ray radiation in XPS.

the one shown in **Figure 2.1.6.1** show how far electrons can travel. The binding energy of these electrons is characteristic of the element from which they are emitted. This can be calculated by measuring the kinetic energy of escape, according to the following relationship:

Equation 2.1.6.1: Binding energy calculated from XPS analysis

$$E_B = h\nu - E_{KIN} - \Phi$$

Where E_B is the electron binding energy, $h\nu$ is the photon energy, E_{KIN} is the measured kinetic energy of the electron, and Φ is the spectrometer work function. A schematic representation of photoionisation is shown in **Figure 2.1.6.2**.

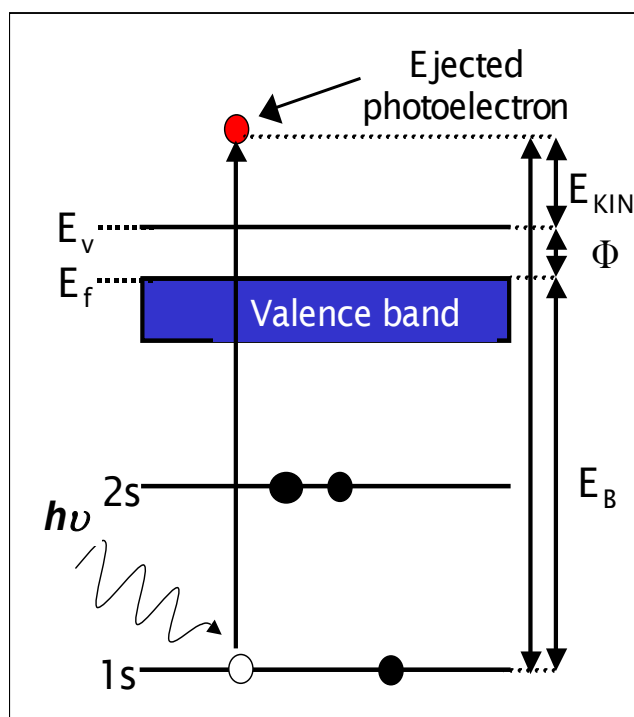


Figure 2.1.6.2: Schematic representation of photoionization.

Depending on the orbital being probed, the peak may be split by spin orbit coupling into a doublet with a separation characteristic of the element. For

quantum number $l > 0$ (p,d,f orbitals), the total angular momentum j for each state is the sum of the spin angular momentum s , and the orbital momentum l . As the spin of the electron can be up or down, s can have a value of $\pm \frac{1}{2}$, leading to two j values. The ratio of the occupancy of these two states is fixed by the multiplicity of the states equal to $2j+1$. Therefore 3d, such as in Rhodium, orbitals where $l = 2$, the two j values are therefore $5/2$ and $3/2$ leading to two peaks with a 3 : 2 ratio in area. The Full Width Half Maximum (FWHM) and line shape are the same for both of the peaks. Probing the d-electrons such as Rhodium leads to a characteristic asymmetric line-broadening towards higher binding energy. This is due to shake-up of valence band electrons. This is a multielectron process whereby an atom is left in an excited state following photoionisation with the outgoing electron therefore having a E_{KIN} less than the parent photoelectron.

Small variations in binding energy arising from differing chemical environments can be detected and quantified by peak fitting. These shifts can be up to 3-4 eV and can be due to initial state or final state effects. Binding energies as well as doublet splittings are readily available on the NIST photoelectron spectroscopy database.¹²

Initial state effects are due to changes in the charge on the atom being probed. For example electron deficient Rh trichloride has a Rh $3d_{5/2}$ binding energy about 2 eV higher than its metallic counterpart. The higher the energy of the orbital from which an electron is photoionised, the larger the effect on the binding energy. Therefore it is advantageous to probe the outer shells for greatest resolution of different oxidation states. Unfortunately in the case of Ru the 4s and 3d orbital peaks overlap with W 5s and C 1s respectively. For Rh the 4s orbital is in close proximity of W 5s. For this reason the 3p and 3d orbital peaks are used for analysis of Ru and Rh respectively.

X-ray photoelectron spectra were acquired at normal emission on a Kratos AXIS HSi spectrometer equipped with a charge neutraliser and Mg $K\alpha$ excitation source (1253.6 eV). Binding energy (BE) referencing was employed using the adventitious carbon peak (285 eV) and valence band. Wide scans were recorded for surface elemental analysis (pass energy 160 eV), with high resolution spectra

recorded at 40 keV pass energy and X-ray power of 225 W. Spectral fitting was performed using CasaXPS Version 2.3.5 with Shirley background-subtraction and a common line shape based on a Gaussian / Lorentzian (40 : 60) mix as well as asymmetry based on a Doniach-Sunjic¹³ mix of 0.01. FWHM, peak separation and response factors for analysis are shown in **Table 2.1.6.1**. For further information on XPS see reference 10.

Table 2.1.6.1: FWHM, peak separation and response factors used for XPS analysis.

Element (orbital)	FWHM	Peak separation eV	Response factor
Ag (3d)	1.64	6.00	5.99
C (1s)	0.53	-	0.28
Cl (2p)	3.10	0.90	0.89
N (1s)	1.80	-	0.48
O (1s)	1.90	-	0.78
P (2p)	1.27	0.85	0.49
Rh (3d)	2.82	4.75	4.82
Ru (3p)	3.12	22.1	2.04
Si (2p)	1.68	0.61	0.33
W (4f)	1.62	2.10	3.52

2.1.7 - X-Ray absorption spectroscopy (XAS)

XAS is a non destructive technique which employs monochromatic X-rays from a synchrotron radiation source, to obtain bulk structural information of solid catalysts. **Figure 2.1.7.1** shows a typical EXAFS spectrum. Photons of a certain energy, are fired at the sample just below the absorption edge, i.e. the minimum energy to eject an electron from the particular core shell of interest, and then scanning the photon energy across it. Typically the photon energy is scanned from approximately -300 eV below the absorption edge up to 1000 eV above it. For the Ru and Rh catalysts studied, the Ru and Rh K-edges are most useful in catalyst characterisation, at ~ 22119 eV and 23222 eV respectively.

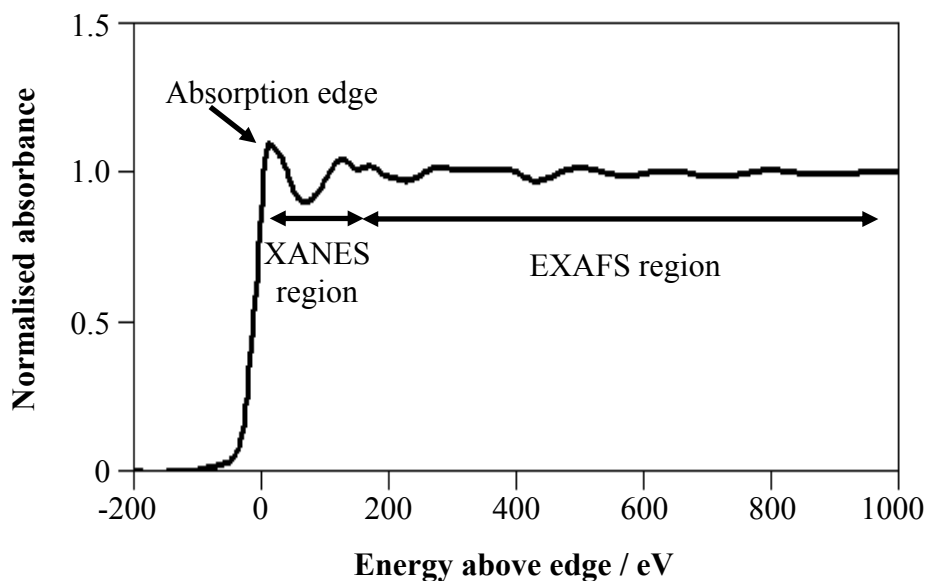


Figure 2.1.7.1: Example of a full EXAFS spectrum.

Just above the absorption edge, up to approximately 100 eV is known as the X-ray Absorption Near Edge Structure (XANES) region. This region is dominated initially by the promotion of electrons into higher energy unoccupied orbitals above the Fermi level, followed by the ejection of an extremely low energy electron. The promotion of electrons into unoccupied higher energy orbital can be used to quantify the oxidation state of a metal. High Ru/Rh oxidation states give rise to a strong peak in the absorption just above the edge-jump (termed the white-line), due to excitation of core electrons into unoccupied (predominantly) 3d states. This absorbance is attenuated in metallic Rh due to the greater 3d-band occupancy.

Beyond the XANES region up to approximately 1000 eV is known as the Extended X-ray Absorption Fine Structure (EXAFS) region. This region is dominated by the interference created between the incident photons and the ejected photoelectrons which are backscattered by atoms surrounding the probed atom. This is seen as an oscillation in the absorption spectrum. The phase and amplitude of these oscillations depends on the type of atom involved in the backscattering as well as the distance from the probed atom. These oscillations

can be fit mathematically to determine the local co-ordination environment of the atom. For more in depth discussion on EXAFS see reference.¹⁴

XAS measurements were recorded both at the Daresbury facility stations 9.3 and 16.5, as well as the XAFS beamline at the ELETTRA sincrotrone facility in Trieste. Ru/Rh data was recorded in transmission mode for more ‘metal dense’ samples (~ 20 wt %) and fluorescence using 9 detector channels for dilute samples (0.1 – 3 wt %), employing a Si(220) monochromator set at 70 % harmonic rejection, with a beam current/energy of 150 mA/ 2 GeV, typically over 45 minutes. A typical scan involved scanning 150 eV below the excitation edge collecting data with an energy step of 5 eV. At ~ 15 eV below the absorption edge the energy step was reduced to 0.3 eV for enhanced resolution followed by an increase to 1 eV for 500 eV directly after the edge and the final 500 eV with steps of 3 eV. The integration time per point was held constant at 2 seconds. Ru (22119 eV) K edge spectra were baseline subtracted using EXSPLINE and fitted in EXCURV98, over the range 0-14 Å. Rh (23222 eV) were baseline subtracted using Athena version 0.8.56 and off-line DL-EXCURV fitting package. All XANES linear combination fit analysis was performed using Athena version 0.8.56. Samples were prepared in 2 mm stainless steel washers sealed with Kapton and where necessary, diluted with boron nitride to attain appropriate concentrations where Ru/Rh content was typically in the range 0.1 – 3 wt %.

2.1.8 - *In-situ* XANES

Rh K-edge (23222 eV) XANES spectra were collected in transmission mode using synchrotron radiation at the ELETTRA facility in Trieste. Powder samples of bulk and silica supported ‘RhXHPW1:1’ were loaded into a purpose built vacuum chamber at the beam line (**Figure 2.1.8.1**). 1-2 mm of catalyst powder was loaded into a sample holder (A) between two borosilicate wafer windows. The sample holder was then loaded into the sample cell (B). The sample cell was in-turn mounted into the main chamber (C), connecting to the gas / vacuum inlet and outlet and thermocouple, which are found inside the main chamber. The graphite windows of the cell were aligned with the windows of the main chamber and the main chamber positioned in the beam using the motorised sample table (D). The main chamber was evacuated during analysis to rough vacuum (1×10^{-5} torr).

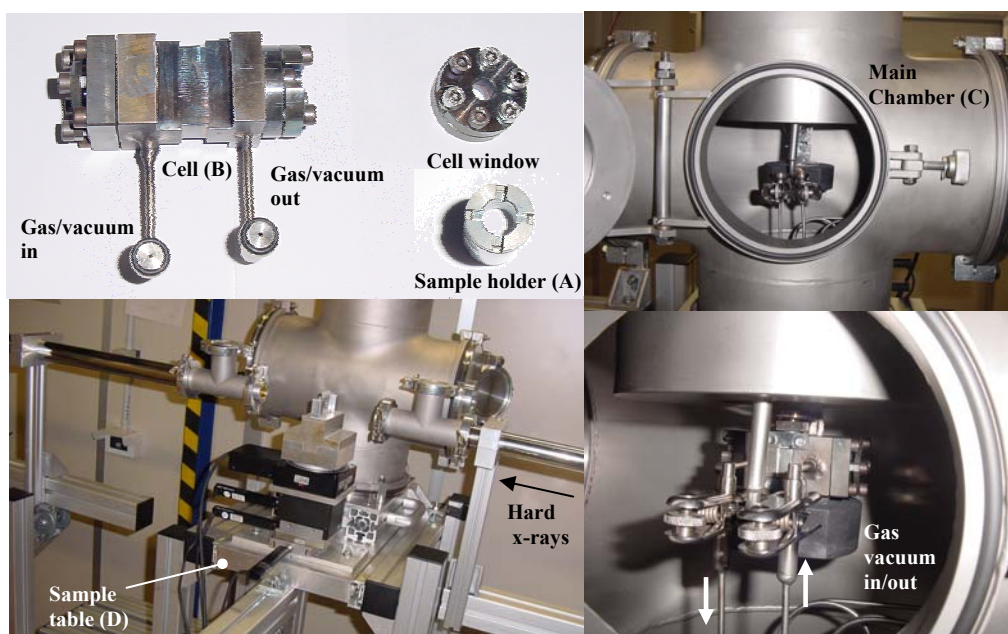


Figure 2.1.8.1: In-situ EXAFS Chamber, (top left) Sample holder and cell for loading sample for in-situ analysis (top right) main chamber for mounting sample cell (bottom left) sample table showing direction of beam entrance and exit (bottom right) inside of main chamber showing mounted cell and gas inlet/outlet.

Samples were analysed at room temperature with either 20 ml min^{-1} He or 5 % CO / He mix and temperature ramp using a PID temperature controller at a rate of $5 \text{ }^\circ\text{C min}^{-1}$ up to $350 \text{ }^\circ\text{C}$. Each sample was analysed by acquiring 4 EXAFS spectra

followed by a temperature ramp to 100 °C where the sample was held for 5 minutes at temperature followed by 4 additional EXAFS scans. This protocol was repeated at 150, 200, 225, 250 °C. At 250 °C the 4 EXAFS spectra were not reproducible indicating that samples were undergoing a physical change during scanning at temperature. As the scanning time to collect EXAFS spectra (~ 45 minutes) limited the ability to resolve the time scale of these changes, spectra for elucidation of the Rh local coordination shell were unobtainable. XANES spectra were collected at temperatures above 250 °C (250, 300 and 350) to identify the nature of the Rh oxidation state. Spectra were collected using the same protocol as described for the initial collection of EXAFS spectra up to 300 eV above the absorption edge. To reduce collection time, the integration time per point was reduced to 0.5 seconds. This allowed the collection of up to 7 spectra at ~ 7 minutes per spectrum where changes in the intensity of the absorption edge and therefore oxidation state could be monitored.

2.1.9 - Porosimetry

Textural properties of the prepared catalysts were determined by N₂ adsorption-desorption porosimetry.¹⁵ The BET isotherm is an extension of the Langmuir isotherm, and can be used to calculate surface areas based on a model of adsorption employing the assumption that all adsorption takes place on identical sites, the energy of adsorption is independent on how many surrounding sites are occupied and that only monolayer coverage occurs i.e. after each surface site is filled with one adsorbate molecule, adsorption ceases (**Equation 2.1.9.1**).¹⁶ The monolayer volume V_m is combined with the absorption cross section mass of adsorbate (nitrogen) to calculate the surface area of the catalyst.

Equation 2.1.9.1: BET equation

$$\frac{P}{v(P_0 - P)} = \frac{c - 1}{v_m c} \cdot \frac{P}{P_0} + \frac{1}{v_m c}$$

P= equilibrium pressure, **P₀** = saturation pressure, **c** = BET constant,
v = quantity of absorbed gas, **v_m** = quantity of monolayer absorbed gas

Pore-size distributions were calculated using the Barrett, Joyner and Halenda (BJH) method. As the relative pressure of the isotherm increases beyond 0.2, a rapid rise in N₂ adsorption is observed as the mesopores saturate by capillary condensation. The pressure required for saturation is dependant on the pore diameter and radius of curvature of the resulting meniscus formed by the condensation of N₂. The BJH method applies the Kelvin equation (**Equation 2.1.9.2**) to the isotherm data.

Equation 2.1.9.2: Kelvin equation

$$\ln \frac{P}{P_0} = -\frac{2\gamma V_L}{RT r_m}$$

Where P/P₀ is the relative pressure of vapour in equilibrium with the meniscus of the condensed gas which has radius (r_m); surface tension (γ); molar volume (V_L); at temperature, T.

Porosity and surface areas were determined by N₂ adsorption-desorption on a Quantachrome Nova 1200 porosimeter. Samples were degassed under vacuum at 100 °C for 1 hour prior to analysis. Surface areas were calculated using the Brunauer-Emmet-Teller (BET)¹⁷ equation over the pressure range P/P₀ = 0.02–0.2, where a linear relationship was maintained. Barrett Joyner Halenda (BJH) analysis was used for pore radius and volume using Quantachrome NovaWin2 computer software.

2.1.10 - Solution state NMR

A Jeol ECX400 400 MHz NMR spectrometer was used for ¹H and ³¹P solution state analysis. Due to the slow relaxation of HPA phosphorus, relaxation time was set to 7.5 ms as apposed to the preset, 1.5 ms. All samples were prepared in D₆-DMSO or C₆D₆ specified in Section 2.2.

2.1.11 - Structural MS analysis

The York MS analytical facility was used for ESI-MS for both positive and negative ion analysis. A Bruker Daltonics microTOF mass spectrometer was used, and all materials were dissolved in CH₃CN.

MALDI-TOF solid state MS was provided by the EPSRC Mass Spectrometry Service (Swansea).

2.1.12 - Solid state MAS-NMR

Solid state ¹³C and ³¹P MAS-NMR was carried out by the Durham University facility using a Varian UNITY Inova spectrometer with a 7.05 T ("300 MHz") Oxford Instruments magnet.

2.1.13 - ICP-MS and CHN elemental analysis

Ruthenium, tungsten and chlorine content as well as CHN elemental analysis were carried out at the MEDAC analytical facility. Metal analysis (Ru, Rh and W) were accomplished using a Varian Vista MPX ICP-OES system. Chlorine analysis was assessed using Schöniger flask combustion followed by either titration or ion-chromatography. CHN analysis was performed on CE-440 and Carlo Erba elemental analysers.

2.1.14 - Pyridine titrations

Samples of HPW and **RhHPW_n:1-SiO₂** (where n = 0.5, 1, 2, 3) were soaked in a molar excess (10 : 1, eg. for Rh : HPW ratio of 1 : 1, 10 µl pyridine for 45 mg of sample) pyridine (≥ 99 %, ACS reagent). The excess pyridine was evaporated under vacuum. The samples were then mixed in a 1 : 1 mass ratio by grinding with spectroscopic grade potassium bromide (Fisher). The samples were loaded into a Thermo electron corporation Nicolet Avatar 370 DRIFTS spectrometer with accessories and scanning parameters identical to those

described in Section 2.1.2. Spectra were collected with increasing temperature under a flow of nitrogen, until complete loss of pyridinium bands (1485-1500, 1540, 1620, 1640 cm^{-1}) was observed.

2.1.15 - Methanol carbonylation tests

The materials (5 mg of M per sample, M = Ru, Rh) were diluted in low surface area Fisher quartz chips to obtain a volume of 1 cm^3 in each sample. Masses of actual catalyst used are shown in **Table 2.1.15.1**. All materials tested were packed into a quartz tube (1 cm i.d.) with silica wool. The tube was secured

Table 2.1.15.1: Mass of catalyst used for flow reactor tests.

Material	Mass / mg
RuHPW	107
RudppeHPW	101
HPW	80
HPW-SiO ₂ (50 wt %)	250
RhXHPW_n:1 (n = 0.5, 1, 2)	316, 211, 107
RhXHPW_n:1-SiO₂ (n = 0.5, 1, 2, 3)	590, 311, 166, 133
Cs/Ag doped RhXHPW0.5:1-SiO₂	596
RhAHPW, RhAHPW-SiO₂	152, 329
RhTHPW, RhTHPW-SiO₂	125, 563

into a Swagelok stainless steel pipe flow system leading from reactant inlets to a mass spectrometer and GC / exhaust. The tube containing the powder sample was secured inside a furnace (**Figure 2.1.15.1**, 'reactor') which could be temperature programmed. For the tests carried out in this study, two temperature regimes were employed. For temperature stability and optimum conversion studies the reactor tube was heated to 350 °C at 5 °C min^{-1} , for steady state measurements the reactor was heated at 5 °C min^{-1} to 180 °C, 200 °C and 250 °C and held at these temperatures for up to 5 hours. The whole system was heated to retain all reactants and products in the gas phase. All reactor experiments started at 100 °C where the reactor tube and sample were held for 1 hour under a 32 ml min^{-1} He

flow to remove any physisorbed water. After this, CO was introduced at 8 ml min⁻¹ while retaining the total gas flow of 32 ml min⁻¹ in a CO/He co-feed. Methanol was pumped using a peristaltic pump at 0.7 ml h⁻¹ (~ 18 mmol h⁻¹) which constituted to a LHSV of ~ 1 h⁻¹. A flow of gas was passed over the sample at the rate of 8 ml min⁻¹. The gas flow was made up to 32 ml min⁻¹ (GHSV 1920 h⁻¹) by flowing He at 24 ml min⁻¹. All gases were controlled using Brooks 5850TR mass flow controllers. Reactor constituent concentrations were detected and followed by online GC (Carboxen 1006 Plot column (30 m x 0.53 film)) and mass spectrometry, using a Shimadzu GC-14B and a VG 300 amu MiniTorr quadrupole mass spectrometer (with dual Faraday/SEM detectors) respectively. Both systems were interfaced to a PC for data acquisition. The gaseous product stream was monitored by tracking specific mass to charge ratios (m/z) as follows: He (4), Water (18), Ethane (26), CO (28), MeOH (32), Propane (39), DME (46), AcOOH (60), MeOAc (74), as well as 43, which is the major components for both acetyls and propane, representing CH₃CO or C₃H₇ fragments respectively.

GC and MS were corrected for appropriate response factors to calculate mass balances based on MeOH conversion (which were ~ 98 %), and selectivity to acetyls from GC analysis defined in **Equation 2.1.15.1** with product concentrations in mmols per hour. Due to the relatively high 1:1 MeOH : CO molar ratio employed, methyl acetate was the dominant acetyl product with negligible acetic acid observed.

Equation 2.1.15.1: Calculation for acetyl selectivity in methanol carbonylation experiments.

$$Acetyl\ Selectivity\ \% = \frac{\{[MeOAc] + [AcOOH]\}}{\{[MeOAc] + [AcOOH] + [DME]\}} \times 100$$

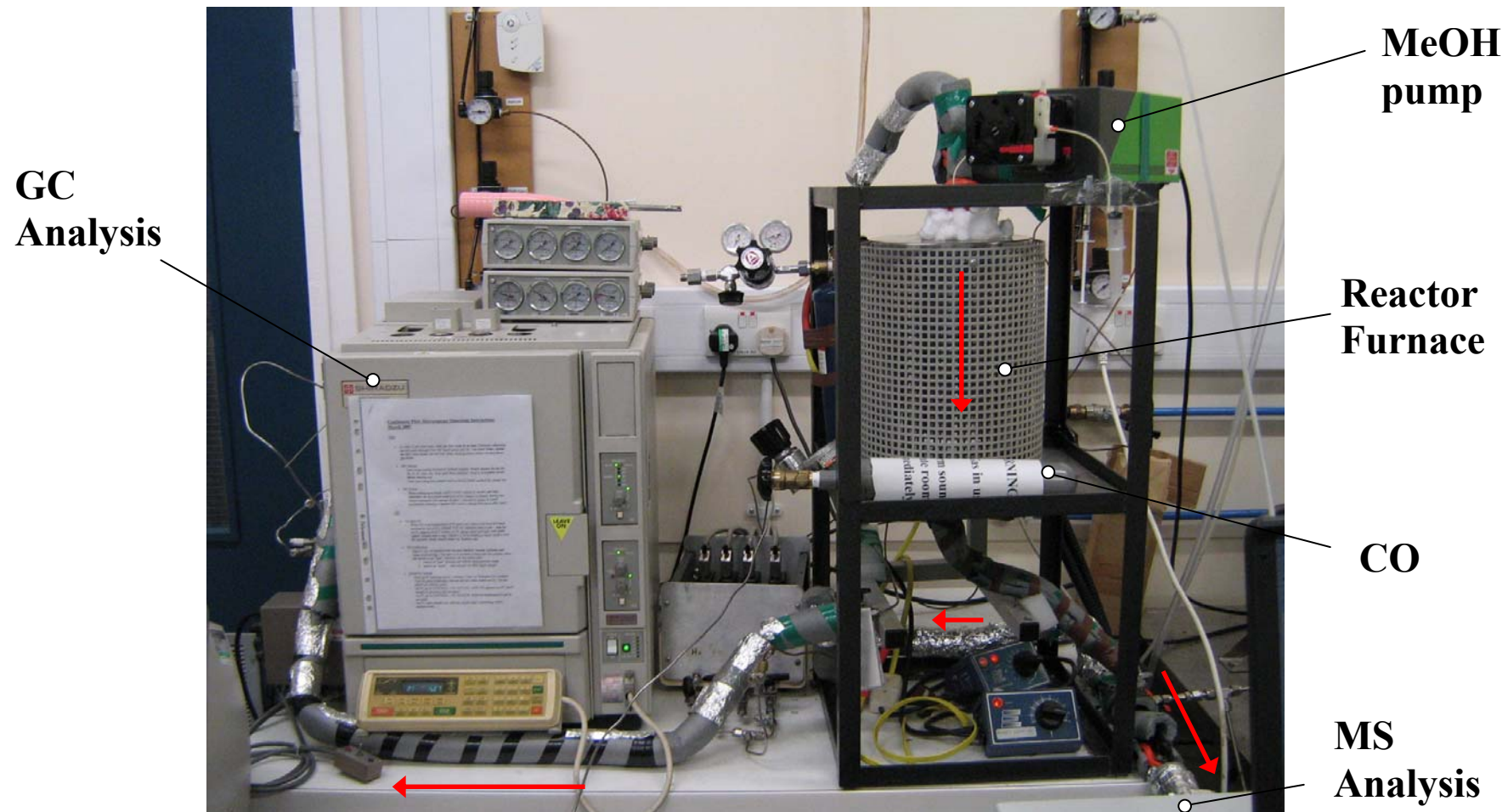


Figure 2.1.15.1: Continuous flow reactor with on-line GC and MS.

2.1.16 - Dimethyl ether carbonylation tests

Carbonylation experiments were performed on **RhXHPW-SiO₂** with 1 : 1 Rh : HPW ratio. GHSV and catalyst bed size were identical to MeOH carbonylation experiments, 1920 h⁻¹, 1 cm³ respectively. The catalyst was treated with a CO/DME/He gas flow under steady state conditions for up to 4 hours at 200 °C. Reactant gas flow rate was kept constant at 8 ml min⁻¹ with DME flow rates of 1, 2 and 4 ml min⁻¹ constituting to 7 : 1, 3 : 1 and 1 : 1 molar ratio respectively.

2.1.17 - Ethanol dehydration tests

The use of ethanol (analytical reagent grade $\geq 98\%$, Fisher) as a feedstock in the flow reactor was employed under the same conditions as those discussed in Section 2.1.14. Ethanol was fed at 0.7 ml h⁻¹ (12 mmol h⁻¹) with 8 ml min⁻¹ CO. The catalysts sample was held under steady state at 200 °C for 4 hours and cooled under He (32 ml min⁻¹). Under ethanol dehydration conditions, no CO was consumed therefore, m/z 28 could be used as well as m/z 46 for tracking ethene and ethanol respectively, consistent with GC data and resulting response factors.

2.1.18 - Phenyl acetylene oligomerisation tests

Reactions were performed under an atmosphere of N₂ in a Radley's carousel containing 1 cm³ of phenyl acetylene, 1 mol % [Ru] and stirrer bar at 700 RPM. The resulting mixture was heated to 100 °C for 24 hours. Samples were periodically removed from the reaction tube for GC analysis. The samples were filtered over a silica bed (Fisher, 35-70 μ , 40 Å) on tissue paper to remove catalyst and diluted in toluene with a mesitylene standard. The depletion of phenyl acetylene and formation of dimer and oligomer species was followed by GC analysis over 24 hours. A Varian GC-3800 gas chromatograph was used, fitted with a flame ionisation detector (FID), a CP-8400 Autosampler and VF-1 capillary column (film thickness 0.25 μ m, i.d. 0.32 mm, length 30 m) with a 5 m

EZ Guard column. 1 μ l was injected to a pre heated injector at 240 °C with a flow rate of 3 ml min⁻¹. The programmed temperature ramp of the column was controlled by the GC oven which was held at 80 °C for 2 minutes, ramped at 30 °C min⁻¹ to 250 °C, held for a further 6 minutes, then ramped at 30 °C min⁻¹ to 300 °C. This gave a total run time of 15.33 minutes. The sample was analysed with the detector at 250 °C. Peak retention times were as followed, toluene (solvent) 3.744, phenyl acetylene, 4.453, mesitylene 5.307, phenyl acetylene dimer-*Z*, 12.890, phenyl acetylene dimer-*E*, 13.066 higher oligomers, 13.788, 14.969 minutes. The selectivity towards the dimers was confirmed by GCMS (70 % *E* : 30 % *Z*).

2.2 - Synthesis of Ru Compounds

2.2.1 - Synthesis of Ru(Cl)(Cp)(PPh₃)₂

Ru(Cl)(Cp)(PPh₃)₂ was synthesised in accordance with the literature preparation by Triechel¹⁸ and on the scale described here.

In a 2 necked round bottom flask fitted with a reflux condenser, triphenyl phosphine (21 g, 0.08 mol) was dissolved in 1 L of ethanol.

Cyclopentadiene was cracked from its dimer and distilled at *ca.* 39-40 °C. A Vigreux column was used between the flask containing the dimer and still head of the distillation set-up.

The triphenyl phosphine in ethanol was heated to reflux. RuCl₃·nH₂O (5 g, 0.02 mol) was dissolved in 80 ml of ethanol. The freshly distilled cyclopentadiene (10 ml, 8.0 g, 0.12 mol) was dissolved separately in ethanol. The dark brown RuCl₃ was rapidly transferred, under vacuum, to the refluxing triphenyl phosphine solution followed immediately by the cyclopentadiene solution.

The dark brown reaction mixture was heated at reflux for 1 hour until the solution changed to a dark red orange colour. The solution was then air stable and could be cooled over night at -20 °C, (note: crystal seeds were added to promote crystal growth). Orange crystals of Ru(Cl)(Cp)(PPh₃)₂ were formed which were filtered and washed with 4 x 25 ml ethanol and 4 x 25 ml diethyl ether over a Büchner funnel and dried in air.

The filtrate liquor was reduced in volume on a rotary evaporator cooled and filtered as before, and washed with ethanol and ether to obtain a second residual crop of crystals.

Yield 14.2 g (95 mass %) – based on 3 H₂O

NMR for comparison with literature:

¹H NMR (CDCl₃) δ = 4.09 (s, -C₅H₅), 7.11 – 7.35 (m, PPh₃, 6 x C₆H₅).

$^{31}\text{P}\{^1\text{H}\}$ NMR (CDCl_3) $\delta = 40.47$ (s, PPh_3)

NMR for comparison with **RuHPW** compound:

^1H NMR (D_6 -DMSO) $\delta = 4.03$ (s, $-\text{C}_5\text{H}_5$), 7.17 – 7.24 (m, PPh_3 , 6 x C_6H_5), $^{31}\text{P}\{^1\text{H}\}$ NMR (D_6 -DMSO) $\delta = 39.30$ (s, PPh_3)

2.2.2 - Synthesis of RuHPW

RuHPW was made on several scales, a common example is shown here.

$\text{Ru}(\text{Cl})(\text{Cp})(\text{PPh}_3)_2$, (750 mg, 1.02 mmol) was added to a 250 ml round bottom flask with magnetic stirrer bar. 50 ml of methanol was added to the flask to make an orange suspension. While stirring; one equivalent of phosphotungstic acid, $\text{H}_3\text{PW}_{12}\text{O}_{40}\cdot 20\text{H}_2\text{O}$, (3.30 g, 1.185 mmol) and NEt_3 (150.0 μl , 1.08 mmol) was added to the suspension. [On addition of phosphotungstic acid to the suspension no change was noticed, however on addition of NEt_3 the suspension began to dissolve.]

A rubber stopper was added to the neck of the round bottomed flask and the solution was left to stir for 23 hours at ambient temperature and pressure. '**RuHPW**' was filtered on a Büchner funnel and washed with methanol (4 x 25 ml) to yield 2.8 g of an orange brown powder.

Yield: 2.79 g (62.7 mol% - based on Ru)

^1H NMR (D_6 -DMSO) $\delta = 1.1$ (t, 9, NCH_2CH_3), 3.0 (m, 6, NCH_2CH_3), 4.9 (s, 5, C_5H_5), 7.0 (m, 10, PPh_3 , 2 x C_6H_5), 7.4 (m, 10, PPh_3 , 2 x C_6H_5), 7.3 m, PPh_3 , 6 x C_6H_5), 8.9 (br s, 1, NH^+). $^{31}\text{P}\{^1\text{H}\}$ NMR (D_6 -DMSO) $\delta = -15.0$ (s, $\text{PW}_{12}\text{O}_{40}$), 37.7 (s, PPh_3).

Experimental XPS atom % - C 37.5, N 0.5, O 19.8, P 2.0, Ru 0.9, W 4.1

Full characterisation reported in chapter 3

2.2.3 - Synthesis of $[\text{NEt}_3\text{H}]^+_3[\text{PW}_{12}\text{O}_{40}]^{3-}$ (NEt_3HPW)

200 mg (6.9×10^2 mmol) of phosphotungstic acid (HPW), $\text{H}_3\text{PW}_{12}\text{O}_{40} \cdot 20\text{H}_2\text{O}$ was dissolved in the minimum amount of methanol *ca.* 2 ml in a 60 ml sample bottle with lid. Methanol was added using a Pasteur pipette down the side of the bottle to make an interface layer of methanol with lower concentration of HPW.

In a separate vial 21 mg of triethylamine (0.21 mmol) was dissolved in methanol in equal amounts to that used to dissolve HPW. The solution was then added to the sample bottle using a Pasteur pipette down the side of the bottle to form a double layered system.

The triethylamine diffused into the HPW methanol layer forming a white crystalline solid. The salt was then analysed by ^{31}P MAS NMR.

^1H NMR (D_6 -DMSO) $\delta = 1.5$ (t, CH_2CH_3), 1.7 (q, CH_2CH_3), 9.1 (br s, NEt_3H^+).

$^{31}\text{P}\{^1\text{H}\}$ NMR (D_6 -DMSO) $\delta = -15.0$ (s, $\text{PW}_{12}\text{O}_{40}$)

2.2.4 - Synthesis of $\text{Ru}(\text{Cl})(\text{Cp})(\text{dppe})^{18}$

$\text{Ru}(\text{Cl})(\text{Cp})(\text{PPh}_3)_2$ (0.5 g, 0.69 mmol) and an excess of bis(diphenyl phosphino) ethane (dppe) (882 mg, 16.5 mmol) were put into a reflux Schlenk tube with a stirrer bar and degassed.

Ca. 50 ml of toluene was degassed in a second Schlenk tube. Enough toluene was transferred to the first Schlenk tube, using a cannula, to dissolve the powders. The resulting solution was heated at reflux for 26 hours.

After cooling, the solvent was removed *in vacuo* leaving an orange / brown oil. The oil was sparingly soluble but dissolved in the minimum amount of CH_2Cl_2 . An alumina (Sigma Aldrich) chromatographic column was packed in CH_2Cl_2 . The dissolved oil was added to the column and CH_2Cl_2 was used to elute

the colourless fraction (PPh₃). Acetone was used to elute the yellow-orange product fraction. The solvent was removed from the product fraction.

The resulting red-orange crystals were recrystallised from diethyl ether and hexane.

Yield 280 mg (55.3 mass %)

¹H NMR (CDCl₃) δ = 4.03 (s, -C₅H₅), 7.06 – 7.29 (m, PPh₂, 4 x C₆H₅)

³¹P{¹H} NMR (CDCl₃) δ = 39.45 (s, PPh₃)

2.2.5 - Synthesis of 'RudppeHPW' compound

Ru(Cl)(Cp)(dppe), (100 mg, 0.15 mmol) was added to a 100 ml round bottom flask with a stirrer bar. Methanol (20 ml) was added to the flask and the mixture was stirred to form an orange suspension.

440 mg (0.144 mmol) of HPW was added to the suspension while stirring was continued. 20 μl (0.144 mmol) of NEt₃ was added to the suspension [The suspension dissolved upon addition of NEt₃ *c.f.* Section 2.1.2]. The flask was capped with a rubber stopper and stirred for 23 hours. A rusty coloured powder precipitated out of solution. The product was isolated on a Büchner funnel and washed with methanol (4 x 10 ml). The filtrate was reduced on a rotary evaporator and washed to yield a second batch of powder.

Yield 350 mg (60.0 mol% - based on Ru)

¹H NMR (D₆-DMSO) δ = 1.1 (t, 9, NCH₂CH₃), 2.2 (s, 4, P(CH₂)₂P), 3.0 (m, 6, NCH₂CH₃), 5.3 (s, 5, C₅H₅), 7.0 (m, 10, PPh₂, 8 x C₆H₅), 7.2 (m, 8, PPh₂), 7.5 (m, 12, PPh₂), 8.9 (br s, 1, NH⁺). ³¹P{¹H} NMR (D₆-DMSO) δ = -15.0 (s, PW₁₂O₄₀), 36.2 (s, PPh₂)

Experimental XPS atom % - C 52.0, N 0.7, O 33.4, P 3.6, Ru 1.4, W 9.0

Full characterisation assay given in Chapter 3.

2.3 - Synthesis of Rh compounds

Synthesis of Rh compounds were performed under nitrogen or argon atmosphere using standard Schlenk and glove box techniques. THF and hexane were purified with an Innovative Technologies anhydrous solvent engineering system. Where bulk elemental analysis data is shown, theoretical calculated values are shown for clarity of comparison. Where only XPS (surface sensitive data is available theoretical mass % were not calculated for silica supported samples due to the inherent inhomogeneity of the materials with higher bulk Si and O within the silica support.

2.3.1 - Synthesis of Rh(acac)(CO)(Xantphos)¹⁹

Rh(acac)(CO)₂ (Purum, Fluka) (53.0 mg, 0.211 mmol) and Xantphos (119.5 mg, 0.212 mmol) (97 % Aldrich) were added to a Schlenk tube with stirrer bar and degassed. 6 ml of dried and degassed THF were added via a cannula to the solids which were stirred under nitrogen. The green Rh(acac)(CO)₂ turned a red/brown with evolution of gas (presumably CO). The gas was removed under vacuum to force the reaction to completion. When bubbling was complete the solution was stirred for a further 15 minutes. The solvent was removed *in vacuo* and the resulting yellow / brown powder was washed with hexane by cannula filtration.

Yield 153.6 mg (nominal yield 90 % **RhXantphos**)

Expected mass % - C 66.84, H 4.86, O 7.91, P 7.66, Rh 12.73

Experimental mass % - C 67.29, H 5.06, P 7.23, Rh 12.01

¹H NMR (C₆D₆) δ = 6.6 – 7.8 (26H, m, Xantphos - ph-H), 1.6 (6H s, Xantphos CH₃)

³¹P {¹H} NMR (C₆D₆) δ = 11.0 (d, 90.2 Hz Rh-P)

IR (Rh-CO): 1974 cm⁻¹

2.3.2 - Synthesis of RhXHPW_n:1 (*n* = 0.5, 1, 2, 3)

Rh(acac)(CO)(Xantphos) was synthesised as described in Section 2.3.1. In a separate round bottom flask H₃PW₁₂O₄₀.20H₂O (HPW) ({eg. For 0.5Rh : 1HPW})

1.246 g, 0.39 mmol) was stirred in 10 ml of degassed THF. The HPW solution was added to the Schlenk tube containing Rh(acac)(CO)(Xantphos) (0.038 mmol solution) and stirred for a further 15 minutes. The solvent was removed *in vacuo* and the resulting brown powder was washed with hexane by cannula filtration.

Yield 1.12 g (80 mol %)

Elemental analysis:

Expected mass % - C 13.00, H 1.25, O 20.77, P 2.51, Rh 2.78, W 59.68

Experimental mass % - C 15.59, H 1.97, P 2.56, Rh 2.64, W 56.27

^1H NMR (D_6 DMSO) $\delta = 6.8 - 8.2$ (26H, m, Xantphos - ph-*H*), 1.7 (6H s, Xantphos CH_3)

^{31}P $\{^1\text{H}\}$ NMR (D_6 DMSO) $\delta = 45.0$ (bs, Rh-*P*), -15.0 (s, HPW)

^{13}C $\{^1\text{H}\}$ NMR (D_6 DMSO) $\delta = 171.8$, (Rh-CO), 124.2 – 134.3 (Xantphos aryl-C), 32.4 (s, Xantphos - CH_3)

IR (Rh-CO), 2008 cm^{-1}

2.3.3 - Synthesis of RhXHPW n :1 supported on Davisil 100 silica ($n = 0.5, 1, 2, 3$)

Rh(acac)(CO)(Xantphos) was synthesised as described in Section 2.3.1. In a separate round bottom flask, $\text{H}_3\text{PW}_{12}\text{O}_{40}\cdot 20\text{H}_2\text{O}$ (HPW) ($\{eg. \text{For } 0.5\text{Rh} : 1\text{HPW}\}$) 1.246 g, 0.39 mmol) and Davisil 100 silica (1.099 g) were stirred in 10 ml of degassed THF for 3 hours. After the HPW had been impregnated on to the silica the Rh(acac)(CO)(Xantphos) solution was added and the solution stirred for a further 15 minutes. The solvent was removed from the resulting solid using a rotary evaporator. The brown powder was then dried at 60 °C over night in a vacuum oven. Elemental analysis and relative number of atoms per Keggin are given in **Table 2.3.3.1**.

Yield 2.47 g (98 mass %)

Table 2.3.3.1: Elemental analysis for all RhX : HPW ratio materials studied.
(Mass % and normalised per Keggin unit (W₁₂))

Element	<i>RhXantphos : Keggin ratio</i>							
	<i>0.5:1</i>		<i>0.5:1</i>		<i>0.5:1</i>		<i>0.5:1</i>	
	<i>Mass %</i>	<i>Atoms per Keggin*</i>	<i>Mass %</i>	<i>Atoms per Keggin*</i>	<i>Mass %</i>	<i>Atoms per Keggin*</i>	<i>Mass %</i>	<i>Atoms per Keggin*</i>
C	8.9	35.2(20)	8.5	49.3(40)	14.6	98.5(80)	19.5	143.6(120)
H	1.3	61.0(19)	1.6	109.4(34)	1.5	117.5(65)	1.7	152.4(96)
P	1.6	2.5(2)	1.4	3.0(3)	2.1	5.5(5)	2.7	7.8(7)
Rh	1.0	0.45(0.5)	1.4	0.96(1)	2.6	2.0(2)	3.7	3.1(3)
W	46.3	12	31.8	12	27.2	12	25.0	12

* 'Experimental value (calculated theoretical value)'

IR (Rh-CO): 2008 cm⁻¹

2.3.4 - Synthesis of RhXHPW_n:1 supported on Davisil 100 silica with Cs/Ag dopants

{eg. for 0.5Rh : 1HPW system}

The synthetic procedure in Section 2.3.3 was followed with the initial addition of caesium acetate stock solution (1.2 ml of 3.3 mM in H₂O) and silver acetate (32.1 mg, 0.142 mmol) to the HPW/silica suspension before addition of the Rh complex solution.

Yield 2.50 g (98 mass %)

Elemental analysis %:

Experimental mass % (XPS) - C 8.02, O 43.30, P 0.28, Ag 0.48, Rh 0.46, Si 27.69, W 19.77

Atoms per Keggin: C 76, O 308, P 1, Ag 1, Rh 1, Si 112, W 12

IR (Rh-CO) 2008 cm⁻¹

2.3.5 - Synthesis of Rh(acac)(CO)(Terpyridine)

Rh(acac)(CO)₂ (purum, Fluka) (50.0 mg, 0.194 mmol) and Terpyridine (45.2 mg, 0.194 mmol) (Sigma Aldrich) were added to a Schlenk tube with stirrer bar and degassed. 6 ml of dried and degassed THF were added via a cannula to the

solids which were stirred under nitrogen for 15 minutes. The green Rh(acac)(CO)₂ dissolved into a pale yellow / green solution which turned red/purple after *ca.* 5 minutes. The solvent was removed in *vacuo* and the resulting red / purple powder was washed with hexane by cannula filtration.

Yield 85 mg (89 mass %)

¹H NMR (D₆-DMSO) δ = Terpy-*H* – 7.6 (4H, m), 8.2 (3H, m), 8.8 (2H, m) 9.0 (2H, m)

MS (m/z): 234 (minor peak, {Terpy-H}⁺), 364 {Rh(CO)(Terpy)}⁺, 494 {Rh(acac)(CO)₂(Terpy)-H⁺}

Elemental analysis %:

Expected mass % - C 48.65, H 3.65, N 8.64, Rh 17.42

Experimental mass % - C 52.62, H 3.76, N 8.77, O 13.35, Rh 21.47

IR (Rh-CO): 2069, 2010 cm⁻¹

2.3.6 - Synthesis of RhTerpyHPW1:1

Rh(acac)(CO)(Xantphos) was synthesised as described in Section 2.3.5. In a separate round bottom flask H₃PW₁₂O₄₀·20H₂O (HPW) (0.623 g, 0.194 mmol) was stirred in 10 ml of degassed THF. The HPW solution was added to the Schlenk tube containing Rh(acac)(CO)(Terpy) and stirred for a further 15 minutes. The solvent was removed *in vacuo* and the resulting red/purple powder was washed with hexane by cannula filtration.

Yield 0.757 g (97 mass %)

Elemental analysis %:

Expected mass % - C 5.58, H 1.40, N 1.15, P 0.85, Rh 2.81, W 60.25

Experimental mass % - C 8.55, H 1.69, N 1.14, P 0.79, Rh 1.81, W 55.62

MS (m/z): ESI⁺: 115.1 {(Terpy)(H)₂}⁺, 338.4 {Rh(Terpy)(H)}⁺, 494 ESI⁻: 958.6 {PW₁₂O₄₀}³⁻

¹H NMR (D₆ DMSO) δ = Terpy-*H* – 7.6 (3H, m), 7.8 (2H, m), 8.37 (4H, m) 9.0 (2H, m)

³¹P {¹H} NMR (D₆ DMSO) δ = -15.0 (s, HPW)

IR (Rh-CO): 2030 br, 2113 cm⁻¹

2.3.7 - Synthesis of RhTerpyHPW1:1 supported on Davisil 100 silica

Rh(acac)(CO)(Terpy) was synthesised as described in Section 2.3.5. In a separate round bottom flask H₃PW₁₂O₄₀.20H₂O (HPW) (0.623 g, 0.194 mmol) and Davisil 100 silica (0.550 g) were stirred in 10 ml of degassed THF for 3 hours. After the HPW had been impregnated on to the silica the Rh(acac)(CO)(Terpy) solution was added and the solution stirred for a further 15 minutes. The solvent was removed from the resulting solid using a rotary evaporator. The red/purple powder was then dried at 60 °C over night in a vacuum oven.

Yield 1.18 g (93 mass %)

Elemental Analysis %:

Experimental mass % - C 4.79, H 1.54, N 0.3, P 0.39, Rh 0.57, W 32.76

Atoms per Keggin: C 16, H 61, N 2, P 1, Rh 1

IR (Rh-CO): 2030 br, 2113 cm⁻¹

2.3.8 - Synthesis of RhAnthraphosHPW1:1

Rh(Anthraphos)(CO) (supplied by Prof. Paul Pringle *et al.* at University of Bristol) (mass 131.2 mg, 0.194 mmol). In a separate round bottom flask H₃PW₁₂O₄₀.20H₂O (HPW) (0.623 g, 0.194 mmol) was stirred in 10 ml of degassed THF. The HPW solution was added to the Schlenk tube containing Rh(Anthraphos)(CO) and stirred for a further 15 minutes. The solvent was removed *in vacuo* and the resulting brown powder was washed with hexane by cannula filtration.

Yield 0.732 g (97 mass %)

Elemental analysis %:

Expected mass % - C 11.96, H 1.80, P 2.37, Rh 2.63, W 56.33

Experimental mass % - C 12.15, H 1.82, P 1.95, Rh 2.18, W 54.81

MS (m/z): ESI⁺: 649.1, {Rh(Anthraphos)(H)⁺}, 677.1
 {Rh(Anthraphos)(CO)(H)⁺}, 690.1 {Rh(Anthraphos)(CH₃CN)(H)⁺}, ESI⁻: 958.6
 {PW₁₂O₄₀}³⁻
¹H NMR (C₆D₆) δ = of δ = -6.9 (dt, 11.57 Hz, Rh-*H*), -12.7 (dt, 23.86 Hz, Rh-*H*),
 -17.4 (dt, 31.5 Hz, Rh-*H*), 7.0 – 8.8 (m, Anthraphos aryl-*H*)
³¹P{¹H} NMR (C₆D₆): 52.5, (d, 287 Hz) 56.0 (d, 368 Hz), -15.0 (s, HPW)
¹³C (C₆D₆): δ = 133.3, 131.0, 129.7 (Anthraphos aryl-*C*)
 IR (Rh-CO): 2003, 2079, 2096 cm⁻¹

2.3.9 - Synthesis of RhAnthraphosHPW1:1 supported on Davisil 100 silica

Rh(Anthraphos)(CO) (supplied by Prof. Paul Pringle *et al.* at Bristol University) (mass 131.2 mg, 0.194 mmol.). In a separate round bottom flask H₃PW₁₂O₄₀.20H₂O (HPW) (0.623 g, 0.194 mmol) and Davisil 100 silica (0.550 g) were stirred in 10 ml of degassed THF for 3 hours. After the HPW had been impregnated on to the silica the Rh(Anthraphos)(CO) 1.94 mmolar solution was added and the solution stirred for a further 15 minutes. The solvent was removed from the resulting solid using a rotary evaporator. The red / purple powder was then dried at 60 °C over night in a vacuum oven.

Yield 1.28 g (98 mass %)

Elemental Analysis %:

Experimental mass % - C 10.01, H 1.65, P 1.11, Rh 1.3, W 31.15

Atoms per Keggin – C 59, H 116, P 3, Rh, 1 W 12

IR (Rh-CO): 2096 cm⁻¹

2.4 - Chemicals List

- Acetic Acid, 99.7+ %, Aldrich
- Acetone, Laboratory Reagent Grade, Fisher Scientific
- Alumina, Chromatography Grade, Fluka
- Bis(diphenyl phosphino)ethane, 99 %, Aldrich
- Boron Nitride, powder ~1 micron, 98 %, Aldrich
- D₆-Benzene, 99.9 atom % D, Aldrich

- Carbon Monoxide, 99.0 + %, Aldrich
- Caesium acetate, 99.9 %, Aldrich
- Chloroform, HPLC Grade, Fisher Scientific
- Deuterated chloroform, 99.9 atom % D, Aldrich
- Cyclopentadiene, cracked from dicyclopentadiene, ≥ 95 %, Aldrich
- Dichloromethane, HPLC Grade, Fisher Scientific
- Diethyl ether, Anhydrous, Fisher Scientific
- Dimethyl ether, 99 + %, Aldrich
- D₆-DMSO, 99.9 atom % D, Aldrich
- Ethanol, Analytical reagent grade ≥ 98 %, Fisher
- Helium, ≥ 99.995 %, Aldrich
- Hexane, HPLC Grade, Fisher Scientific
- Methanol, Analytical reagent grade, Fisher
- Methyl acetate, Laboratory Reagent Grade, Fisher
- Pentane, HPLC Grade, Fisher Scientific
- Phosphotungstic acid hydrate, reagent grade, Sigma Aldrich
- Phenyl acetylene, 98 %, Acros Organics
- Potassium bromide, Spectrograde for IR spectroscopy, Fisher
- Pyridine, ≥ 99.0 %, ACS reagent
- Rh(acac)(CO)₂, Purum, Fluka
- Rhodium (III) trichloride, assay 42.33 %, Johnson Matthey
- Rhodium (IV) oxide, 99.8 %, Aldrich
- Ruthenium (III) trichloride, assay 41.98 %, Johnson Matthey
- Ruthenium (IV) oxide, Johnson Matthey
- Silica (Davisil) 100 Å, Thermo Fisher Scientific
- Silica 40 Å, Quartz chip, Fisher Scientific
- Silver acetate, Purum ≥ 99.0 %, Purum, Fluka
- Tetrahydrofuran, HPLC Grade, Fisher Scientific
- Terpyridine, 98 %, Sigma Aldrich
- Triethylamine, Lab Reagent Grade, Fisher Scientific
- Triphenyl phosphine, ReagentPlus 99 %, Sigma Aldrich
- Xantphos, 97 %, Aldrich

2.5 - References

1. <http://www.picotech.com>.
2. E. F. Kozhevnikova and I. V. Kozhevnikov, *Journal of Catalysis*, 2004, **224**, 164-169.
3. N. X. Song, C. Rhodes, D. Johnson and G. J. Hutchings, *Catalysis Letters*, 2005, **102**, 271-279.
4. I. V. Kozhevnikov, S. Holmes and M. R. H. Siddiqui, *Applied Catalysis A: General*, 2001, **214**, 47-58.
5. S. H. M.R.H. Siddiqui, H. He, W. Smith, E.N. Coker, M.P. Atkins and I.V. Kozhevnikov, *Catalysis Letters*, 2000, **66**, 53-57.
6. L. H. Little and C. H. Amberg, *Canadian Journal of Chemistry-Revue Canadienne De Chimie*, 1962, **40**, 1997-2006.
7. S. Derrouiche and D. Bianchi, *Applied Catalysis A: General*, 2006, **313**, 208-217.
8. J. W. Niemansverdreit, *Spectroscopy in Catalysis*, VCH, 1995.
9. B. D.Cullity, *Elements of X-ray diffraction*, 2nd Edition edn., Addison-Wesley Publishing Company inc., 1978.
10. D. Briggs and M. P. Seah, *Practical Surface Analysis - Auger and X-Ray Photoelectron Spectroscopy*, second edn., John Wiley and sons 1990.
11. W. N. Delgass, G. L. Haller, R. Kellermann and J. H. Lunsford, *Spectroscopy in Heterogeneous catalysis*, Academic Press, inc., 1979.
12. <http://srdata.nist.gov/xps/>.
13. S. Doniach and M. Sunijic, *J. Phys.*, 1970, **C3**, 285.
14. B. K. Teo and D. C. Joy, *EXAFS spectroscopy*, Plenum Press, New York 1981.
15. S. Lowell, *Introduction to powder surface area*, Wiley-Interscience, John Wiley and sons, 1979.
16. E. M. McCash, *Surface Chemistry*, OUP, 2001.
17. S. Brauner, P. H. Emmett and E. Teller, *Journal of the American Chemical Society*, 1938, **60**, 309-319.
18. P. M. Treichel, D. A. Komar and P. J. Vincenti, *Synthesis and Reactivity in Inorganic and Metal-Organic Chemistry*, 1984, **14**, 383-400.
19. A. J. Sandee, J. N. H. Reek, P. C. J. Kamer and P. W. N. M. van Leeuwen, *Journal of the American Chemical Society*, 2001, **123**, 8468 - 8476.

Chapter 3 - Synthesis, characterisation and catalysis of Ru- polyoxometallates

3.1 - Introduction

The use of organoruthenium complexes in catalysis is well established wherein they can perform a range of synthetically useful transformations. Of these systems, a variety of mechanistically very different processes such as reactions initiated by metallocycle formation, vinylidene formation, C-H activation, and activation of carbon-carbon multiple bonds by coordination.¹⁻³ The development of the ruthenium catalyst field has benefited by the huge popularity of Grubbs-type catalysts^{4, 5} generating a library of inexpensive Ru complexes. The ability of ruthenium to assume a wide range of oxidation states (from 2- to 8+) and coordination geometries provides unique opportunities for catalysis. The ruthenium complexes used herein are in the 2+ oxidation state. For many transition metal catalysts the ability to change oxidation state is a crucial part of their activity, however, in many ruthenium-mediated processes, the 2+ oxidation state is dominant. Many ruthenium transition metal complexes operate in catalytic cycles where all intermediates are in a formal 2+ oxidation state. This is the case for ruthenium half-sandwich complexes of formula $\text{Ru}(\eta^5\text{-C}_5\text{R}_5)(\text{PR}'_3)_2\text{Cl}$, where R is typically H or Me and R', a variety of alkyl, aryl or allyl groups, in catalytic cycles such as inter- and intra-cyclizations as well as oligomerisations.⁶⁻⁹ Ru(II) half-sandwich mediated oligomerisation reactions of alkynes have received significant coverage as an attractive, atom-economical route to C-C bond formation in organic synthesis.¹⁰⁻¹² There are some other successful candidates for this type of coupling chemistry such as the use of cobalt dicarbonyl half-sandwich complexes in cyclotrimerizations including that of *bis*-[(diarylamino)aryl]alkynes to the hexa-paradiarylamino phenyl benzenes¹³ as well as numerous intramolecular^{14, 15} and intermolecular cyclotrimerizations by similar complexes.^{16, 17} However, generally these systems require activation by additives such as Zn to reduce Co(II) to active Co(I)¹⁸ do not have the range or high

conversions (*ca.* ~ 90-100 %) accessible. In the case of ruthenium catalysts, this is true for both cyclisations¹⁹ and linear reactions such as the head-to-head dimerization of terminal alkynes to give enynes,²⁰ the addition of terminal alkynes to internal alkynes to give enynes.²¹ and the head-to-head cross dimerization of alkenes with alkynes to give dienes.²² Heterogenising such complexes while maintaining catalytic activity at the ruthenium centre, either through their attachment to an inert support phase or, more usefully, a secondary active component, is a very desirable trait, unifying catalytic potential and structural robustness. There are various examples where organometallic complexes including that of Ru and Rh have been immobilised on silica, zeolites and organic polymers to form heterogeneous catalysts in chemistries such as hydrogenation²³,²⁴ hydroformylation²⁵⁻²⁷ and methanol carbonylation.²⁴

Polyoxometallate (POM) materials have captivated both academic and commercial interest due to their intriguing structural diversity and application in areas such as catalysis, magnetochemistry, materials science and medicine,²⁸⁻³² described in more detail in Section 1.8-10. Organometallic polyoxometallates, in particular ruthenium derived species are of growing industrial importance due to the unique redox and catalytic activity of ruthenium.^{33, 34} The inclusion of organoruthenium species into polyoxometallates reported in the literature commonly employs either single ligands, such as benzene or *p*-cymene^{35, 36} or coordinated solvent molecules such as DMSO.^{37, 38} These kind of species have been considered more of structural interest than for their catalytic application. Polyoxometallates have been used as models for metal-oxides commonly used as supports in transition metal catalysis, but generally these hybrid materials operate as soluble catalysts under homogeneous reaction conditions.³⁹⁻⁴¹ Heterogenisation of ruthenium complexes is known but this generally utilises inactive support phases such as silica or organic polymers such as polystyrene.⁴²⁻⁴⁴ Developing organoruthenium polyoxometallates to include ligand character employed in conventional homogeneous catalysis, would offer the prospect of harnessing the spectrum of ruthenium chemistries available to date for heterogeneous reactions and continuous processing while offering the acid and redox character of the phosphotungstate cage.

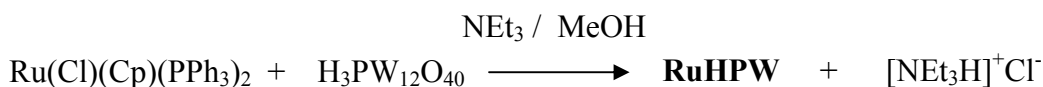
Currently, methanol carbonylation catalysis is performed using primarily Rh and Ir homogeneous species. Ru-CO organometallic species are well established in the literature.⁴⁵ The high cost of Rh and Ir⁴⁶ metals has sparked interest in utilising other more economical metal sources. Previous studies illustrate the need for new more robust ligand systems to stabilise transition metal systems for the carbonylation of methanol.⁴⁷ To this end Ru-organometallic systems were investigated. In this work the phosphines; PPh₃ (P(C₆H₅)₃) and dppe ((C₆H₅)₂P(CH₂)₂P(C₆H₅)₂) as well as the cyclopentadienyl ring are considered in the Ru ligand framework due to their wide availability and proven record at successfully activating small organic molecules in particular for C-C bond formation.⁴⁸⁻⁵⁰

Here the syntheses of ruthenium-containing polyoxometallate (POM) species based on the phosphotungstate Keggin anion (PW₁₂O₄₀³⁻) are discussed in terms of the introduction of an organometallic ruthenium species Ru(Cl)(η^5 -C₅H₅)(L)₂ (where L = PPh₃ or dppe), in the presence of NEt₃ liberates the three protons from phosphotungstic acid (H₃PW₁₂O₄₀, HPW), as well as Cl⁻ from the Ru complex. Structural conclusions are proposed based on an extensive solution and solid state characterisation study with focus on application of these systems as potential methanol carbonylation catalysts.

3.2 - Synthesis and characterisation of RuHPW

An easily accessible ruthenium species was used which is known to be air stable. $\text{Ru}(\text{Cl})(\text{Cp})(\text{PPh}_3)_2$ ($\text{Cp} = \eta^5\text{-C}_5\text{H}_5$) was synthesised according to the literature¹¹ (Section 2.2.1) All preparations were performed in ethanol. A dark brown solution of RuCl_3 was rapidly transferred to a solution of triphenyl phosphine at reflux followed by addition of freshly distilled cyclopentadiene. After one hour at reflux the dark brown solution changed to red orange. The solution was cooled for 16 hours yielding a crop of air stable orange crystalline $\text{Ru}(\text{Cl})(\text{Cp})(\text{PPh}_3)_2$. The successful synthesis of $\text{Ru}(\text{Cl})(\text{Cp})(\text{PPh}_3)_2$ was established by ^1H NMR in deuterated chloroform showing characteristic triphenyl phosphine aryl C-H chemical shifts between 7.1 – 7.4 ppm and a single peak at 4.1 attributed to the C_5H_5 Cp ring with relative integrations of 30 to 5, as expected for a 2 : 1 ratio of triphenyl phosphines : cyclopentadienyl ring. This was accompanied by $^{31}\text{P}\{^1\text{H}\}$ NMR showing a singlet peak at 40.5 ppm for two equivalent triphenylphosphine ; ligands reported in Section 2.2.1 with reference to the synthetic procedure outlined by Treichel.⁵¹ This batch of the resulting Ru parent complex was used for subsequent syntheses of prospective catalytic materials.

The synthesis of **RuHPW** is quite facile. All preparations were accomplished in an air atmosphere. A suspension of $\text{Ru}(\text{Cl})(\text{Cp})(\text{PPh}_3)_2$ was prepared in methanol, with addition of one equivalent of phosphotungstic acid ($\text{H}_3\text{PW}_{12}\text{O}_{40}\cdot 20\text{H}_2\text{O}$). On addition of three equivalents triethylamine the formation of a short lived white precipitate was observed followed by the complete dissolution of the suspension. This change in solubility indicates a change in the nature of the Ru precursor complex. The resulting solution was stirred for 23 hours. The air-stable tan coloured solid (**RuHPW**) was isolated by filtration and washed with methanol. This simple synthetic procedure adds to its appeal as a potential catalytic material. The general schematic for the synthesis of this material is shown in **Equation 3.2.1**.



Equation 3.2.1: Reaction schematic for the synthesis of **RuHPW**.

The new material was analysed by XPS, CHN and elemental analysis of Ru, W and Cl content: Cl analysis showed no Cl within the detection limits of the technique (± 0.2 atom %). The stoichiometry was calculated for the material based on 12 tungsten atoms which would be consistent with 1 Keggin unit from the HPW ($\text{PW}_{12}\text{O}_{40}$) (**Table 3.2.1**). The observed 2Ru : 5P : 12W ratio is consistent with that expected for 2 Ru units for each Keggin. As the initial stoichiometry of the two components is 1 : 1, it could be hypothesised that some phosphotungstic acid was lost in the filtrate. This was later confirmed by a weak ^{31}P solution NMR signal at -15 ppm, consistent with the phosphorus resonance from the phosphotungstate cage. This is in agreement with preliminary studies by Corcorran, a BSc student from within the author's research group, where it was found that the Ru : HPW : NEt_3 observed in the final **RuHPW** species is insensitive to initial ratio of starting materials.⁵²

Table 3.2.1: Elemental atom % data taken from XPS, CHN and elemental analysis studies. Stoichiometry calculated relative to 12 tungsten atoms.

Element	Experimental Composition (atom %) ± 0.2 %	Experimental Stoichiometry	Theoretical Stoichiometry
C	37.5	100	88
H*	34.9	95	86
N	0.5	1	1
Ru	0.9	2	2
W	4.1	12	12
P	2.0	5	5
O	19.8	58	40

*experimental data from bulk CHN analysis only

In order to deduce a structure for the **RuHPW** compound based on the starting materials, it was necessary to confirm that the Ru species maintains its ligand structure and the Keggin remains intact. This was proved by ESI-MS, DRIFTS and NMR. The ESI-MS positive spectrum shows a dominant positive ion peak at

m/z 691.12 representing the $[\text{Ru}(\text{Cp})(\text{PPh}_3)_2]^+$ ion. The negative spectrum shows peaks at m/z 958.73 and 1449.58 which represent $[\text{PW}_{12}\text{O}_{40}]^{3-}$ and $[\text{HPW}_{12}\text{O}_{40}]^{2-}$ respectively. A comparison of DRIFTS spectra of **RuHPW** with the $\text{Ru}(\text{Cl})(\text{Cp})(\text{PPh}_3)_2$ and HPW precursors, (**Figure 3.2.1**) shows that the characteristic peaks observed for the two precursors are preserved in the **RuHPW** compound. Definitive bands are summarised in **Table 3.2.2**.

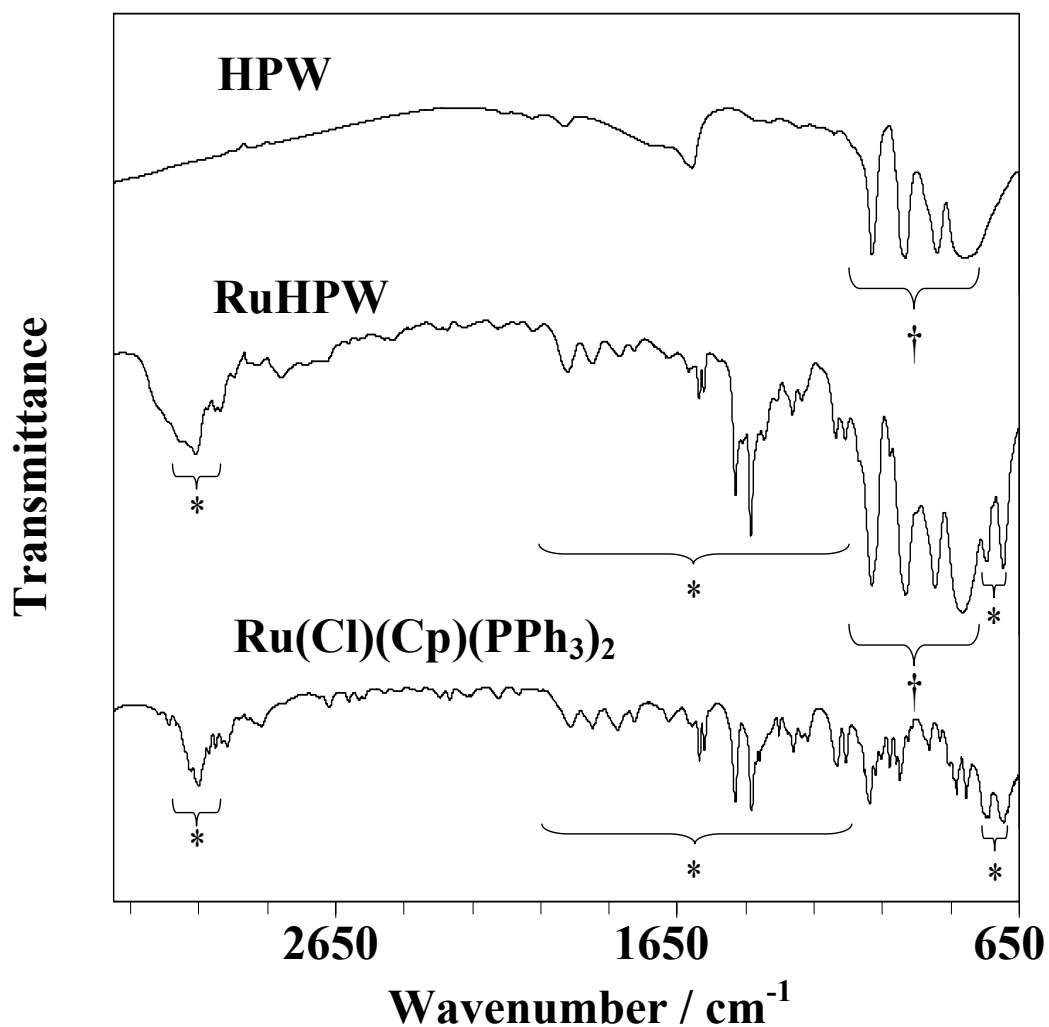


Figure 3.2.1: DRIFTS spectra of **RuHPW**. Comparative spectra are shown for the $\text{Ru}(\text{Cl})(\text{Cp})(\text{PPh}_3)_2$ (*) and HPW (†) precursors.

Table 3.2.2: IR bands of DRIFTS spectra for polyoxometallates and organo-Ru framework.

IR Band	Band wavenumber (cm ⁻¹)
W-O _{int} -W _{symm} ^a	830
W-O _{ext} -W _{assym} ^a	890
W=O _{ext} ^a	990
P-O _{assym} ^a	1090
P-C ^b	1435 ⁵³
C-C ^b	1483 ⁵⁴
C-H ^b	3004, 3075 ⁵⁴

^abands associated with the polyoxometallate Keggin,^{47, 55, 56} ^bbands associated with the {Ru(Cp)(PPh₃)₂} functionality

TGA (**Figure 3.2.2**) was employed to measure the thermal stability of **RuHPW** and consequently its suitability for application in methanol carbonylation catalysis where current homogeneous catalytic processes typically work at 200 °C.⁵⁷⁻⁵⁹ Inspection of the mass loss profile of **RuHPW** indicates that the compound is stable up to 280 °C due to substantial mass loss below this temperature. It is only at 80 °C where solvent loss equating to ~ 2 % is consistent with weakly bound physisorbed solvent, believed to be methanol. In contrast, TGA of the HPW precursor shows mass losses for physisorbed water (~ 110 °C) and crystalline water (~ 175 °C), both of which are absent from the **RuHPW** compound suggesting breakdown of the secondary Keggin structure and associated water expulsion.^{32, 60} **RuHPW** shows only high temperature mass losses, the first between ~ 280 and 450 °C where a loss of 16 % in accordance with the major decomposition of the parent Ru complex is consistent with loss and decomposition of four equivalents of PPh₃ and two cyclopentadienyl rings associated with 2 {Ru(Cp)(PPh₃)₂}. This is supportive of the proposed 2 : 1 ruthenium to Keggin consistent with the Ru : W ratio observed in composition analysis. A plateau at 500 °C and subsequent second smaller mass loss of 10 % above 500 °C reflects further decomposition of the Ru ligands (at this point it is likely that the ligands are unbound due to the inherent stability of the ruthenium organometallic species, where decomposition typically occurs at ~ 250 °C⁶¹⁻⁶³). Additional decomposition of the triethylammonium cation between 400 °C and 600 °C⁶⁴ is considered to be hidden within the mass loss observed for the bulk of the ruthenium ligand structure. Eventual decomposition of the primary Keggin

polyoxometalate cage around 620 °C only accounts for 0.9 % of the mass loss from the parent HPW^{56, 65} and < 0.5 % of that from **RuHPW**.

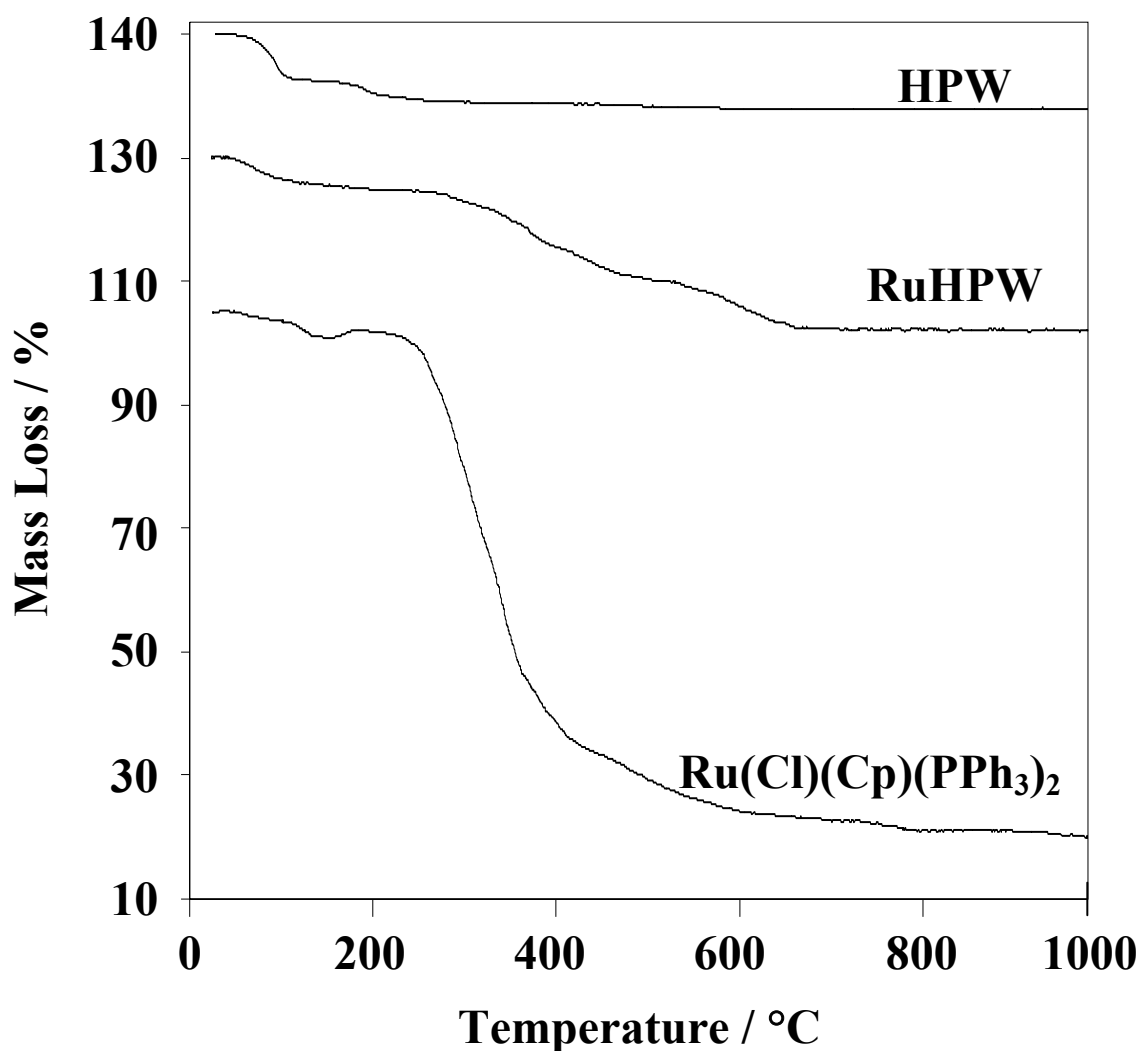


Figure 3.2.2: TGA profiles of **RuHPW**, $\text{Ru}(\text{Cl})(\text{Cp})(\text{PPh}_3)_2$ and HPW precursors.

It is evident from the powder XRD patterns of **RuHPW** that (**Figure 3.2.3**) some local crystallinity is preserved. New peaks can be identified differing from the $\text{Ru}(\text{Cl})(\text{Cp})(\text{PPh}_3)_2$ and HPW precursors. This supports the formation of a novel structure with new crystallinity. The HPW crystal pattern shown in **Figure 3.2.3** occurs due to the secondary crystalline structure due to interlinking H_5O_2^+ units.^{66, 67} The lack of HPW character is consistent with the observed loss in crystalline water in the **RuHPW** from TGA measurements.

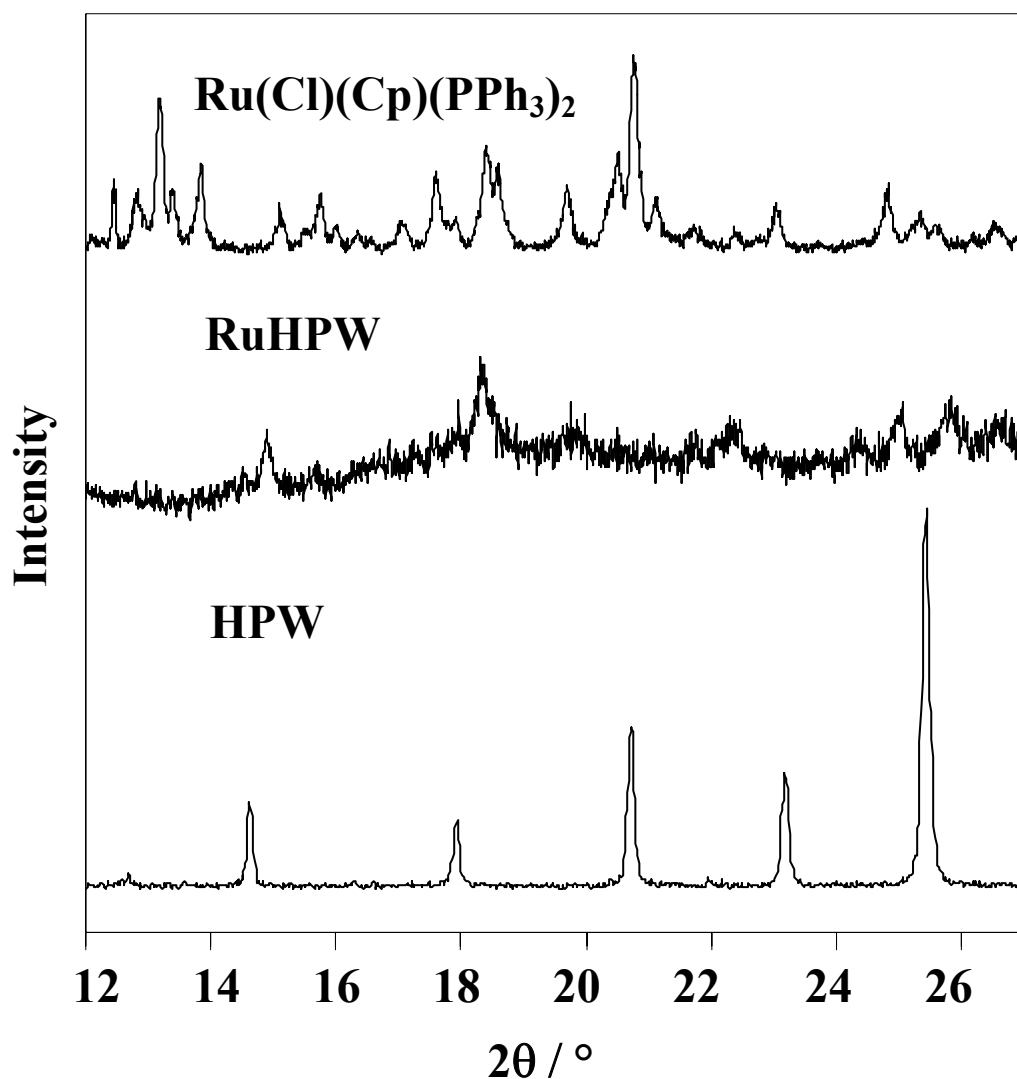


Figure 3.2.3: Powder X-ray diffractograms of **RuHPW** and the $\text{Ru}(\text{Cl})(\text{Cp})(\text{PPh}_3)_2$ and HPW precursors.

RuHPW was analysed by ^1H solution NMR spectroscopy, (Table 3.2.3) where $\text{D}_6\text{-DMSO}$ was employed as solvent as **RuHPW** proved to be insoluble in other common NMR solvents. Protons associated with the phenyl groups of the ligated triphenyl phosphine ligands were observed between δ 7.0 and 7.5 ppm. Close inspection of this region show the distinct chemical environments at δ 7.0, 7.3 and 7.4 ppm of equal intensity equating to 30 H's, consistent with that observed for the parent complex and $^{31}\text{P}\{^1\text{H}\}$ NMR spectrum gave evidence consistent with a ruthenium fragment containing both the proton and phosphorus environments of ' $\text{Ru}(\text{Cp})(\text{PPh}_3)_2$ '. In addition there is a second phosphorus environment which is comparable with that of the Keggin unit at δ -15.1 ppm.

The Cp ^1H peak position shifts from 4.0 ppm to 4.9 ppm in the Ru fragment of **RuHPW**. This supports a change in the ligands coordinated around the metal centre from the $\text{Ru}(\text{Cl})(\text{Cp})(\text{PPh}_3)_2$. This is consistent with the substitution of Cl for a less electron donating ligand at the Ru metal, responsible for inducing a peak shift to low field similar to that observed in the literature where shifts of ~ 0.6 ppm are evident for cationic vinylidene complexes.⁶⁸

Table 3.2.3: ^1H NMR assignments for **RuHPW** in D_6 -DMSO.

^1H NMR 400 MHz (D_6 -DMSO / 298K)		
δ / ppm	Assignment	Integration
1.1 (t)	Me	9
3.0 (m)	Et	6
4.9 (s)	Cp	5
7.0 (s)	Ph	10
7.4 (m)	Ph	10
7.3 (m)	Ph	10
8.9 (br s)	NH^+	1

From early studies⁵² it was found that phosphotungstic acid (HPW) would not interact with the ruthenium species without the addition of triethylamine base. This was demonstrated by the inherent leaching of the ruthenium parent from the material accompanied by no chloride loss from XPS studies and no change in the solution state ^1H NMR spectrum from interaction in the absence of base. This is due to the dual role of the base abstracting Cl^- and deprotonating of HPW allowing the interaction between the phosphotungstate and Ru species. The phosphotungstate acts as a 3- anion, the phosphotungstate then interacts with two mono-cationic Ru species. Direct coordination at external POM oxygens is possible (evident in bulky alkoxy esters of phosphotungstic acid in the literature⁶⁹⁻⁷¹) at the vacant Ru site formed from loss of Cl^- (evident from lack of chloride signal from XPS compositional analysis is investigated). The single negative charge induced on the heteropolytungstate by substitution of 2 cationic Ru species is countered by HNEt_3^+ formed from protonation of the base. This ratio is

consistent with the composition analysis where a ratio of 2Ru : 1N : 12W is observed. ^1H NMR spectroscopy supports this observation, where a broad peak at δ 8.9 ppm consistent with the presence of an NH^+ species can be noted with a triplet and multiplet peak at δ 1.1 and 3.0 ppm integrating to 9 and 6 protons corresponding to the methyl and CH_2 group of the triethyl ammonium species respectively. The ammonium salt of HPW (NEt_3HPW) was synthesised, by recrystallization of HPW from methanol in the presence of NEt_3 giving ^1H NMR peak positions which confirmed these assignments. Loss of HPW crystallinity from TGA studies discussed earlier and powder XRD where no parent HPW peaks were observed is consistent with complete ion exchange for two ruthenium and one triethylammonium cation. The $^{31}\text{P}\{^1\text{H}\}$ NMR shows two phosphorus environments at 37.7 and -15.0 ppm. These peaks represent the triphenyl phosphine ligands of the Ru species and the Keggin phosphorus atom^{60, 72, 73} respectively. These results demonstrate that the $\text{Ru}(\text{Cp})(\text{PPh}_3)_2$ fragment is still present in **RuHPW**.

A $^{31}\text{P}\{^1\text{H}\}$ MAS NMR spectrum allowed the **RuHPW** to be compared to the precursor $\text{Ru}(\text{Cl})(\text{Cp})(\text{PPh}_3)_2$ in the solid state (**Figure 3.1.4**). Two environments were observed centred around δ 38.5 ppm and -15.4 ppm attributed to the Ru phosphines and central phosphorus of the Keggin respectively. These environments were integrated without taking into consideration spinning side band structure allowing the quantification of the phosphine : Keggin phosphorus ratio. It was found that the phosphorus environments integrate to 4 : 1, consistent with two Ru species to each Keggin. Close inspection of the Keggin region (**Figure 3.2.4** inset top left) reveals an upfield peak shift previously reported upon X-O=W linkage formation of Keggin type polyoxometallates.^{69, 74}

The presence of the triethyl ammonium salt $[\text{NEt}_3\text{H}]^+[\text{PW}_{12}\text{O}_{40}]^{3-}$, readily synthesised from a stoichiometric mixture of base and HPW in methanol, as an impurity can be discounted as it exhibits a resonance in the $^{31}\text{P}\{^1\text{H}\}$ solid state NMR spectrum at -11.1 ppm, distinct from both the parent HPW and **RuHPW**, -14.2 and -15.4 ppm respectively (**Figure 3.2.4** inset top left).

Confirmatory evidence for the structure for the Ru-POM in **Figure 3.2.5** is provided by MALDI-TOF solid state MS (**Appendix 1**), which shows fragments

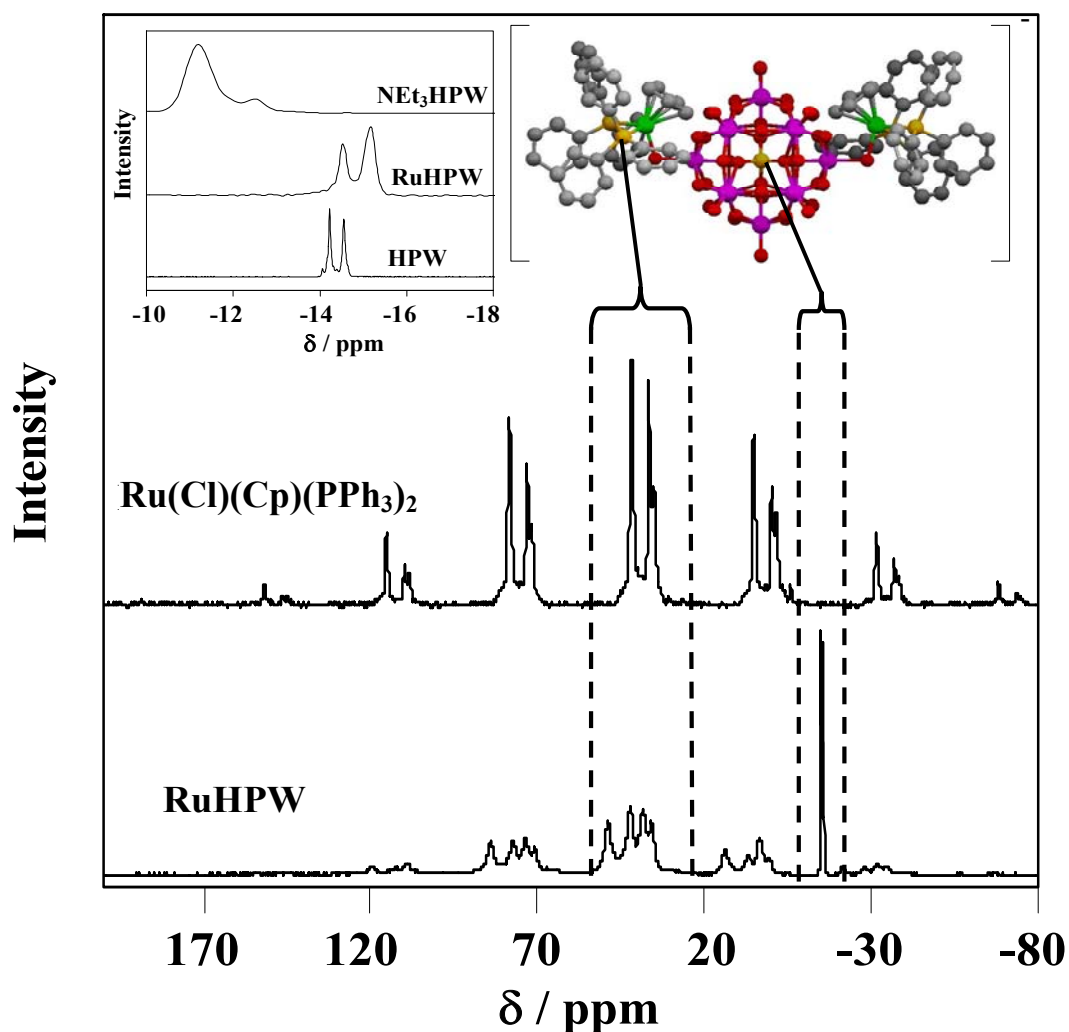


Figure 3.2.4: ^{31}P MAS-NMR spectra of **RuHPW** and the $\text{Ru}(\text{Cl})(\text{Cp})(\text{PPh}_3)_2$ precursor. Spectral peaks used for integration are encapsulated in dotted lines. Inset shows comparison spectra of the Keggin region for **RuHPW**, HPW and NEt_3HPW .

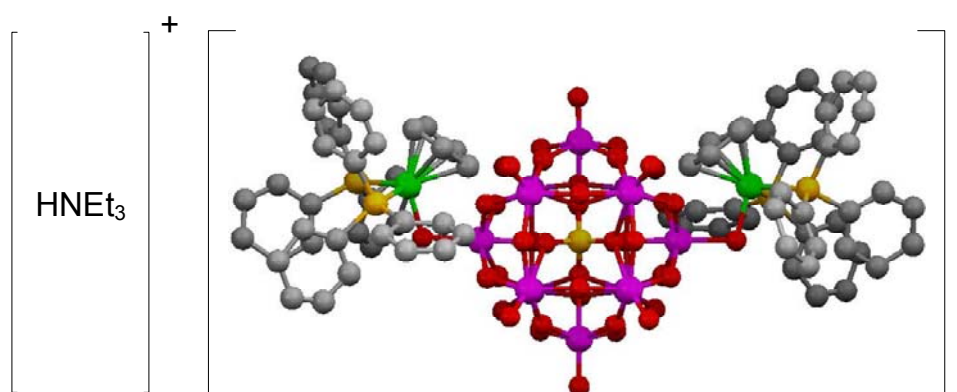


Figure 3.2.5: Proposed structure and cation in covalently bound **RuHPW**.

with the correct isotopic distribution including an ion peak at m/z 3568 consistent with $[(\text{Ru}\{\eta^5\text{-C}_5\text{H}_5\}\{\text{PPh}_3\}_2)(\text{PW}_{12}\text{O}_{40})]^-$. This provides evidence for a direct interaction between ruthenium and the POM cage supporting the hypothesis of a Ru-O=W bond. The identification of NEt_3H^+ in **RuHPW** complements the negative charge generated from the *di*-Ru-POM species balancing the charge ascertaining the formula represented in **Figure 3.2.5**.

XPS studies of the ruthenium 3p orbitals in **RuHPW**, were compared to the $\text{Ru}(\text{Cl})(\text{Cp})(\text{PPh}_3)_2$ precursor, RuCl_3 and RuO_2 , (oxidation states 2, 3 and 4 respectively) (**Figure 3.2.6**). The binding energy of the $3p_{3/2}$ electron in **RuHPW** was shown to be 462.2 eV: this compares to energies for Ru(II) and Ru(III)

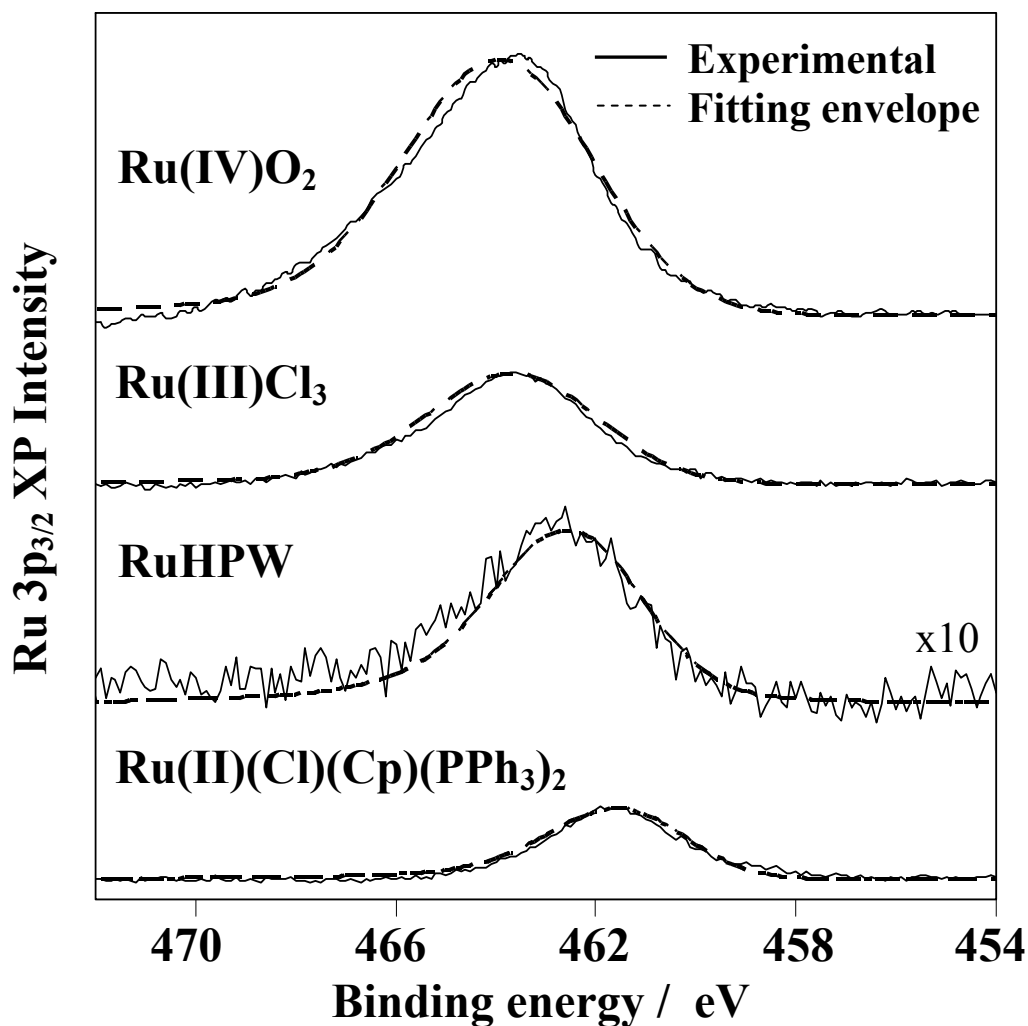


Figure 3.2.6: Ru $3p_{3/2}$ XP spectra of **RuHPW**. Comparative spectra are shown for $\text{Ru}(\text{Cl})(\text{Cp})(\text{PPh}_3)_2$, RuCl_3 and RuO_2 .

standards of 461.8 and 463.2 eV respectively. The greater binding energy in the case of **RuHPW**, when compared to the Ru(II) may be attributable to the formal positive charge on the complex.

Ruthenium XANES analyses of the **RuHPW**, Ru(Cl)(Cp)(PPh₃)₂, RuCl₃, RuO₂ and Ru metal provides bulk information, this complements the observation of an increase in oxidation state observed in XPS measurements. From a linear combination fit of Ru standards shown in **Figure 3.2.7** of 0, 2+, 3+ or 4+, a good fit with 68 % Ru(II) from the parent complex in addition to a 32% contribution of Ru(IV). This indicates good agreement of the surface with bulk properties.

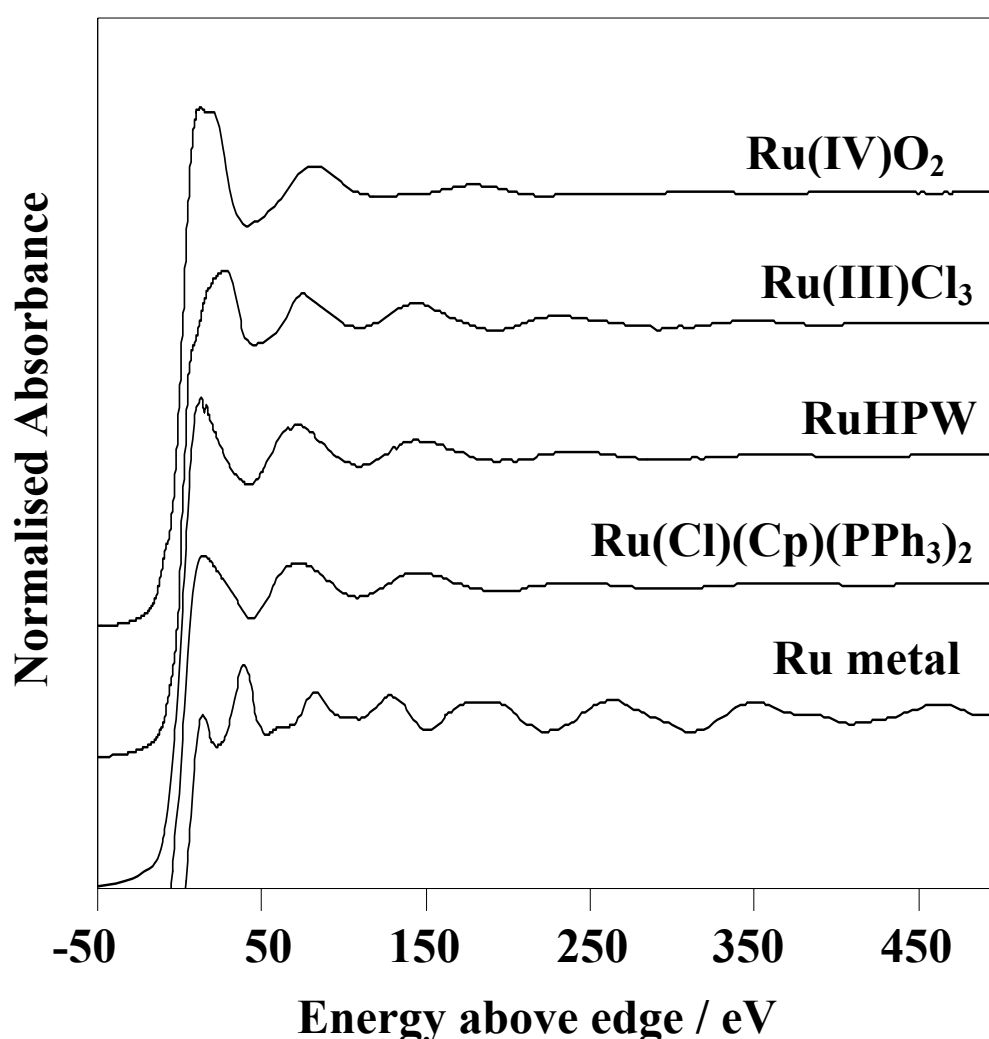


Figure 3.2.7: Ru K-edge normalised EXAFS of **RuHPW**, Ru metal, Ru(Cl)(Cp)(PPh₃)₂, RuCl₃ and RuO₂.

Fitting of EXAFS measurements to a model based on the local coordination shell of the structure proposed in **Figure 3.2.5** was in excellent agreement, with

the cyclopentadienyl ring positioned 2.2 Å, the PPh₃ ligands 2.35 Å from Ru (**Figure 3.2.8, Table 3.2.4**). The Fourier-transformed EXAFS radial distribution plot of **RuHPW** was compared with that of the precursor complex, Ru(Cl)(Cp)(PPh₃)₂ (**Figure 3.1.8**). A more strongly scattering broader shell in the precursor complex is indicative of the more electron dense Cl ligand. This is consistent with crystallographic studies from the Cambridge Crystallographic Database^[JM1] (search - March 2010) where a search for Ru half-sandwich complexes of type 'Ru(Cp)(PR₃)(L)' included results where 'L' was for example CO, Cl, Br, I.⁷⁵⁻⁷⁹ This indicated that carbons in the Cp ligand lie at 2.2 Å, with the more strongly scattering phosphorus and chloride lying further away from the Ru metal centre at 2.35 and 2.31 Å respectively.

Crystallographic evidence for functionalised Keggin polyoxometallates and coordinated organo-transition metal species, such as those containing Zr(Cp)₂,⁸⁰ suggest a linear X-O=W interaction at a terminal oxygen atom on the Keggin.⁸¹ In order to test the hypothesis as to whether HPW is coordinated to

Table 3.2.4: Parameters for EXAFS fitting of Ru(Cl)(Cp)(PPh₃)₂ and **RuHPW** (with and without HPW coordination)

Sample	CN1 Ru- C	CN2 Ru- P	CN3 Ru- Cl	CN3' Ru- O	CN4 Ru- W	R1 (Å) Ru- C	R2 (Å) Ru- P	R3 (Å) Ru- Cl	R3' (Å) Ru- O	R4 (Å) Ru- W	σ_1 Ru-C	σ_2 Ru-P	σ_3 Ru-Cl	$\sigma_{3'}$ Ru-O	σ_4 Ru-W	R ²
Ru(Cl)(Cp)(PPh ₃) ₂	5	2	1	-	-	2.20	2.35	2.35	-	-	0.015	0.015	0.005	-	-	24.60
RuHPW <i>without HPW</i>	5	2	-	-	-	2.20	2.35	-	-	-	0.005	0.007	-	-	-	35.99
RuHPW <i>with HPW</i>	5	2	-	1	1	2.20	2.35	-	2.10	4.34	0.015	0.004	-	0.005	0.015	35.57

82

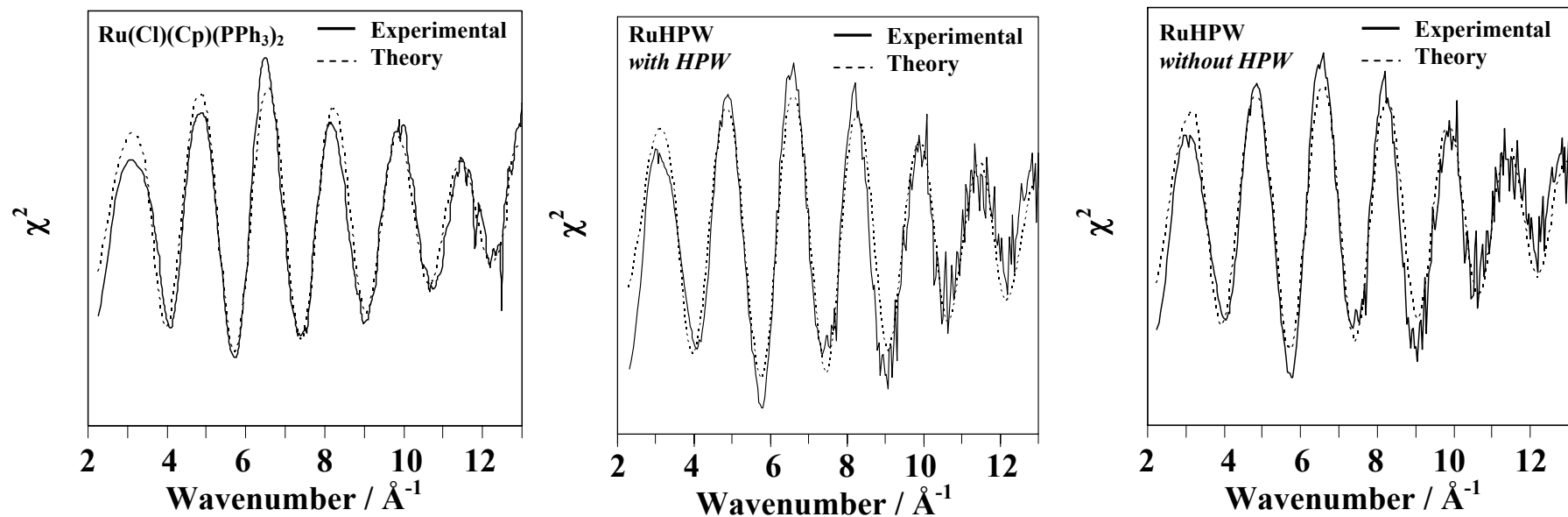


Figure 3.2.9: EXAFS χ^2 plots, experimental and theory Ru(Cl)(Cp)(PPh₃)₂ and **RuHPW** (with and without HPW coordination)

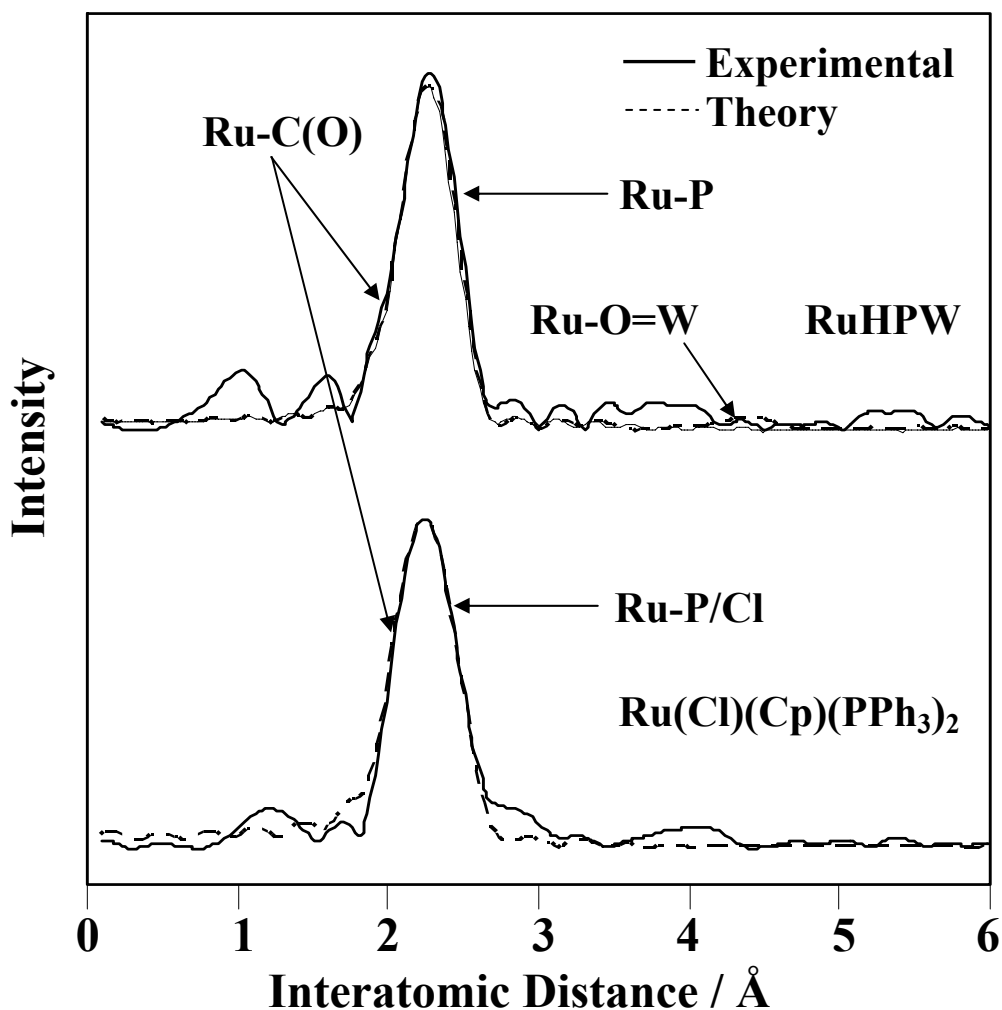


Figure 3.2.8: Fitted radial distribution functions of **RuHPW** and the **Ru(Cl)(Cp)(PPh₃)₂** precursor.

ruthenium, an O atom at 2.1 Å and subsequent W at 4.34 Å, were introduced to the model in accordance with the crystal structure of the HPW Keggin⁸² and expected for a linear Ru-O=W interaction. The quality of fit is comparable in both models with an R^2 value of 35.99 and 35.57 for the non-coordinated and coordinated Keggin model respectively. Although the tungsten atom has a greater amount of electron density in comparison to C, O and P, the peak observed in the Fourier transform fit is of low intensity due to the relative distance from the ruthenium centre. A slight improvement of the fit with a Ru-O=W interaction is considered to be primarily due to the introduction of greater electron density in the first shell due to coordinated oxygen. Although an improvement to the fit is observed, the relative intensity of the W shell does not provide the necessary substantial evidence to confirm this interaction as initially anticipated. A

complementary study of the W L(III) EXAFS may be advisable to support further structural conclusions. It is worth noting that additional electron density to the first coordination shell much greater than that of oxygen (eight electrons), such as phosphorus, chloride or a diatomic heteroatom containing species, (eg. N₂, O₂) sees a decline in the goodness of fit.

The MS evidence for a Ru-polyxometallate species was supported by the postulation of several ligands in the place of Cl occupying the co-ordination site (of which the loss has already been discussed due to elemental analysis and XPS). Methanol may have coordinated to the ruthenium from the solvent. A sample of **RuHPW** was vacuum dried for 6 hours to ensure all residual physisorbed methanol, (due to residual solvent from the synthetic reaction) was removed. This was confirmed by ¹H NMR of a pre-weighed sample with the absence of a characteristic methyl and OH peak at ca. δ 3.2 and 4.0 ppm respectively. Two equivalents of methanol were added to the NMR sample and the resulting spectra was scrutinised for the appearance of methanol-related peaks. Peaks integrated to two equivalents of methanol were observed as expected for un-coordinated methanol. No resonances which could account for ligated methanol were observed. Other possibilities for the ligand coordinated to the ruthenium typically present in the gas phase were considered, these included CO, N₂, and O₂. CO was not observed from IR analysis where no carbonyl bands were observed, and through examination of the elemental analyses (including CHN and XPS).

[RuCp*(PR₃)₂L]⁺ species (Cp* = (C(CH₃)₅)) are known in which L = η²-O₂. Crystal structures for these complexes have been documented by Tenorio *et al.* and others in the literature.⁸³⁻⁸⁸ N₂ complexes are also known, however it has been observed that these complexes are air sensitive and can readily decompose to the O₂ complex⁸⁶ and so due to the ‘air-insensitive’ conditions used for the preparation of **RuHPW** this was an unlikely candidate. Nitrogen co-ordination induces a dipole in the N₂ molecule making it IR-active and indeed in analogous Ru-N₂ half-sandwich complexes, bands in the region of 400 – 700 cm⁻¹ are observed.⁸⁹ However due to limitation in the spectrometers used for analysis of **RuHPW**, this region can not be observed, however, elemental analysis and XPS where the nitrogen content was in good agreement with one nitrogen atom present

accountable to the triethylammonium cation. This discredits the likelihood of formation of a di-nitrogen complex. This is also the case for triethylammonium co-ordination where a nitrogen-enriched species should be observed. In addition ^1H NMR chemical shifts were not observed which could account for coordinated amines of this kind.⁹⁰ Consideration of a species with $\text{Ru}(\eta^2\text{-O}_2)$ gave a reasonable match from XPS atom % calculations but in order to explore this further Raman spectroscopy was employed.

Figure 3.2.10 shows the Raman spectra for **RuHPW** and the chloride precursor complex. Bands associated with the $\{\text{Ru}(\text{Cp})(\text{PPh}_3)\}$ backbone are evident, key features at 102, 213, 1000, 1586 and 3061cm^{-1} are denoted by an asterisk. **RuHPW** also contains strong characteristic bands associated with the external W-O-W symmetric stretch of HPW,⁹¹ at 525cm^{-1} , and an intense band characteristic of terminal W=O stretches at 987cm^{-1} .⁹² In addition, a shoulder on the parent Ru bands at 949cm^{-1} is consistent with an asymmetric P-O band, supporting existing DRIFTS data. In addition to Ru and HPW bands an intense peak at 83cm^{-1} is associated with C-H bands of the HNEt_3^+ cation present in the bulk **RuHPW** consistent with other cationic heteropolyacid species in the literature.⁹³

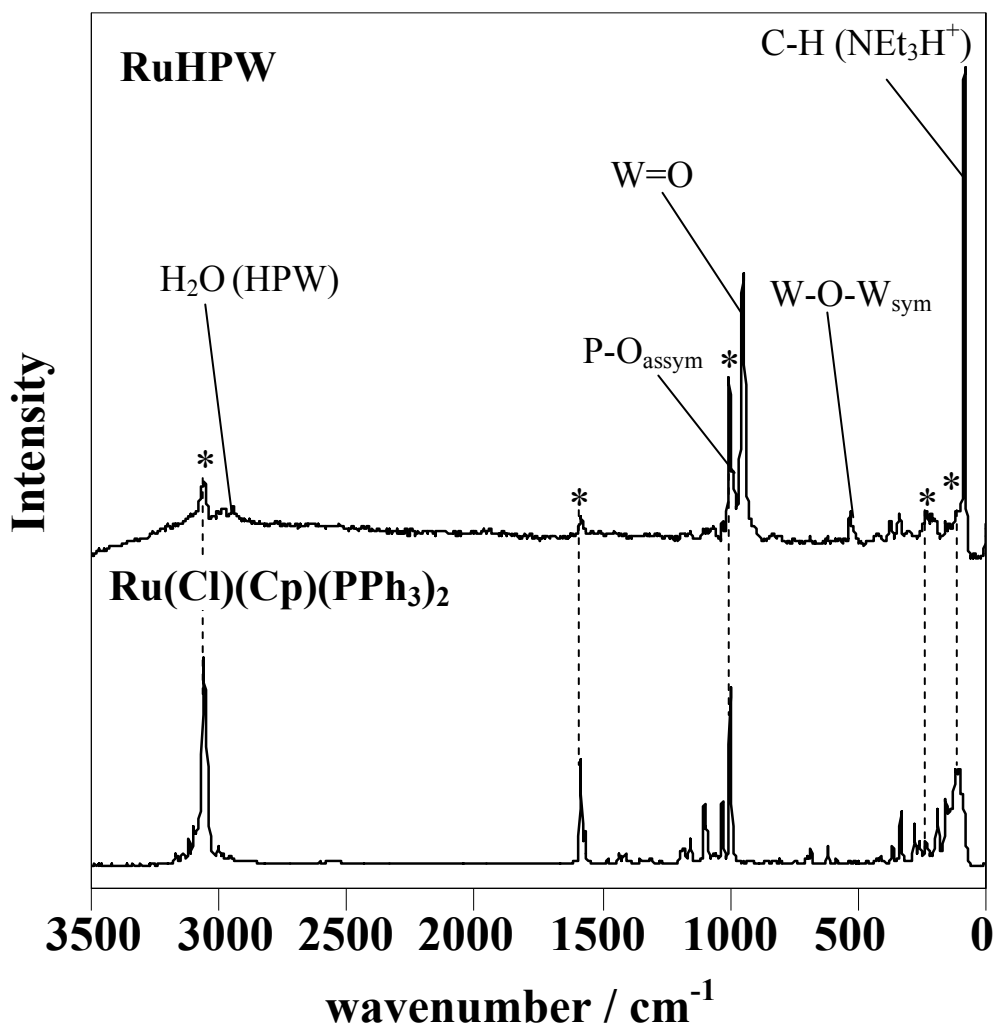


Figure 3.2.10: Raman spectra of **RuHPW** and **Ru(Cl)(Cp)(PPh₃)₂** precursor. * and dotted lines denote the fingerprint bands associated with {Ru(Cp)(PPh₃)₂}. Intense HPW and associated cationic triethylammonium ([HNEt₃H]⁺) bands in **RuHPW** are noted.

The absence of a characteristic Raman peak for O₂ bound through the double bond at ~550 cm⁻¹ discounts the possibility of a Ru(η^2 -O₂) species.^{33, 87} With the elimination of other possible ligands associated with the co-ordination site left vacant by the loss of Cl⁻, it can be proposed that the HPW Keggin is the only species associated with the {Ru(Cp)(PPh₃)₂}, indicating that the final nature of the system is that of formula [NEt₃H]⁺[{Ru(Cp)(PPh₃)₂]₂{PW₁₂O₄₀}]⁻ where the Ru interact either by an ionic structure or covalent structure consistent with that shown in **Figure 3.2.5**.

3.3 - CO Binding Studies of RuHPW

In order to assess **RuHPW** for its potential in carbonylation, DRIFTS was employed to observe the adsorption of CO to the compound. An environmental cell with gas inlet and temperature programming facilities was charged with a sample of **RuHPW** which in turn was loaded into the infrared spectrometer. After exposure of **RuHPW** to 5 % CO in helium, the sample cell was purged with N₂ both at a constant flow rate of 20 mlmin⁻¹. The N₂ purge removed any residual CO in the cell and that which is physisorbed to the sample. The DRIFTS spectrum of **RuHPW** under temperature programmed CO exposure (**Figure 3.3.1**) shows the formation of a new Peak (A) observed at 1980 cm⁻¹. Studies of ruthenium half-sandwich carbonyl complexes by Knox *et al.* indicate that this band is attributed to [Ru(Cp)(PPh₃)₂(CO)]⁺.⁴⁵ This is associated with a broadening and loss in intensity of the P-C band of the triphenylphosphine group at 1438 cm⁻¹ consistent with ligand substitution for CO. The new CO band continued to grow in intensity up to 250 °C after which a loss in band intensity signifies decomposition of the resulting complex.

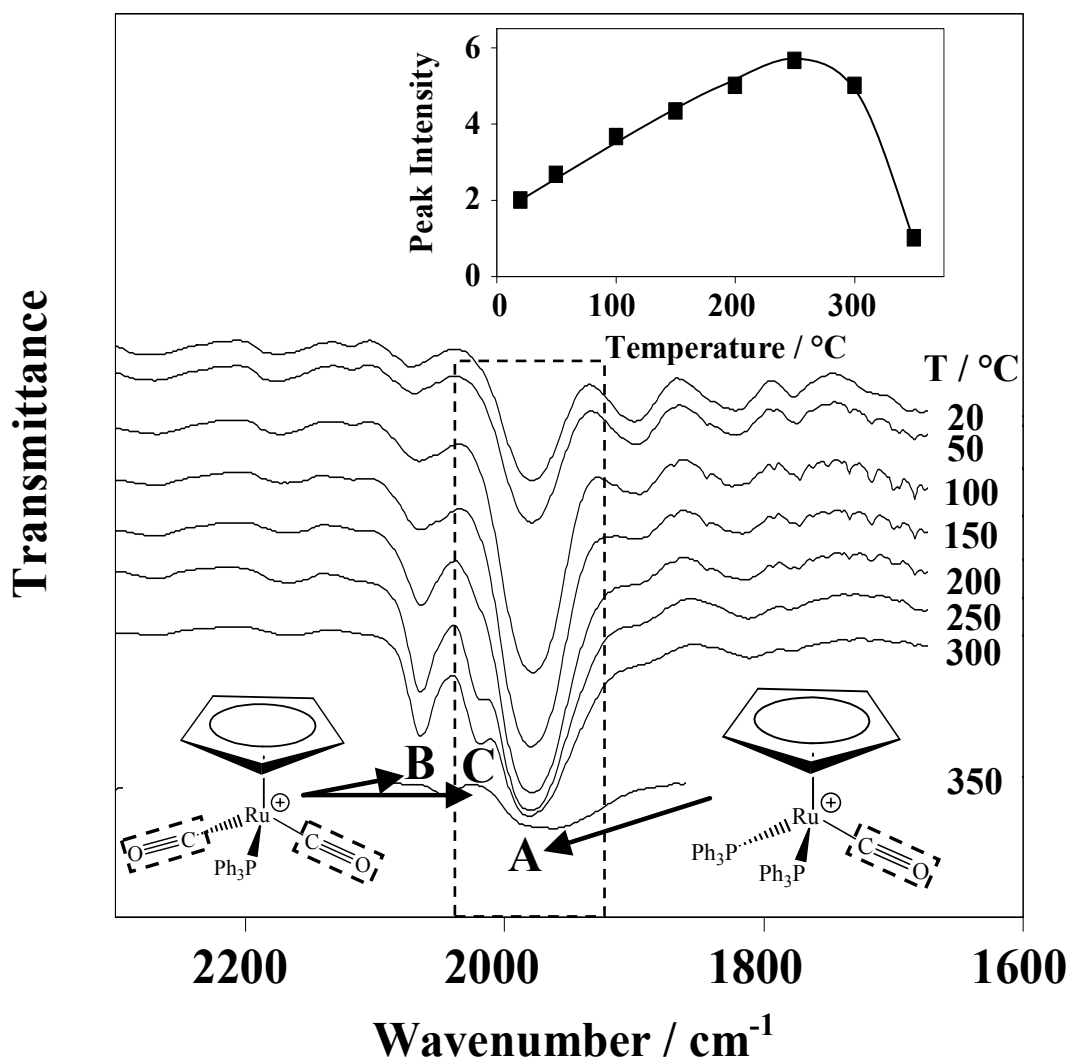


Figure 3.3.1: DRIFTS spectra of **RuHPW** showing CO adsorption as a function of temperature. Inset show mono CO derivative of **RuHPW** peak intensity (A) as a function of sample temperature. **B** and **C** indicate dicarbonyl species.

Infra-red bands **B** (2071cm⁻¹) and **C** (2021cm⁻¹) represent the growth of the minor dicarbonyl **RuHPW** species. This is consistent with an analogous [Ru(Cp)(PPh₃)(CO)₂]⁺[BF₄]⁻ complex observed in the literature⁴⁵ and are not uncommon under these conditions for similar Ru species.^{94, 95} After heating the sample to 200 °C under CO it was evident that the **RuHPW** compound remained intact and CO remained bound. Regeneration of the material may be accessible *via* a solvent wash.

DRIFTS and XRD studies on **RuHPW** indicate that the material remains intact at catalytically useful temperatures (**Figure 3.2.2**). A sample of **RuHPW** was heated to 200 °C for 1 hour showing identical diffraction patterns and

characteristic IR bands for the fresh **RuHPW**. This indicates that the compound retains structural integrity.

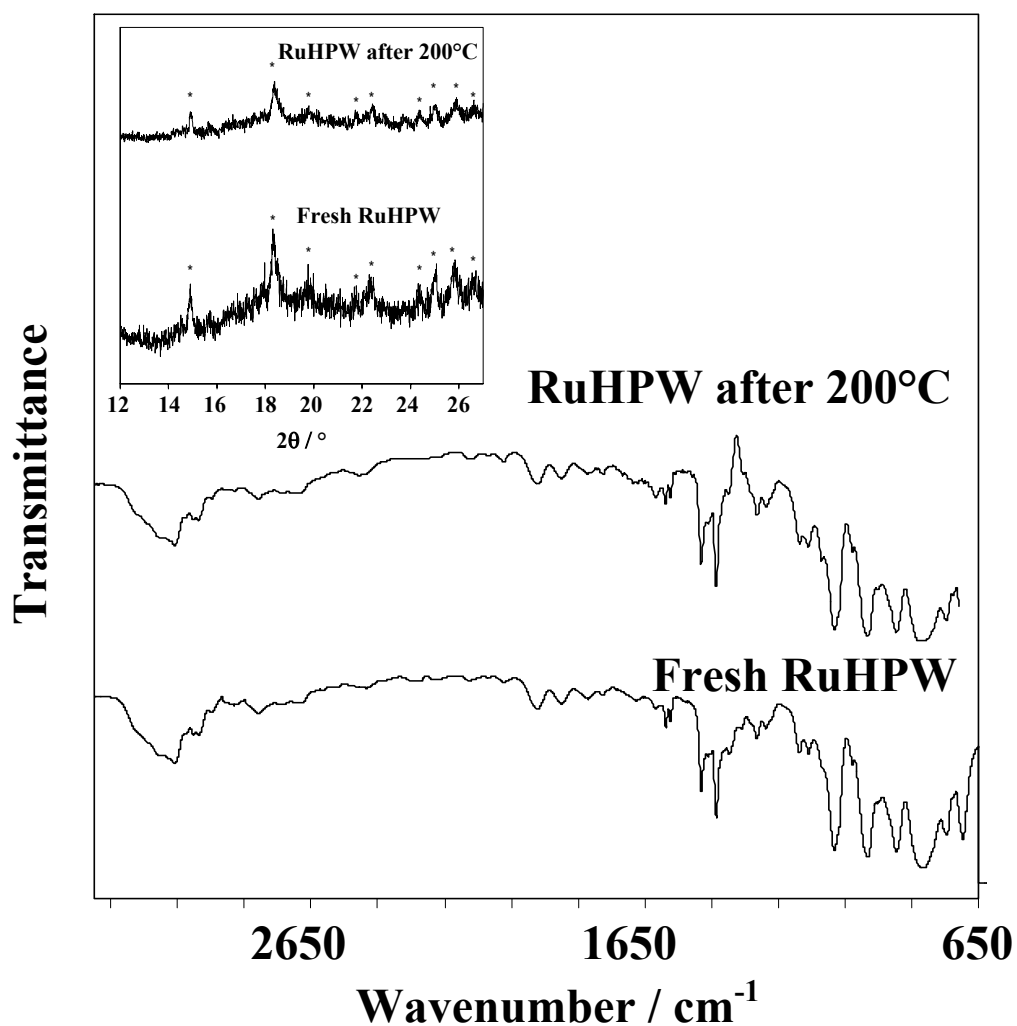


Figure 3.3.2: DRIFTS comparison between **RuHPW** and treated at 200 °C. Inset: Powder X-ray diffractograms of fresh **RuHPW** and **RuHPW** after heating at 200 °C (* denotes common peaks).

3.4 - Synthesis and characterisation of RudppeHPW

Leading from the work described in Section 3.2 where two triphenylphosphine ligands were employed in the organoruthenium ligand framework. Investigation into other multidentate ligands was considered. The dppe ($\text{Ph}_2\text{P}\{\text{CH}_2\}_2\text{PPh}_2$) ligand occupies two of the six coordination sites available at the ruthenium centre analogous to the 2 monodentate triphenyl phosphines. From a catalytic perspective where labile phosphines are required, dppe was considered to offer an alternative reversible bidentate / monodentate ligand interaction. It was therefore considered a more stable alternative to PPh_3 where this type of mechanistic pathway is required and provides an interesting comparative study for catalytic reactions discussed in Section 3.5-6.

$\text{Ru}(\text{Cl})(\text{Cp})(\text{dppe})$ (**Figure 3.4.1**) was synthesised according to the literature procedure⁵¹ from $\text{Ru}(\text{Cl})(\text{Cp})(\text{PPh}_3)_2$ by ligand exchange. $\text{Ru}(\text{Cl})(\text{Cp})(\text{PPh}_3)_2$ and dppe were heated at reflux in toluene under an atmosphere of nitrogen. After solvent removal under vacuum, unbound triphenylphosphine was removed by column chromatography yielding a yellow-orange oil. A recrystallization produced a crop of red-orange crystals used for subsequent doping into HPW. The **RuHPW** analogue incorporating this ligand was synthesised, (**RudppeHPW**) using the same preparation method employed for the **RuHPW** case. The same observations were made with the exception of the resulting compound being a rusty coloured powder. Full characterisation of the material using the techniques employed for **RuHPW** was undertaken.

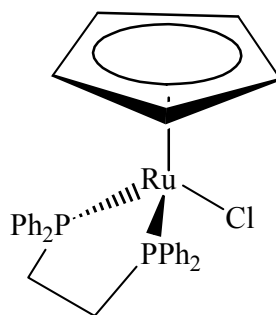


Figure 3.4.1: $\text{Ru}(\text{Cl})(\text{Cp})(\text{dppe})$, used to provide an alternative ligand system to triphenylphosphine (PPh_3) in **RuHPW**.

Elemental compositional analysis (**Table 3.4.1**) matched the expected 2 Ru : 1 Keggin for an analogous di-Ru-POM. A calculated stoichiometry based on 12 W (1 Keggin) was in good agreement with the theoretical values for all elements observed. In particular no Cl was observed in the **RudppeHPW**, indicative of the successful association of the Keggin with the organo-Ru species. Stoichiometry consistent with the inclusion of a triethylammonium counterion was confirmed by the observation of its protons in from ¹H NMR spectrum (**Table 3.4.2**).

The observation of all proton environments in the Ru ligand structure was consistent with that expected for dppe and Cp co-ordination. The Cp protons shifted from 4.50 to 5.25 ppm in accordance with loss of Cl comparable with **RuHPW**. The preservation of {Ru(Cp)(dppe)} co-ordination and retention of HPW Keggin structure is supported by DRIFT spectroscopy where common peaks with both precursor materials are observed in accordance with those bands outlined in **Table 3.2.1**.

Table 3.4.1: XPS Elemental atom % data and calculated stoichiometry for **RudppeHPW**

Element	Experimental Composition (atom %) ± 0.2 %	Experimental Stoichiometry*	Theoretical Stoichiometry
C	52.0	70	68
N	0.7	1	1
Ru	1.4	2	2
W	9.0	12	12
P	3.6	5	5
O	33.4	45	40

Stoichiometry calculated relative to 12 tungsten atoms.

Table 3.4.2: ^1H NMR assignments for **RudppeHPW** in $\text{D}_6\text{-DMSO}$

^1H NMR 400 MHz ($\text{D}_6\text{-DMSO}$ / 298K)		
δ / ppm	Assignment	Integration
1.1 (t)	Me	9
2.2 (s)	$(\text{CH}_2)_2$	4
3.0 (m)	Et	6
5.3 (s)	Cp	5
7.2 (m)	Ph	8
7.5 (m)	Ph	12
8.9 (br s)	NH^+	1

TGA (**Figure 3.4.3**) shows thermal robustness comparable to the **RuHPW** analogue. Thermal decomposition begins at ca. 300 °C which offers the same thermal window for catalytic application. A 4 % initial mass loss in **RudppeHPW** at 100 °C correlates with loss of some physisorbed solvent (MeOH and H_2O). Ru ligand loss occurs between 300 and 700 °C, equivalent to a mass loss of 20 % of the sample. This is consistent with that expected for Cp and dppe from two Ru functionalities (922 amu).

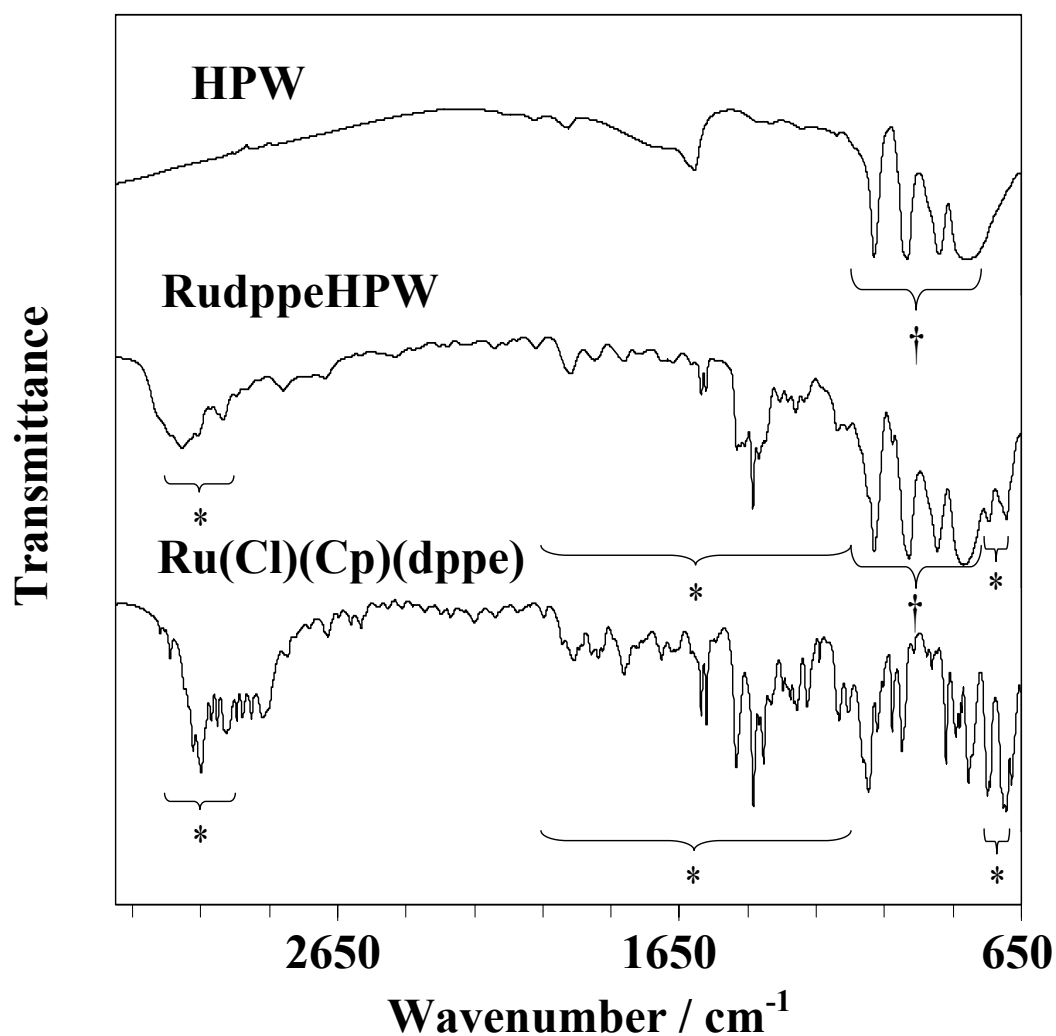


Figure 3.4.2: DRIFTS spectra of **RudppeHPW**. Comparative spectra are shown for the Ru(Cl)(Cp)(dppe) (*) and HPW (†) precursors.

Some crystallinity is observed in the new **RudppeHPW** (Figure 3.3.4). No HPW crystal peaks are observed due to the loss of crystalline water as discussed for the **RuHPW** case.^{66, 67} Some intense peaks in the Ru(Cl)(Cp)(dppe) spectrum at 2θ 10.3, 11.4, 17.9, 18.3 and 23.9 ° do correlate with those observed in the **RudppeHPW** spectrum. However these differ in intensity and are associated with other weaker peaks which do not correlate with that observed in either the HPW precursor or the Ru(Cl)(Cp)(dppe). This is indicative of a new micro-crystalline material.

XANES analysis of **RudppeHPW** compared with standards of known oxidation state indicate a formal 2+ oxidation state (**Figure 3.3.5**) with only 10 % Ru(IV) character (*c.f.* **RuHPW**, 32 %). However, close inspection of Ru 3p XPS reveals a 1.9 eV shift in binding energy from 461.5 to 463.4 from the parent chloride complex, analogous to that observed in **RuHPW** (**Figure 3.3.6**), indicating a comparable increase in oxidation state.

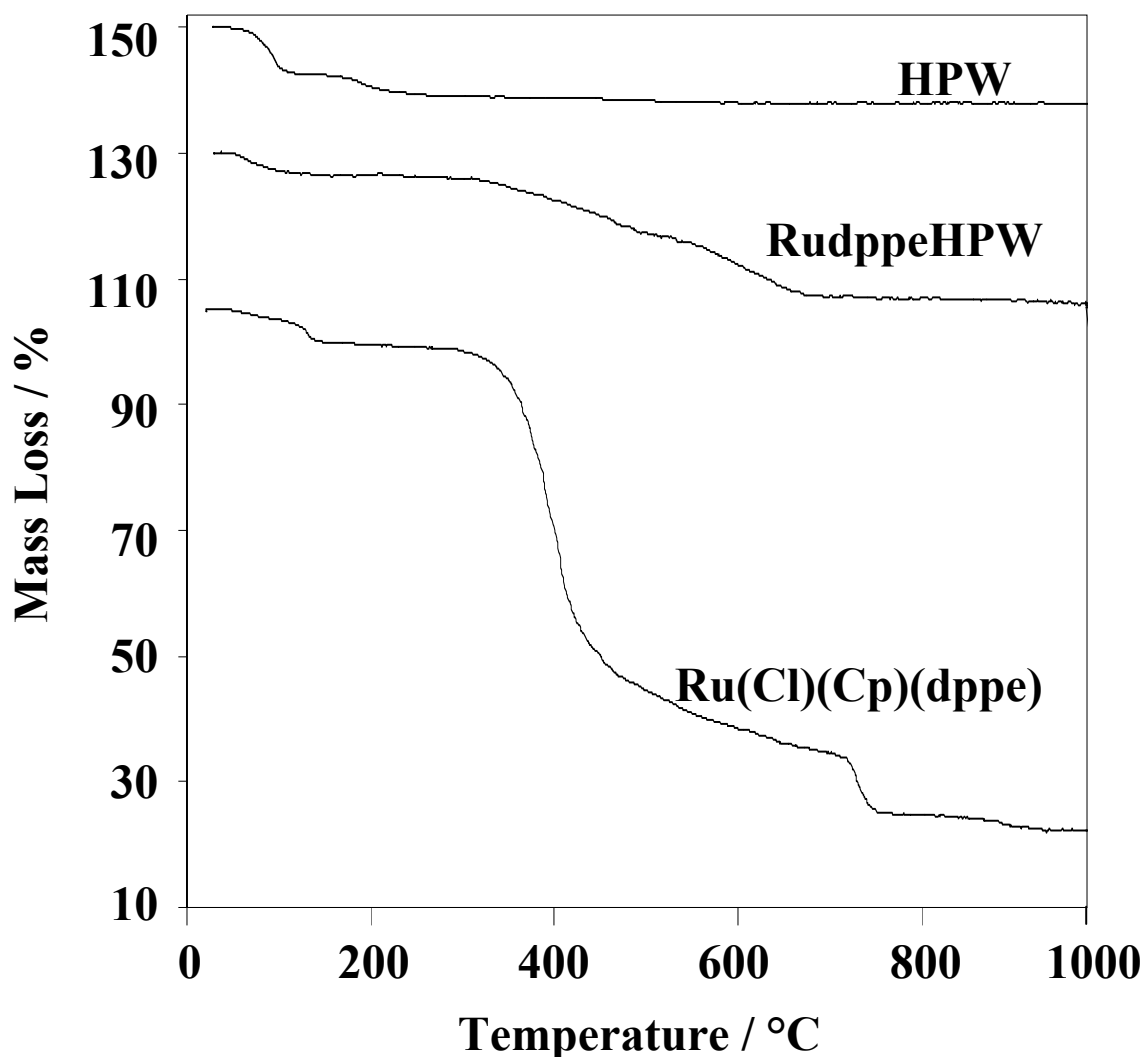


Figure 3.4.3: TGA profiles of **RudppeHPW**, **Ru(Cl)(Cp)(dppe)** and **HPW** precursors

Due to the robust nature of the material and insolubility in common laboratory solvents which could be used for crystallisation, a single crystal could not be grown for close structural analysis, as in the case of **RuHPW**.

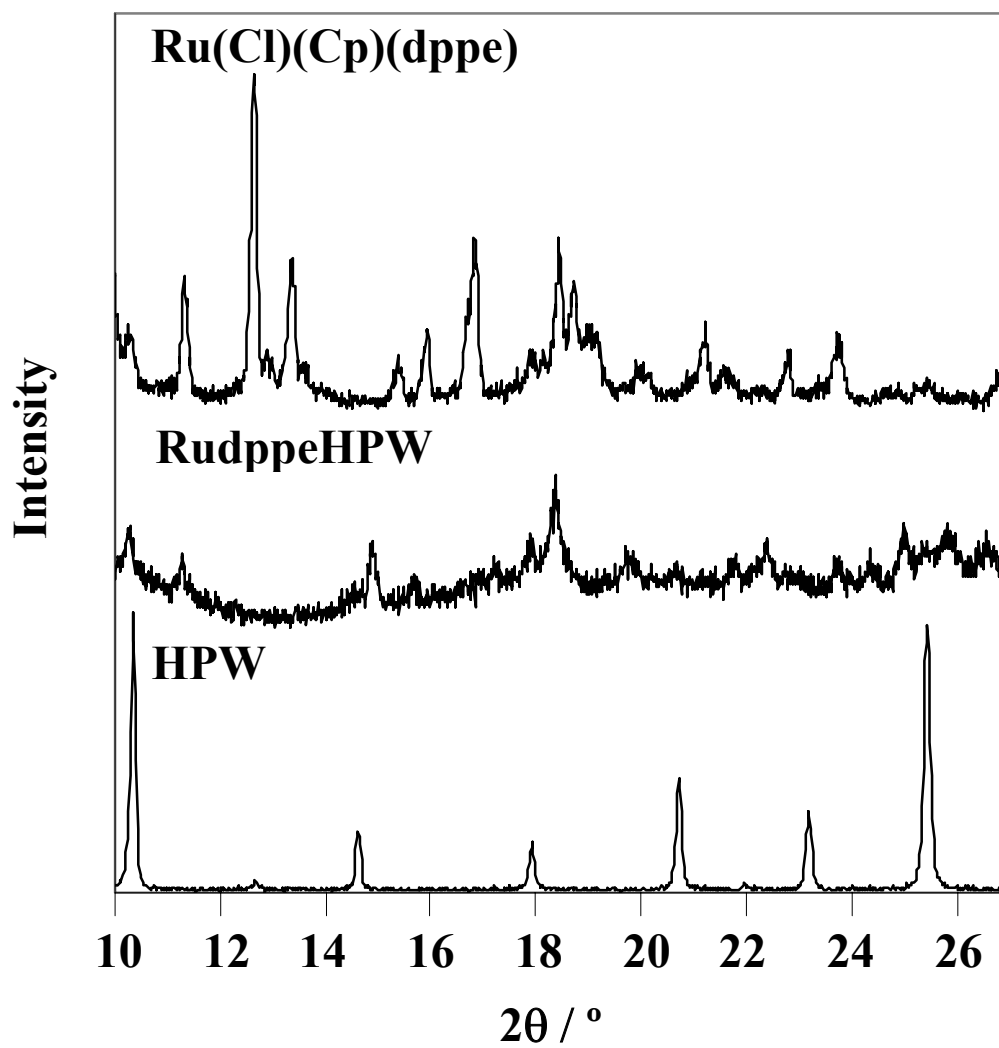


Figure 3.4.4: Powder X-ray diffractograms of **RudppeHPW** and **HPW** and **Ru(Cl)(Cp)(dppe)** precursors .

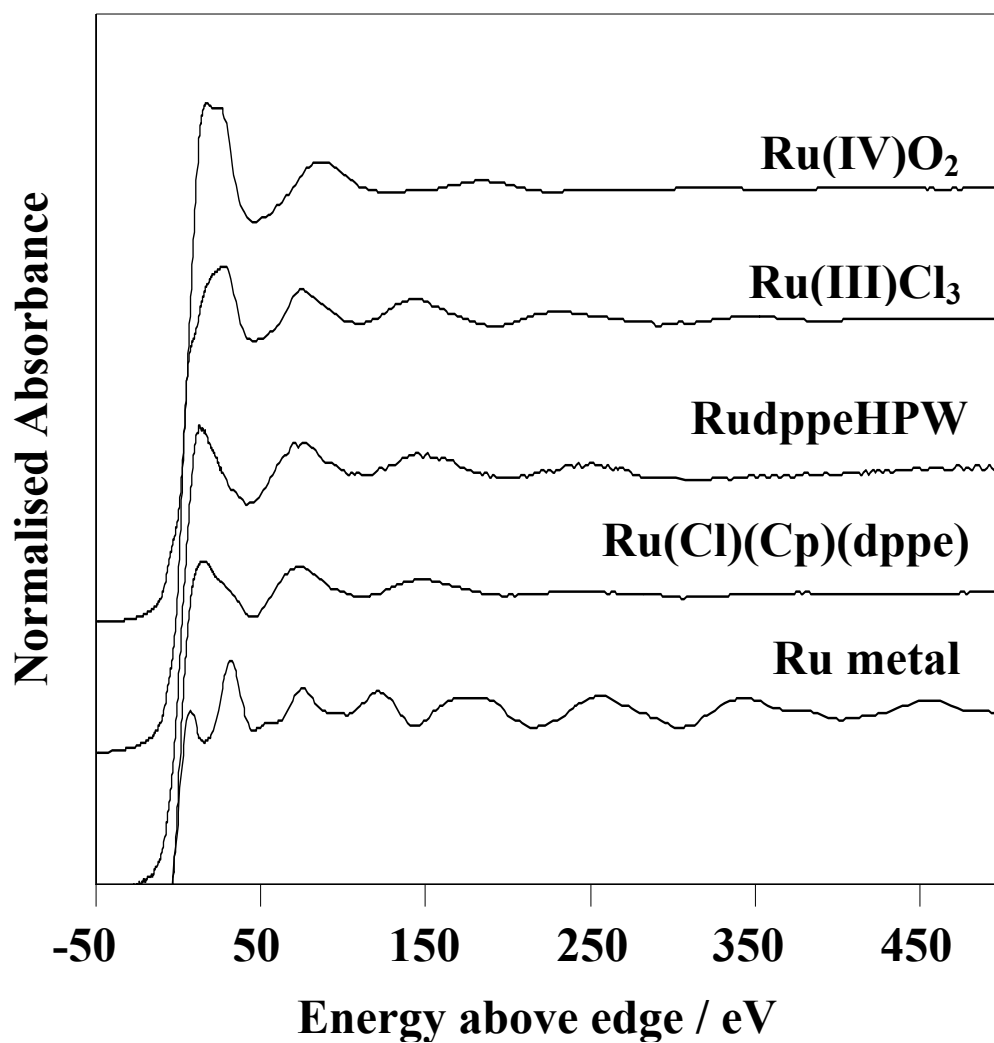


Figure 3.4.5: Ru K-edge normalised EXAFS of RudppeHPW, Ru(Cl)(Cp)(dppe), and RuCl₃, RuO₂ and Ru metal standards.

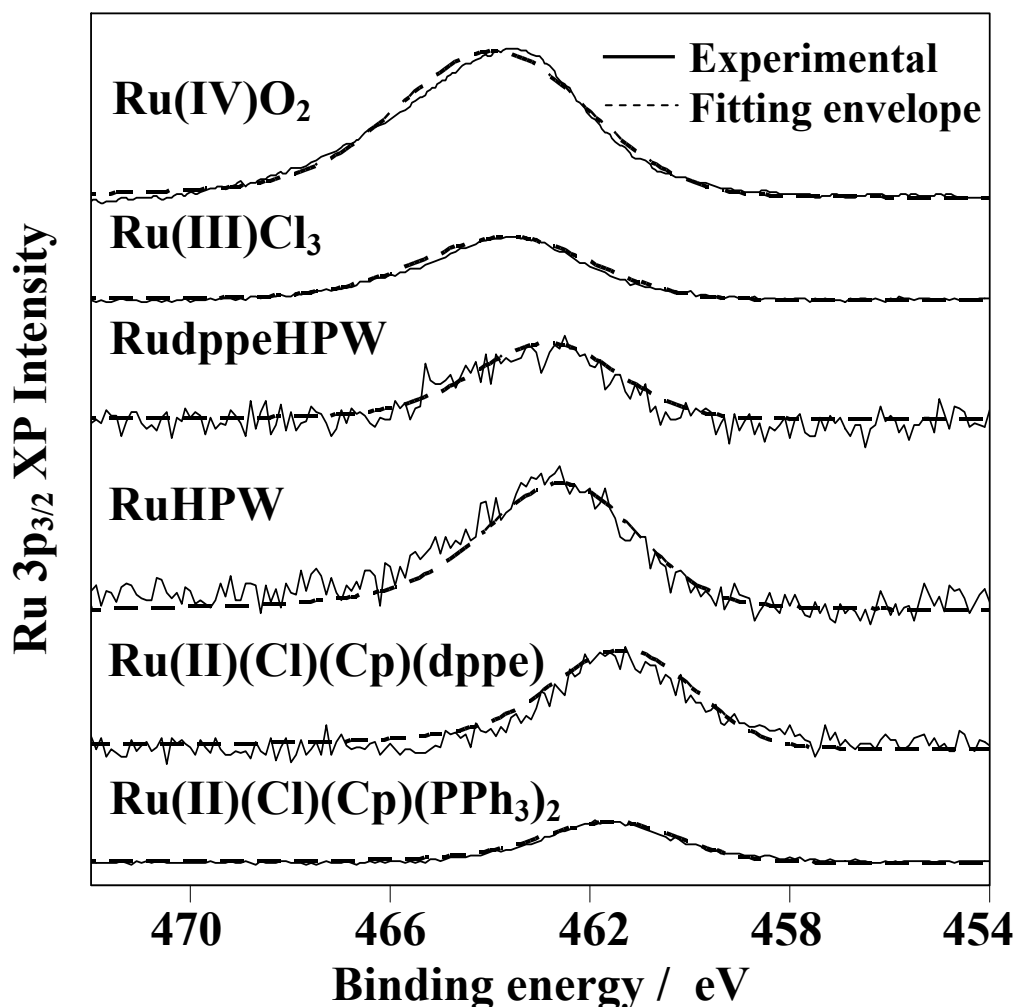


Figure 3.4.6: Ru $3p_{3/2}$ XP spectra of **RudppeHPW** and **RuHPW**. Comparative spectra are shown for **Ru(Cl)(Cp)(PPh₃)₂**, **Ru(Cl)(Cp)(dppe)**, **RuCl₃** and **RuO₂**.

MALDI-TOF solid state MS (**Appendix 2**) showed peaks at m/z 3443.2 and 4007.3 consistent with that of the mono-Ru and di-Ru HPW species of formula, $[(Ru\{\eta^5-C_5H_5\}\{dppe\})(PW_{12}O_{40})(H^+)]^-$ and $[(Ru\{\eta^5-C_5H_5\}\{dppe\})_2(PW_{12}O_{40})]^-$ respectively, with the correct isotope distributions. This provides direct evidence of a HPW species bound directly to two ruthenium cations. In light of this evidence, EXAFS was used to test the model for the closest co-ordination shell at the Ru centre as in **RuHPW** (**Figure 3.4.7**, **Table 3.4.3**) The model for incorporation of the Keggin to the Ru co-ordination shell by direct complexation to the metal centre with an oxygen in the first coordination shell at 2.10 Å and a tungsten atom in the second coordination shell at 4.34 Å (**Table 3.4.3**), analogous to **RuHPW**, is in good agreement with the overall data. However there is no overall improvement

Table 3.4.3: Parameters for EXAFS fitting of Ru(Cl)(Cp)(dppe) and **RudppeHPW** (with and without HPW coordination)

Sample	CN1 Ru- C	CN2 Ru- P	CN3 Ru- Cl	CN3' Ru- O	CN4 Ru- W	R1 (Å) Ru- C	R2 (Å) Ru- P	R3 (Å) Ru- Cl	R3' (Å) Ru- O	R4 (Å) Ru- W	σ_1 Ru-C	σ_2 Ru-P	σ_3 Ru-Cl	σ_3' Ru-O	σ_4 Ru-W	R ²
Ru(Cl)(Cp)(dppe)	5	2	1	-	-	2.20	2.35	2.35	-	-	0.031	0.022	0.020	-	-	37.75
RudppeHPW <i>without HPW</i>	5	2	-	-	-	2.19	2.34	-	-	-	0.010	0.002	-	-	-	40.79
RudppeHPW <i>with HPW</i>	5	2	-	1	1	2.19	2.34	-	2.10	4.33	0.010	0.002	-	0.002	0.005	41.51

86

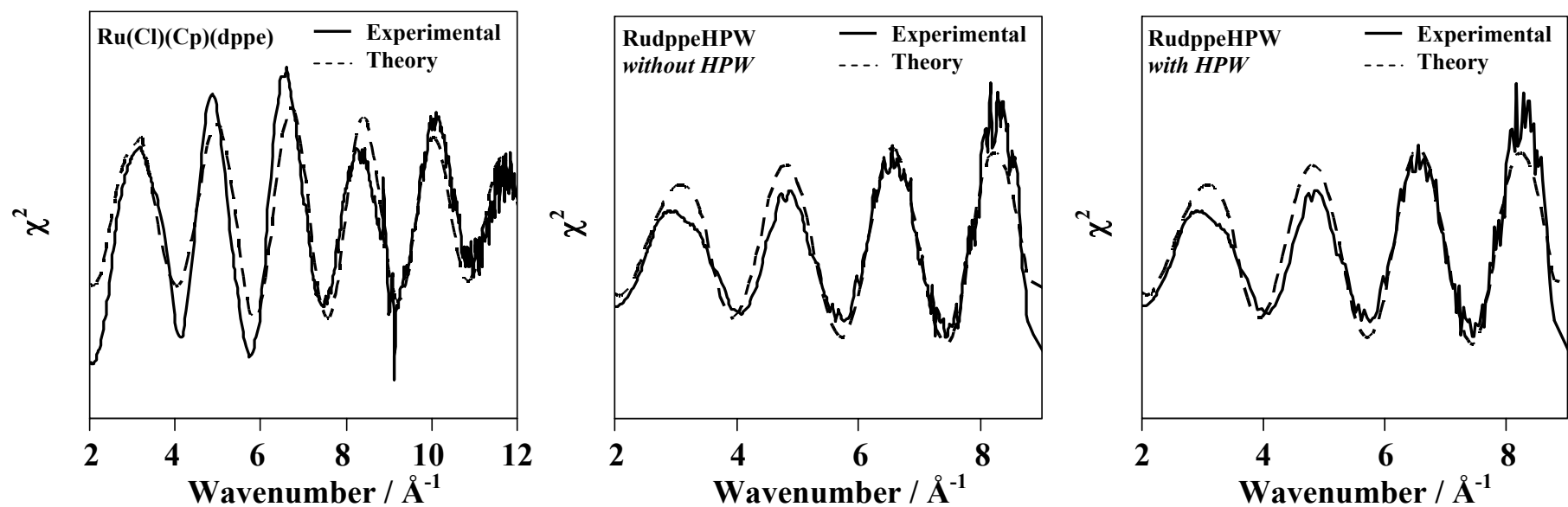


Figure 3.4.7: EXAFS χ^2 plots, experimental and theory Ru(Cl)(Cp)(dppe) and **RudppeHPW** (with and without HPW coordination)

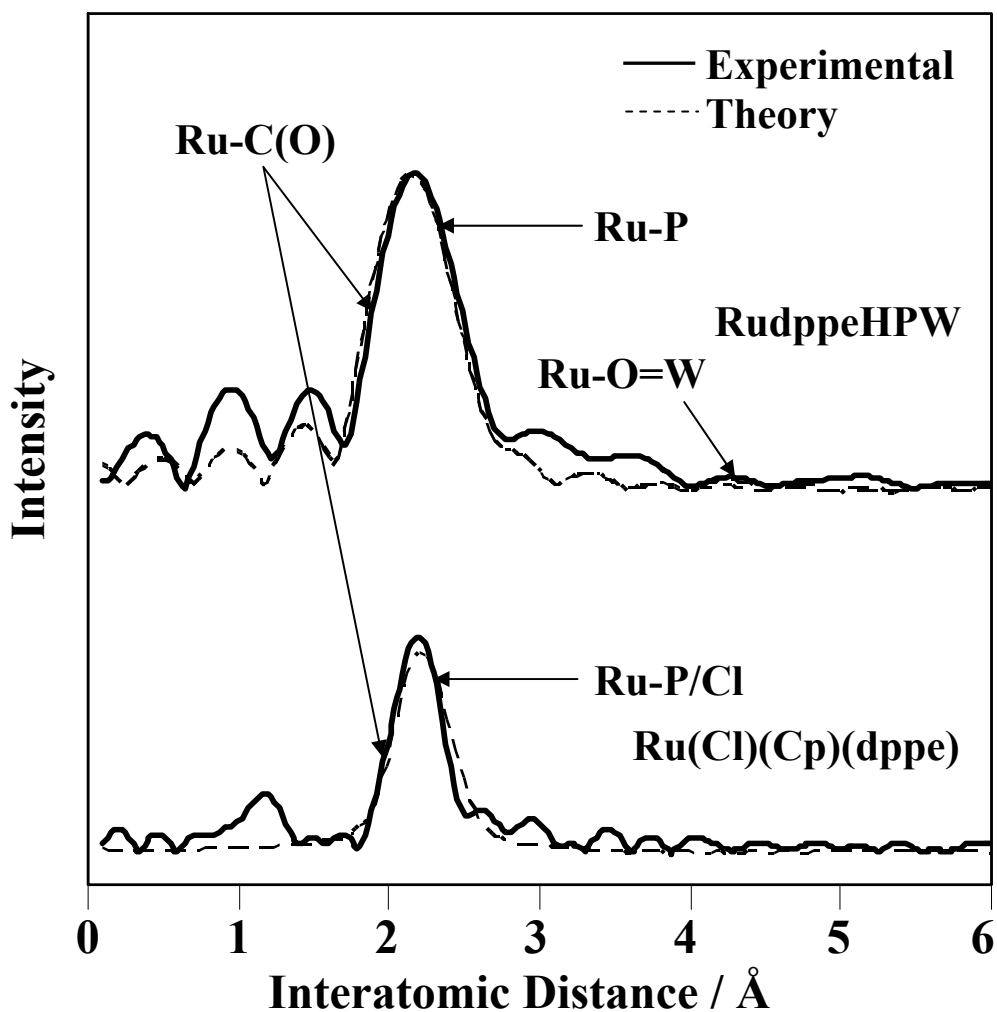


Figure 3.4.8: Fitted radial distribution functions of **RudppeHPW** and the **Ru(Cl)(Cp)(dppe)** precursor.

in the fit compared to that of a model without HPW showing a difference in R^2 value of only 0.72. This is clearly observed in **Figure 3.4.8**, which shows the Fourier Transformed EXAFS spectra. Both models showing **RudppeHPW** with and without HPW overlay on each other showing the majority of surrounding electron density as expected. Electron density at 4.34 Å is consistent with that expected for a tungsten shell in accordance with a linear model as discussed for **RuHPW**. As in **RuHPW**, additional atoms in the first local coordination shell cause a loss in goodness of fit. However, the similarity in profile to analogous **RuHPW** does not provide distinctive evidence for a formal interaction.

3.5 - CO Binding Studies of RudppeHPW

CO adsorption analysis was undertaken for **RudppeHPW** using an identical protocol to that which was described for **RuHPW**. **Figure 3.5.1** shows the growth of a band at 1990 cm^{-1} (**D**) analogous to that of the Ru-CO observed in CO treatment of **RuHPW** and identified in the literature as $\{\text{Ru}(\text{Cp})(\text{dppe})(\text{CO})\}^+$.⁴⁵ Co-ordination on exposure to CO increases with temperature up to $250\text{ }^{\circ}\text{C}$ where subsequent loss due to decomposition occurs, (evidenced by TGA shown in **Figure 3.4.3**). A dicarbonyl species was expected to be short lived due to the intrinsic bidentate nature of the dppe ligand and therefore undetectable in DRIFTS IR. However band **E** was observed at 2067 cm^{-1} attributed to $\{\text{Ru}(\text{Cp})(\kappa^1\text{dppe})(\text{CO})_2\}^+$ (also noted by Knox⁴⁵) was identified as the minor dicarbonyl **RudppeHPW** species (also responsible for loss in intensity of band **D** due to additional CO coordination forming species **E** from **D**). A second band, expected for an additional stretching mode for a dicarbonyl species (as observed in the **RuHPW**) is expected to be hidden in the more prominent monocarbonyl band and so not observed in the **RudppeHPW** analogue. Further evidence for this is shown by the residual intensity of the monocarbonyl peak after expected decomposition shown in the intensity plot in **Figure 3.5.1**. On careful inspection of the P-Ph band region, the 1438 cm^{-1} band associated with dppe broadens and undergoes a red shift of 2 cm^{-1} to 1436 cm^{-1} . This shift and broadening of the P-C band is consistent with the retention but change in environment of the dppe phosphine. The observation of a dicarbonyl species provides evidence for a change from bidentate to monodentate of the dppe ligand. A loss in overall intensity is not observed until $300\text{ }^{\circ}\text{C}$ where complete dissociation of the phosphine begins in favour of the tricarbonyl. The retention of the phosphine ligand backbone is a valuable trait for carbonylation chemistry as a second CO binding site with retention of ligands would be desirable for the synthesis of a robust heterogeneous catalyst.

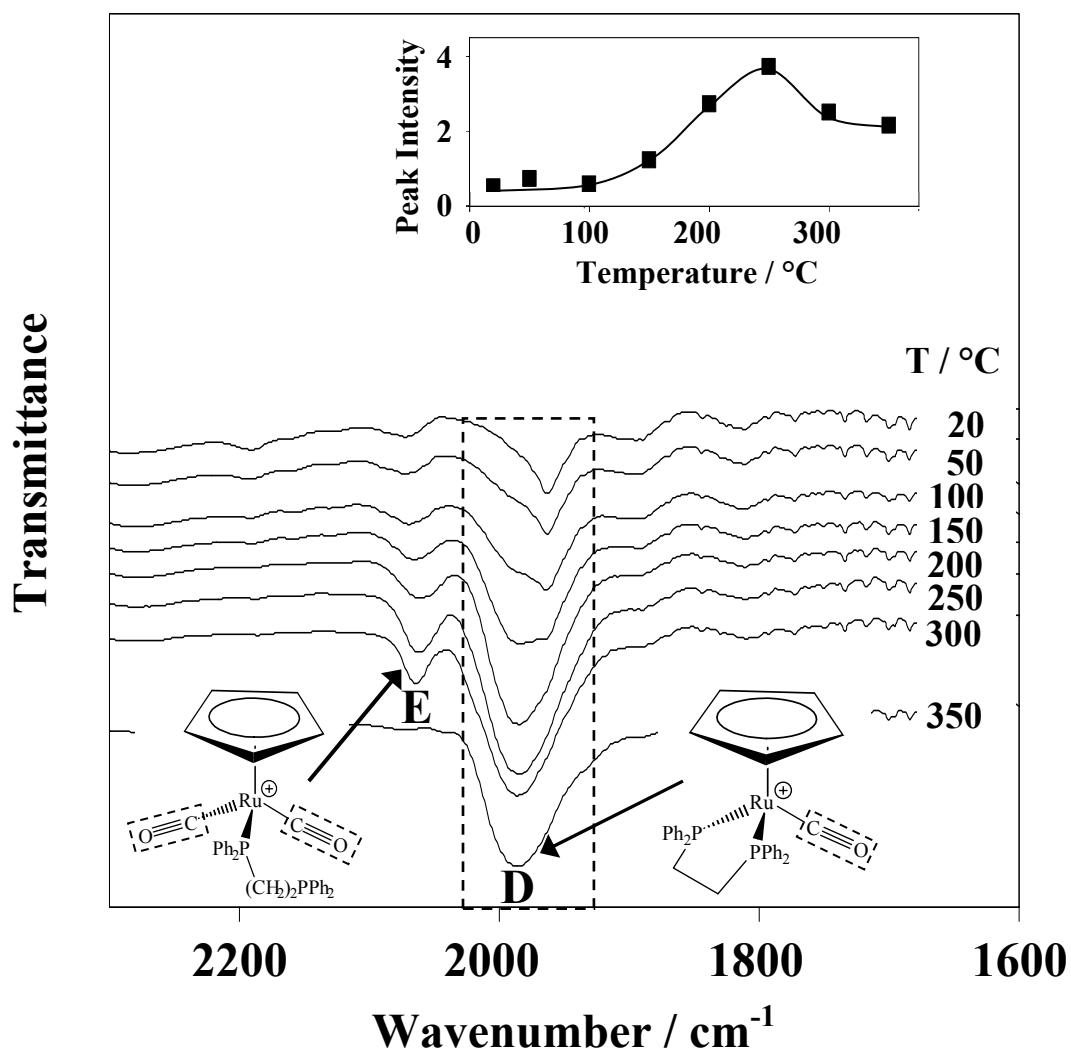


Figure 3.5.1: DRIFTS spectra of **RudppeHPW** showing CO adsorption as a function of temperature. Inset show mono CO derivative of **RudppeHPW** peak intensity (A) as a function of sample temperature.

3.6 - RuHPW and RudppeHPW methanol carbonylation tests

RuHPW was screened for activity towards methanol carbonylation under conditions outlined in Section 2.11. **RuHPW** showed no formation of acetyl species from a feed stock of methanol vapour and CO gas. Methanol is known to condense in the presence of heteropolyacid species, as a result of acid catalysis. Therefore it was considered that dimethyl ether (DME), a product of methanol condensation (reaction outlined in **Equation 3.6.1**) would be observed if **RuHPW** retained any of its HPW acid character. The formation of DME was not observed which indicates that HPW does not retain enough acidity to catalyse condensation. This is likely to be due to presence of the NEt_3 base used for abstraction of chloride from the ruthenium centre abstracting all protons to form triethylammonium, inactive for catalysis.

As a base is required to form **RuHPW**, possibilities for eliminating the loss of acidity during formation of **RuHPW** may include using a weaker or non-nucleophilic base such as DBU or DABCO, rather than using NEt_3 which is strong enough to remove all acidic protons, effectively neutralising the acid. Ion exchange to provide the compound with H^+ may allow acid recovery of the **RuHPW** compound.

To investigate the hypothesis that acidity is lost due to neutralisation, **RuHPW** was doped with one equivalent of HPW. These were tested for activity in methanol carbonylation under the same reaction conditions. Methanol conversion to DME was observed consistent with that of pure HPW, starting at ~ 170 °C consistent with the literature.⁴⁷ Loss of 5 – 10 % at temperatures greater than 300 °C due to methanol to gasoline chemistry (MTG) where trace amounts of methane, ethane and propane observed, is likely to be due to DME dehydration.⁹⁶ Generally, direct methanol to light alkanes occurs above 400 °C and so this route is unlikely. The **RuHPW** doped with HPW has an average 5 % lower MeOH conversion to DME. This may be caused by disruption of the HPW secondary structure which constituted to the acid catalysed DME mechanism. No acetyls were produced which infers that in the presence of an acid dopant, **RuHPW** can not release an active form of CO to form acetyl species. The dppe analogue of

RuHPW shows similar characteristics with 20 % peak methanol conversion to DME consistent with pure HPW.

Equation 3.6.1: Acid catalysed methanol condensation to dimethyl ether

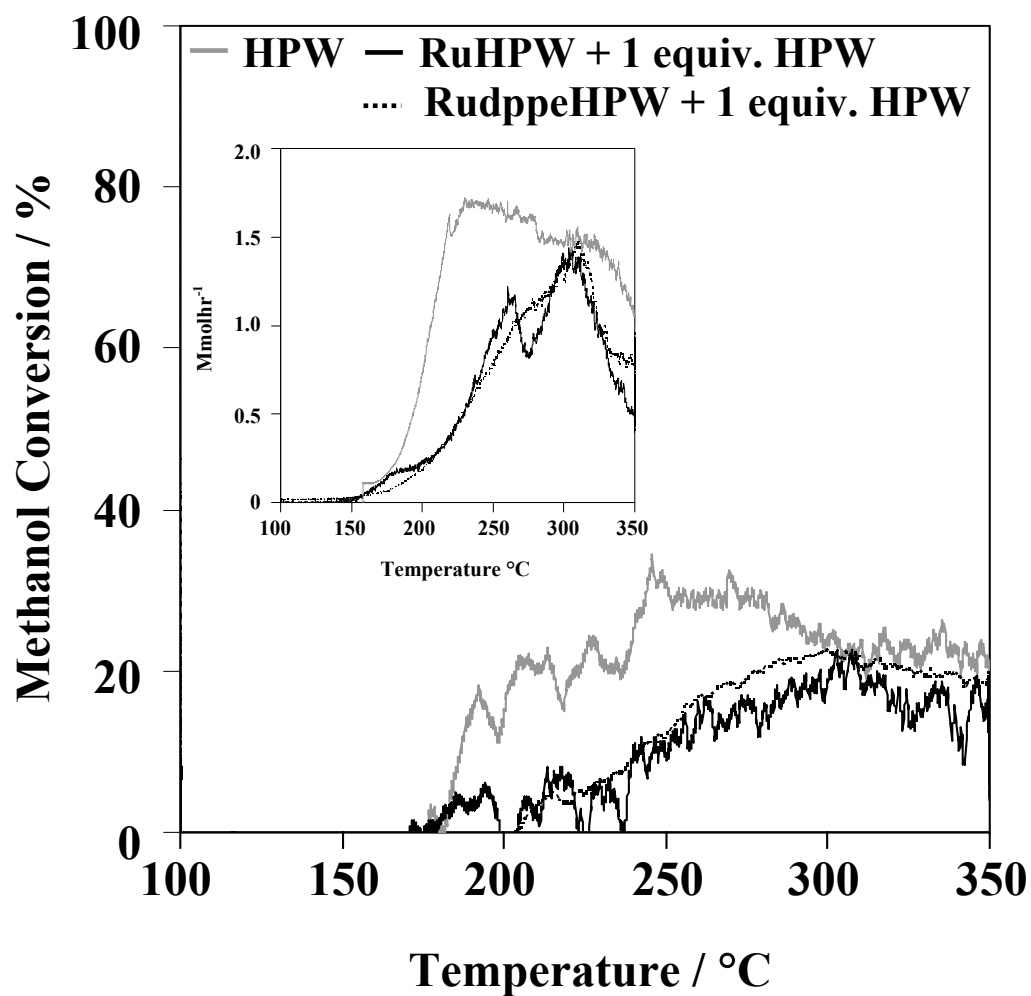
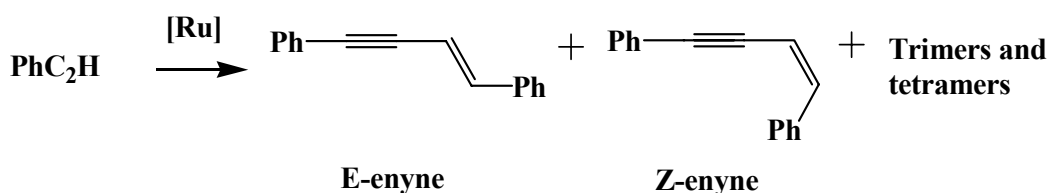


Figure: 3.6.1: Methanol % conversion comparison of HPW and the bifunctional **RuHPW** and **RudppeHPW** both with 1 equivalent of HPW. Inset: DME production mmolh⁻¹.

3.7 - RuHPW and RudppeHPW as catalysts in phenyl acetylene oligomerisation

Ruthenium half-sandwich compounds are known to be good catalysts for diverse chemistries including carbon–carbon bond forming reactions.⁹⁷ The reactivity of **RuHPW**, a heterogeneous analogue of known catalytically active Ru-complexes, was examined towards phenyl acetylene oligomerisation (**Scheme 3.7.1**), a reaction in which the selectivity of *E* versus *Z* dimerisation is an



Scheme 3.7.1: Schematic of phenyl acetylene oligomerisation using a Ru catalyst.

important issue. In this reaction, 1 mol % of the catalyst was stirred in pure phenylacetylene which is desirable from an environmental perspective due to the inherent lack of solvent necessity. **RuHPW** exhibited both high activity (TON 5400, TOF 225 h^{-1}) and good selectivity towards the (*E*)-enyne. **Figure 3.7.1** shows reaction profiles for the *E* : *Z* selectivity ratio using 1 mol % of **RuHPW** catalyst during the dimerisation, compared against the homogeneous $\text{Ru}(\text{Cl})(\text{Cp})(\text{PPh}_3)_2$ catalyst precursor. In both catalytic systems, isomer selectivity is approximately independent of reaction time, indicating that both isomers form as primary products, with no subsequent bond rearrangement. This is consistent with the proposed reaction mechanism for homogeneous catalysts, wherein addition of one alkyne to form a vinylidene intermediate, is followed by association of a second alkyne and dissociation of the enyne dimer.^{98, 99} Steric factors would suggest that subsequent bonding interactions between the dimer and catalyst active site, which would favour further oligomerisation, should be rare, and indeed the maximum amount of higher alkyne oligomers observed (mainly trimers and tetramers) was below 8 %, indicating a high selectivity towards dimeric products. Alternative mechanisms for trimer and tetramer formation

involving the stepwise addition of three or four phenylacetylene monomers are presumably unfavourable. It is worth noting here that no organoruthenium species were observed in the filtered reaction product by ^1H NMR indicating a heterogeneous mode of action. It was only by solution state ^{31}P NMR that a trace amount of free PPh_3 was observed after 24 hours which would be expected for catalysis requiring phosphine lability. While the parent complex is unselective towards either enyne dimer, **RuHPW** is 70 % selective to the (E)-enyne. *E*-selectivity is commonly observed in non-polar reaction systems and has been attributed to stable complex intermediates with high steric demand, which disfavour the *Z*-enyne forming pathway.¹⁰⁰

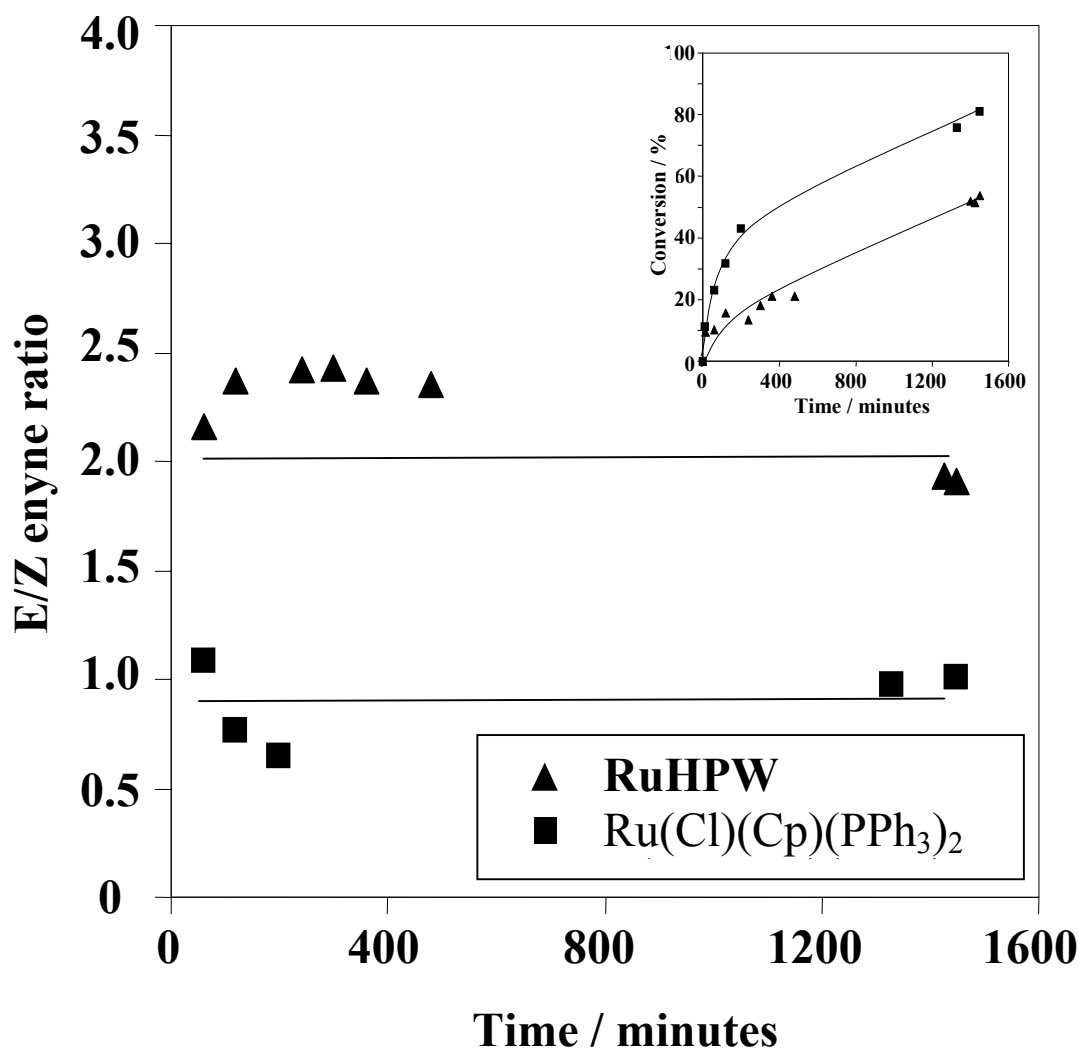


Figure 3.7.1: Heterogeneous and homogeneous *E/Z*-enyne selectivity profiles in phenyl acetylene oligomerisation over **RuHPW** and $\text{Ru}(\text{Cl})(\text{Cp})(\text{PPh}_3)_2$, respectively. Inset (top right) shows phenyl acetylene conversion profiles.

In order to assess the sensitivity of **RuHPW** to the choice of phosphine ligand (and therefore whether the latter play an important steric role in the co-ordination sphere of the active catalyst), the analogous Ru complex, **RudppeHPW** was tested under the same conditions. **RudppeHPW** exhibited similar heterogeneous activity to **RuHPW** towards the formation of phenylacetylene dimers, however, an increase in selectivity at high conversions was observed (**Figure 3.7.2**). This could be a result of a combination of steric contributions from the HPW and the bidentate nature of the dppe ligand imposed on the active Ru centre which could support a second co-ordination of *Z*-dimer and subsequent isomerization. It can be hypothesised that the formation of trimer/tetramer molecules would be more favourable *via* a pathway involving multiple coordination of substrates in *Z* conformation, enhancing observed selectivity towards the *E*-dimer. Confirmation of the impact of the Keggin cage would benefit from further studies using other bulky non-coordinating anions as the nature of the enhanced selectivity is still unclear. However, the enhanced selectivity in the parent complex does suggest that the effect of phosphine ligand does have a role in catalysis. The conformationally restrictive nature of the dppe ligand places restraints on the co-ordination of phenyl acetylene at the Ru centre. The bidentate dppe induces selectivity towards formation of the *E*-enyne dimer through the less sterically demanding intermediates in the homogeneous precursor complex, consistent with a slower rate and 20 % drop in total conversion after 24 hours. It should be noted that the initial rates for both heterogeneous Ru-POM catalysts were approximately half of those observed for the free parent homogeneous Ru complexes; (**Table 3.7.1**) this may reflect either slower mass-transport through the solid state POM compound or steric hindrance around the active Ru centre due to the bulky POM cage. Solution state ¹H NMR again showed that no organoruthenium species were present in the filtered product. However, this was coupled with no free phosphine observed in the ³¹P NMR spectrum indicative of a more stable yet hemi-labile bidentate phosphine. GC-MS analysis of the product distribution after 24 hours shows only trace amounts of higher oligomers for all catalysts tested and no oligomers larger than tetrameric species were observed. This suggests that all reactions undergo a similar reaction mechanism *via* Ru=C=C(Ph)(H) vinylidene intermediates identified in the literature for analogous organoruthenium complexes.¹⁰¹ **RuHPW** acts as a proficient organoruthenium

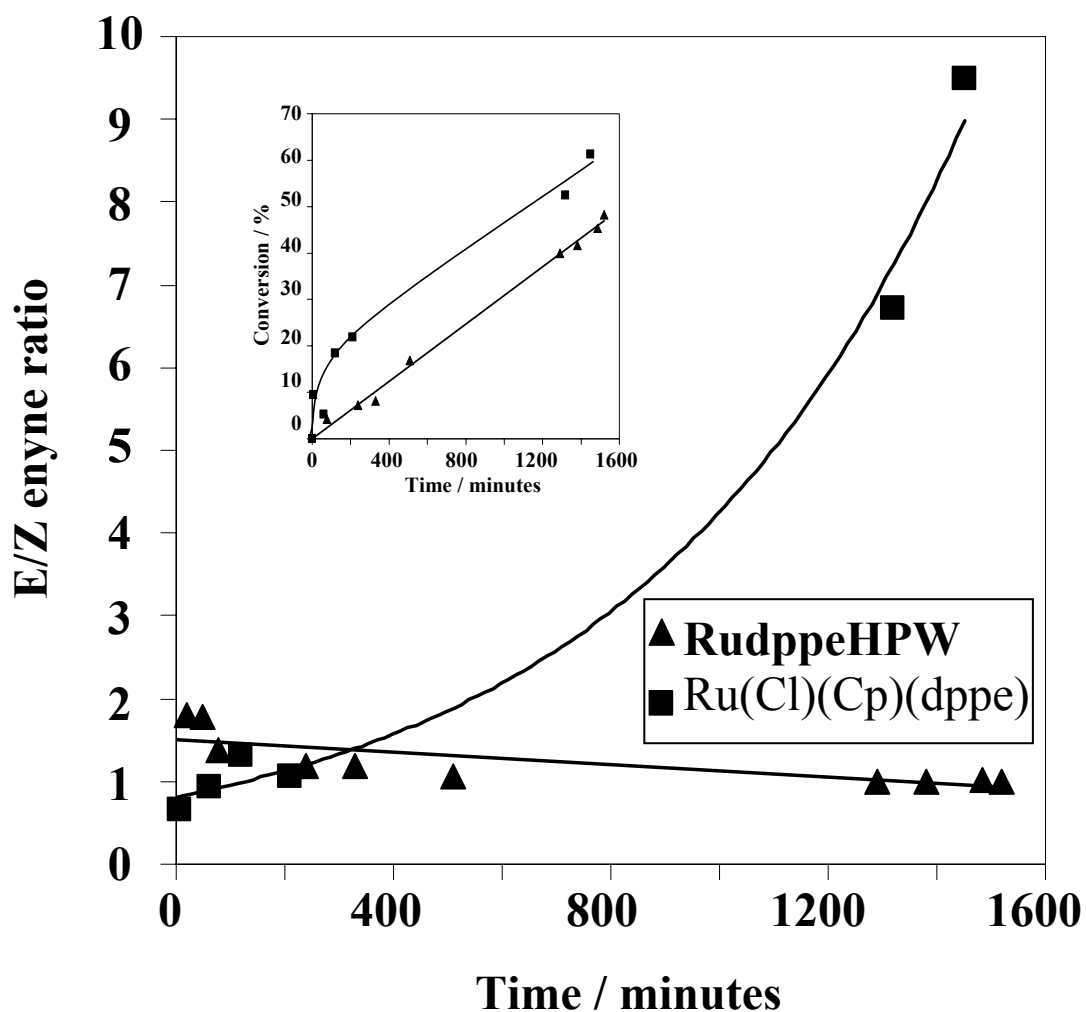


Figure 3.7.2: Heterogeneous and homogeneous E/Z-ene selectivity profiles in phenyl acetylene oligomerisation over **RudppeHPW** and **Ru(Cl)(Cp)(dppe)**, respectively. Inset (top left) shows phenyl acetylene conversion profiles.

Table 3.7.1: Table comparing heterogeneous and homogeneous initial rate in phenyl acetylene oligomerisation over **RuHPW**, **RudppeHPW**, **Ru(Cl)(Cp)(PPh₃)₂** and **Ru(Cl)(Cp)(dppe)**

Catalyst	Initial rate (mmolh ⁻¹ g _{Ru} ⁻¹)
Ru(Cl)(Cp)(PPh ₃) ₂	22
Ru(Cl)(Cp)(dppe)	11
RuHPW	14
RudppeHPW	5

POM for phenyl acetylene oligomerisation *via* an atom-efficient, solvent-free protocol.¹⁰¹ Additional work could be considered to adapt this class of system for synthesising important structural building blocks for natural product synthesis and conjugated optically active materials.^{102, 103} An area of interest for simple helical polymers is that of poly(triaryl- methyl methacrylate)s, derived from phenyl acetylenes for instance, poly(triphenyl- methyl methacrylate) (PTrMA) with a one-handed helical structure are used to resolve various racemates as a chiral stationary phase for high performance liquid chromatography (HPLC).^{104,}

105

3.8 - Conclusions

Catalytically interesting novel compounds based on ruthenium and HPW have been synthesised. It is believed that these materials have a Ru-O=W interaction composed of two {Ru(Cp)L₂} units (L = PPh₃, 1/2 dppe) with a triply deprotonated Keggin anion. These mono-anionic di-Ru polyoxometallates are associated with a charge balancing triethylammonium cation. The resulting **RuHPW** and **RudppeHPW** species taking on the general formula of [NEt₃H]⁺[{Ru(Cp)(L)₂}₂{PW₁₂O₄₀}]⁻. The compounds are synthesised in powder form in a facile synthetic procedure, beneficial for industrial exploitation. In addition, these compounds have heterogeneous characteristics such as their insolubility in common laboratory solvents and thermal stability to 280 °C.

A characterisation and testing protocol has been devised which should provide a means of tuning future materials to improve and develop desirable properties for use in methanol carbonylation. A protocol for testing materials for CO-binding properties has been developed. *In-situ* DRIFT spectroscopic measurements can be taken of materials with variables including temperature, gas flow rate and composition. This offers a wealth of information about potential transition metal CO binding.

These ruthenium/HPW species can bind CO at the ruthenium centre unlike their corresponding Cl complexes. Although initial studies show that methanol carbonylation does not occur with these systems, the hindering properties have been identified as loss of acidity due to the proton coordinating base and the

strength of CO binding at the Ru centre preventing release under reaction conditions. Addition of HPW to both **RuHPW** and **RudppeHPW** showed activation of methanol leading to the formation of DME, a methanol dimerisation product formed in the absence of activated CO. This supports the absence of acidity in the unsupported compounds.

Phenylacetylene oligomerisation using these Ru-POMs shows catalytic activity which differ from their parent RuL_nCl complexes. In particular **RuHPW** was found to offer improved selectivity (70 *E* /30 *Z*) while maintaining competitive conversion rates. This demonstrates proof of concept where a transition metal complex can interact with a polyoxometallate where both functionalities are intact and the organometallic functionality in this case, an organoruthenium species, can perform catalytic manipulations analogous to that of its homogeneous counterpart while being influenced by the polyoxometallate.

3.9 - References

1. Y. Wakatsuki and H. Yamazaki, *Journal of Organometallic Chemistry*, 1995, **500**, 349-362.
2. M. Pagliaro, S. Campestrini and R. Ciriminna, *Chemical Society Reviews*, 2005, **34**, 837-845.
3. J. Faller and J. Parr, *Current Organic Chemistry*, 2006, **10**, 151-163.
4. R. H. Grubbs and S. Chang, *Tetrahedron*, 1998, **54**, 4413-4450.
5. T. M. Trnka and R. H. Grubbs, *Accounts of Chemical Research*, 2001, **34**, 18-29.
6. L. S. Hegedus, *Coordination Chemistry Reviews*, 2000, **204**, 199-307.
7. M. Jimenez-Tenorio, M. C. Puerta and P. Valerga, *European Journal of Inorganic Chemistry*, 2004, 17-32.
8. R. Schmid and K. Kirchner, *European Journal of Inorganic Chemistry*, 2004, 2609-2626.
9. H. Shen and Z. W. Xie, *Chemical Communications*, 2009, 2431-2445.
10. M. Bassetti, S. Marini, F. Tortorella, V. Cadierno, J. Diez, M. P. Gamasa and J. Gimeno, *J. Organomet. Chem.*, 2000, **593**, 292-298.
11. M. I. Bruce, B. C. Hall, B. W. Skelton, A. H. White and N. N. Zaitseva, *Journal of the Chemical Society-Dalton Transactions*, 2000, 2279-2286.
12. R. U. Kirss, R. D. Ernst and A. M. Arif, *J. Organomet. Chem.*, 2004, **689**, 419-428.
13. C. Lambert and G. Noll, *Angewandte Chemie-International Edition*, 1998, **37**, 2107-2110.
14. I. G. Stara, I. Stary, A. Kollarovic, F. Teply, D. Saman and M. Tichy, *Journal of Organic Chemistry*, 1998, **63**, 4046-4050.
15. P. Phansavath, R. Stammler, C. Aubert and M. Malacria, *Synthesis-Stuttgart*, 1998, 436-443.
16. G. Mehta and S. Kotha, *Tetrahedron*, 2001, **57**, 625-659.
17. I. Omae, *Applied Organometallic Chemistry*, 2007, **21**, 318-344.
18. S. Mannathan and C. H. Cheng, *Chemical Communications*, 2010, **46**, 1923-1925.
19. W. J. Zuercher, M. Scholl and R. H. Grubbs, *Journal of Organic Chemistry*, 1998, **63**, 4291-4298.
20. J. P. Qu, D. Masui, Y. Ishii and M. Hidai, *Chem. Lett.*, 1998, 1003-1004.
21. C. S. Yi, J. R. Torres-Lubian, N. H. Liu, A. L. Rheingold and I. A. Guzei, *Organometallics*, 1998, **17**, 1257-1259.
22. M. Murakami, M. Ubukata and Y. Ito, *Tetrahedron Letters*, 1998, **39**, 7361-7364.
23. A. R. McDonald, C. Muller, D. Vogt, G. P. M. van Klinka and G. van Koten, *Green Chem.*, 2008, **10**, 424-432.
24. E. Tempesti, A. Kaddouri and N. De Blasio, *J. Therm. Anal.*, 1998, **53**, 177-187.
25. N. Sudheesh, S. K. Sharma, R. S. Shukla and R. V. Jasra, *Journal of Molecular Catalysis a-Chemical*, 2010, **316**, 23-29.
26. N. Sudheesh, S. K. Sharma, R. S. Shukla and R. V. Jasra, *Journal of Molecular Catalysis a-Chemical*, 2008, **296**, 61-70.
27. K. Mukhopadhyay and R. V. Chaudhari, *Journal of Catalysis*, 2003, **213**, 73-77.
28. E. Coronado and C. J. Gomez-Garcia, *Chem. Rev.*, 1998, **98**, 273-296.

29. C. L. Hill, *Journal of Molecular Catalysis a-Chemical*, 2007, **262**, 2-6.
30. N. Mizuno and M. Misono, *Chem. Rev.*, 1998, **98**, 199-217.
31. J. T. Rhule, C. L. Hill and D. A. Judd, *Chem. Rev.*, 1998, **98**, 327-357.
32. I. V. Kozhevnikov, *Catalysis Reviews-Science and Engineering*, 1995, **37**, 311-352.
33. R. Neumann and M. Dahan, *Nature*, 1997, **388**, 353-355.
34. R. A. Sheldon, I. Arends and A. Dijkstra, *Catalysis Today*, 2000, **57**, 157-166.
35. R. Villanneau, V. Artero, D. Laurencin, P. Herson, A. Proust and P. Gouzerh, *Journal of Molecular Structure*, 2003, **656**, 67-77.
36. Y. Sakai, A. Shinohara, K. Hayashi and K. Nomiva, *Eu. J. Inorg. Chem.* , 2006, **1**, 163-167.
37. L. H. Bi, M. H. Dickman, U. Kortz and I. Dix, *Chemical Communications*, 2005, 3962-3964.
38. L. H. Bi, F. Hussain, U. Kortz, M. Sadakane and M. H. Dickman, *Chemical Communications*, 2004, 1420-1421.
39. C. N. Kato, A. Shinohara, N. Moriya and K. Nomiya, *Catalysis Communications*, 2006, **7**, 413-416.
40. D. Laurencin, R. Thouvenot, K. Boubekur and A. Proust, *Dalton Transactions*, 2007, 1334-1345.
41. K. Nomiya, K. Hayashi, Y. Kasahara, T. Iida, Y. Nagaoka, H. Yamamoto, T. Ueno and Y. Sakai, *Bulletin of the Chemical Society of Japan*, 2007, **80**, 724-731.
42. P. M. Maitlis, H. C. Long, R. Quyoun, M. L. Turner and Z. Q. Wang, *Chemical Communications*, 1996, 1-8.
43. C. Bianchini, V. Dal Santo, A. Meli, S. Moneti, M. Moreno, W. Oberhauser, R. Psaro, L. Sordelli and F. Vizza, *Journal of Catalysis*, 2003, **213**, 47-62.
44. G. C. Zhou and Harruna, II, *Macromolecules*, 2004, **37**, 7132-7139.
45. A. P. Humphries and S. A. R. Knox, *Journal of the Chemical Society-Dalton Transactions*, 1975, 1710-1714.
46. Johnson-Matthey, *The platinum metals report*, August 2008.
47. A. D. Newman, PhD Thesis, York, 2007.
48. W. Baratta, W. A. Herrmann, R. M. Kratzer and P. Rigo, *Organometallics*, 2000, **19**, 3664-3669.
49. J. M. Lynam, T. D. Nixon and A. C. Whitwood, *Journal of Organometallic Chemistry*, 2008, **693**, 3103-3110.
50. M. J. Tenorio, M. C. puerta and P. Valerga, *European Journal of Inorganic Chemistry*, 2004, 17-32.
51. P. M. Treichel, D. A. Komar and P. J. Vincenti, *Synthesis and Reactivity in Inorganic and Metal-Organic Chemistry*, 1984, **14**, 383-400.
52. C. Cocorran, *BSc report*, University of York, 2006.
53. D. H. Williams and I. Fleming, *Spectroscopic methods in organic chemistry*, 5th edn., McGraw-Hill publishing company, 1995.
54. L. A. Harrah, M. T. Ryan and C. Tamborski, *The infra-red spectrum of the phenyl compounds of group IVb, Vb, and VIIb Elements*, 1960.
55. A. K. K. Pamin, Z. Olejniczak, J. Haber, and B. Sulikowski, *Applied Catalysis A: General*, 2000, **194-195**, 137-146.
56. T. Blasco, A. Corma, A. Martinez and P. Martinez-Escolano, *Journal of Catalysis*, 1998, **177**, 306-313.

57. M. J. Howard, M. D. Jones, M. S. Roberts and S. A. Taylor, *Catal. Today*, 1993, **18**, 325-354.
58. A. Haynes, P. M. Maitlis, G. E. Morris, G. J. Sunley, H. Adams, P. W. Badger, C. M. Bowers, D. B. Cook, P. I. P. Elliott, T. Ghaffar, H. Green, T. R. Griffin, M. Payne, J. M. Pearson, M. J. Taylor, P. W. Vickers and R. J. Watt, *Journal of the American Chemical Society*, 2004, **126**, 2847-2861.
59. P. M. Maitlis, A. Haynes, G. J. Sunley and M. J. Howard, *Journal of the Chemical Society-Dalton Transactions*, 1996, 2187-2196.
60. I. V. Kozhevnikov, *Chemical Reviews*, 1998, **98**, 171-198.
61. L. Luo, S. P. Nolan and P. J. Fagan, *Organometallics*, 1993, **12**, 4305-4311.
62. R. T. Lubian and M. A. PazSandoval, *J. Organomet. Chem.*, 1997, **532**, 17-29.
63. P. Diversi, M. Fontani, M. Fuligni, F. Laschi, S. Matteoni, C. Pinzino and P. Zanello, *J. Organomet. Chem.*, 2001, **626**, 145-156.
64. B. C. Gagea, Y. Lorgouilloux, Y. Altintas, P. A. Jacobs and J. A. Martens, *Journal of Catalysis*, 2009, **265**, 99-108.
65. T. Blasco, M. Boronat, P. Concepcion, A. Corma, D. Law and J. A. Vidal-Moya, *Angewandte Chemie-International Edition*, 2007, **46**, 3938-3941.
66. I. V. Kozhevnikov, S. Holmes and M. R. H. Siddiqui, *Appl. Catal. A-Gen.*, 2001, **214**, 47-58.
67. B. B. Bardin and R. J. Davis, *Journal of Applied Catalysis A: General*, 2000, **200**, 219-231.
68. M. J. Cowley, J. M. Lynam, R. S. Moneypenny, A. C. Whitwood and A. J. Wilson, *Dalton Transactions*, 2009, 9529-9542.
69. W. H. Knoth and R. D. Farlee, *Inorganic Chemistry*, 1984, **23**, 4765-4766.
70. J. C. Duhacek and D. C. Duncan, *Inorganic Chemistry*, 2007, **46**, 7253-7255.
71. W. H. Knoth and R. L. Harlow, *Journal of the American Chemical Society*, 1981, **103**, 4265-4266.
72. I. V. Kozhevnikov, A. Sinnema and H. Vanbekkum, *Catalysis Letters*, 1995, **34**, 213-221.
73. H. L. Zhang, A. M. Zheng, H. G. Yu, S. H. Li, X. Lu and F. Deng, *Journal of Physical Chemistry C*, 2008, **112**, 15765-15770.
74. F. Lefebvre, *J. Chem. Soc.-Chem. Commun.*, 1992, 756-757.
75. M. Bruce, F. Wong, B. Skelton and A. White, *Dalton Transactions*, 1981, 1398.
76. M. Bruce, P. Low, B. Skelton, E. Tiekink, A. Werth and A. White, *Australian Journal of Chemistry*, 1995, **48**, 1887.
77. A. Tenaglia and L. Giordano, *Synlett*, 2003, 2333.
78. D. Herbert, I. Manners and A. Lough, *Private Communication*, 2007.
79. G. Doyle and D. Van Engen, *Journal of Organometallic Chemistry*, 1985, **280**, 253-259.
80. E. V. Radkov, V. G. Young and R. H. Beer, *Journal of the American Chemical Society*, 1999, **121**, 8953-8954.
81. A. R. Siedle, P. A. Lyon, S. L. Hunt and R. P. Skarjune, *Journal of the American Chemical Society*, 1986, **108**, 6430-6431.
82. J. F. Keggin, *Proceedings of the Royal Society: A*, 1934, **144**, 75-100.
83. M. J. Tenorio, K. Mereiter, M. C. Puerta and P. Valerga, *Journal of the American Chemical Society*, 2000, **122**, 11230-11231.

84. M. J. Tenorio, M. C. Puerta and P. Valerga, *J. Organomet. Chem.*, 2000, **609**, 161-168.
85. T. Arliguie, C. Border, B. Chaudret, J. Devillers and R. Poilblanc, *Organometallics*, 1989, **8**, 1308-1314.
86. I. delosRios, M. J. Tenorio, J. Padilla, M. C. Puerta and P. Valerga, *Organometallics*, 1996, **15**, 4565-4574.
87. I. delosRios, M. J. Tenorio, J. Padilla, M. C. Puerta and P. Valerga, *Journal of the Chemical Society-Dalton Transactions*, 1996, 377-381.
88. K. Kirchner, K. Mereiter, R. Schmid and H. Taube, *Inorganic Chemistry*, 1993, **32**, 5553-5561.
89. M. S. Quinby and R. D. Feltham, *Inorganic Chemistry*, 1972, **11**, 2468-&.
90. F. L. Joslin, M. P. Johnson, J. T. Mague and D. M. Roundhill, *Organometallics*, 1991, **10**, 2781-2794.
91. R. Thouvenot, M. Fournier, R. Franck and C. Rocchicciolideltcheff, *Inorganic Chemistry*, 1984, **23**, 598-605.
92. U. Mioc, P. Colomban and A. Novak, *Journal of Molecular Structure*, 1990, **218**, 123-128.
93. U. B. Mioc, M. R. Todorovic, S. M. Uskokovic-Markovic, Z. P. Nedic and N. S. Bosnjakovic, *Journal of the Serbian Chemical Society*, 2000, **65**, 399-406.
94. R. Goddard, A. P. Humphries, S. A. R. Knox and P. Woodward, *J. Chem. Soc.-Chem. Commun.*, 1975, 507-508.
95. R. Goddard, A. P. Humphries, S. A. R. Knox and P. Woodward, *J. Chem. Soc.-Chem. Commun.*, 1975, 508-509.
96. M. Stöcker, *Microporous and Mesoporous Materials*, 1999, **29**, 3-48.
97. C. Bruneau and P. H. Dixneuf, *Angewandte Chemie-International Edition*, 2006, **45**, 2176-2203.
98. C. Slugovc, K. Mereiter, E. Zobetz, R. Schmid and K. Kirchner, *Organometallics*, 1996, **15**, 5275-5277.
99. C. Bianchini, C. Bohanna, M. A. Esteruelas, P. Frediani, A. Meli, L. A. Oro and M. Peruzzini, *Organometallics*, 1992, **11**, 3837-3844.
100. K. Ogata and A. Toyota, *J. Organomet. Chem.*, 2007, **692**, 4139-4146.
101. J. M. Lynam, T. D. Nixon and A. C. Whitwood, *Journal of Organometallic Chemistry*, 2008, **693**, 3103-3110.
102. T. Takahashi, Y. H. Liu, A. Iesato, S. Chaki, K. Nakajima and K. Kanno, *Journal of the American Chemical Society*, 2005, **127**, 11928-11929.
103. Y. Kishimoto, P. Eckerle, T. Miyatake, M. Kainosho, A. Ono, T. Ikariya and R. Noyori, *Journal of the American Chemical Society*, 1999, **121**, 12035-12044.
104. E. Yashima, S. L. Huang, T. Matsushima and Y. Okamoto, *Macromolecules*, 1995, **28**, 4184-4193.
105. Y. Okamoto and K. Hatada, *J. Liq. Chromatogr.*, 1986, **9**, 369-384.

Chapter 4 - Synthesis, characterisation and catalysis of Rh- polyoxometallates

4.1 - Introduction

Acetic acid is an important industrial chemical, used in paints, plastics, and as a solvent for many important reactions including the formation of many household polymers. As a result of this heavy demand, 8 million tonnes of acetic acid are produced annually, of which 80 % is produced by methanol (MeOH) carbonylation (**Scheme 4.1.1**).¹ Current industrial processes utilise rhodium and iridium catalysed homogeneous reactions, which can deliver high activity and selectivity but utilise high CO pressures and methyl iodide, liberating highly corrosive and hazardous HI *in-situ*.² However, there is considerable interest in the development of alternative, heterogeneous catalyst technologies able to activate both methanol and CO,³⁻⁵ and promote carbonylation over the competing condensation or dehydration pathways shown in **Scheme 4.1.1**. Solid catalysts offer several advantages including simplified product separation, elimination of corrosive halide promoters (and thus mild reaction conditions), and the possibility of continuous processing.



Scheme 4.1.1: Important reaction pathways during methanol carbonylation; (1) direct methanol carbonylation to methyl acetate (2) methanol condensation to dimethyl ether (DME), (3) direct DME carbonylation to methyl acetate, (4) methanol dehydration to higher alkenes, (5) methanol reduction to higher alkanes (MTG chemistry).

Several strategies for heterogeneous carbonylation to acetic acid have been devised, including direct syngas conversion thereby bypassing the need for preliminary methanol production. Unfortunately, syngas to acetyls processes favour hydrocarbon and polymeric products (leading to catalyst coking), yielding little oxygenates. Rhodium-based catalysts are the most effective for the syngas route due to their unique selectivity towards C₂ oxygenates,^{6, 7} and usually doped with alkali or transition metals (e.g. Sc, Mn, Ir, Ti) to improve selectivity and/or conversion.⁸⁻¹⁰ Selectivities > 65 % to acetic acid have been achieved over Rh-Mn-Ir-Li/SiO₂, albeit using an artificially CO-rich syngas feed. Another problem with the syngas approach is the facile reduction of many rhodium complexes at temperatures as low as 120 °C under hydrogen atmospheres.¹¹ While non-rhodium, iodide-free systems are attractive due to lower costs, few have been successfully developed, although Ru-Sn catalysts can generate C₂ oxygenates from a MeOH-only feed *via* dehydrogenation to methyl formate followed by isomerisation to acetic acid.¹² However, these bimetallic catalysts suffer from low conversions (~ 5 %) and methyl formate selectivity (~ 60 %), hence the prevalence of commercial direct methanol carbonylation processes.

Metal loaded mordenites (a natural zeolite of general formula, (Ca, Na₂, K₂) Al₂Si₁₀O₂₄·7H₂O) are capable of carbonylating methanol,¹³⁻¹⁶ however little non-iodide work has been undertaken on these systems. Copper mordenite exhibits acetyl selectivities > 70 % under forcing conditions (350 °C and 25 bar), but undergoes methanol to gasoline (MTG) chemistry before forming acetyls, and also deactivates on-stream. In an interesting variation, Copper mordenite was recently combined with Pd/CeO₂ to enable *in-situ* CO generation and thus subsequent carbonylation using a MeOH-only reactor feed, though with comparatively low space time yields.¹⁷ Other solid acid catalysts, such as heteropolyacids (HPAs), have shown promise for the vapour phase carbonylation of methanol^{5, 18} or dimethyl ether¹⁹ when combined with rhodium *via* simple ion-exchange.²⁰ HPAs are polyoxometalate inorganic cage structures, which may adopt the Keggin form with the general formula H₃MX₁₂O₄₀, where M is typically P or Si, and X W or Mo. They have been widely studied as catalytic materials due to their tuneable (strong) acidity and redox capacity.²¹⁻²³ Phosphotungstic acid, H₃PW₁₂O₄₀·6H₂O, is one of the most acidic and stable of the Keggin HPAs,²⁴

whose acidity originates from H_5O_2^+ crystallised between Keggin units. This crystalline water can be ion exchanged with other cations, e.g. Na^+ , K^+ , Cs^+ or Ag^+ , to regulate HPA solubility and Keggin unit separation or acid strength, or exchanged with a catalytically active component to facilitate bifunctional catalysis. A characteristic of their superacidity is the facility for low temperature alkane and alcohol activation, the latter representing a key step in methanol carbonylation.²⁵ Despite their versatility, HPAs have a poor affinity for CO, and are hence inactive for continuous carbonylation when used alone. Their bulky nature and distributed charge does offer a solution to this problem however, since HPAs can be considered as weakly coordinating anions, and thus able to stabilise organorhodium complexes already discussed as known for reversibly CO binding.

The industrial sponsors of this work indicated rhodium acetate as a potential precursor for a bifunctional Rh-HPW system in-line with previous work.²⁶ This was particularly attractive as it was simple to prepare, involving no calcination or reduction steps. Work at the University of York showed that simple bulk and SiO_2 supported Rh-HPW, where Rh(II) and Rh(III) ligated by acetate or chloride show activity and selectivity in the formation of acetyls in vapour phase heterogeneous methanol carbonylation.²⁷ However, these systems suffered from rapid deactivation which has been shown to result from reduction of Rh^{n+} to Rh(0) this is thought to be due to facile dissociation of the ligands from the complex under reaction conditions.

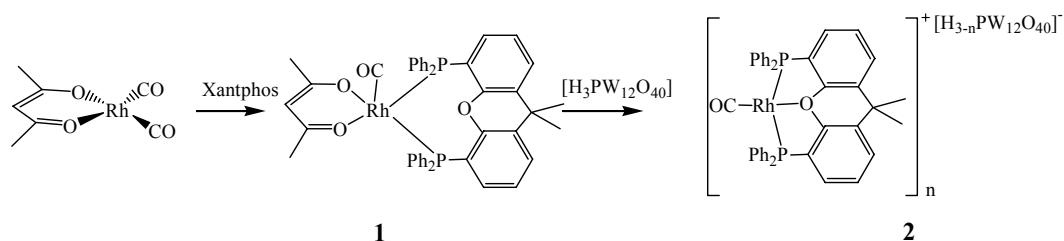
A more robust ligand system could offer enhanced oxidation state stability therefore retaining carbonylation activity and selectivity on stream. Various organorhodium complexes with multidentate ligands are known to reversibly bind CO (and active in alkene hydroformylation).^{28, 29} Many are cationic with bulky charge balancing anions e.g. BF_4^- which could be considered analogous to heteropolyanions found in Rh-HPWs, and therefore suitable for incorporation as a CO activation functionality. An important aspect of these Rh(I) complexes is their good thermal and chemical tolerance, imparted through coordination to Xantphos, a polydentate, organophosphorous heterocyclic ligand with a wide bite angle. In this work, we explore whether the CO capture properties of such robust Rh-Xantphos containing cations can be combined with the solid acidity of $\text{H}_3\text{PW}_{12}\text{O}_{40}$

to create a new bifunctional catalyst capable of low temperature methanol carbonylation.

4.2 - Rh(Xantphos)(CO)HPW (RhXHPW) synthesis

The Rh(η^2 -acac)(CO)₂ precursor was used for all catalyst systems discussed herein. A Xantphos-bound Rh complex was synthesised from the green crystalline starting Rh complex by stirring at room temperature with Xantphos in THF solvent for 15 minutes. An evolution of gas was noted, believed to be carbon monoxide, indicative of the loss of CO to accommodate Xantphos. The yellow / orange crystalline material was isolated in vacuo and washed with hexane. The Rh-Xantphos provided a broad ³¹P NMR signal in CDCl₃ at 11.0 ppm with a coupling constant of 90 Hz characteristic of Rh(η^2 -acac)(CO)(Xantphos), ‘**RhXantphos**’ reported in the literature and in agreement with elemental analysis.^{28, 30} Additional solid state analysis reported in this work contributes to the characterisation of this complex present in the literature (*q.v.*).

Synthesis of a 1:1 Rh : Keggin HPW derivative of **RhXantphos** (Scheme 4.2.1 (1)) was accomplished by adding the required one equivalent of H₃PW₁₂O₄₀·20H₂O to a THF solution of **RhXantphos** generated *in-situ* in the manner described above. Proton decoupled ³¹P NMR of the new ‘**RhXHPW**’ (2) material in D₆-DMSO shows total consumption of the **RhXantphos** parent signal and generation of a new broad singlet resonance at 44.97 ppm, indicative of formation a new Rh-Xantphos species. A characteristic resonance at -14.97 ppm is consistent with the presence of HPW indicating the parent polyoxometallate remains intact on interaction with a Rh-Xantphos functionality. Further solid state characterisation and discussion of the stability of **RhXHPW** is discussed below.



Scheme 4.2.1: Synthesis and proposed structures of **RhXantphos** (1) and **RhXHPW** (2) from Rh(η^2 -acac)(CO)₂.

Preservation of the parent frameworks was first explored by DRIFTS (**Figure 4.2.1**), which showed that the combination of **RhXantphos** and acidic HPW gave a solid compound with peaks at 670, 1400 and 2800 cm^{-1} characteristic of the C-P, C-C and phenyl/methyl C-C stretching modes of Xantphos, indicating retention of the organic ligand. **RhXantphos** itself also exhibits a single CO stretching band

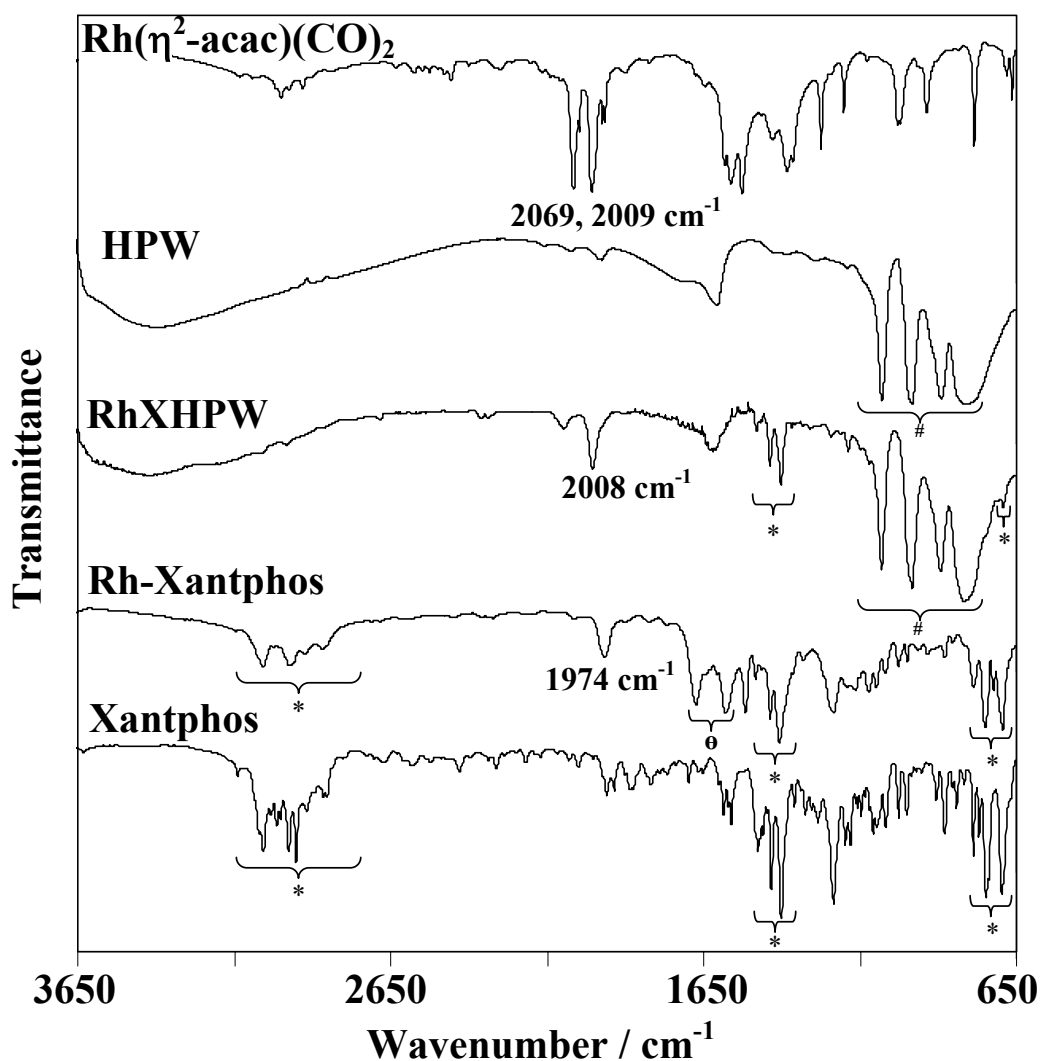


Figure 4.2.1: DRIFTS of **RhXantphos** precursor and bulk **RhXHPW1:1** together with representative Rh standards. Characteristic Xantphos (*), HPW (#) and η^2 -acac bands (θ) are highlighted, together with Rh-CO stretches.

at 1974 cm^{-1} arising from loss of one CO ligand upon Xantphos complexation with $\text{Rh}(\eta^2\text{-acac})(\text{CO})_2$, which in turn originally displayed bands at 2069 and 2009 cm^{-1} due to the asymmetric and symmetric dicarbonyl stretches.³¹ This Rh-

CO band is blue shifted to 2008 cm⁻¹ in the **RhXHPW** compound, indicating the electronic structure of Rh is perturbed *via* interaction with the Keggin anion, likely reflecting protonation and loss of the acac ligand (supported by ¹H NMR evidenced by ¹H NMR showing residual acacH on partial drying of bulk **RhXHPW**, see **Appendix 3**) to yield an ionic [Rh(CO)(Xantphos)]⁺[H₂PW₁₂O₄₀]⁻ compound. The integrity of the phosphotungstate cage within **RhXHPW** is apparent from the characteristic bands between 700-1200 cm⁻¹ and overtone at 2100 cm⁻¹.³² The surface compositions of **RhXantphos** and the **RhXHPW** materials were determined by XPS (**Table 4.2.1**). These are in good agreement with their nominal bulk stoichiometries and structures proposed in **Scheme 4.2.1**, with a 1 (Rh) : 2 (P) ratio observed for **RhXantphos**, and 1 (Rh) :3 (P) :12 (W) ratio for **RhXHPW**.

Table 4.2.1: RhXantphos and RhXHPW stoichiometries^a

Element	Theoretical RhXantphos	Experimental RhXantphos	Theoretical RhXHPW	Experimental RhXHPW
Rh	1	1	1	1
P	2	2	3	3
W	-	-	12	12
O	4	23	42	42
C	45	68	40	63

^aCalculated from XPS derived atom % content (**Appendix 4**) normalised to Rh.

The oxidation state of Rh within both **RhXHPW** and **RhXHPW-SiO₂** was subsequently probed by XANES and XPS to confirm that the electronic structure of rhodium remained essentially unchanged in accordance with our proposed synthetic route. **Figure 4.2.2** reveals the XANES spectrum of the Rh(η^2 -acac)(CO)₂ precursor is intermediate between representative Rh(0) and Rh(III) standards, consistent with a formally 1+ oxidation state, and closely resembles that of the pure and supported **RhXHPW** samples. As might be anticipated from **Scheme 4.2.1**, sequential exchange of CO for Xantphos and acac for a Keggin anion does not appear to strongly perturb the Rh oxidation state. This observation is supported by high resolution Rh 3d XP spectra (**Figure 4.2.3a**) which shows both **RhXantphos** and **RhXHPW** exhibit 3d_{5/2} binding energies consistent with

Rh(I),³³ although displacement of the acac ligand from the free **RhXantphos**

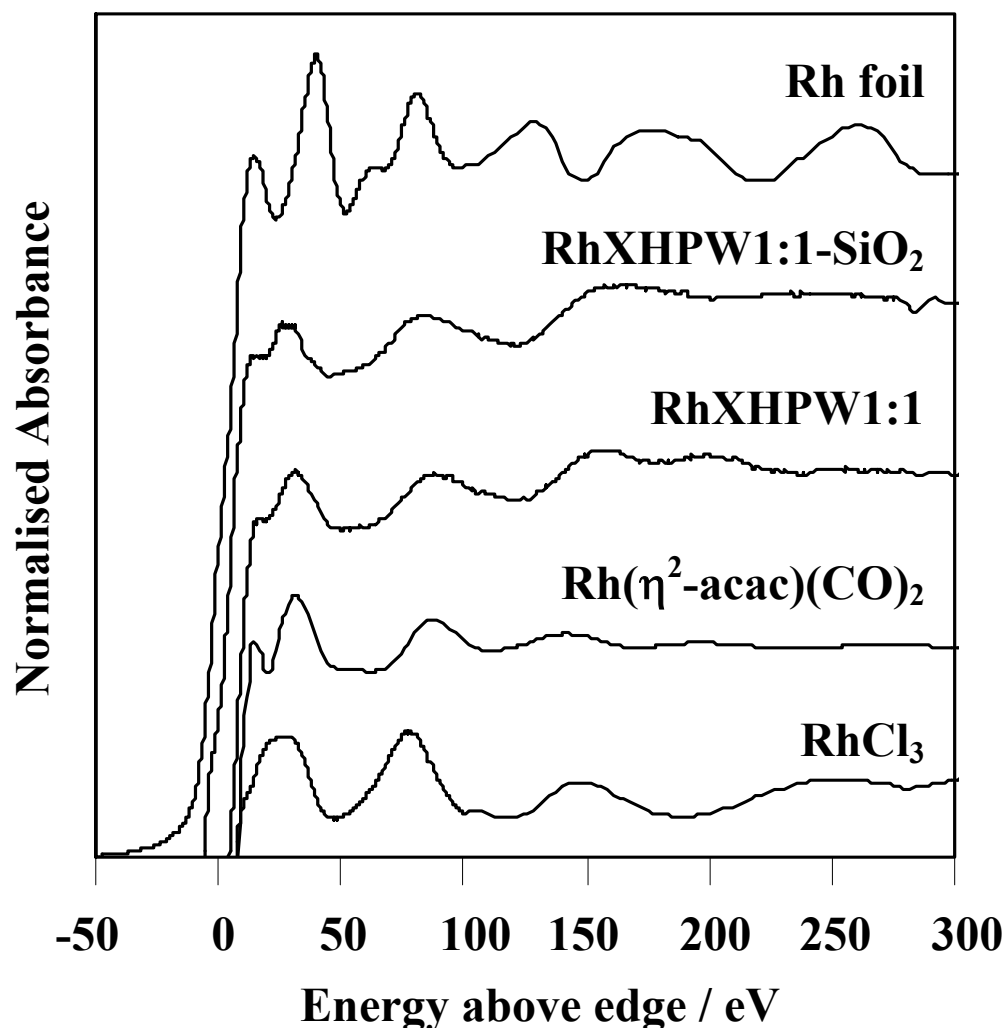


Figure 4.2.2: Normalised Rh K-edge XANES of bulk and silica supported **RhXHPW1:1** and representative Rh standards showing HPW materials contain Rh(I).

complex by the non-coordinating, doubly protonated $\text{H}_3\text{PW}_{12}\text{O}_{40}$ anion induces a 0.6 eV shift to higher energy which is attributed to a change in the Madelung potential and final state screening upon embedding the organorhodium species within an ionic framework. A corresponding decrease in the W 4f binding energy of the Keggin unit from 36.8 to 36.3 eV is also observed following crystallisation with **RhXantphos** (**Figure 4.2.3b**), consistent with the greater electropositive character of Rh(I) compared to H_5O_2^+ and thus greater initial state tungsten charge. Similar shifts have been reported for Cs(I) exchanged heteropolyacids.³⁴

Around 20 % of Keggin units retain characteristics of the parent HPW precursor within the **RhXHPW** material.

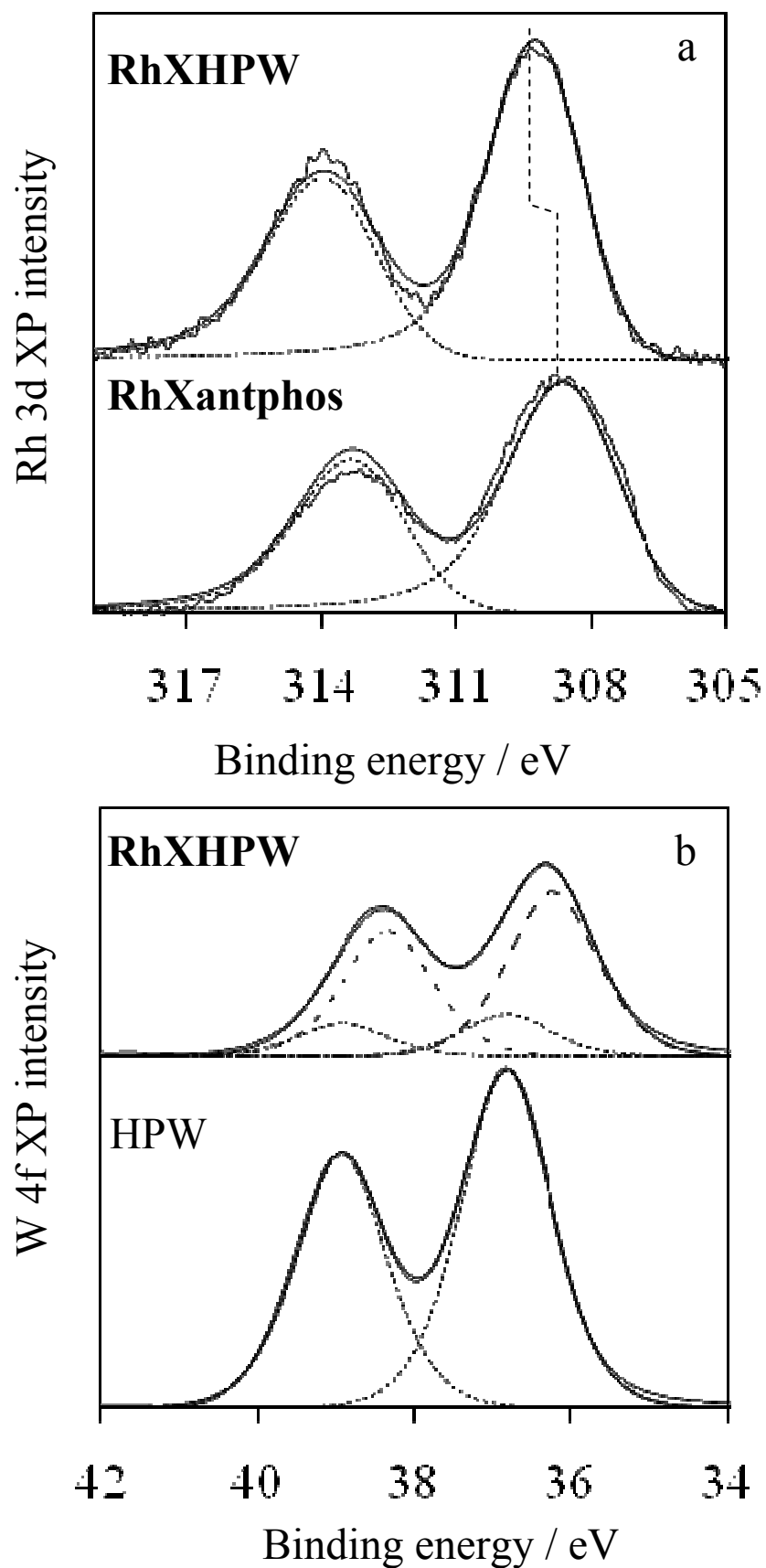


Figure 4.2.3: Comparison of a) Rh 3d XPS and b) W 4f regions for RhXantphos, ion exchanged RhXHPW and bulk HPW.

The local chemical environment of Rh within **RhXantphos** and **RhXHPW** was further probed by EXAFS (**Figure 4.2.4**), and the resulting fitted radial distribution functions are shown in **Figure 4.2.5**. It is evident from the fitted parameters in **Table 2** that the first coordination shells of both **RhXantphos** and **RhXHPW** are in good agreement with the structures proposed in **Scheme 4.2.1**, and by van Leeuwen for Rh(η^2 -acac)(CO)(Xantphos) and the analogous [Rh(CO)(Xantphos)]⁺[OTf]⁻ or [Rh(CO)(Xantphos)]⁺[BF₄]⁻ variants. In addition to the infrared shift in CO frequency noted earlier. Indeed the Rh-P bond lengths of 2.26-2.29 Å, and Rh-O/C distances of 2.05 Å, are very close to those derived from the crystal structure of [Rh(CO)(Xantphos)]⁺[BF₄]⁻.

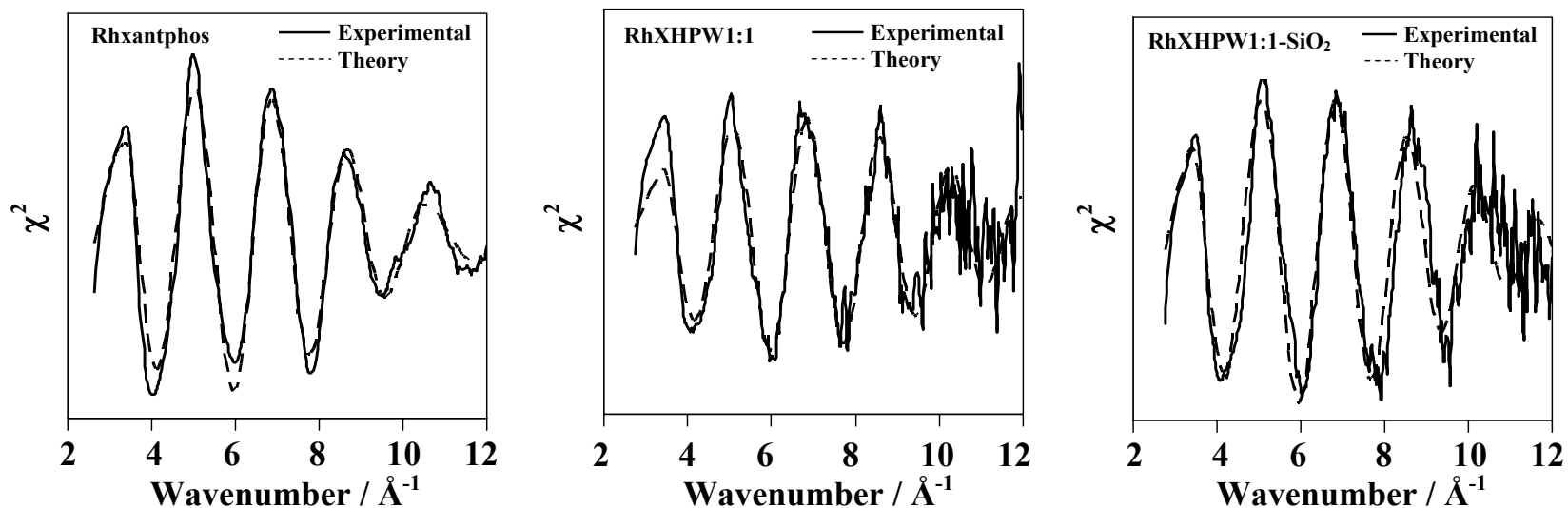
Incorporation of next nearest neighbour W scatterers (~ 4 Å) failed to improve the fit, discounting the possibility of a formal covalent Rh-O=W interaction (as observed in related Ru complexes³²), and supporting the proposed ionic compound in **Scheme 4.2.1**. It is important to note that supporting on silica had minimal influence on the **RhXHPW** structure. On careful examination of the total first coordination shell intensity it is evident that some electron density is lost from the Rh centre on incorporation of HPW. This is consistent with loss of acac ligand and reduction in coordination number.

In addition to EXAFS analysis to obtain Rh coordination information, efforts were made at growing single crystals of the precursor **RhXantphos** complex and

Table 4.2.2: Fitting parameters for EXAFS analysis of **RhXantphos**, **RhXHPW**, **RhXHPW1:1-SiO₂**.

Rh species	CN1 Rh-O ^a	CN2 Rh-O ^b	CN3 Rh-P ^b	CN4 Rh-C	CN5 Rh-W	R1 (Å) Rh-O ^a	R2 (Å) Rh-O ^b	R3 (Å) Rh-P ^b	R4 (Å) Rh-C	R5 (Å) Rh-W	σ_1 Rh-O ^a	σ_2 Rh-O ^b	σ_3 Rh-P ^b	σ_4 Rh-C	σ_5 Rh-W	R ²
Rh-Xantphos	2	-	2	1	-	2.04	-	2.29	2.05	-	0.002	-	0.005	0.002	-	21.00
RhXHPW	-	1	2	1	1	-	2.06	2.27	2.06	4.01	-	0.031	0.009	0.010	0.005	57.52
RhXHPW1:1-SiO ₂	-	1	2	1	1	-	2.05	2.26	2.05	4.11	-	0.002	0.005	0.002	0.011	35.67

^aatom from acac ligand, ^batom from Xantphos ligand

**Figure 4.2.4:** χ^2 plots for **RhXantphos**, **RhXHPW1:1** and **RhXHPW1:1-SiO₂**.

RhXHPW. A suitable solvent system was not obtained, however, a small number of crystals were identified and analysed from a THF / hexane recrystallization which identified a $\text{RhCl}(\text{CO})(\text{Xantphos})$ species (**Figure 4.2.6**, crystallographic refinements are summarised in **Table 4.2.3**) which provides an insight into the phosphine bond angle and distance one could expect and the accessibility of the Rh centre for application in methanol carbonylation catalysis. **Table 4.2.2** indicates the Rh-P distances are consistent with those observed in the EXAFS study of $\text{Rh}(\eta^2\text{-acac})(\text{CO})(\text{Xantphos})$ and **RhXHPW** which illustrates the rigidity of the Xantphos backbone. The Rh-CO bond distance is considerable shorter in the chloride complex which is consistent with the addition of the trans-chloride ligand which is pi-basic donating electrons to the metal improving back donation

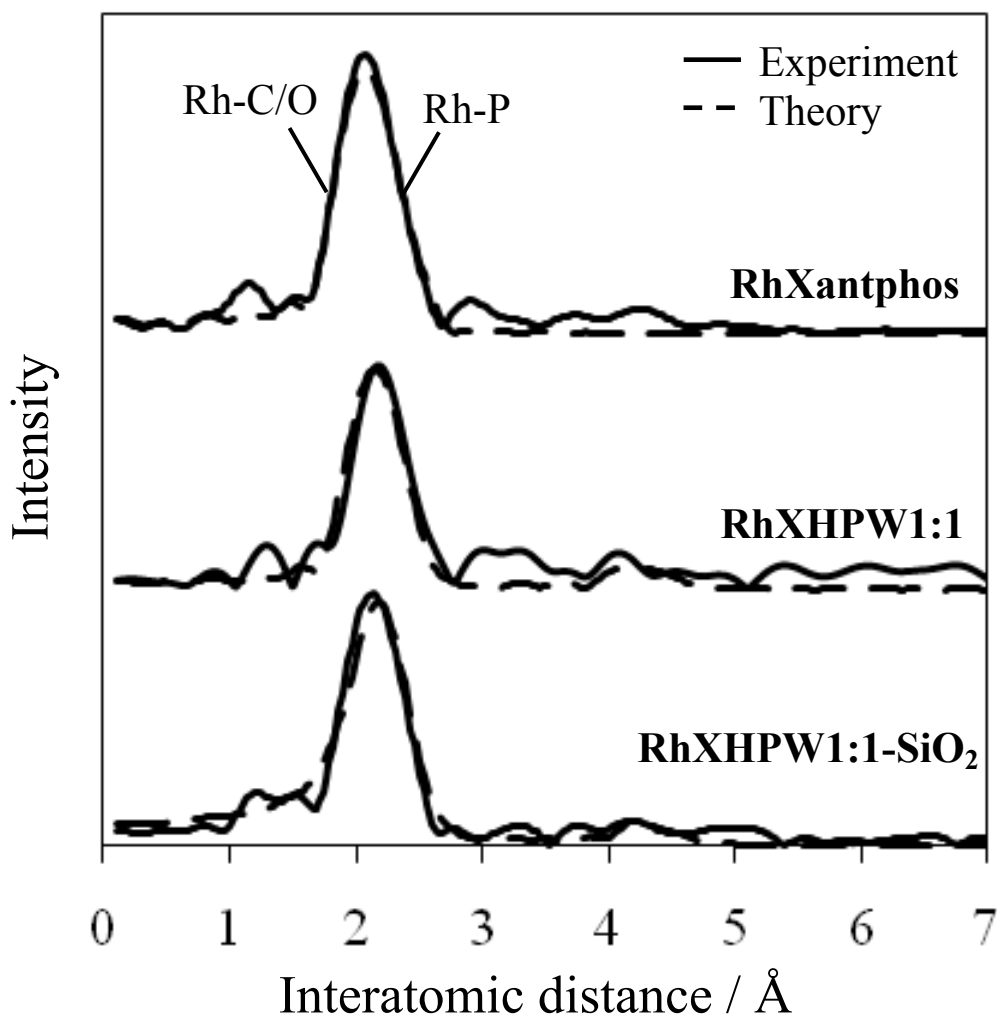


Figure 4.2.5: Fitted Rh K-edge EXAFS radial distribution functions of **RhXantphos**, bulk **RhXHPW1:1** and **RhXHPW1:1-SiO₂**. Contributions to the electron density from C, O and P in the first shell are indicated.

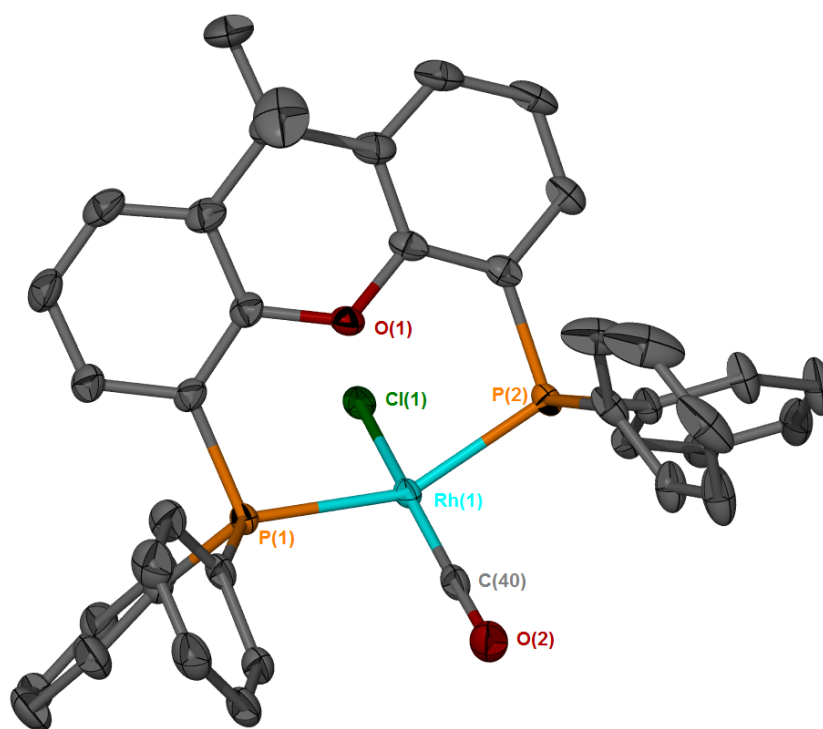


Figure 4.2.6: Crystal structure of RhCl(CO)(Xantphos) (image created using ORTEP³⁵)

Table 4.2.2: Selected bond lengths (Å) and angles (°) for RhCl(CO)(Xantphos)

Bond/angle	Bond distance / Å	Bond angle / °
Rh-P1	2.304(1)	-
Rh-P2	2.283(2)	-
Rh-C(carbonyl)	1.809(3)	-
Rh-Cl	2.412(4)	-
Rh – O	2.671(1)	-
P1 – Rh – P2	-	149.42(2)
Cl – Rh – C(carbonyl)	-	166.08(7)

of electrons into the pi-antibonding orbital of the carbonyl, strengthening the Rh-carbon bond. The P-Rh-P bond angle is 149 ° which is consistent with that expected for this kind of ligand backbone.^{36, 37} Indeed, the P-P distance observed is 4.42 Å, which is only 0.34 Å change in the natural P-P distance of 4.08 Å³⁸ which is consistent with the facile nature of ligation. The Xantphos backbone although covering one face of the Rh coordination sphere leaves an ideal site for further ligand attachment and an openness which encourages its application in catalytic CO activation.^{36, 39}

Table 4.2.3: Crystallographic details for RhCl(CO)(Xantphos)·1.5THF (full details included on CD1)

Empirical formula	C ₄₆ H ₄₄ ClO _{3.5} P ₂ Rh
f_w	853.11
Temperature (K)	110(2)
Wavelength (Å)	0.71073
Crystal system, space group	Monoclinic, C2/c
a (Å)	38.420(3)
b (Å)	9.7562(7)
c (Å)	23.1445(14)
α (deg)	90
β (deg)	112.564(4)
γ (deg)	90
v (Å ³)	8011.2(10)
Z, D _c (Mg m ⁻³)	8, 1.415
Abs coeff (mm ⁻¹)	0.615
F(000)	3520
Crystal size (mm ³)	0.15 x 0.10 x 0.07
Θ range for data collection (deg)	1.81 to 28.32
Limiting indices	-51 ≤ h ≤ 51
	-13 ≤ k ≤ 13
	-30 ≤ l ≤ 30
Number of reflections collected	40558
Independent reflections	9971 [R(int) = 0.0330]
Completeness to theta = 28.32 °	99.8 %
Absorption correction	Semi-empirical from equivalents
Max. and min. transmission	0.958 and 0.860
Refinement method	Full-matrix least-squares on F ²
GOF on F ²	1.034
Number of data/restraints/parameters	9971 / 30 / 536
Final R indices ($I > 2\sigma(I)$)	R1 = 0.0358, wR2 = 0.0911
R indices (all data)	R1 = 0.0460, wR2 = 0.0973
Largest diff peak and hole (e Å ⁻³)	0.929 and -0.579

Methanol carbonylation is often conducted at elevated temperature, hence the thermal robustness of **RhXHPW** was subsequently assessed by TGA (**Figure 4.2.6**) which revealed the loss of physisorbed and crystalline water at 100 °C and 200 °C respectively. However, the residual Xantphos ligand and partially dehydrated (HPW·6H₂O) Keggin cage impart good thermal stability to **RhXHPW** up to 400 °C, providing a wide temperature regime for catalytic operation.

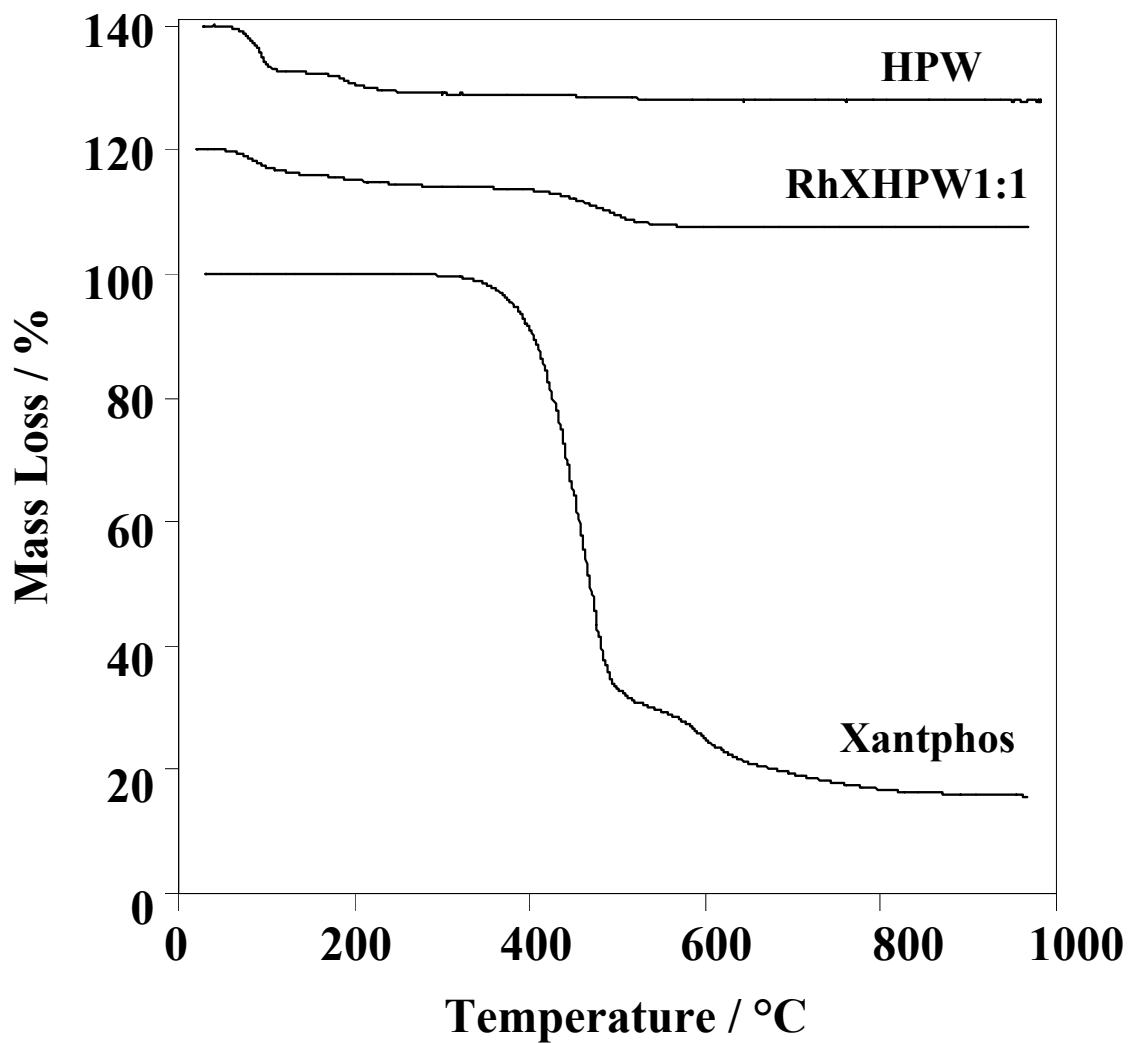


Figure 4.2.7: TGA comparison between 20 and 950 °C of RhXHPW1:1 with HPW and Xantphos ligand

4.3 - Methanol Carbonylation

Catalytic performance of **RhXHPW** materials was subsequently investigated towards ambient pressure methanol carbonylation (**Figure 4.3.1**). For all catalytic studies, the continuous flow reactor shown in **Figure 2.1.15** and reaction protocol outlined in Section 2.1.14 was used. The **RhXHPW** systems were benchmarked against pure HPW, which is known to selectively catalyse MeOH condensation to DME (noted in Chapter 3.5) above 170 °C,⁴⁰ favouring light alkanes at above 300 °C. Under light-off conditions the unsupported HPW performed poorly, with only 30 % conversion reached by 280 °C. Despite the bulk **RhXHPW1:1** containing only one third the number of acid sites present within the reactor charge, it significantly out-performed this HPW benchmark, evidencing a synergy between the organorhodium and heteropoly acid functions (the **RhXantphos** precursor is catalytically inactive under MeOH/CO conditions studied) which had been a goal of this project. However, the bulk **RhXHPW** still only delivered 40 % conversion at temperatures low enough to minimise MTG chemistry. The limited conversions for both these unsupported systems likely reflects their low surface areas and concomitant poor acid site accessibility,⁴¹ acting together with rapid coking of the parent HPW. This hypothesis is confirmed by the dramatic decrease in light-off temperature and/or enhanced MeOH conversion seen upon supporting either HPW or **RhXHPW** on a high area silica support.

Davisil silica has particular effective at stabilising HPW monolayers due to its high surface area ($300 \text{ m}^2\text{g}^{-1}$), wide pores and high hydroxyl density which facilitates multiple cluster attachment points.⁴² In the present case, both silica supported catalysts achieved conversions $\geq 80 \%$ by 200 °C, with the **RhXHPW1:1-SiO₂** again demonstrating excellent activity despite fewer acid sites than the comparable HPW-SiO₂ sample (further evidence for a synergic interaction between Rh and acid functions).

Figure 4.3.2 shows a typical product distribution for the **RhXHPW1:1-SiO₂** material. Although methanol condensation is the major low temperature reaction pathway, methyl acetate production commences $> 150 \text{ °C}$, reaching a maximum at

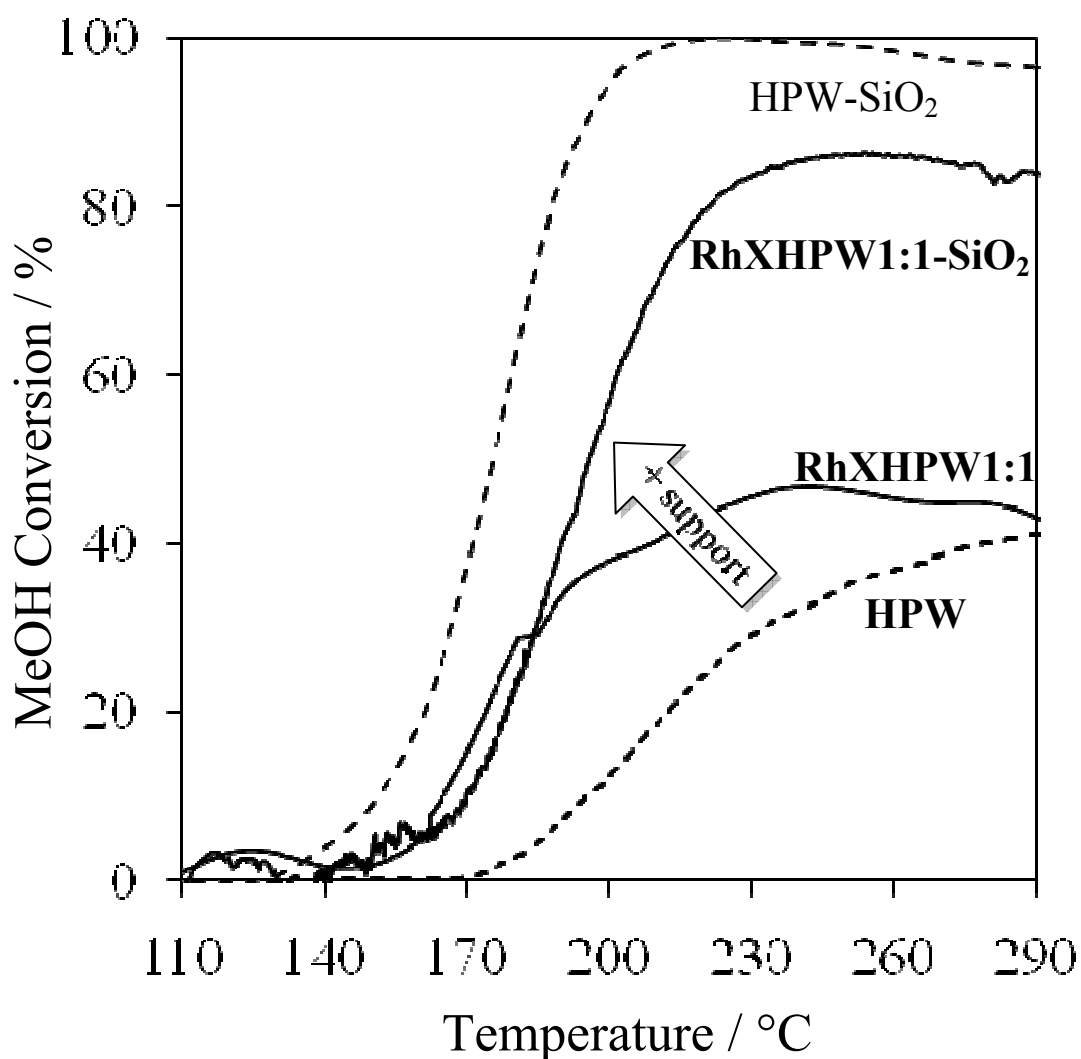


Figure 4.3.1: Methanol Conversion profiles of supported and unsupported **RhXHPW** catalysts compared to pure HPW. (Catalyst amounts: 80 mg HPW, 56 mg **RhXHPW1:1**, 311 mg **RhXHPW1:1-SiO₂** and 250 mg 50 wt % HPW-SiO₂ reproduced from ref 17)

200 °C corresponding to a peak acetyl selectivity of 56 %. DME and acetyl formation remains fairly constant between 200 - 250 °C, above which undesired MTG chemistry becomes the dominant process. Dispersing **RhXHPW1:1** on silica had little influence on the temperature dependent product distributions, confirming both catalysts operated *via* a common reaction mechanism and the greater reactivity of **RhXHPW1:1-SiO₂** over **RhXHPW1:1** seen in **Figure 4.3.1** is indeed associated with a higher density of similar active sites. The HPW-only materials did not catalyse carbonylation chemistry, and were only active towards methanol condensation over the same temperature regime.

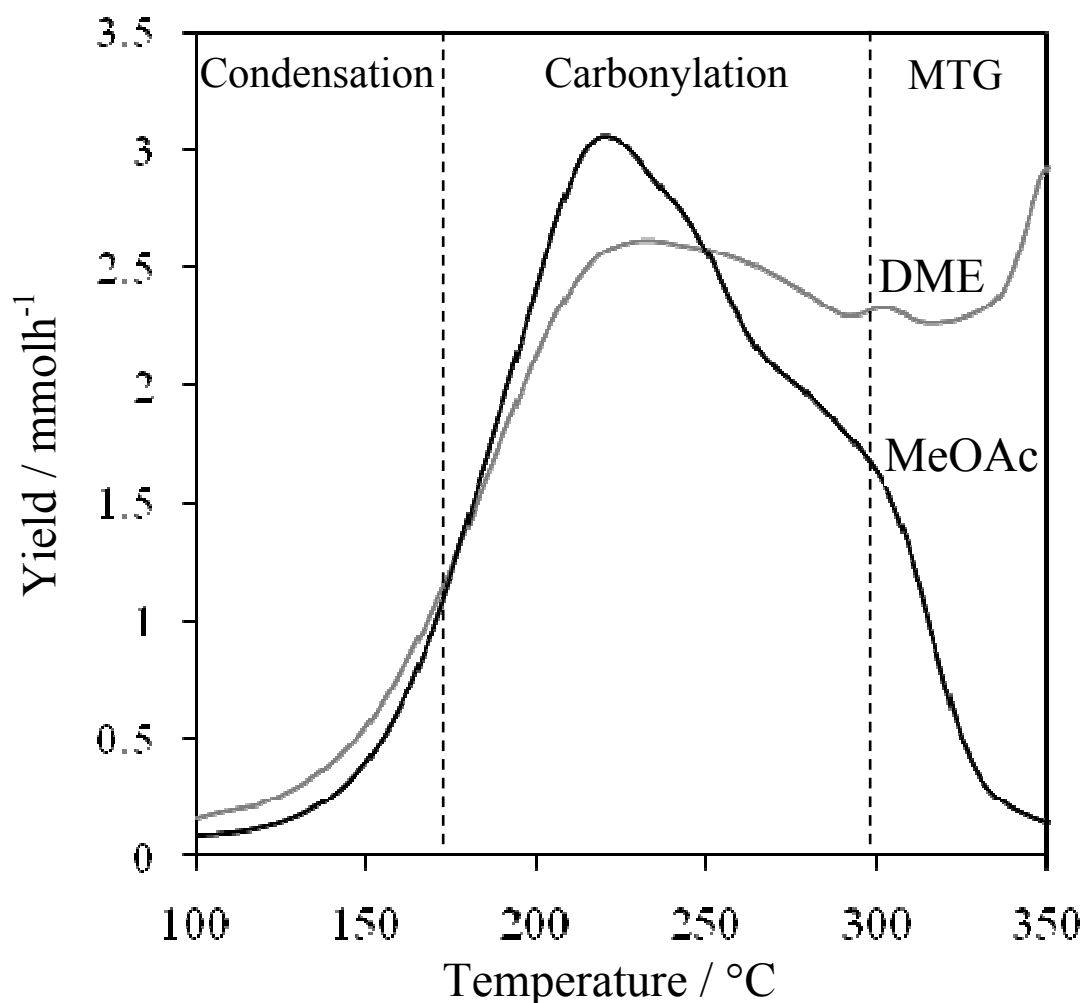


Figure 4.3.2: Light-off between 100 and 350 °C showing product distributions during methanol carbonylation over **RhXHPW1:1-SiO₂** (Rh : HPW = 1 : 1; HPW 50 %), (where acetyls = methyl acetate and acetic acid).

In contrast to 'RhPW₁₂O₄₀-SiO₂' catalysts prepared *via* ion-exchange of HPW with a Rh(III) precursor,¹⁸ **RhXHPW1:1-SiO₂** also exhibits good catalytic activity towards DME carbonylation (and at a higher GHSV), achieving 59 % conversion using a 1 : 7 DME : CO mix at 200 °C over 4 hours (**Figure 4.3.3**), with 55 % converted to acetyls and only 4 % to MeOH. Despite the expected drop in conversion with increasing DME concentration, the methyl acetate to methanol product ratio remained > 9 : 1.

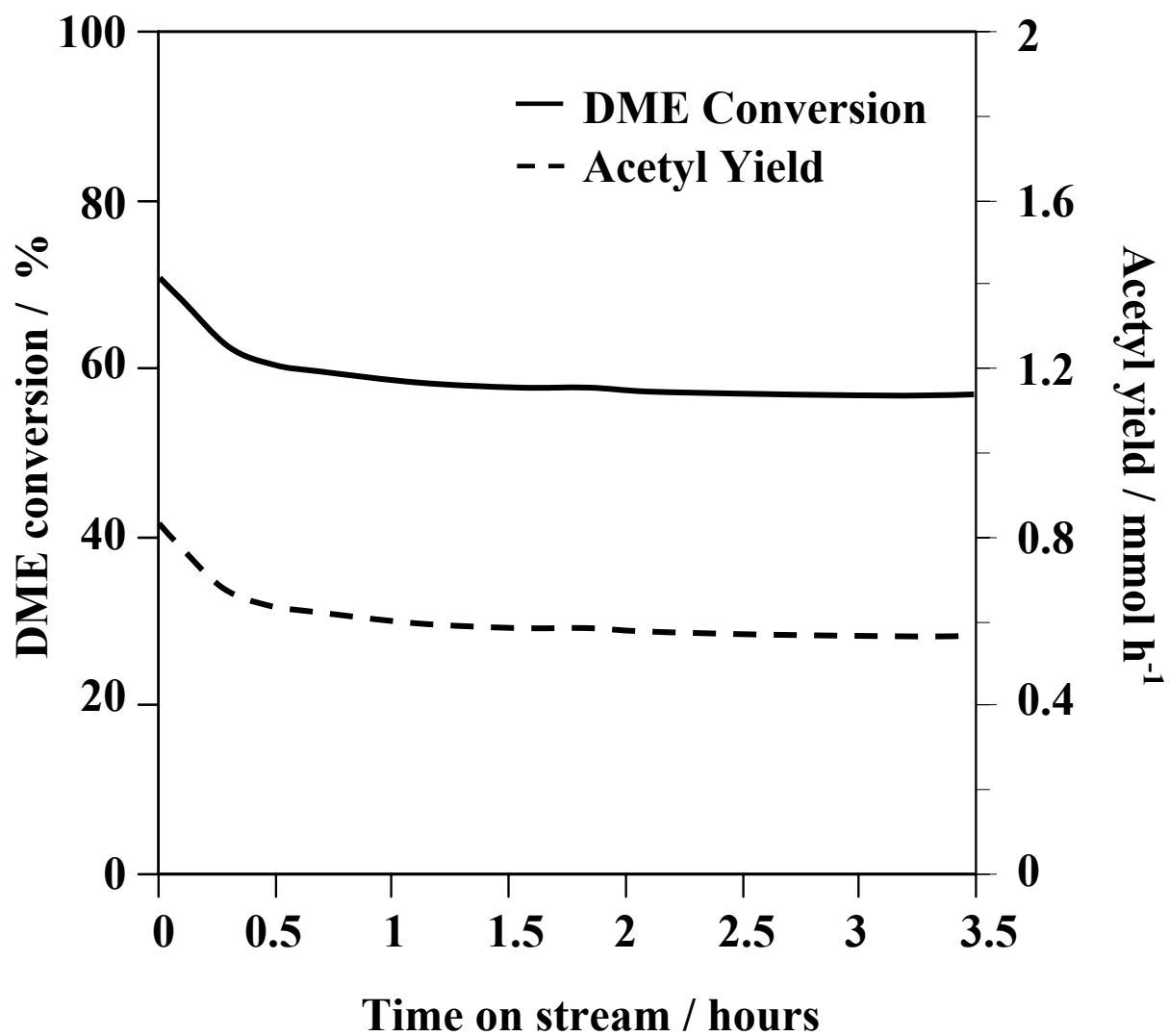


Figure 4.3.3: DME reaction profile of **RhXHPW1:1-SiO₂** at 200 °C showing conversion to acetyls and acetyl yield over 3.5 hours on stream DME : CO = 1 : 7.

4.4 - Catalyst deactivation studies

Stability of the **RhXHPW1:1-SiO₂** catalyst was subsequently assessed by monitoring its time-dependent reactivity at both 200 °C (where peak acetyl production occurs during light-off) and at 250 °C (on the threshold for MTG chemistry). **Figure 4.4.1** shows the evolving MeOH conversion and acetyl selectivity during the first 2 h on-stream. At both temperatures, rapid initial deactivation occurs over the first 15 minutes of reaction, however this is much more severe at 250 °C, for which MeOH conversion falls by 40 %, compared with a drop of only 13 % at the lower temperature. The steady state activity is also better at 200 °C, and in longer test runs 25 % methanol conversion is maintained,

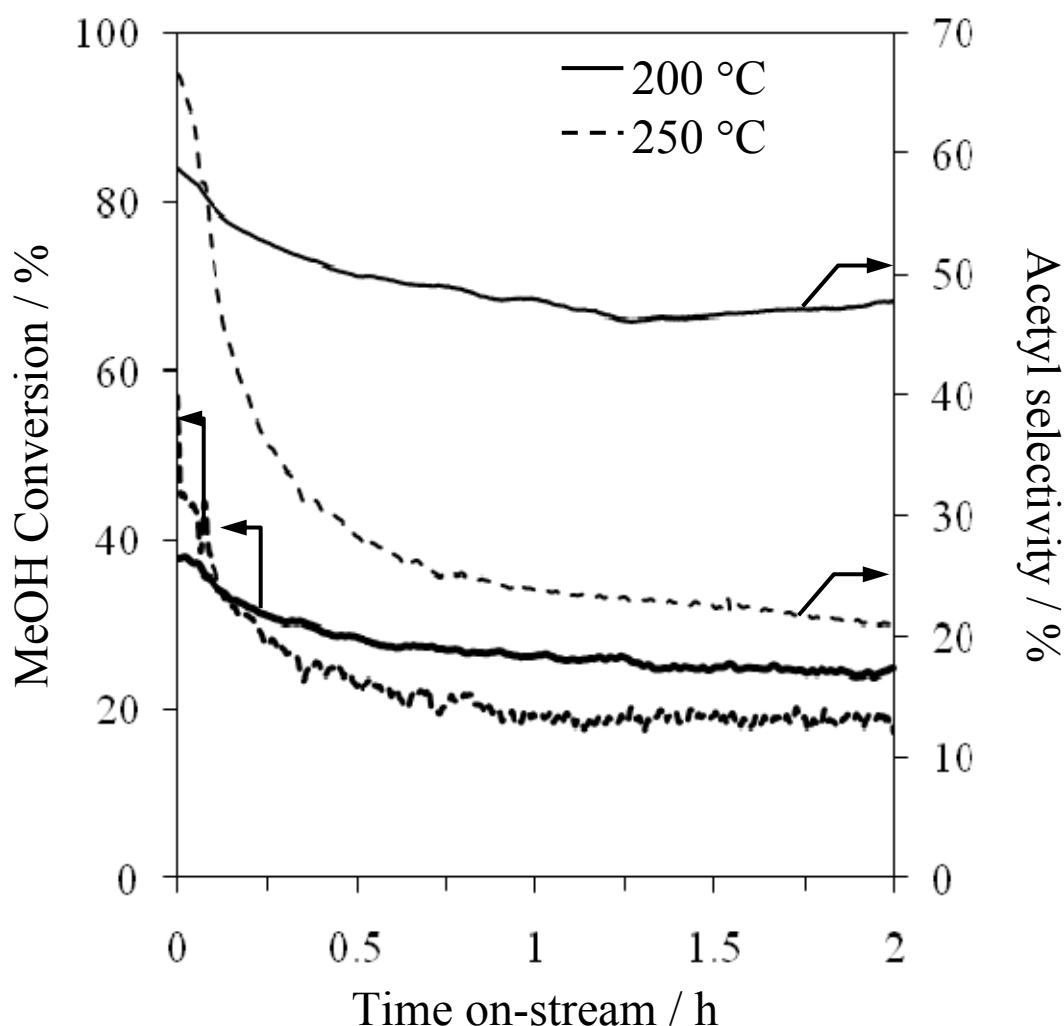


Figure 4.4.1: Methanol conversion and acetyl selectivity of in methanol carbonylation over **RhXHPW1:1-SiO₂** showing superior stability at 200 °C compared to operation at 250 °C.

for in excess of 5 h. Similar temperature- dependent deactivation is reported during methanol carbonylation over ion-exchanged Rh heteropolyacids.¹⁸ The acetyl selectivity observed mirrors these changes decreasing precipitously at 250 °C from 66 % to only 20 % within the same period, with a much smaller decrease observed at 200 °C for which **RhXHPW1:1-SiO₂** remains almost 50 % selective to methyl acetate for the 5 hour duration of the study. There are three distinct explanations for this deactivation: loss of CO binding through decomposition of the cationic Rh complex; loss of acidity from the HPW component; or morphological changes resulting in a lower surface area or accessibility of both active centres. Each possible process is considered in turn here.

Thermal analysis indicates the **RhXantphos** complex and **RhXHPW** ionic compound are stable to 300 °C under helium. However, the reducing environment employed in reactor tests could facilitate the formation of rhodium metal, and associated loss of the positive synergic interaction with HPW anions, which would be particularly detrimental to acetyl selectivity more so than conversion. *In-situ* Rh K-edge XANES spectra of the **RhXHPW1:1-SiO₂** catalysts were therefore acquired as a function of time under a highly reducing CO/He flow at 250 °C. The Rh(I) content, derived by least squares fitting of the normalised XANES to Rh metal, Rh(η^2 -acac)(CO)₂ and RhCl₃ standards, shows a steep fall during the first 15 minutes from ~ 75 to 55 %, Rh(I) mirroring the falling acetyl yield (**Figure 4.4.2**). Hence, the [Rh(CO)(Xantphos)]⁺ component appears readily reducible, with barely half of the Rh remaining ligated after one hour at 250 °C. TPO and TGA studies of the **RhXHPW1:1-SiO₂** catalyst on short exposure (2 mins) to methanol carbonylation conditions and for 2.5 hours on stream at 200 °C, were subject to thermal analysis. Differential scanning calorimetry of the resulting post reactor samples are shown in **Figure 4.4.3**. It is clear that the catalyst does encounter a small loss in thermal stability which increases with time on stream. This loss in stability may account for the formation of catalytic intermediates (discussed in more detail in Section 4. 10) but does not fall below ~ 350 °C. This indicates the suitability of the catalyst for recycle under low temperature conditions. Further insight into the nature of the species present in the spent catalyst arises from TPO studies of the short-exposure sample which reduces the decomposition temperature in accordance with the prolonged-exposure sample.

This is in accordance with the loss of an endotherm at 190 °C and exotherm at ~ 290 °C consistent with that expected for HPW crystalline methanol and HPW bound methoxy species respectively.⁴³ This may be indicative of the formation of Rh complex functionalities of higher oxidation states analogous to those intermediates observed in classic Monsanto type carbonylation chemistries.⁴⁴ Thermal evolution of lower temperature species evident for the sample treated to 350 °C is indicative of Rh-Xantphos destabilisation consistent with *in-situ* Rh reduction studies shown in **Figure 4.4.2**.

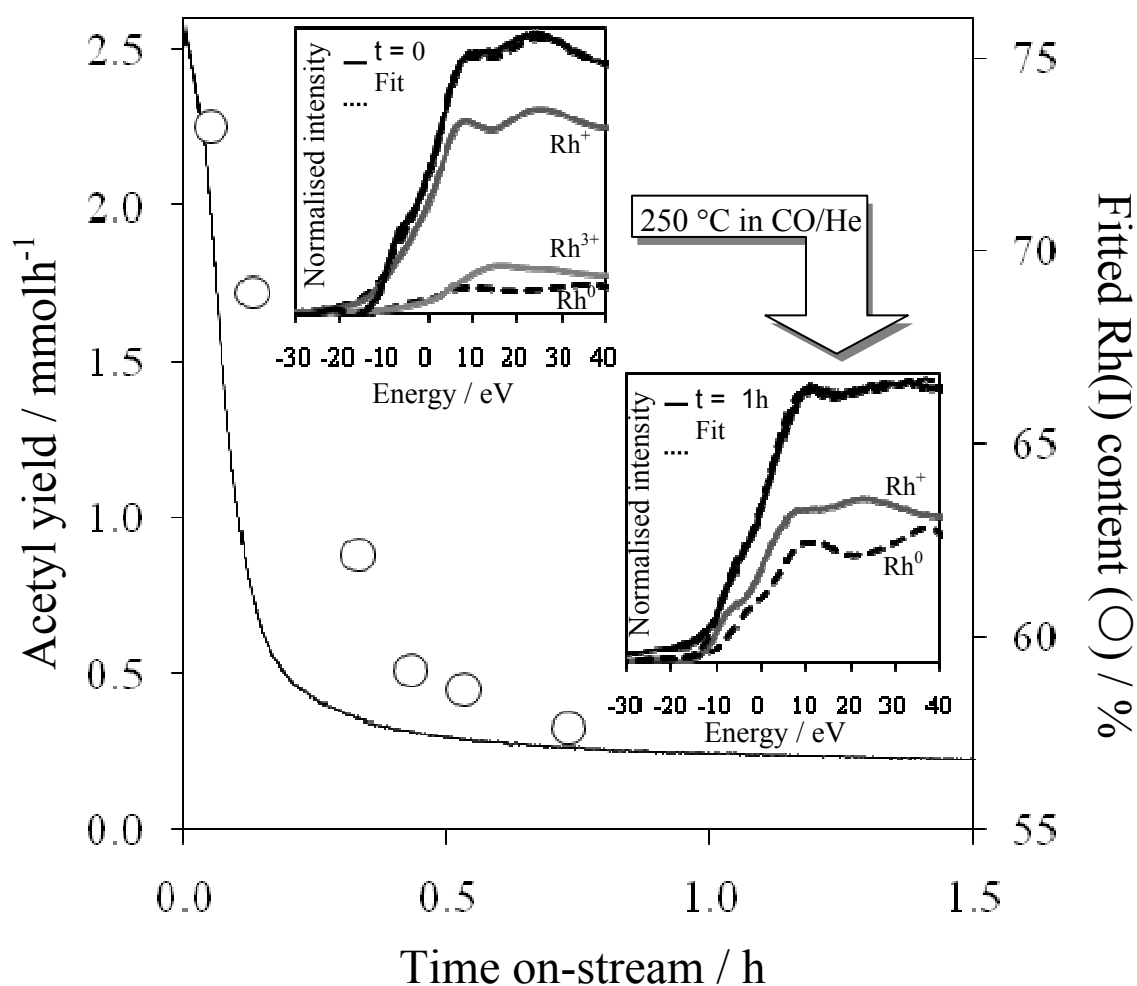


Figure 4.4.2: Comparison deactivation of **RhXHPW1:1-SiO₂** at 250 °C during methanol carbonylation with reduction in Rh (I) content as determined by *in-situ* XANES.

Although this reduction is disappointing from an application perspective, it should be noted that **RhXHPW1:1-SiO₂** catalyst is much more robust than simpler Rh(OAc)₂ or RhCl₃ complexes, which are fully reduced over this

timescale under the same experiment protocol.²⁷ This close temporal correspondence between oxidation state and reactivity strongly implicates Rh reduction in the isothermal deactivation apparent in **Figure 4.4.1**.

As noted above, although Rh decomplexation would disfavour selective carbonylation chemistry, it is not obvious that this should affect the intrinsic acidity, and therefore activity, of the HPW component. The parallel drop in MeOH conversion with selectivity therefore suggests rhodium reduction is accompanied by the loss of acid sites, possibly due to coking or dehydration.⁴⁵

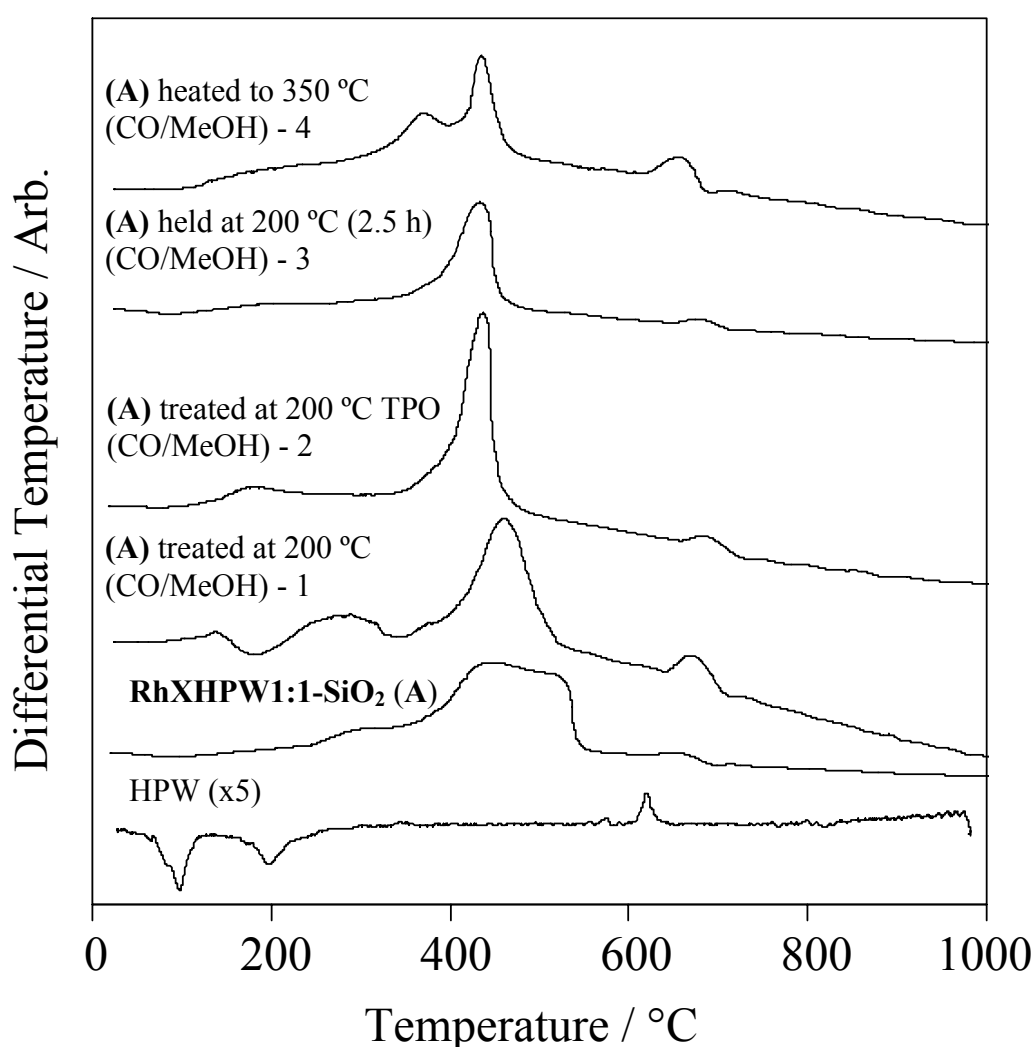


Figure 4.4.3: DSC plots showing thermal evolution of fresh HPW and **RhXHPW1:1-SiO₂** compared with **RhXHPW1:1-SiO₂** ramped to 200 °C under carbonylation condition and cooled under He - **1**, (He), **2**, (20 % O₂/He) and ramped to 200 °C under carbonylation condition, held for 2.5 h and cooled under He - **3** (He) as well as ramped to 350 °C under carbonylation conditions - **4** (He) Showing the effects of time and temperature on catalyst stability.

The latter may occur via hydrolysis of the desired methyl acetate product to acetic acid and methanol. In order to study whether product self-poisoning was involved in deactivation of the **RhXHPW1:1-SiO₂** catalyst, a fresh sample was pre-treated with MeOAc at 200 °C for 20 minutes prior to exposure to the standard MeOH/CO carbonylation mixture. **Figure 4.4.4** compares the resulting carbonylation performance with that for a fresh catalyst simply held at reaction temperature under He for the same period. Under standard conditions the acetyl yield decays from $\sim 2 \text{ mmolh}^{-1}$ (i.e. $400 \text{ mmolh}^{-1} \text{g}_{\text{Rh}}^{-1}$) to a plateau of 0.55 mmolh^{-1} , however the MeOAc pretreatment completely suppresses this initial high activity phase, apparently transforming the **RhXHPW1:1-SiO₂** into the same low activity state Inset to **Figure 4.4.4** clearly shows MeOAc triggers a rapid burst of

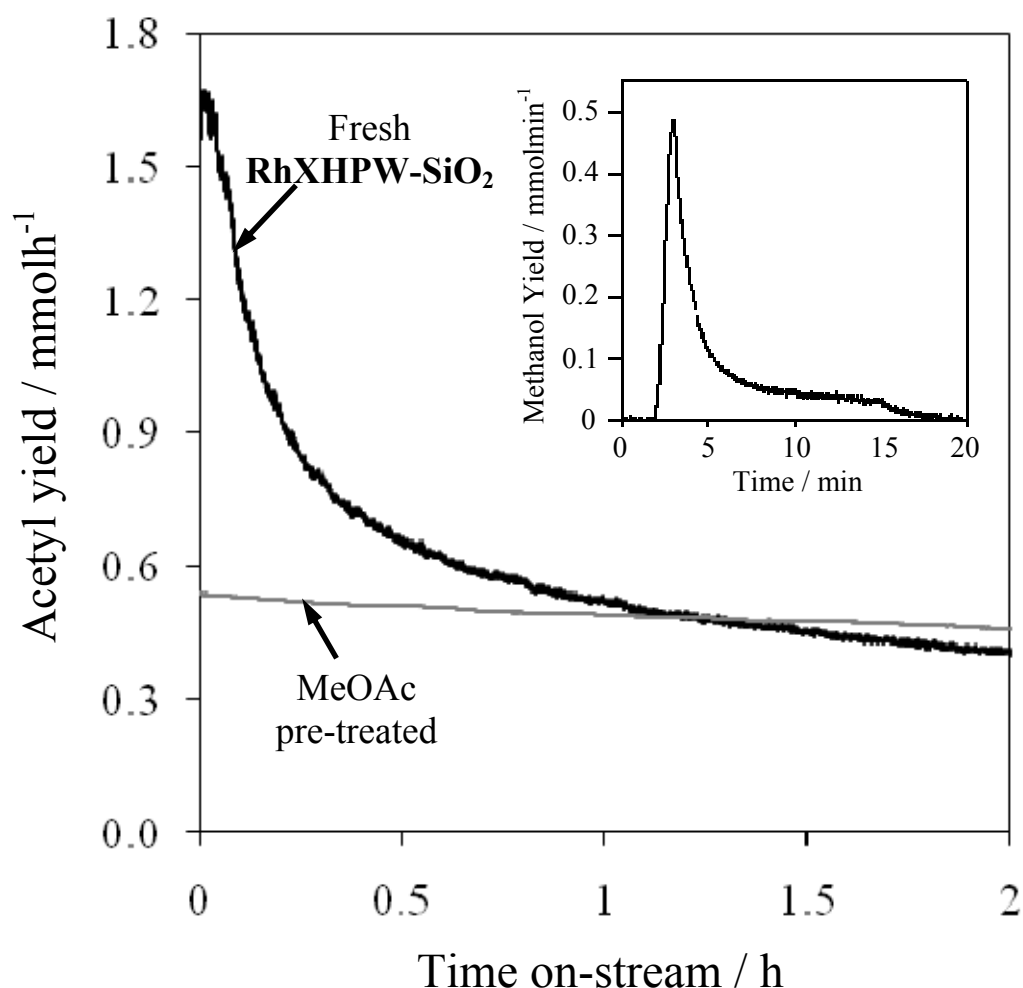


Figure 4.4.4: Effect of methyl acetate (MeOAc) pre-treatment on acetyl yield of **RhXHPW1:1-SiO₂** showing loss of initial high acetyl yield with a constant 0.55 mmolh^{-1} over 2 hours on-stream. Inset: methanol yield during pre-treatment step showing methanol generated from ester hydrolysis of MeOAc.

reactively-formed methanol, from ester hydrolysis implicating catalyst dehydration and not coking as a contributor to the deactivation seen in **Figure 4.4.1**. Indeed, the integrated yield of this MeOH usually only attained after 2 h reaction. Since this MeOAc-induced deactivation could reflect either coking or the loss of crystalline water from the vicinity of HPW Keggin units (and therefore acidity) due to hydrolysis, the gas phase methanol concentration was closely monitored during acetate introduction. The spike of methanol formed can be integrated, this totals 0.12 mmols, close to the theoretical maximum 0.17 mmol of crystalline H₂O molecules available within the catalyst charge, suggesting that high local acetyl concentrations could destroy **RhXHPW1:1-SiO₂** solid acidity under reaction conditions. This hypothesis is supported by the result of co-feeding 5 mol % H₂O during a standard 200 °C isothermal carbonylation experiment over **RhXHPW1:1-SiO₂**. **Figure 4.4.5** reveals that water addition triples initial acetyl production, and slows the rate of deactivation, conferring a four-fold enhancement

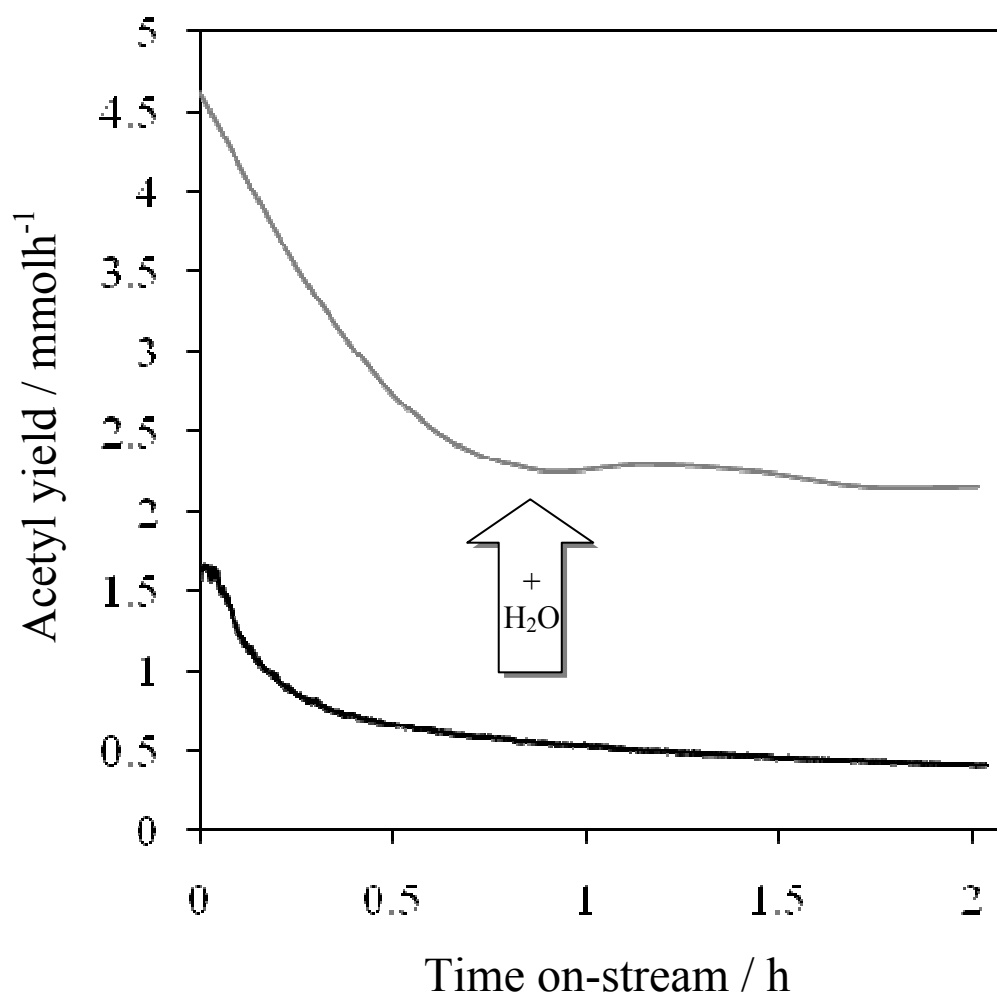


Figure 4.4.5: Effect of co-fed H₂O on methanol conversion and acetyl selectivity during carbonylation at 200 °C over **RhXHPW1:1-SiO₂** showing enhanced acetyl yield with the introduction of H₂O over 2 hours on stream.

on the steady state acetyl yield. However, the precise origin for this promotion is not clear, as water also participates in competing reactions operating during methanol carbonylation (**Scheme 4.1.1**); for example, H₂O addition may shift the MeOH condensation equilibria away from DME, thus increasing overall selectivity to MeOAc. Porosimetry on fresh and spent catalysts showed no evidence for morphology changes under reaction conditions, with the surface area only exhibiting a marginal drop from 115 m²g⁻¹ to 102 m²g⁻¹ post-reaction, and the pore volume remaining constant at 0.3 cm³ after 5 h reaction at 200 °C. Therefore processes such as crystallisation of the silica support or pore blocking by coke can be discounted as responsible for the observed deactivation.

4.5 - Cs/Ag doped RhXHPW-SiO₂

In light of the deactivation studies on **RhXHPW-SiO₂** (where Rh : HPW ratio is 0.5 : 1) an effort was made to alleviate the effects of reduction and subsequent ligand degradation. Cs(I) and Ag(I) are known to enhance the catalytic performance of heteropolyacids by substituting for some (H₅O₂)⁺ units spacing out the acidic Keggin and providing new crystallinity.^{16, 23, 46-48} This observation has shown to improve catalyst stability by either preventing re-dispersion of HPW or tuning acid strength.³⁴ Separating the Keggin and ionically associated {Rh(CO)(Xantphos)}⁺ cationic complexes, was intended to reduce the opportunity for Rh agglomeration and deter particulate Rh(0) from forming on the silica surface. Studies by BP Chemicals on Cs(I) and Ag(I) doping of Rh exchanged HPW systems have shown most promising effects arising from silica supported materials being doped with 0.05 % Cs(I) and Ag(I). This formulation was employed and materials synthesized as described in Section 2.3.4.

Doping this system with Cs(I) and Ag(I) was hypothesized to separate individual bifunctional **RhXHPW** units while retaining the stability of the intimate interaction between Rh and HPW toward sustained methanol carbonylation. An increase in surface area and pore volume (130 m²g⁻¹ and 0.53 m²g⁻¹ respectively, **Table 4.5.1**) is consistent with improved dispersion of the HPW for better surface coverage and relatively less catalyst in the silica pores.

Table 4.5.1: Porosimetry analysis of silica supported **RhXHPWs**

Sample	BET surface area m ² g ⁻¹	BJH pore radius Å	Pore volume cm ⁻³ g ⁻¹
Davisil-100 silica	324	65	1.18
RhXHPW-SiO₂	109	69	0.41
Cs/Ag RhXHPW-SiO₂	130	65	0.53

XPS elemental composition analysis of the doped samples provides a 1Rh : 12W stoichiometry consistent with 1 {Rh(CO)(Xantphos)}⁺ species per Keggin at the surface (**Table 4.5.2**). Comparison of the silica at the surface reveals that the

doped analogue exhibits much lower exposure. This is consistent with the hypothesis that the HPW would have a greater coverage with dopant metals. (Note: Cs was not observed in the XPS expected from low loading (expected 0.01 atoms per Keggin)), The presence of the Keggin packing effect observed for Cs doped HPW was confirmed by characteristic Cs-Keggin phases observed in powder XRD (**Figure 4.5.2**) where a second ‘CsHPW’ phase observed with peaks shifted by ca. 0.6 ° (**D**) observed for Cs and similar systems in the literature.⁴⁹

Table 4.5.2: Stoichiometry based on XPS atom % of un-doped and Cs/Ag doped **RhXHPW-SiO₂**

Element	RhXHPW-SiO₂	Cs/Ag-RhXHPW-SiO₂
Rh	1	1
P	1	1
W	12	12
O	769	308
C	161	76
Si	277	112
Ag	-	1

Calculated relative to 12W \equiv 1 Keggin

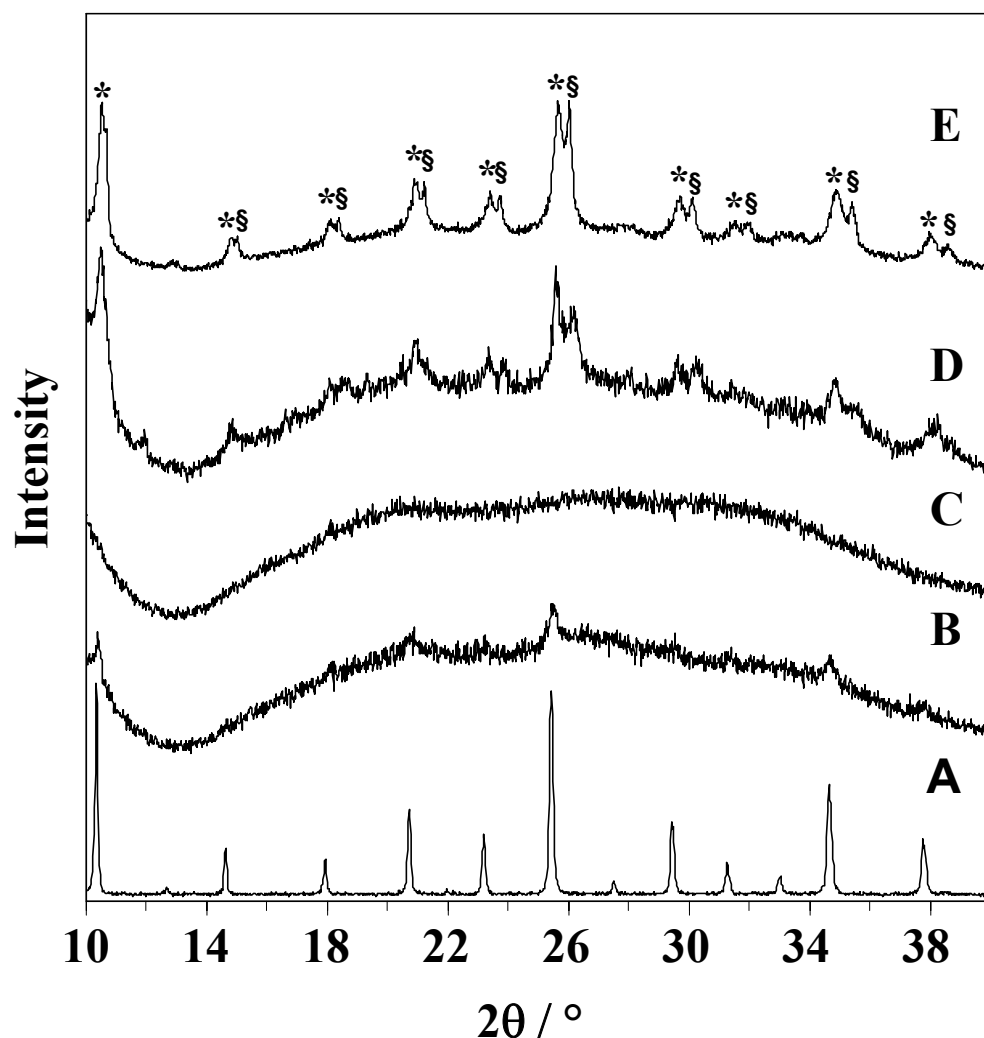


Figure 4.5.2: Powder XRD pattern showing dopant effect on crystallinity; **A** HPW, **B** HPW-SiO₂, **C** RhXHPW-SiO₂, **D** Cs/Ag-RhHPW-SiO₂, **E** Cs/Ag-HPW-SiO₂ *denotes the crystalline HPW phase and § indicates cation-exchanged crystal phase.

The doped RhXHPW-SiO₂ was tested for activity in methanol carbonylation at 250 °C to identify any potential improvements in stability to reduction over the un-doped system. Cs/Ag-RhXHPW-SiO₂ showed comparable activity in methanol conversion to HPW-SiO₂ (**Figure 4.5.3**) with the majority of methanol being converted to DME indicated by loss in initial acetyl selectivity (10 %). After 3.5 hours on stream, acetyl selectivity drops to 5 % whereas MeOH conversion remains constant at ~ 85 %. This implies that although the affects of the dopants have a beneficial effect on HPW loss in Rh stability and subsequent catalyst deactivation towards methanol carbonylation still occurs.

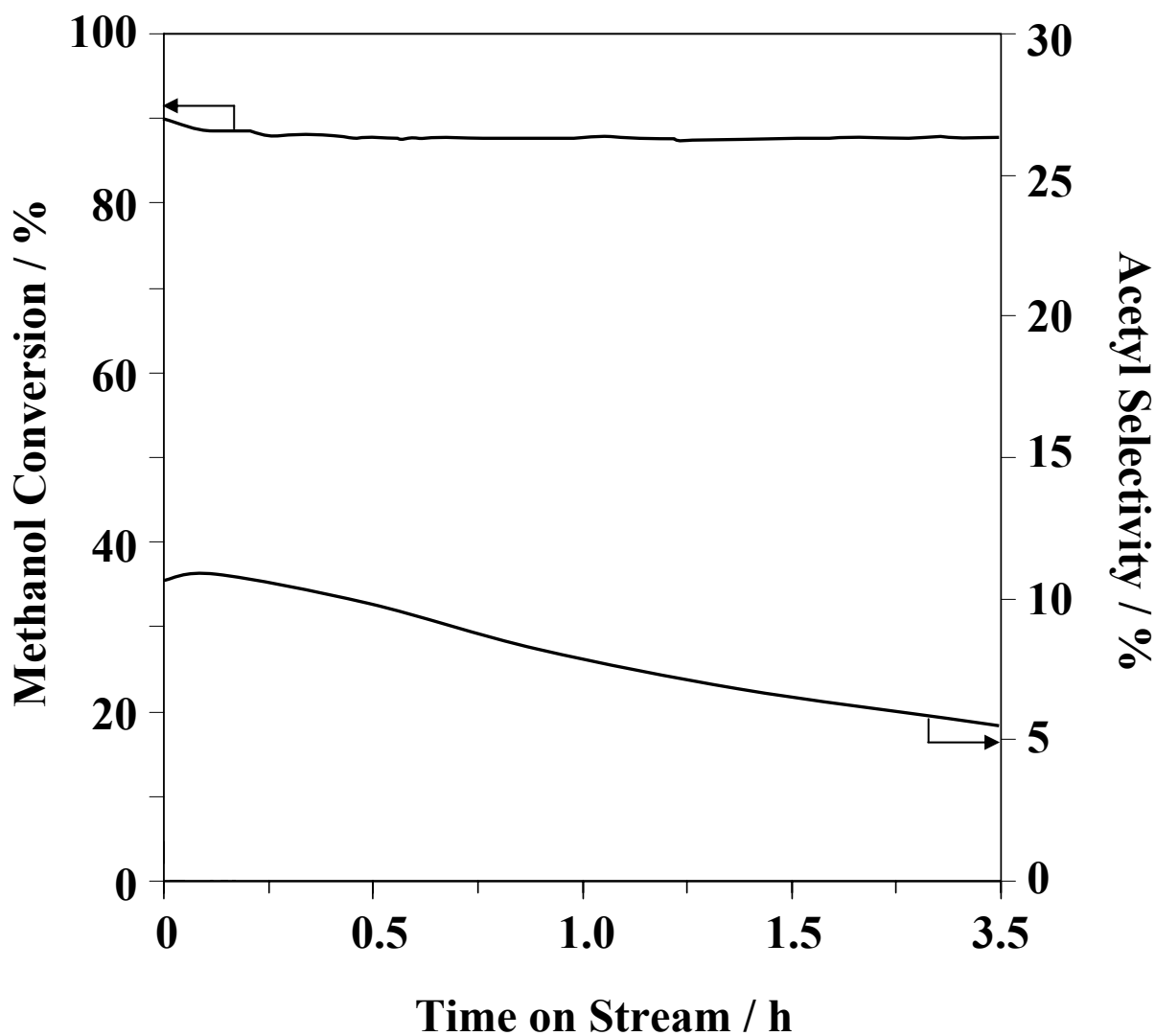


Figure 4.5.3: Methanol conversion and MeOAc production over total carbon-oxygenates for **Cs/Ag-RhXHPW-SiO₂** held at 250 °C for 2 hours under methanol carbonylation conditions.

The Rh K-edge of the post reactor catalyst was examined using XANES spectroscopy (**Figure 4.5.4**). Samples taken from spent **Cs/Ag-RhXHPW-SiO₂** used at 250 °C and also at 350 °C showed partial reduction to Rh(0). Linear combination fits to Rh standards indicate a 45 % and 39 % reduction to Rh(0) for the sample treated at 250 and 350 °C respectively (**Figure 4.5.4**, inset). The growth of a Rh(0) phase correlates with loss of efficacy of the catalyst.

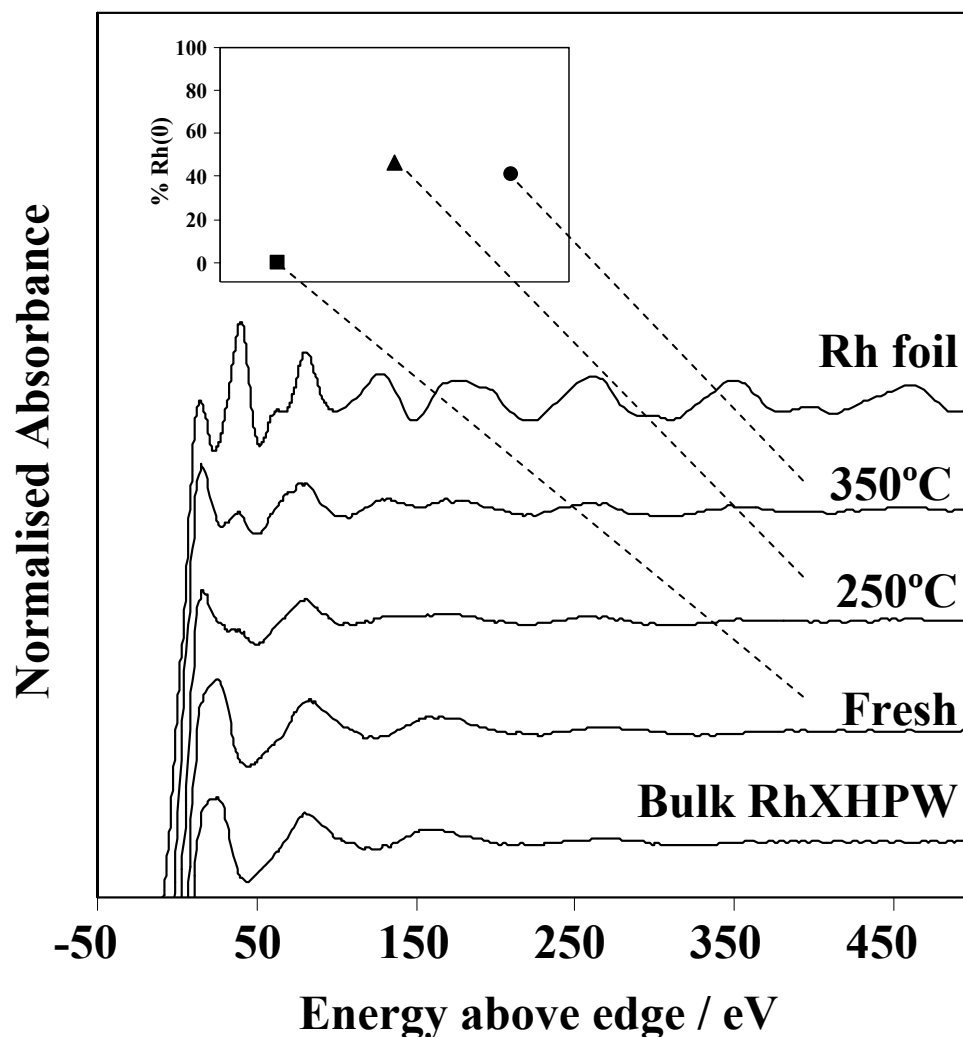


Figure 4.5.4: *Ex-situ* Rh K-edge XANES profiles of fresh bulk and silica supported **RhXHPW** compared to spent catalysts ramped to 250 °C and 350 °C showing the effect of temperature on oxidation state under methanol carbonylation conditions. Inset: linear combination fit of 1+ and 0 oxidation states showing percentage quantification of reduction to Rh(0).

Further scrutiny of the whole spectra allowed the utility of EXAFS to identify the local coordination shell of Rh in the spent catalysts (**Figure 4.5.5**, **Table 4.5.2**). A theoretical model with the expected Rh centred structure based on the closest neighbouring shells was fitted to the acquired data with the amount of Rh(0) observed from XANES linear combination fitting. This was in good agreement with that observed from shell intensity observed in the spent samples. **Figure 4.5.6** shows Fourier transformed spectra to illustrate the effects of reduction on-stream. The appearance of metallic Rh associated with the transformation of organometallic to metallic Rh can be identified by a

Table 4.5.2: Parameters for Rh K-edge EXAFS fitting of fresh and spent (250 °C and 350 °C) Cs/Ag-RhXHPW-SiO₂

Sample	CN1 Rh-C	CN2 Rh-P	CN3 Rh-Rh	CN4 Rh-Rh	R1 (Å) Rh-C	R2 (Å) Rh-P	R3 (Å) Rh-Rh	R4 (Å) Rh-Rh	σ_1 Rh-C	σ_2 Rh-P	σ_3 Rh-Rh	σ_4 Rh-Rh	R ²
Fresh	2	2	-	-	2.04	2.29	-	-	0.002	0.005	-	-	31.45
250 °C	2	2	1.23	0.61	2.13	2.39	2.68	3.79	0.002	0.040	0.006	0.023	34.01
350 °C	2	2	2.25	1.12	2.12	2.43	2.68	3.79	0.007	0.021	0.006	0.023	30.60

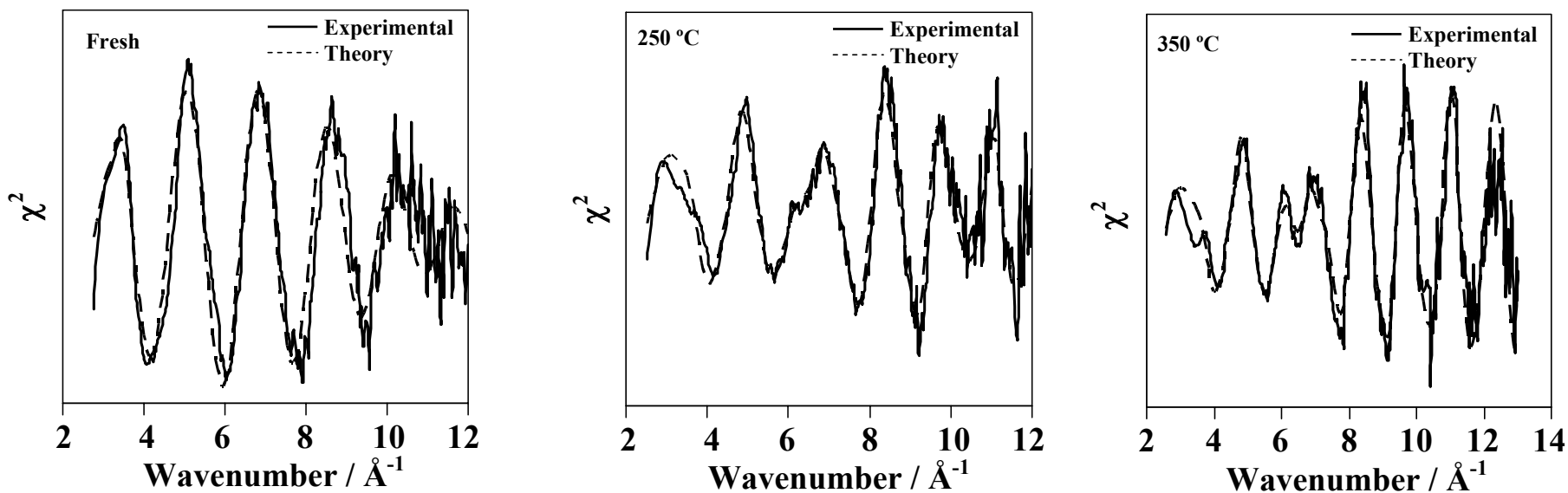


Figure 4.5.5: EXAFS for Rh K-edge χ^2 plots, experimental and theory for fresh and spent (250 °C and 350 °C) Cs/Ag-RhXHPW-SiO₂

characteristic Rh shell at 2.68 Å. This supports the observed changes in oxidation state of the bulk material and fitted Rh(0) content observed in the XANES spectra.

A lengthening of the Rh-P bond from 2.29 to 2.43 Å and Rh-C from 2.02 – 2.13 Å in the spent 350 °C catalyst supports the weakening of the metal ligand interaction in favour of Rh(0) formation. One of the objectives of adding dopants to the catalyst was to reduce the likelihood of rhodium agglomeration through formation of Rh(0) clusters. Jentys has developed a method for calculating the mean particle size of metal particles using the intensity of the first 2 metallic shells using EXAFS.⁵⁰ Calculating the mean number of atoms per particle in this study suggest a cluster size of 2.9 and 6.1 atoms per particle for 250 °C and 350 °C. These relatively small clusters do imply that although rhodium is reduced under reaction conditions, the proximity of individual Rh species in **Cs/Ag-RhXHPW-SiO₂** are far enough apart to prevent agglomeration being a contributing factor to catalyst deactivation.

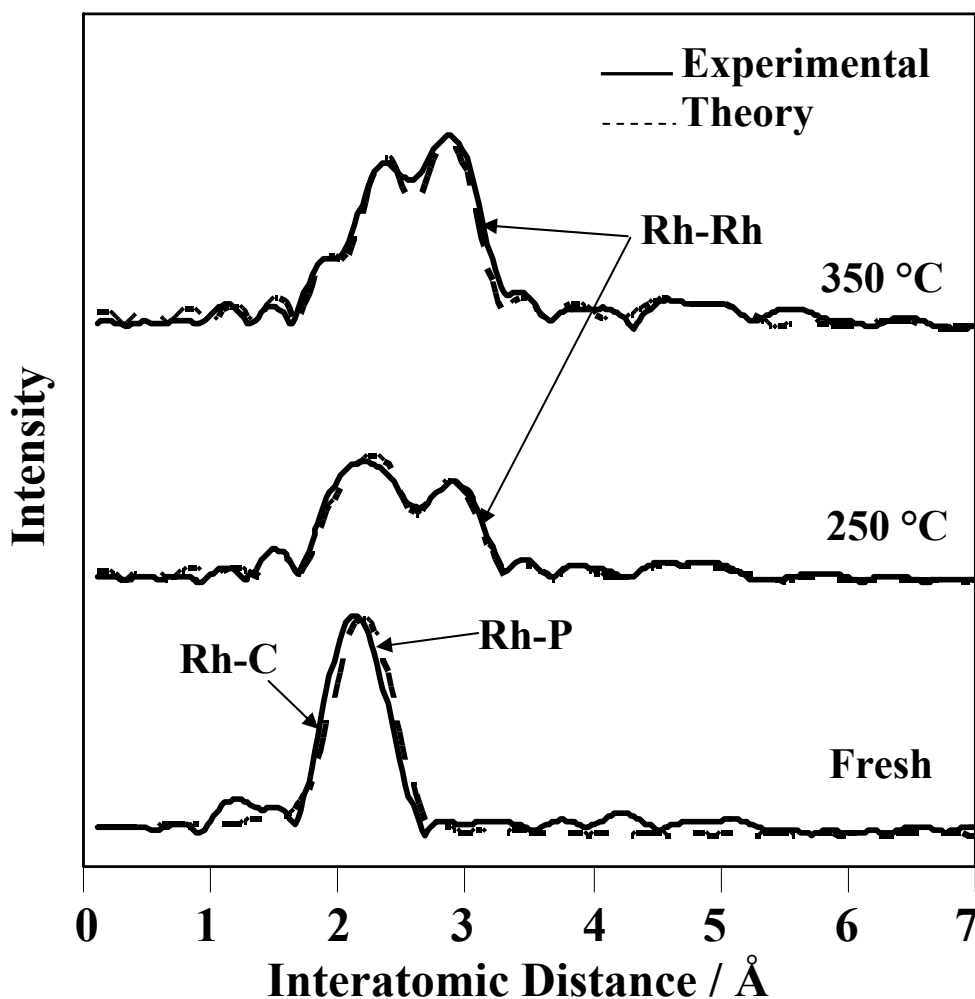


Figure 4.5.6: Fourier Transformed Rh K-edge EXAFS spectra of Cs/Ag-RhXHPW-SiO₂ catalysts showing change of closest neighbouring atomic shells after treatment under methanol carbonylation reaction conditions.

From the results of this study, Cs/Ag dopants do not appear to aid in stabilising the Rh centre to allow operation at higher temperatures. Although these doped systems show improved HPW methanol activation, this is coupled with greater selectivity to methanol condensation over methanol carbonylation with an initial acetyl yield of 0.8 mmolh⁻¹ dropping to ~ 0.4 mmolh⁻¹ after 3.5 hours on stream. Although there is greater scope of understanding of dopants on RhXHPW systems, for the purpose of this work these materials will not be considered further.

4.6 - Optimisation of catalyst composition

The ionic character of bifunctional **RhXHPW** catalysts subsequently enabled exploration of the impact of Rh:HPW ratio, and thus notionally CO binding capacity versus solid acidity, on net carbonylation performance. **RhXHPW-SiO₂** samples with Rh : HPW ratios spanning 0.5 : 1, 2 : 1 and 3 : 1 were prepared with the same 50 wt % HPW/SiO₂ precursor used to synthesise the 1:1 Rh : HPW material, showing comparable surface area properties (110 gcm⁻³, **Appendix 5**) and characteristic IR bands including a notable Rh-CO stretch at 2008 cm⁻¹ consistent with bulk **RhXHPW** (**Appendix 6**). The acidic and reactive properties of this series of supported materials were screened. Elemental analysis (Chaper 2,

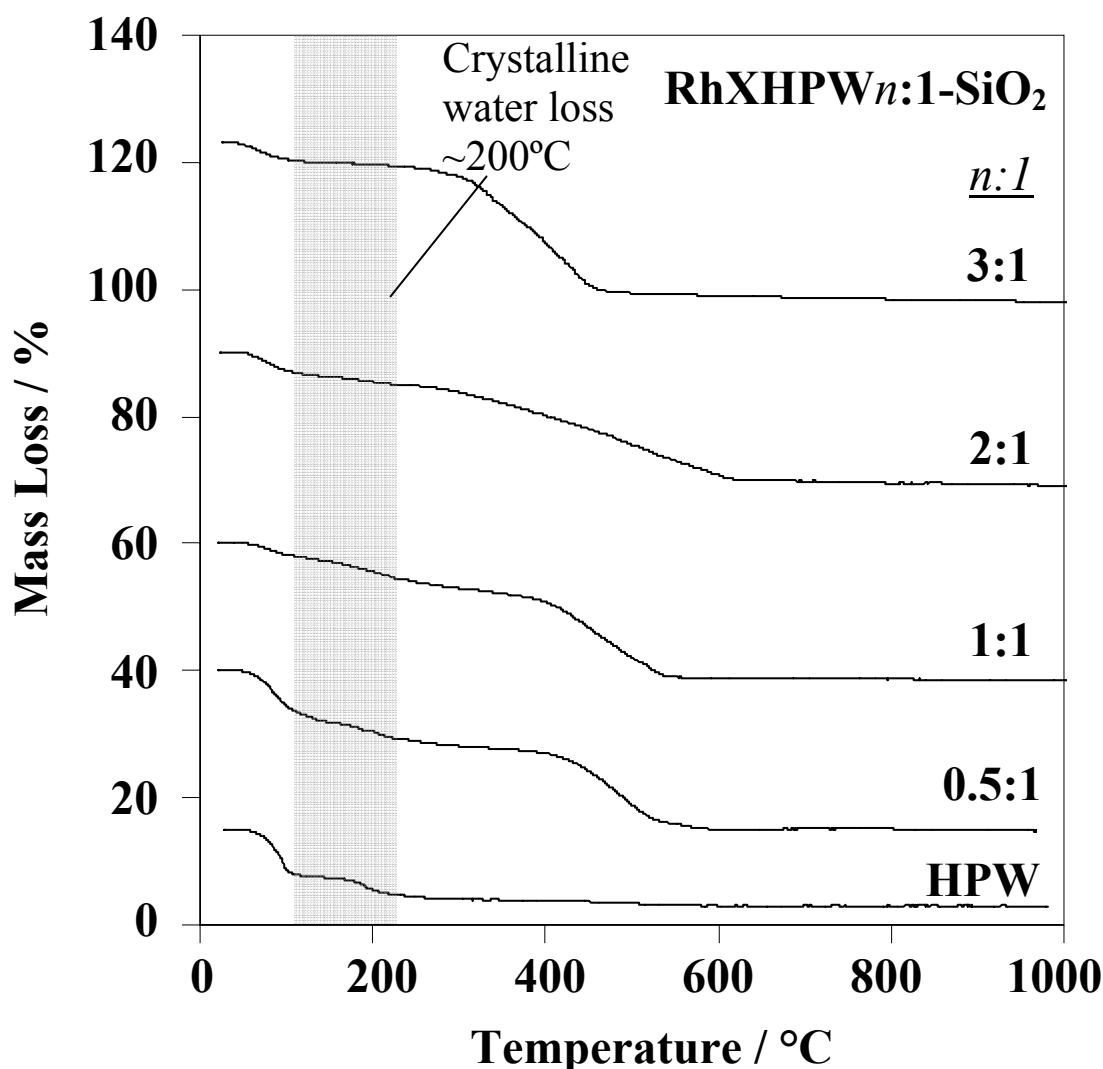


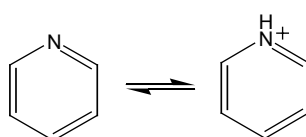
Figure 4.6.1: TGA between 20 and 1000 °C of **RhXHPW-SiO₂** series and HPW reference showing crystalline water loss between 125 and 225 °C and decomposition of Xantphos ligand at ca. 300 – 500 °C.

Table 2.3.3.1) showed the Rh : W : P stoichiometry could be carefully tuned as desired. TGA analysis (**Figure 4.6.1**) on the supported series shows a common mass loss associated with the loss of crystalline water at ca. 200 °C. Crystalline water content was normalised to the number of protons and was found to be consistent with a transition from triply protonated Rh-free precursor to a fully deprotonated **RhXHPW3:1-SiO₂** (**Table 4.6.1**) (confirming the exchange of one proton for each organorhodium cation, and thus Rh(I) oxidation state). It is worth noting here that each Keggin unit has 3 H⁺ associated with it, thus triply exchanged **RhXHPW3:1-SiO₂** should lose all acidity.

Table 4.6.1: mass % crystalline water (wt % crysH₂O) for **RhXHPW-SiO₂** series normalised to H⁺ per Keggin.

Species	H ⁺	Wt % crysH ₂ O	Normalised to protons
HPW	3	3.90	1.3
HPW-SiO ₂	3	4.90	1.6
RhXHPW 0.5:1-SiO₂	2.5	3.99	1.6
RhXHPW 1:1-SiO₂	2	3.34	1.7
RhXHPW 2:1-SiO₂	1	1.75	1.7
RhXHPW 3:1-SiO₂	0	0.53	-

The sequential exchange of Keggin protons was explored further by examining the effects of H⁺ titration for the supported **RhXHPW** series. HPW is known to protonate pyridine providing a measure of number of acid sites and acid strength. Deprotonation of acid sites was achieved by pyridine adsorption and subsequent pyridinium ion formation (**Scheme 4.6.1**). Pyridinium provides a group of characteristic IR bands (**Table 4.6.2**) which are observed in the case of HPW, denoted as **A**, **B**, **C** and **D** in **Figure 4.6.2**. For the **RhXHPW-SiO₂** series the DRIFTS band ‘**B**’ is used to track the pyridinium ion intensity at 1540 cm⁻¹ (**Figure 4.6.3**), characteristic of Brønsted surface acid sites. A correlation is



Scheme 4.6.1: pyridine acidic equilibrium with pyridinium ion

Table 4.6.1: Pyridinium absorption IR bands⁵¹

pyridinium ion (Brønsted site)
1485-1500 cm ⁻¹ (<i>Band A</i>)
1540 cm ⁻¹ (<i>Band B</i>)
1620 cm ⁻¹ (<i>Band C</i>)
1640 cm ⁻¹ (<i>Band D</i>)

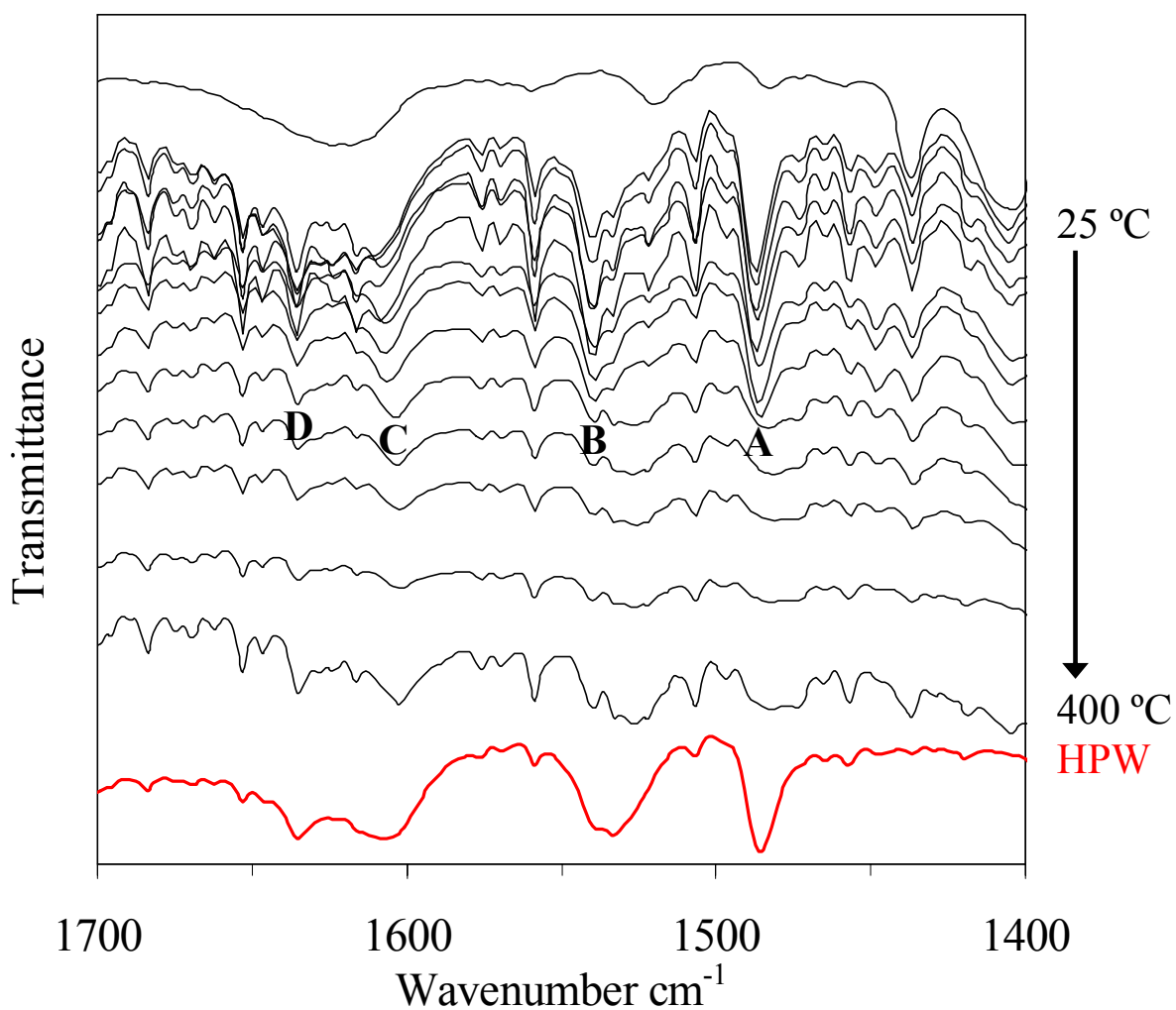


Figure 4.6.2: DRIFTS spectra between 1400 and 1700 cm⁻¹ of temperature controlled pyridinium dissociation from **RhXHPW1:1-SiO₂** between 25 and 400 °C indicative of Brønsted acidity, (pure HPW is shown for reference). Bands **A**, **B**, **C** and **D** are characteristic of surface bound pyridinium (see **Table 4.6.1**)

observed with progressive loss in **RhXHPW-SiO₂** acidity. Pyridinium intensity decreases monotonically with increasing Rh content with the **RhXHPW3:1-SiO₂** losing all Brønsted acidity. This is consistent with TGA studies and the H⁺ ion exchange hypothesis of Rh(I) species.

The corresponding reactivity of this **RhXHPW-SiO₂** series was assessed during 5 h isothermal carbonylation at 200 °C (**Figures 4.6.4 a, b**), the optimal temperature for the **Rh:HPW1:1-SiO₂** catalyst where methanol to gasoline chemistry does not take place. **Figure 4.6.5** shows the resulting MeOH conversion, and acetyl selectivity/yield is strongly influenced by the balance of

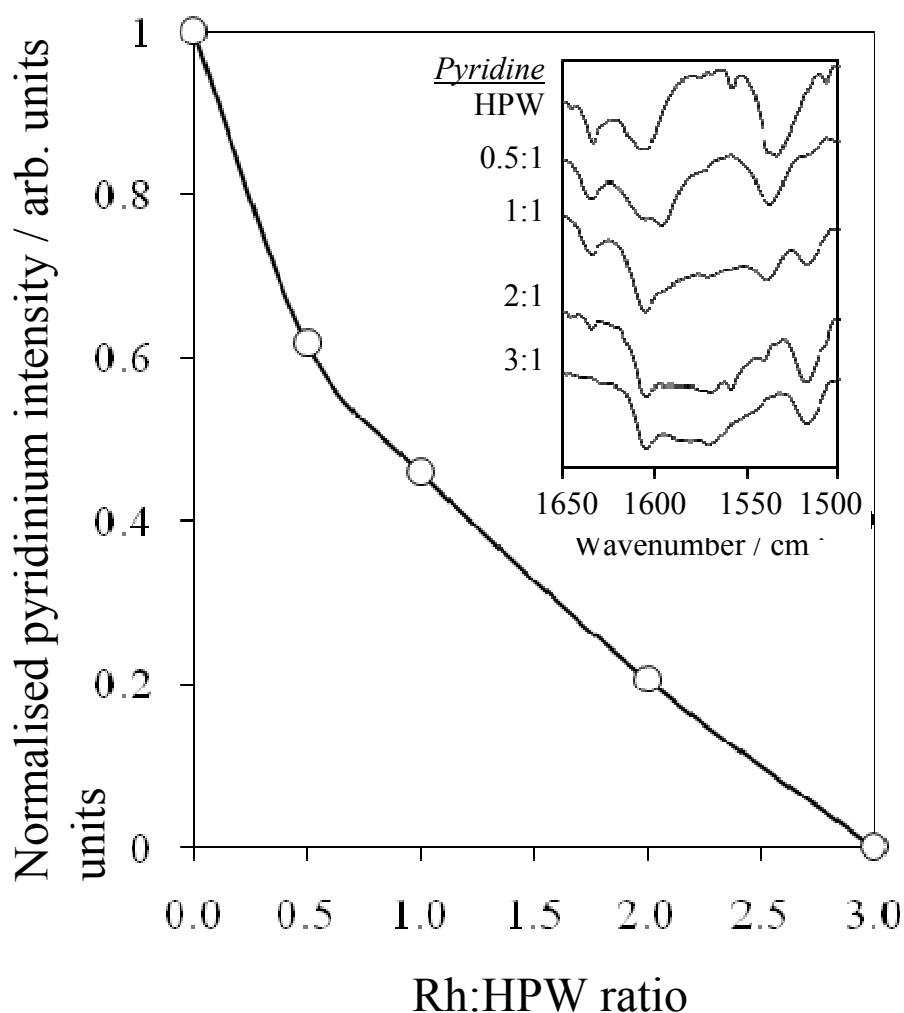


Figure 4.6.3: Influence of Rh content on DRIFTS-derived pyridinium ion intensity at 1540 cm⁻¹ for **RhXHPW1:1-SiO₂**; pyridinium signals have been normalised relative to the 3 protons expected for the parent H₃PW₁₂O₄₀. Inset shows associated DRIFTS spectra with principal pyridinium ion bands highlighted.

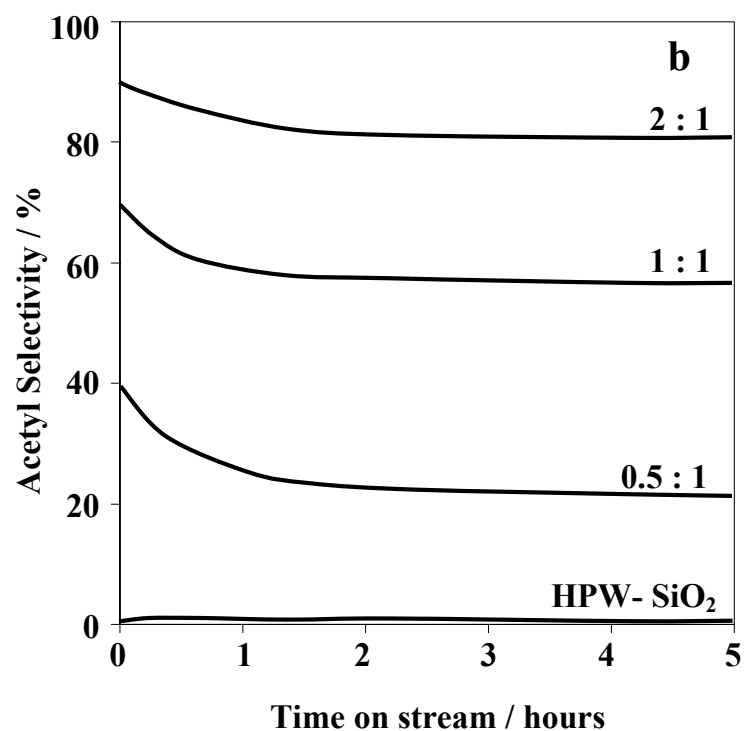
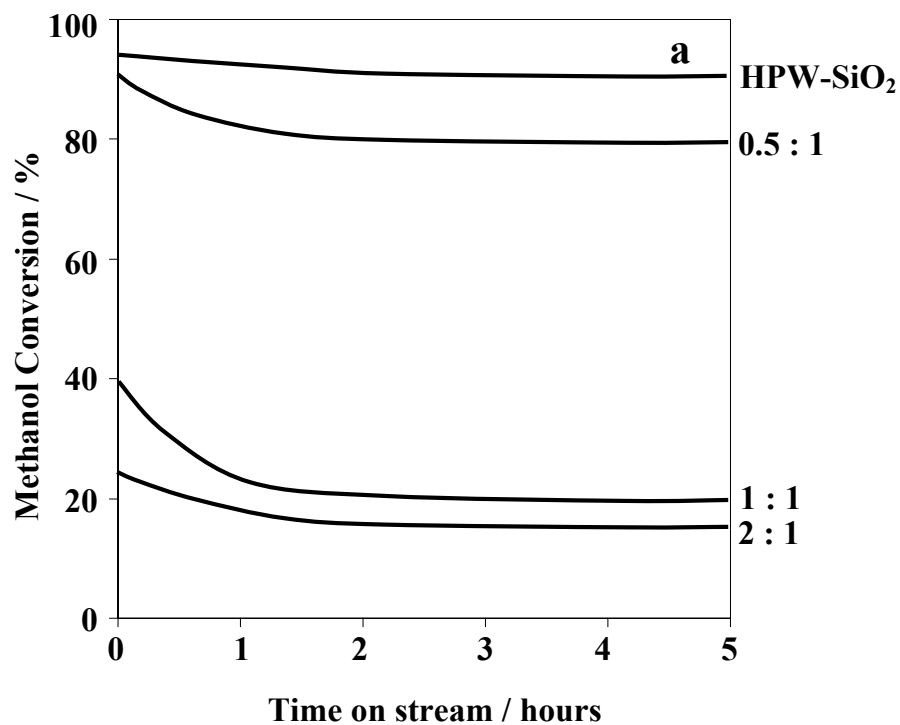


Figure 4.6.4: Reaction profiles of **RhXHPW-SiO₂** series with 0 (HPW-SiO₂), 0.5, 1, 2 Rh's per HPW denoted as 'x : 1', over 5 hours on stream. **a**, methanol conversion **b**, selectivity to acetyls where acetyls are (methyl acetate and acetic acid).

catalyst components. Rh addition enhances acetyl selectivity, as anticipated if the organorhodium complex provides sites for CO activation, at the expense of acid sites required for methanol activation. This balance between the CO affinity and solid acidity of **RhXHPW-SiO₂** produces a volcano dependence on rhodium concentration, with a maximum steady state acetyl yield of 1.5 mmolh⁻¹ for Rh : HPW = 0.5 : 1. Since the peak acetyl yield occurs at a low level of Rh exchange it is likely that carbonylation is limited by CH₃⁺ availability, which in turn may reflect rapid CH₃⁺ consumption via the competing DME condensation pathway. An alternative possibility is that DME itself plays a role in the carbonylation reaction, with low Rh contents (more acid sites) maximising DME

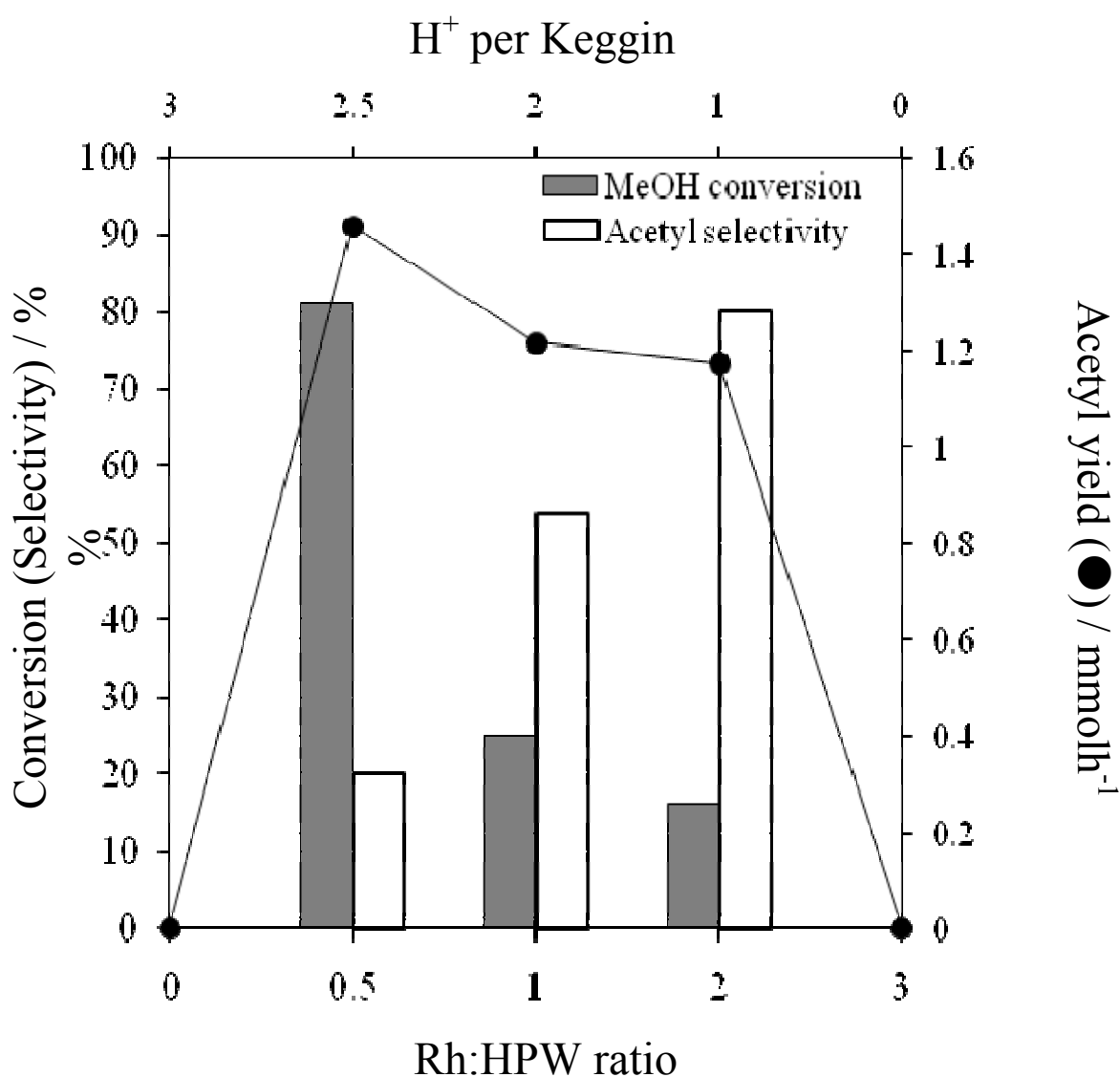


Figure 4.6.5: Influence of Rh/H⁺ content on steady state methanol conversion, acetyl selectivity and acetyl yield of **RhXHPW-SiO₂** series during methanol carbonylation at 200 °C. The total amount of Rh was kept constant at 5 mg for each catalyst. Acetyl yield is the average over 5 h on-stream where steady state is achieved.

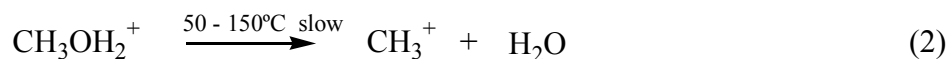
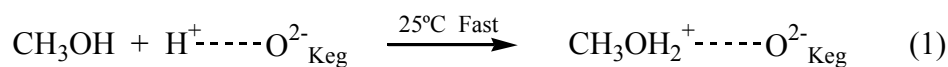
formation *via* condensation, with secondary DME carbonylation responsible for the final methyl acetate product (**RhXHPW-SiO₂** catalysts has notably shown activity for this latter step discussed in Section 4.4).

4.7 - DRIFTS study of the mechanism of methanol carbonylation

Catalytic studies earlier in the chapter have provided an understanding of the mode of catalysis that **RhXHPW** systems take in heterogeneous methanol carbonylation. At 200 °C the 2 processes which take place are methanol condensation and methanol carbonylation. A combination of *in-situ* infrared measurements and post reactor analysis is discussed here to offer an insight into the possible intermediates and hence the mechanism of action in this bifunctional system.

4.8 - Methanol condensation

The method of action of heteropolyacids in condensation of alcohols is already well understood and various examples involving methanol and propanol are provided in the literature.^{52, 53} A generally accepted process is initiated on hydrogen bonding of a MeOH molecule to a Keggin (Keg) heteropolytungstate, proposed by Moffat et al.⁵⁴ **Scheme 4.8.1** illustrates this showing the formation of a source of CH₃⁺ stabilised on the Keggin oxygen.



Scheme 4.8.1: Activation of MeOH on a heteropolyacid Keggin (Keg)

The Brønsted acidic heteropolyacid protonates the methanol forming CH₃OH₂⁺ (1). The protonated methanol associates with the Keggin (**Figure 4.8.1**) In order to generate a source of CH₃⁺ the protonated methanol must dehydrate (2). CH₃⁺ then quickly migrates to the Keggin. This process occurs both in the bulk

and surface of crystalline heteropolyacids and generally when the ratio of MeOH : heteropolyanion ≥ 3 all protons are transferred from anions to methanol.⁵⁵

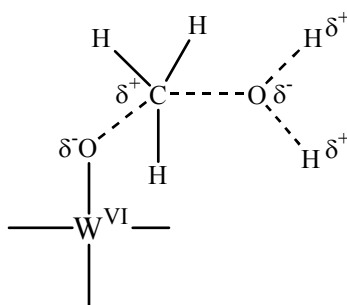


Figure 4.8.1: activated methanol on pendant oxygen of a phosphotungstate anion.

4.9 - *In-situ* DRIFTS study of methanol/HPW interactions

DRIFTS analysis of HPW was used to identify surface methoxy species in accordance with **Scheme 4.8.1**. Exposure of pure HPW to a flow of MeOH under nitrogen allowed the elucidation of several bands associated with surface bound methanol (**Figure 4.9.1**). The parent HPW spectrum was subtracted from subsequent spectra to allow changes to be observed. MeOH vapour was passed over the sample and purged with N₂ to remove physisorbed MeOH. New bands in the CH₃ region remain associated with the HPW after N₂ purge up to 250 °C, (2960, 2935, 2854, 2825 cm⁻¹) with the most intense bands at 150 °C. This is consistent with the formation of surface bound CH₃⁺ dominating ≤ 150 °C.⁴³ Admittedly these bands could either be a combination of surface bound methoxy species or methanol which has crystallised within the HPW. From earlier catalytic observations showing that DME can be activated in the presence of HPW, similar activated CH₃⁺ must be formed to yield both methyl acetate and MeOH. A sample fresh HPW was exposed to DME in the same manner described for MeOH. Strongest bands are observed at 2935 and 2825 cm⁻¹ comparable to that found in the MeOH case. As it is known that $\geq 3:1$ MeOH : HPW ratio generates complete protonation of MeOH, these dominant bands can be attributed to C-H stretches of Keggin bound methoxy species. It is worth noting here that on performing the same measurements on ion exchanged [NEt₃H]₃⁺[PW₁₂O₄₀]³⁻, no bands were observed supporting the requirement of acidity to generate methoxy species.

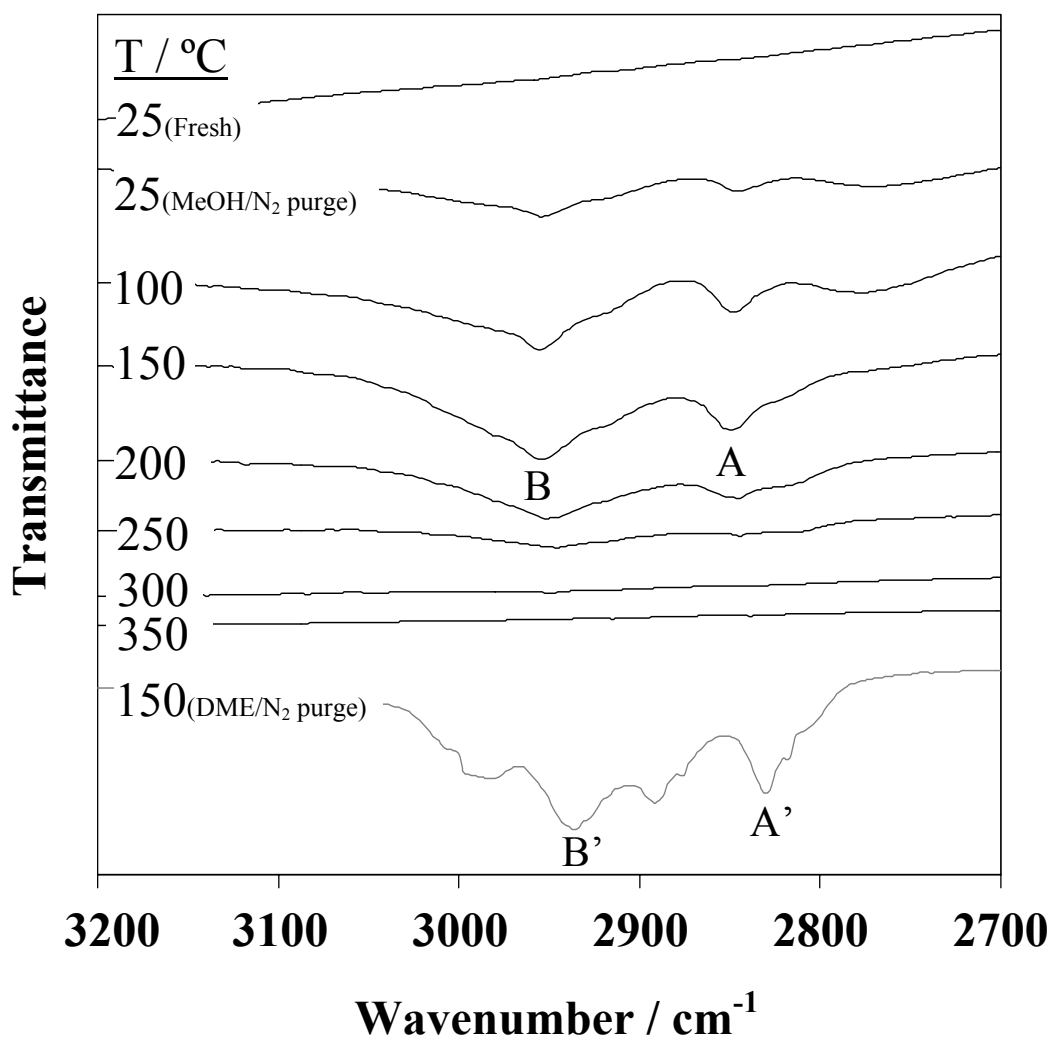


Figure 4.9.1: *In-situ* DRIFTS spectra between 2700 and 3200 cm⁻¹ of N₂ purged bulk HPW after exposure to methanol up to 350 °C showing formation of surface bound methoxy species (C-H bands **A** and **B**) A spectrum of DME treated HPW is shown for comparison showing surface bound C-H, **A'** and **B'**.

Studying the nature of methoxy species on **RhXHPW** proved to be more complicated. On exposure of **RhXHPW1:1-SiO₂** to methanol under the same conditions as described earlier for HPW, methoxy bands were obscured by the C-H bands from the Xantphos ligand backbone from the [Rh(CO)(Xantphos)]⁺ species. To overcome this problem deuterated methanol CD₃OD was employed to induce formation of deuterated methoxy species which are expected to shift to lower wavenumber.⁵⁶ Indeed weak bands, (2229, 2192, 2158, 2061 cm⁻¹) in comparison to the surrounding Rh-CO, were observed at the same temperatures after N₂ purge attributed to C-D from CD₃O-Keggin shifted ~800 cm⁻¹ to lower wavenumber **Figure 4.9.2**.

It is also evident from inspection of the Rh-CO bands that an additional band appears at 2102 cm^{-1} with loss of intensity of the parent Rh-CO (2008 cm^{-1}) at 150 $^{\circ}\text{C}$. The addition of CD_3OD causes stoichiometric titration of the parent Rh complex which indicates methylation of the Rh complex in accordance with a potential route to methanol carbonylation. This is discussed in the next section in reference to CO/MeOH *in-situ* measurements. It is worth noting at this point that no other changes are observed in the spectrum including both Xantphos and Keggin functionalities.

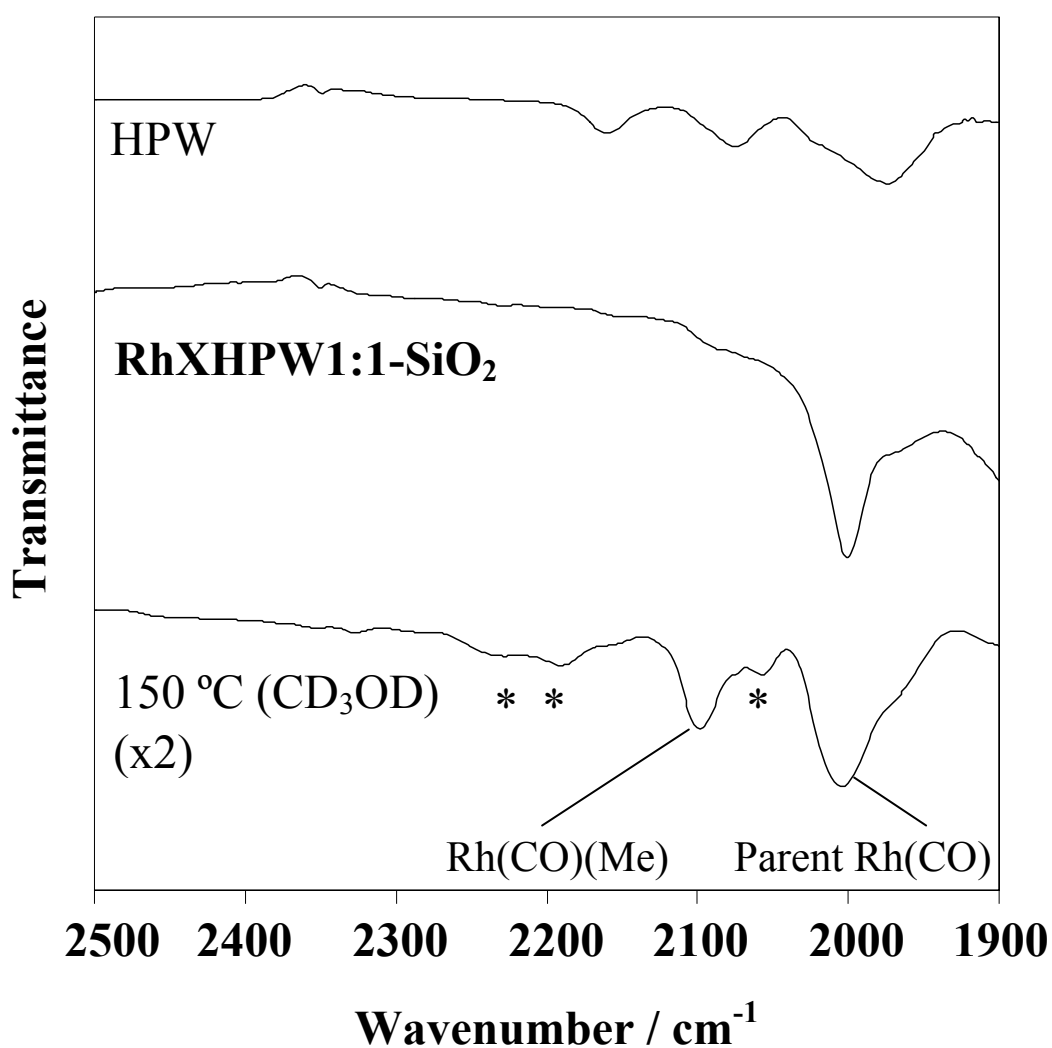


Figure 4.9.2: DRIFTS spectrum of N_2 purged RhXHPW1:1-SiO_2 after exposure to CD_3OD at 150 $^{\circ}\text{C}$ showing formation of deuterated methoxy species denoted by * and the formation of a new CO band associated with methylated $\{\text{Rh}^+(\text{CO})(\text{Xantphos})\}$ functionality.

The use of ethanol as an alcohol source for carbonylation was investigated to explore the effect of chain length and bond strength on the current catalytic process. All carbonylation conditions (temperature, flow rates, time in reactor *etc.*) remained identical to those implemented for methanol experiments. Possible products which could be expected if the carbonylation transformations followed the same mechanistic pathways would be diethylether, propanoic acid and ethyl propanoate. However on heating **RhXHPW1:1-SiO₂** to temperatures > 150 °C the only product observed is ethylene, reported as a function of heteropolyacids in the literature.⁵⁷ Subsequently ~98% conversion of ethanol to ethylene is observed at 200 °C with no loss of activity observed after 4 hours. This is evidently from the employment of the Brønsted acidity of the heteropolyacid in the formation of an ethyl carbocation followed by dehydration to ethylene, further supporting the formation of an activated carbocation as a methyl source in **RhXHPW** catalysed methanol carbonylation.

4.10 - *In-situ* DRIFTS study of methanol/CO/HPW interactions

Observation of a new Rh-CO species on passing CD₃OD vapor over **RhXHPW1:1-SiO₂** provided an insight into a potential pathway to methanol carbonylation. Further investigation of the system using *in-situ* DRIFTS involved utilizing a co-feed of methanol and CO at catalytically relevant temperatures. All spectra used a 25 °C **RhXHPW1:1-SiO₂** background spectrum to provide clarity in the identification of new species.

Figure 4.10.1 shows the growth of new carbonyl bands on interaction of CO and MeOH with the Rh centre. Band **A** at 2096 cm⁻¹ is consistent with the relative position of the species formed in the presence of deuterated methanol. Bands **B** and **C** at 2035 and 2013 cm⁻¹ respectively are new species which are likely to be the result of carbonylation of the parent Rh monocarbonyl to form a di-carbonyl. A weak feature (Band **D**) which grows in intensity up to 200 °C is observed at 1605 cm⁻¹ this is consistent with a Rh bound acyl species.^{56, 58}

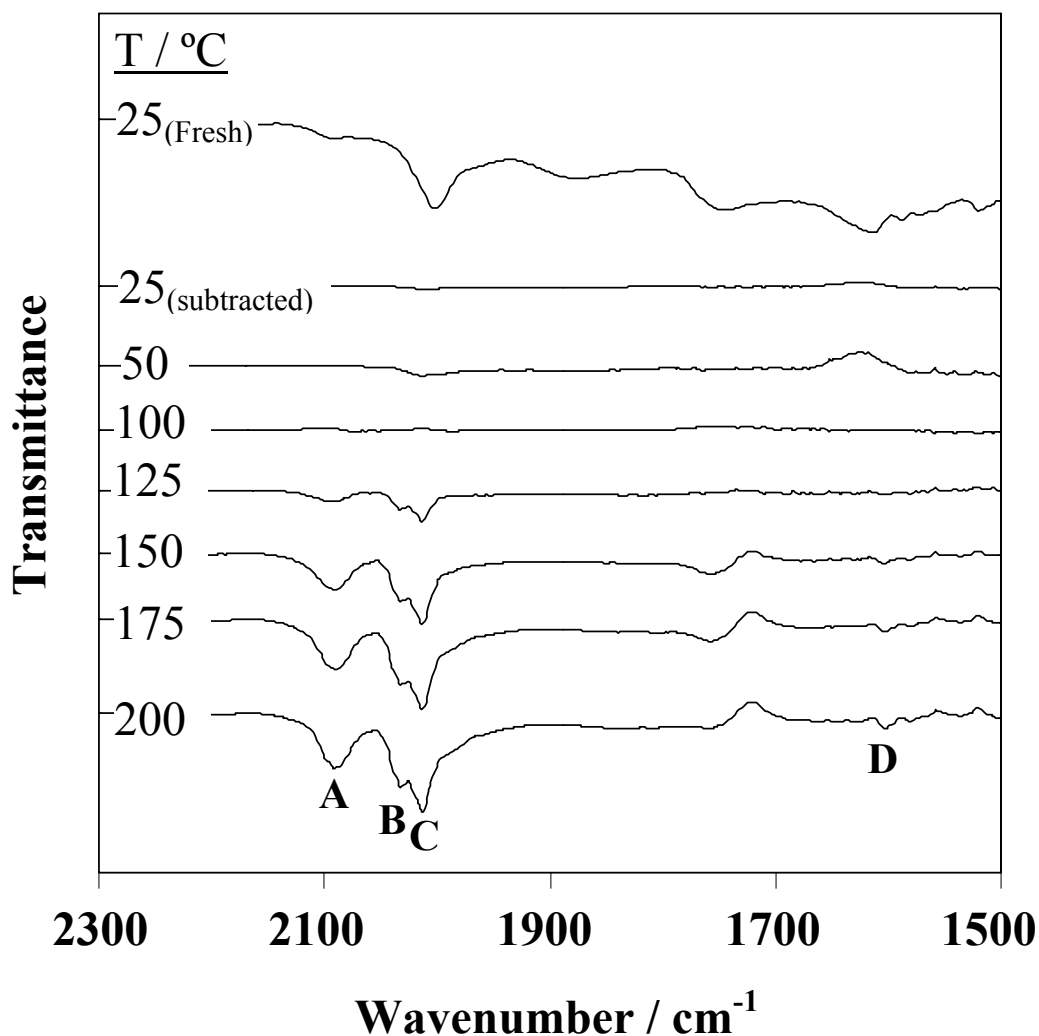


Figure 4.10.1: *In-situ* DRIFTS temperature study of **RhXHPW1:1-SiO₂** exposed to CO/MeOH. bands **A**, **B**, **C** and **D** correspond to 1 Rh(CO)(Me)(X), 2 Rh(CO)₂(X), and 1 Rh(CO)(COMe)(X) respectively. ('X' = xantphos)

The observations made using *in-situ* DRIFTS allows potential mechanistic pathways to be proposed identifying key intermediates in the formation of acetyls by catalytic conversion over **RhXHPW** systems. **Figure 4.10.2** illustrates the possible route to acetyls. Methanol is activated on the heteropolyacid Keggin. This process runs parallel to carbonylation of the parent $\{\text{Rh}(\text{Xantphos})(\text{CO})\}^+$ (**1**) to form (**2**). Species **2** is then methylated by the source of CH_3^+ on the Keggin (**3**) followed by migratory insertion into the carbonyl (**4**) and subsequent cleavage by methanol to regenerate **1** and one equivalent of methyl acetate. A second pathway where

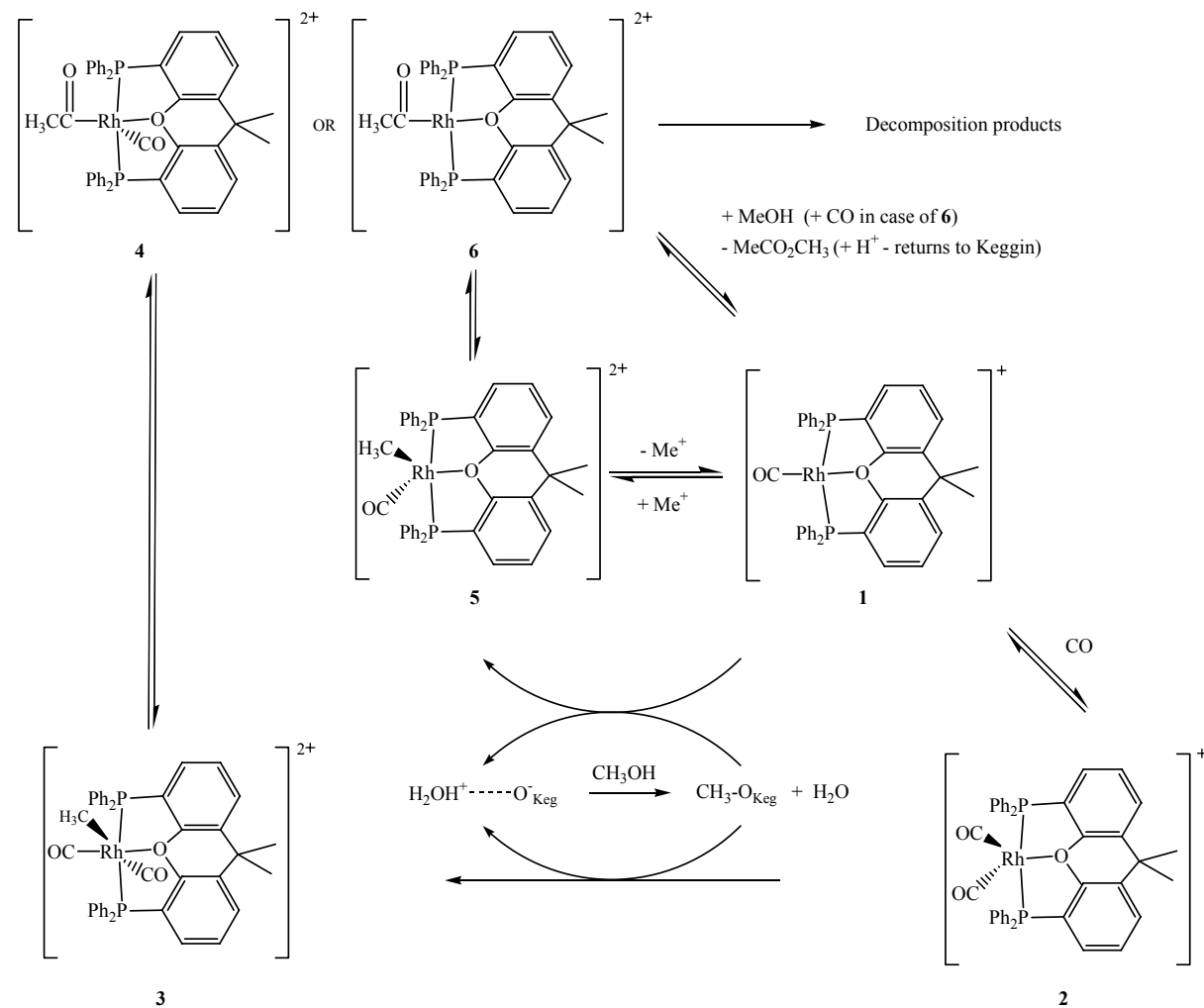


Figure 4.10.2: Proposed mechanism of RhXHPW methanol carbonylation.

monocarbonyl **1** is methylated (**5**) with formation of the acyl (**6**) leads to decomposition of the Rh carbonyl complex to liberate methyl acetate. In order to generate the Rh-acyl species to afford acetyl products, it is necessary for Rh(III) species from methylation from methanol activated on the Keggin (*c.f.* oxidative addition in Monsanto cycle). This is consistent with post-reactor XANES analysis of **RhXHPW1:1-SiO₂** (**Figure 4.10.3**) which had performed carbonylation at 200 °C for 5 hours at steady state, where oxidation is evident. From linear combination of Rh standards, best fit arises from 84 % Rh(II) and 16 % Rh(I).

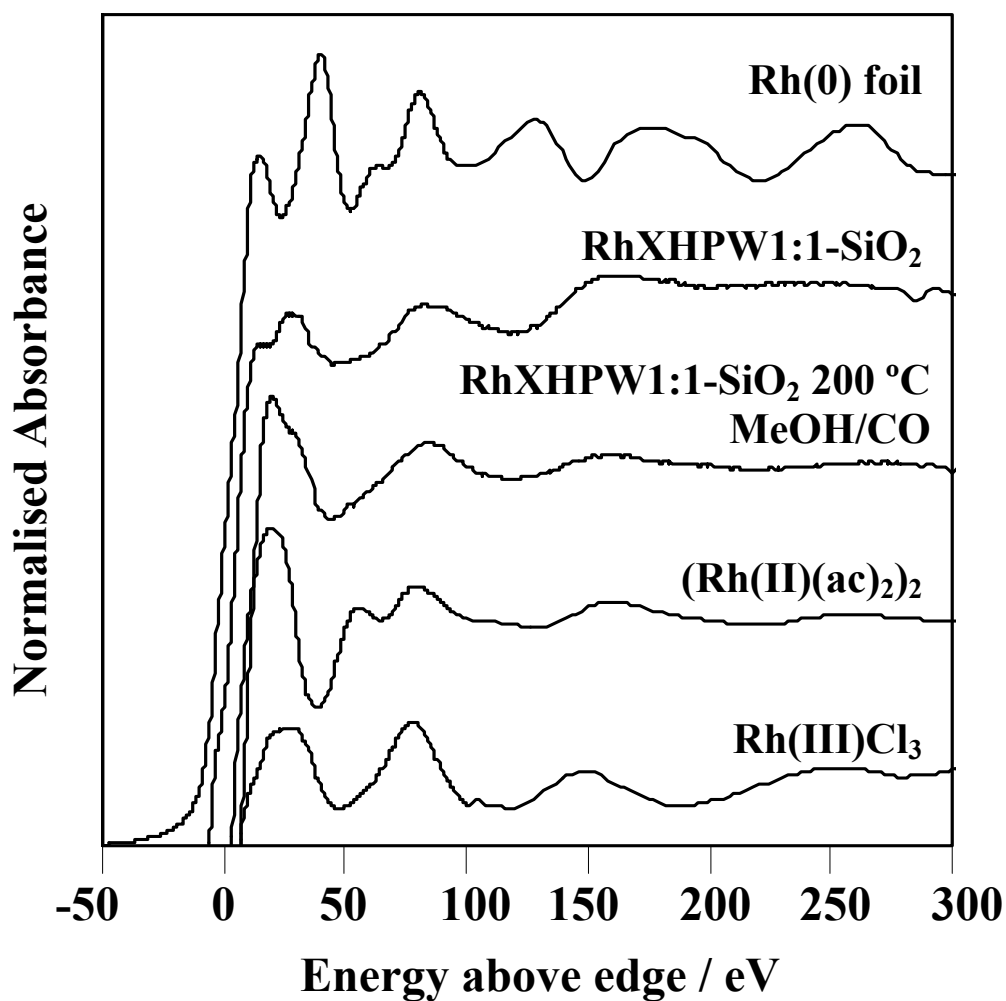


Figure 4.10.3: Rh K-edge XANES analysis of **RhXHPW1:1-SiO₂** both fresh and treated under methanol carbonylation conditions at 200 °C for 5 hours, compared to Rh standards of 0, 2 and 3 oxidation states.

High resolution XPS analysis (**Figure 4.10.4**) shows 3 Rh species consistent with Rh(I), Rh(III) at 308.3 and 309.9 eV respectively in a ~ 3 : 2 ratio and some Rh(0) at 307.5 eV contributing around 9 % of the total Rh content. A combination of these components would render a bulk 2+ oxidation state. This is consistent with XANES analysis suggesting that the distribution of Rh species in the bulk is the same as that observed on the surface of the catalyst during reaction.

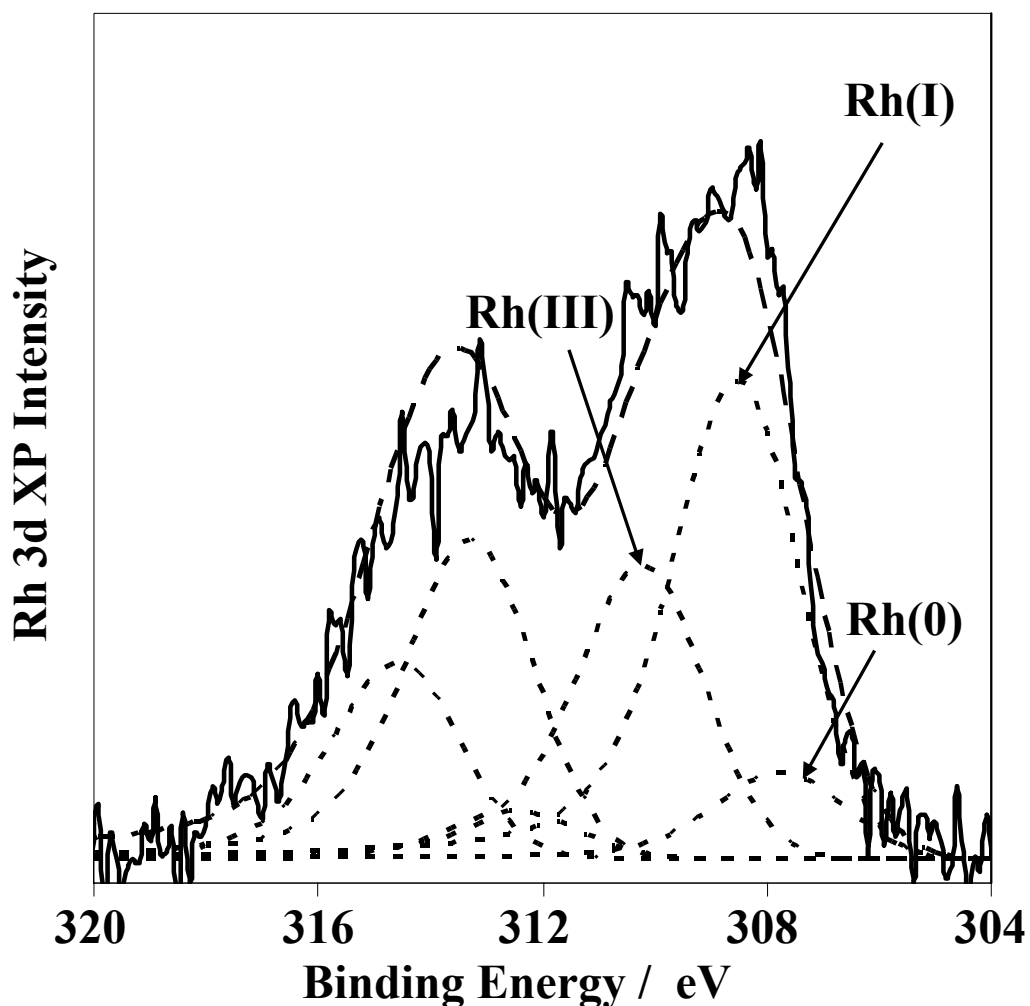


Figure 4.10.4: Rh 3d XPS analysis of **RhXHPW1:1-SiO₂** treated under methanol carbonylation conditions at 200 °C for 5 hours fitted to Rh(0), Rh(I) and Rh(III). showing partial oxidation to catalytically active species Rh(III) and some reduction Rh(0) under carbonylation conditions

4.11 - Syngas sourced CO for methanol carbonylation

Carbonylation studies so far have been performed using a pure CO source. In industry, however this is not the case. CO for many commercialised processes including carbonylation,^{9, 59} hydroformylation^{60, 61} and alcohol synthesis⁶²⁻⁶⁷ use that which has been reformed from fossil fuel based products. Generally syngas compositions are in the region of a 1 : 1 mixture of CO and H₂.^{62, 68} The current supported **RhXHPW1:1-SiO₂** catalyst was subject to carbonylation conditions where a pure CO gas flow was substituted for 1 : 1 CO : H₂. This experiment provides information on the stability of the Rh-Xantphos system under conditions which are more closely related to those of an industrial process. From our current understanding of the partial deactivation of this system due to reduction, it could be expected that the introduction of H₂ to the gas feed may induce further reduction and a loss in catalyst activity and selectivity on stream observed in other Rh and non Rh-based systems.^{59, 69-71}

Studies under these conditions (**Figure 4.11.1**) show catalytic conversion of methanol is essentially unchanged but the selectivity is reduced in the order of 50 % when compared to that in pure CO. These findings suggest that a commercial process using this kind of technology would benefit from a pure source of CO where H₂ is removed from the feed.⁷²

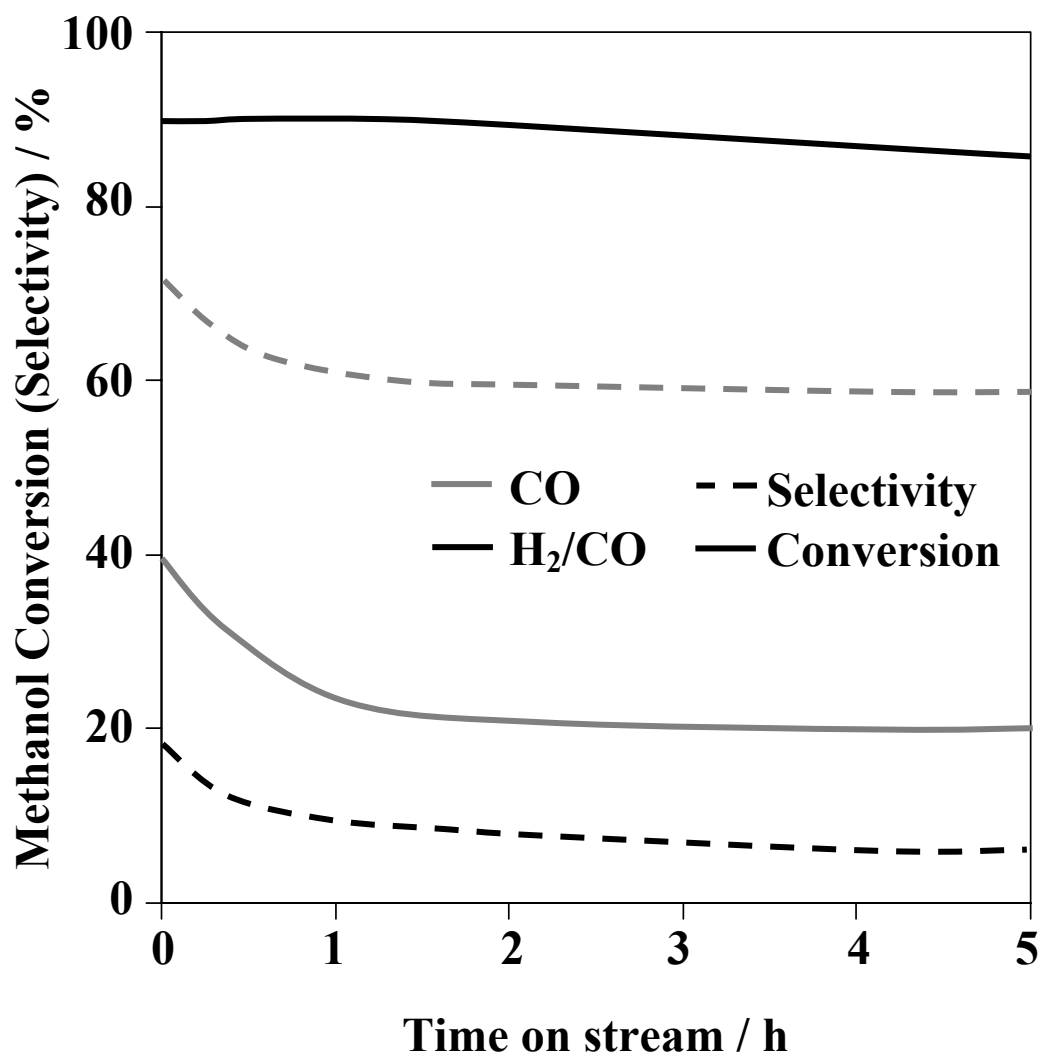


Figure 4.11.1: A comparison of activity and selectivity in acetyl synthesis profiles of RhXHPW1:1-SiO_2 over 5 hours at 200 °C with CO sources of a) pure CO b) 1 : 1 ratio of CO / H₂ showing retention of activity in methanol conversion but a drop in selectivity in b) suspected to be due to Rh reduction from H₂ exposure.

High resolution XPS of the spent catalyst under syngas / methanol carbonylation conditions shows the same ~ 3 : 2 distribution of Rh(III) to Rh(I) which implies this is normal operational state for the catalyst in comparison with the MeOH/CO only feed. An increase in apparent Rh(0) from 9 % in the CO-only spent catalyst to 23 % in the syngas case which shows that the presence of H₂ in the feed causes reduction of the active catalyst species to inactive metallic Rh(0). Negligible additional carbon was observed at the surface of the catalyst and no apparent methanol or syngas to hydrocarbons chemistries occurred during reaction, which suggests that coking is not a cause for loss of activity. In light of

this evidence it is likely that Rh reduction is a key factor in the poorer activity observed in the syngas / MeOH catalyst tests.

Temperature programmed reduction (TPR), DSC studies of the supported catalyst series using a 20 % H₂ / He mix, mimicking that of the reactor gas feed was employed to provide some insight into the thermal stability of **RhXHPW1:1-SiO₂** under reducing conditions **Figure 4.11.1**. A steady loss in mass from 105 °C further evidences the loss in stability due to reduction of the Rh functionality.

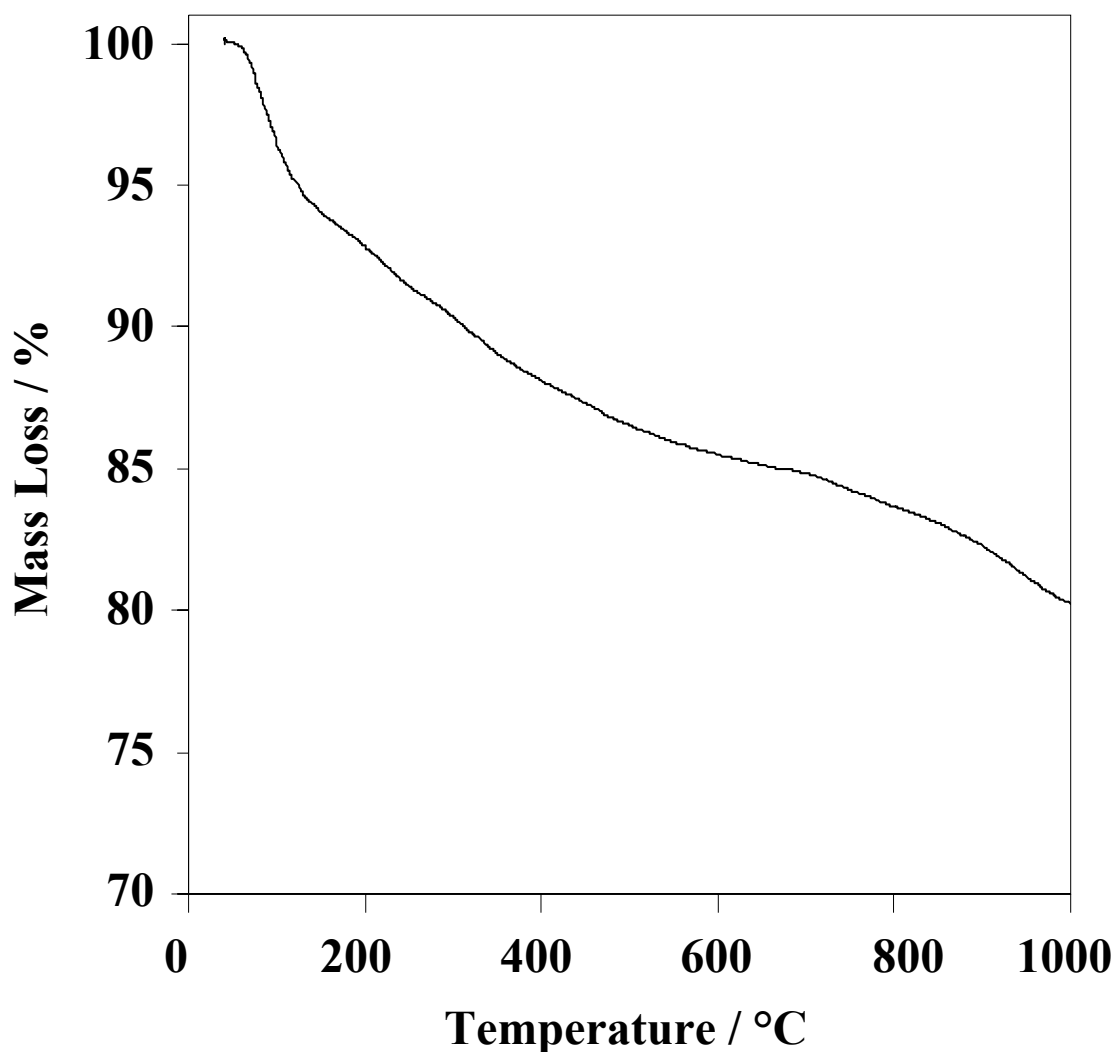


Figure 4.11.2 Temperature programmed reduction (TPR) between 20 – 1000 °C in 20 % H₂ / He gas flow at 20 ml min⁻¹ showing mass loss profile of **RhXHPW1:1-SiO₂** up to 1000 °C.

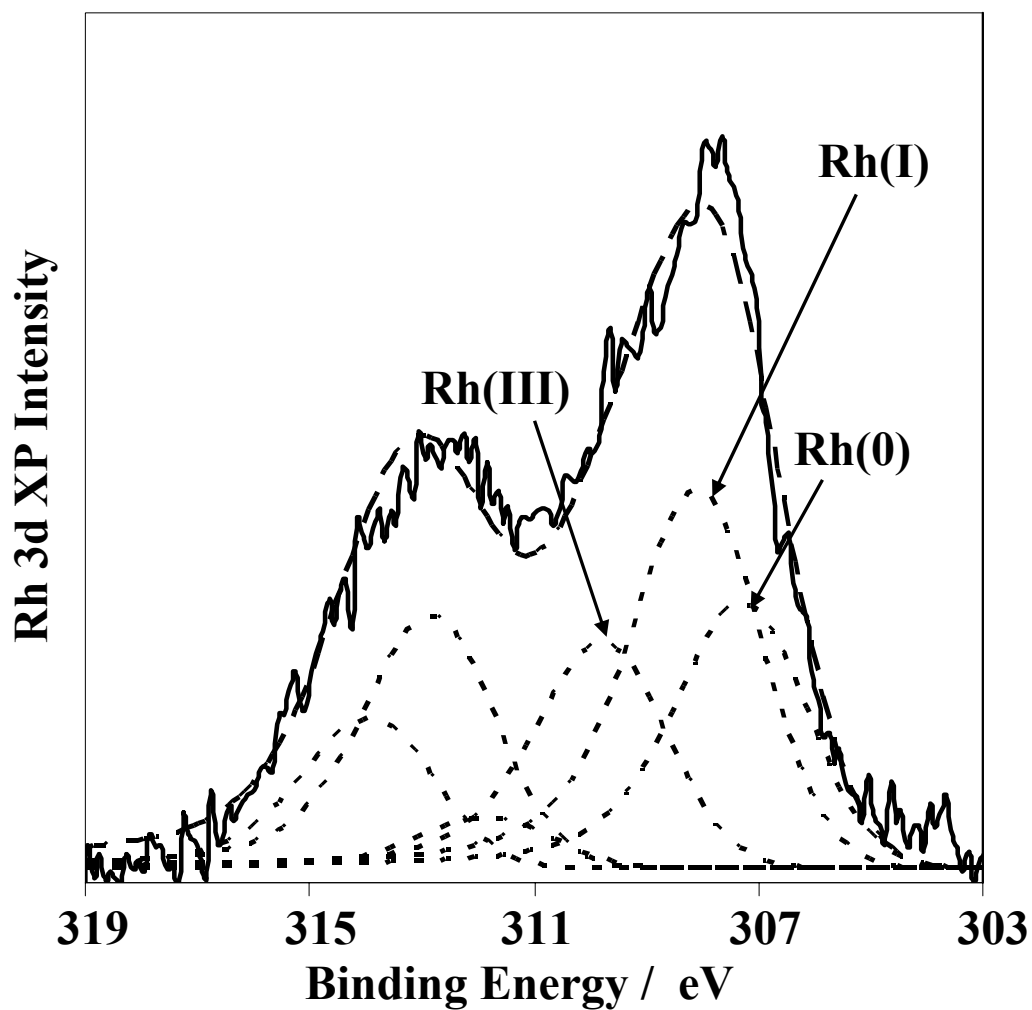


Figure 4.11.3: Rh 3d XPS of **RhXHPW1:1-SiO₂** exposed to methanol carbonylation conditions with 1 : 1 CO : H₂ showing three oxidation state environments. Partial reduction of the parent Rh complex Rh(I) to Rh(0) and oxidation to active Rh (III) catalyst species.

4.12 - Conclusions

In summary, a new compound of formula $[\text{Rh}(\text{CO})(\text{Xantphos})]_n^+[\text{H}_3\text{-nPW}_{12}\text{O}_{40}]^-$ has been synthesized from $\text{Rh}(\eta^2\text{-acac})(\text{CO})_2$ precursor via $\text{Rh}(\eta^2\text{-acac})(\text{CO})(\text{Xantphos})$. The compound demonstrates heterogeneous bifunctional catalytic activity towards methanol carbonylation in a continuous vapour phase regime at atmospheric pressure. Ligation of Xantphos to the Rh centre stabilizes the catalyst to Rh reduction under reaction conditions. Supporting the catalyst on Davisil silica shows an enhancement of methanol conversion while retaining optimum selectivity at 200 °C of 20 % with the remaining product stream consisting on DME, an acid condensation product of methanol and an additional carbonylation feedstock for the production of acetyls. Study of the affect of varying Rh : HPW ratio indicates a trade-off between methanol conversion and acetyl selectivity but demonstrates independence in absolute selectivity and therefore catalyst performance.

A major source of deactivation in this catalyst system is reduction of Rh(I) to Rh(0). This is only prevalent in any considerable amount at temperatures greater than 200 °C. Attempts to stabilize the catalyst at higher temperatures using Cs/Ag dopants were unsuccessful. Reduction of the catalyst using a syngas 1 : 1 CO : H₂ feed as a source of CO for carbonylation resulted in partial reduction (21 %) of active Rh at 200 °C.

The mechanism of methanol carbonylation of **RhXHPW** was studied using *in-situ* DRIFTS. The HPW was found to play a role in activating methanol by dehydration generating a supply of CH₃⁺ stabilized on pendant oxygen's on the polyoxometallate cage. Rh acts in activation of CO and subsequent insertion of a methyl group to form acyl species, suggesting Rh(III) species as reactive intermediates. Activated acyl groups are then cleaved in the presence of methanol to generate methyl acetate. This indicates the synergy of the **RhXHPW** bifunctional system.

4.13 - References

1. A. Haynes, P. M. Maitlis, G. E. Morris, G. J. Sunley, H. Adams, P. W. Badger, C. M. Bowers, D. B. Cook, P. I. P. Elliott, T. Ghaffar, H. Green, T. R. Griffin, M. Payne, J. M. Pearson, M. J. Taylor, P. W. Vickers and R. J. Watt, *Journal of the American Chemical Society*, 2004, **126**, 2847-2861.
2. P. M. Maitlis, A. Haynes, G. J. Sunley and M. J. Howard, *Journal of the Chemical Society-Dalton Transactions*, 1996, 2187-2196.
3. T. Blasco, M. Boronat, P. Concepcion, A. Corma, D. Law and J. A. Vidal-Moya, *Angewandte Chemie-International Edition*, 2007, **46**, 3938-3941.
4. *World Pat.*, 077745, 2009.
5. *US Pat.*, 5,330,955, 1994.
6. S. S. C. Chuang, R. W. Stevens and R. Khatri, *Topics in Catalysis.*, 2005, **32**, 225-232.
7. S. A. Hedrick, S. S. C. Chuang, A. Pant and A. G. Dastidar, *Catalysis Today*, 2000, **55**, 247-257.
8. M. M. Bhasin, W. J. Bartley, P. C. Ellgen and T. P. Wilson, *Journal of Catalysis*, 1978, **54**, 120-128.
9. M. J. Howard, M. D. Jones, M. S. Roberts and S. A. Taylor, *Catalysis Today*, 1993, **18**, 325-354.
10. T. Nakajo, K. Sano, S. Matsuhira and H. Arakawa, *J. Chem. Soc.-Chem. Commun.*, 1987, 647-649.
11. N. E. Fouad, M. A. Mohamed, M. I. Zaki and H. Knozinger, *J. Anal. Appl. Pyrolysis*, 2000, **53**, 185-193.
12. S. Shinoda and T. Yamakawa, *J. Chem. Soc.-Chem. Commun.*, 1990, 1511-1512.
13. P. Cheung, A. Bhan, G. J. Sunley and E. Iglesia, *Angewandte Chemie-International Edition*, 2006, **45**, 1617-1620.
14. B. Ellis, M. J. Howard, R. W. Joyner, K. N. Reddy, M. B. Padley and W. J. Smith, in *11th International Congress on Catalysis - 40th Anniversary, Pts a and B*, eds. J. W. Hightower, W. N. Delgass, E. Iglesia and A. T. Bell, Elsevier Science Publ B V, Amsterdam, Editon edn., 1996, vol. 101, pp. 771-779.
15. K. Fujimoto, T. Shikada, K. Omata and H. Tominaga, *Chemistry Letters*, 1984, 2047-2050.
16. *US Pat.*, 5,420,345, 1995.
17. G. Ormsby, J. S. J. Hargreaves and E. J. Ditzel, *Catalysis Communications*, 2009, **10**, 1292-1295.
18. R. W. Wegman, *J. Chem. Soc.-Chem. Commun.*, 1994, 947-948.
19. G. G. Volkova, L. M. Plyasova, A. N. Salanov, G. N. Kustova, T. M. Yurieva and V. A. Likhilobov, *Catalysis Letters*, 2002, **80**, 175-179.
20. B. Ali, J. Tijani and M. Fettouhi, *Journal of Molecular Catalysis A: Chemical*, 2006, **250**, 153-162.
21. C. L. Hill, *Journal of Molecular Catalysis A: Chemical*, 2007, **262**, 2-6.
22. I. V. Kozhevnikov, *Chemical Reviews*, 1998, **98**, 171-198.
23. N. Mizuno and M. Misono, *Chemical Reviews*, 1998, **98**, 199-217.
24. G. X. Li, Y. Ding, J. M. Wang, X. L. Wang and J. S. Suo, *Journal of Molecular Catalysis A: Chemical*, 2007, **262**, 67-76.

25. M. V. Luzgin, M. S. Kazantsev, W. Wang and A. G. Stepanov, *Journal of Physical Chemistry C*, 2009, **113**, 19639-19644.
26. T. L. Tartamella, PhD Thesis, Univ. Akron, 1997.
27. A. D. Newman, PhD, York, 2007.
28. A. J. Sandee, L. A. van der Veen, J. N. H. Reek, P. C. J. Kamer, M. Lutz, A. L. Spek and P. W. N. M. van Leeuwen, *Angewandte Chemie-International Edition*, 1999, **38**, 3231-3235.
29. P. W. N. M. van Leeuwen, A. J. Sandee, J. N. H. Reek and P. C. J. Kamer, *Journal of Molecular Catalysis A: Chemical*, 2002, **182**, 107-123.
30. *World Pat.*, 101488, 2004.
31. F. Bonati and G. Wilkinson, *Journal of the Chemical Society*, 1964, 3156
32. L. D. Dingwall, C. M. Corcoran, A. F. Lee, L. Olivi, J. M. Lynam and K. Wilson, *Catal. Commun.*, 2008, **10**, 53-56.
33. H. F. J. Vantblik, J. B. A. D. Vanzon, T. Huizinga, J. C. Vis, D. C. Koningsberger and R. Prins, *Journal of the American Chemical Society*, 1985, **107**, 3139-3147.
34. K. Narasimharao, D. R. Brown, A. F. Lee, A. D. Newman, P. F. Siril, S. J. Tavener and K. Wilson, *Journal of Catalysis*, 2007, **248**, 226-234.
35. L. J. Farrugia, *J. Appl. Cryst.*, 1997, **30**, 565.
36. L. A. van der Veen, P. H. Keeven, G. C. Schoemaker, J. N. H. Reek, P. C. J. Kamer, P. van Leeuwen, M. Lutz and A. L. Spek, *Organometallics*, 2000, **19**, 872-883.
37. T. Marimuthu, M. Bala and H. B. Friedrich, *Journal of Coordination Chemistry*, 2009, **62**, 1407-1414.
38. M. Kranenburg, Y. E. M. Vanderburgt, P. C. J. Kamer, P. Vanleeuwen, K. Goubitz and J. Fraanje, *Organometallics*, 1995, **14**, 3081-3089.
39. D. J. Fox, S. B. Duckett, C. Flaschenriem, W. W. Brennessel, J. Schneider, A. Gunay and R. Eisenberg, *Inorganic Chemistry*, 2006, **45**, 7197-7209.
40. A. D. Newman, A. F. Lee, K. Wilson and N. A. Young, *Catalysis Letters*, 2005, **102**, 45-50.
41. I. V. Kozhevnikov, *Catalysis Reviews-Science and Engineering*, 1995, **37**, 311-352.
42. A. D. Newman, D. R. Brown, P. Siril, A. F. Lee and K. Wilson, *Physical Chemistry Chemical Physics*, 2006, **8**, 2893-2902.
43. Y. Ono and T. Mori, *Journal of the Chemical Society-Faraday Transactions I*, 1981, **77**, 2209-2221.
44. L. Gonsalvi, H. Adams, G. J. Sunley, E. Ditzel and A. Haynes, *Journal of the American Chemical Society*, 2002, **124**, 13597-13612.
45. I. V. Kozhevnikov, *Journal of Molecular Catalysis A: Chemical*, 2007, **262**, 86-92.
46. A. Corma, A. Martinez and C. Martinez, *J. Catal.*, 1996, **164**, 422.
47. J. B. McMonagle and J. B. Moffat, *J. Colloid and Interface Science*, 1984, **101**, 479-488.
48. T. Okuhara, H. Watanabe, T. Nishimura, K. Inumaru and M. Misono, *Chem. Mater.*, 2000, **12**, 2230-2038.
49. U. Filek, A. Bressel, B. Sulikowski and M. Hunger, *Journal of Physical Chemistry C*, 2008, **112**, 19470-19476.
50. A. Jentys, *Phys. Chem. Chem. Phys.*, 1999, **1**, 4059-4063.
51. *Applied Catalysis A: General*, 2003, **256**.
52. A. Micek-Ilnicka, *Journal of Molecular Catalysis A: Chemical*, 2009, **308**, 1-14.

53. A. V. Ivanov, E. Zausa, Y. Ben Taarit and N. Essayem, *Applied Catalysis A-General*, 2003, **256**, 225-242.
54. J.G. Highfield and J. B. Moffat, *Journal of Catalysis*, 1985, **95**, 108-119.
55. Y. Hirano, K. Inumaru, T. Okuhara and M. Misono, *Chemistry Letters*, 1996, 1111 – 1112.
56. L. Chateau, J. P. Hindermann, A. Kiennemann and E. Tempesti, *Journal of Molecular Catalysis A: Chemical*, 1996, **107**, 367-378.
57. D. Varisli, T. Dogu and G. Dogu, *Chem. Eng. Sci.*, 2007 **62**, 5349 - 5352.
58. B. J. Borah, B. Deb, P. P. Sarmah and D. K. Dutta, *Journal of Molecular Catalysis A: Chemical*, 2010, **319**, 66-70.
59. G. Lamb, M. Clarke, A. M. Z. Slawin, B. Williams and L. Key, *Dalton Transactions*, 2007, 5582-5589.
60. T. Hanaoka, H. Arakawa, T. Matsuzaki, Y. Sugi, K. Kanno and Y. Abe, *Catalysis Today*, 2000, **58**, 271-280.
61. *US Pat.*, 7,226,548 2007.
62. *World Pat.*, 063173, 2009.
63. Z. L. Fan, W. Chen, X. L. Pan and X. H. Bao, *Catalysis Today*, 2009, **147**, 86-93.
64. H. Arakawa, T. Fukushima, M. Ichikawa, S. Natsushita, K. Takeuchi, T. Matsuzaki and Y. Sugi, *Chemistry Letters*, 1985, 881-884.
65. H. M. Yin, Y. J. Ding, H. Y. Luo, L. Yan, T. Wang and L. W. Lin, *Energy & Fuels*, 2003, **17**, 1401-1406.
66. H. M. Yin, Y. J. Ding, H. Y. Luo, D. P. He, J. M. Xiong, W. M. Chen, Z. D. Pan and L. W. Lin, *Chinese Journal of Catalysis*, 2004, **25**, 547-550.
67. M. A. Haider, M. R. Gogate and R. J. Davis, *Journal of Catalysis*, 2009, **261**, 9-16.
68. *US Pat.*, 5,832,747, 1998.
69. M. E. Halttunen, M. K. Niemela, A. O. I. Krause and A. I. Vuori, *Journal of Molecular Catalysis A: Chemical*, 1999, **144**, 307-314.
70. *World Pat.*, 123158, 2009.
71. E. Tempesti, A. Kaddouri and N. De Blasio, *J. Therm. Anal.*, 1998, **53**, 177-187.
72. *US Pat.*, 4,566,886, 1986.

Chapter 5 - Synthesis, characterisation and catalysis of Rh(Anthraphos)-polyoxometallates

5.1 - Introduction

Chapter 4 showed the successful application of the ‘**RhXHPW**’ system with rigid *pseudo-trans* bidentate Xantphos ligand to heterogeneous methanol carbonylation. However, some inherent deactivation due to ligand decomposition and subsequent reduction of Rh(I) to Rh(0) on stream was observed.

PCP ligands, where a formal oxidative interaction between the metal centre and a carbon atom exists in addition to the bidentate P-Rh-P pincer interaction, are known to increase the stability of transition metal complexes over more classical bidentate phosphine analogues.¹⁻⁴ There are numerous examples where complexes with these ligand types have operated at temperatures greater than 200 °C in homogeneous catalytic reactions.⁵⁻⁷

The Anthraphos ligand (**Figure 5.1.1**) and derivatives have exhibited high thermal stability, stabilising homogeneous catalysts in a variety of chemistries including dehydrogenation of alkanes where temperatures of 250 °C were employed for several days on Ir-Anthraphos hydrides without loss of activity and catalyst stability.⁸ However, application of such ligands in commercially applicable catalysis has been impeded due to the inherent

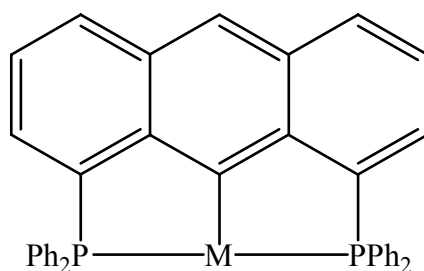


Figure 5.1.1: Anthraphos PCP ligand showing interaction with a transition metal centre where M = Rh, Ir.

complexity of the synthesis of the ligand backbone, typically taking as many as 10 tedious reaction steps for preparation including highly anhydrous conditions to acquire good yields.⁹⁻¹¹ However, recent work in the group of Professor Paul Pringle has identified a new synthetic route to Anthraphos requiring fewer steps making it a more viable alternative ligand for catalytic application. Subsequently, complexes based on a ‘Rh-Anthraphos’ backbone have been successfully applied to homogeneous methanol carbonylation.¹²

In light of recent progress in the application of ‘Rh-Anthraphos’ derived catalysts, systems analogous to those ‘Rh-Xantphos’ employed in Chapter 4 were synthesised to explore the affect of introducing a more strongly coordinating Rh-C interaction (over Rh-O used in the Xantphos case) in ‘Rh(L)HPW’ on heterogeneous methanol carbonylation.

5.2 - Synthesis and characterisation of Rh(Anthraphos)(CO)HPW (RhAHPW) systems

Anthraphos was synthesised in the laboratories of Professor Paul Pringle and complexed to Rh. The neutral coordinatively unsaturated Rh(I) Rh(Anthraphos)(CO) complex (**RhAnthraphos**) was provided by Professor Paul Pringle for subsequent use in the synthesis of bifunctional **RhAnthraphos** doped HPW analogous to those synthesised with Rh-Xantphos.

The purity of this starting complex was 87 % as demonstrated by ¹H NMR spectroscopy. The ³¹P{¹H} (C₆D₆) NMR exhibited a resonance at 56.5 ppm a Rh-

P $^1J_{\text{Rh-P}}$ coupling of 151 Hz. The nature of the 2 minor impurities with ^{31}P $\{^1\text{H}\}$ chemical shifts of 55.18 and 32.5 Hz is unclear but $^1J_{\text{Rh-P}}$ doublet splitting of 100 Hz is indicative of Anthraphos ligation. This is supported by the presence of a broad resonance at 133 ppm in the ^{13}C MAS NMR spectrum (**Figure 5.2.1**) associated with the aryl carbons of the Anthraphos anthracene and phenyl groups attached to phosphorus. Further evidence arises from the observation of the only dominant peaks in the ESI mass spectrum (in acetonitrile solvent) at (m/z) 649.1, 677.1 and 690.1 being attributed to $\{\text{Rh}(\text{Anthraphos})(\text{H})^+\}$, $\{\text{Rh}(\text{Anthraphos})(\text{CO})(\text{H})^+\}$ and $\{\text{Rh}(\text{Anthraphos})(\text{CH}_3\text{CN})(\text{H})^+\}$, containing a common Rh(Anthraphos) backbone.

Interestingly, facile formation of rhodium hydrides complexes from the parent Rh(Anthraphos)(CO) were observed. Three environments with ^1H NMR (C_6D_6) chemical shifts of $\delta = -6.9, -12.7$ and -17.4 sharing common doublet of triplets coupling with coupling constants of 11.57, 23.86 and 31.5 Hz respectively were

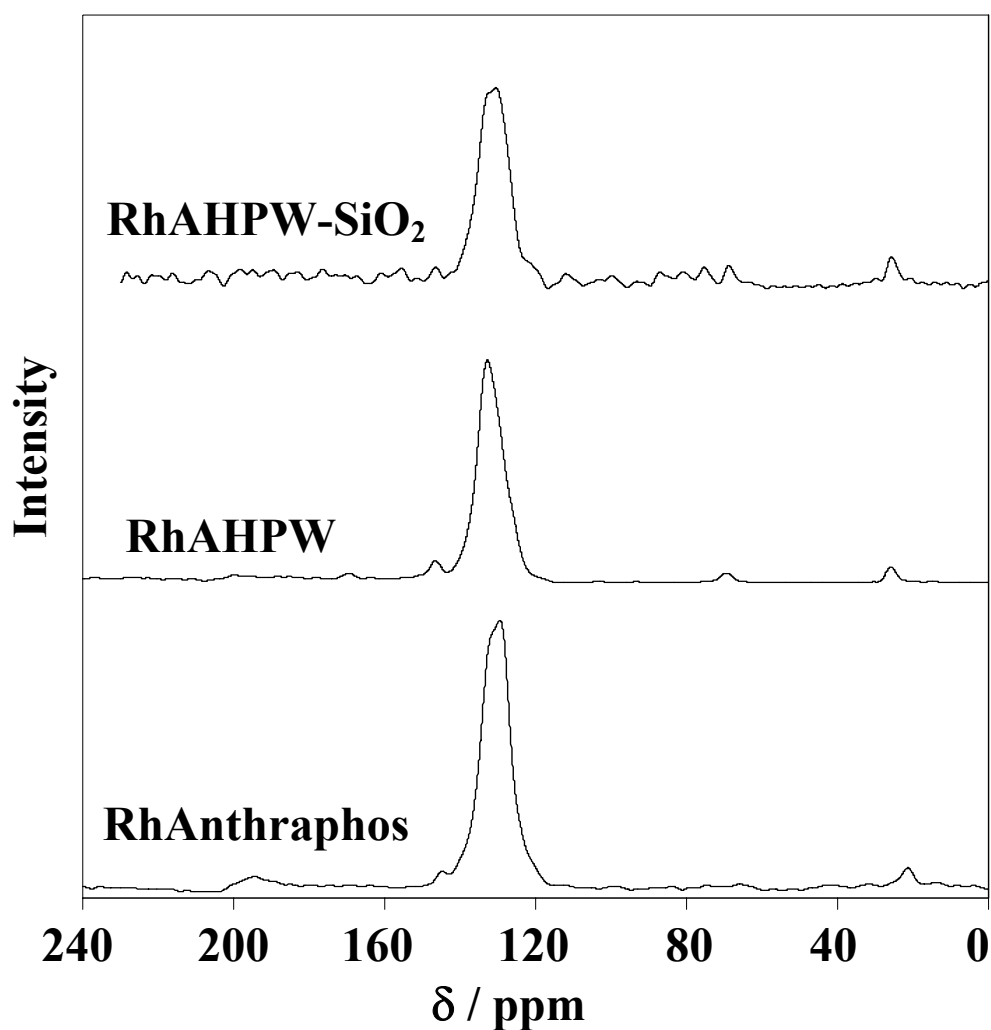


Figure 5.2.1: ^{13}C MAS-NMR showing carbon environments associated with the Anthraphos anthracene and phenyl aryl carbons in the Rh-Anthraphos functionality of **RhAnthraphos**, and **RhAHPW** and **RhAHPW-SiO₂**

observed. DRIFTS analysis of **RhAnthraphos** (Figure 5.1.2) showed a carbonyl band at 1974 cm^{-1} attributed to the $\text{Rh}(\text{Anthraphos})(\text{CO})$ parent. Additional carbonyl bands were observed at 2050 cm^{-1} with shoulders at 2003 and 2079 cm^{-1} which would be consistent with a further three species which may be derived from the three hydride species observed by ^1H NMR. The new bands present in the DRIFTS spectra are blue shifted to higher wave number, consistent with that expected for carbonyls associated with a metal centre with higher oxidation state, required for hydride formation ($\text{Rh}(\text{III})$). It is worth noting that these new carbonyl bands were observed in analysis of KBr and neat samples as well as in solution state spectra, ruling out their formation during analytical preparation.

This phenomenon was observed when handling several batches of the parent complex, even when handled under an inert atmosphere. The formation of hydrides however does suggest that the neutral Rh(Anthraphos)(CO) could provide the same ionic interaction observed in the **RhXHPW** case by becoming cationic in the form of $[\text{Rh}(\text{Anthraphos})(\text{CO})(\text{H})]^+$ and interacting with anionic $[\text{H}_2\text{PW}_{12}\text{O}_{40}]^-$ as was originally hypothesised (**Scheme 5.2.1**) It is unclear

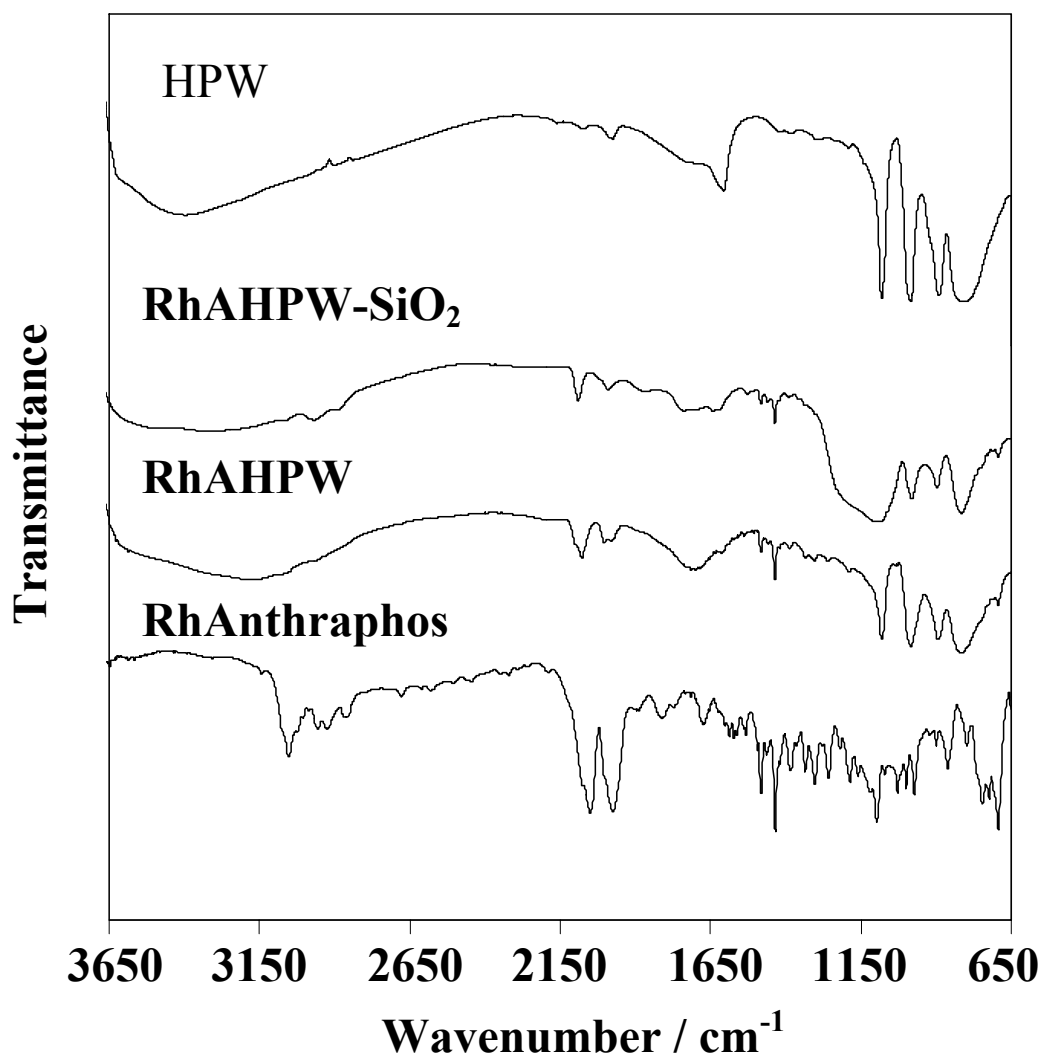
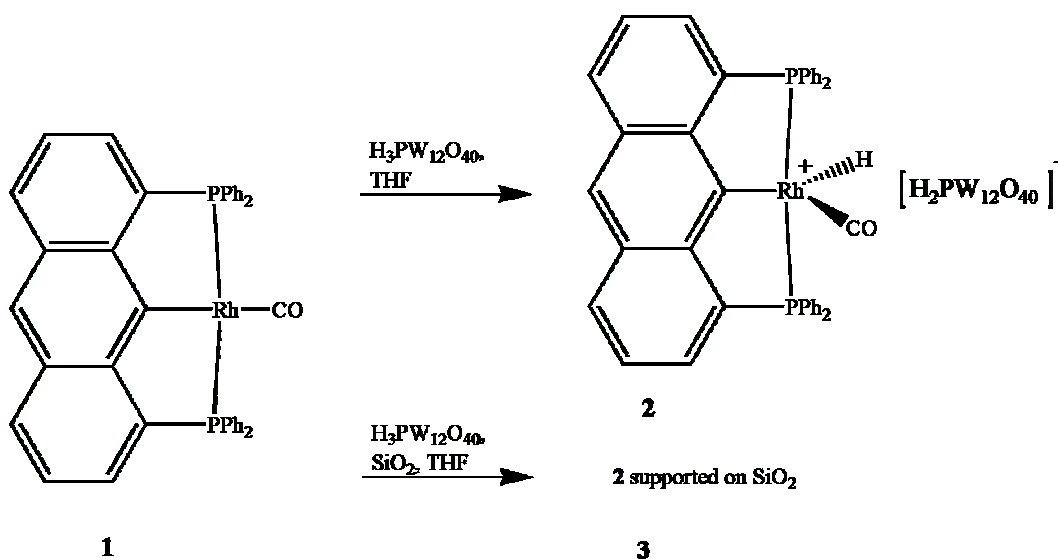


Figure 5.2.2: DRIFTS spectrum showing bulk bifunctional **RhAHPW** and supported **RhAHPW-SiO₂** compared with **RhAnthraphos** and HPW parent species.

why this occurs and the remaining study will consider only the potential of an Anthraphos ligand to provide stability in methanol carbonylation. No insight into the nature of the active rhodium component could be obtained.

The HPW analogue was prepared in the same manner as the analogous **RhXHPW** based on a 1:1 Rh : HPW ratio. Orange **RhAnthraphos** was dissolved in dry degassed THF and subsequent addition of phosphotungstic acid. After stirring under an inert atmosphere for 15 mins, the solvent was removed, and a yellow/brown powder was isolated and washed with hexane. Good yields of > 95 % yield and the correct 1 : 3 : 12 Rh : P : W ratio were observed. In addition, no leaching during synthesis and work-up from ^1H and $^{31}\text{P}\{^1\text{H}\}$ NMR of the washings was observed. ESI mass spectrometry of the Rh-Anthraphos doped HPW, **RhAHPW**, identifies the $[\text{Rh}(\text{Anthraphos})(\text{CO})]$ framework with the observed peaks at (m/z) 649.1, 677.1 and 690.1 (observed in the parent complex



Scheme 5.2.1: Synthesis of **RhAnthraphos** doped HPW, hypothesised by hydride formation of the parent Rh(Anthraphos)(CO) complex.

case). This evidences the Rh-Anthraphos functionality remaining intact in a new **RhAHPW** system. DRIFTS analysis shows retention of common Anthraphos backbone bands observed in the fingerprint region of the spectrum below 1500 cm^{-1} with notably sharp bands at 1434 and 1483 cm^{-1} . Characteristic bands at 835, 898, 993 and 1084 cm^{-1} are clearly observed consistent with preservation of the polyoxometallate framework, indicating both components in the new bifunctional system are retained in **RhAHPW**. Loss of CO bands at 1974 cm^{-1} and 2050 cm^{-1} was observed with retention of the shoulder peaks at 2003 cm^{-1} and 2079 cm^{-1} . Close inspection of the carbonyl region indicates the formation of a new band at 2098 cm^{-1} . $^{31}\text{P}\{^1\text{H}\}$ MAS-NMR of the bulk material (**Figure 5.2.3**) show 3 P

environments at δ 17.3, 36.3 and 60.3 ppm denoted by **A'**, **D** and **C'** respectively in **RhAHPW** associated with phosphine species. **A'** and **C'** are consistent with **A** and **C** observed in the parent **RhAnthrphos** spectrum. The common 2.3 ppm shift is attributed to the new local environment, perturbed by the presence of HPW, with polyoxometallate phosphorus observed at δ -15.2 ppm. The broad phosphine

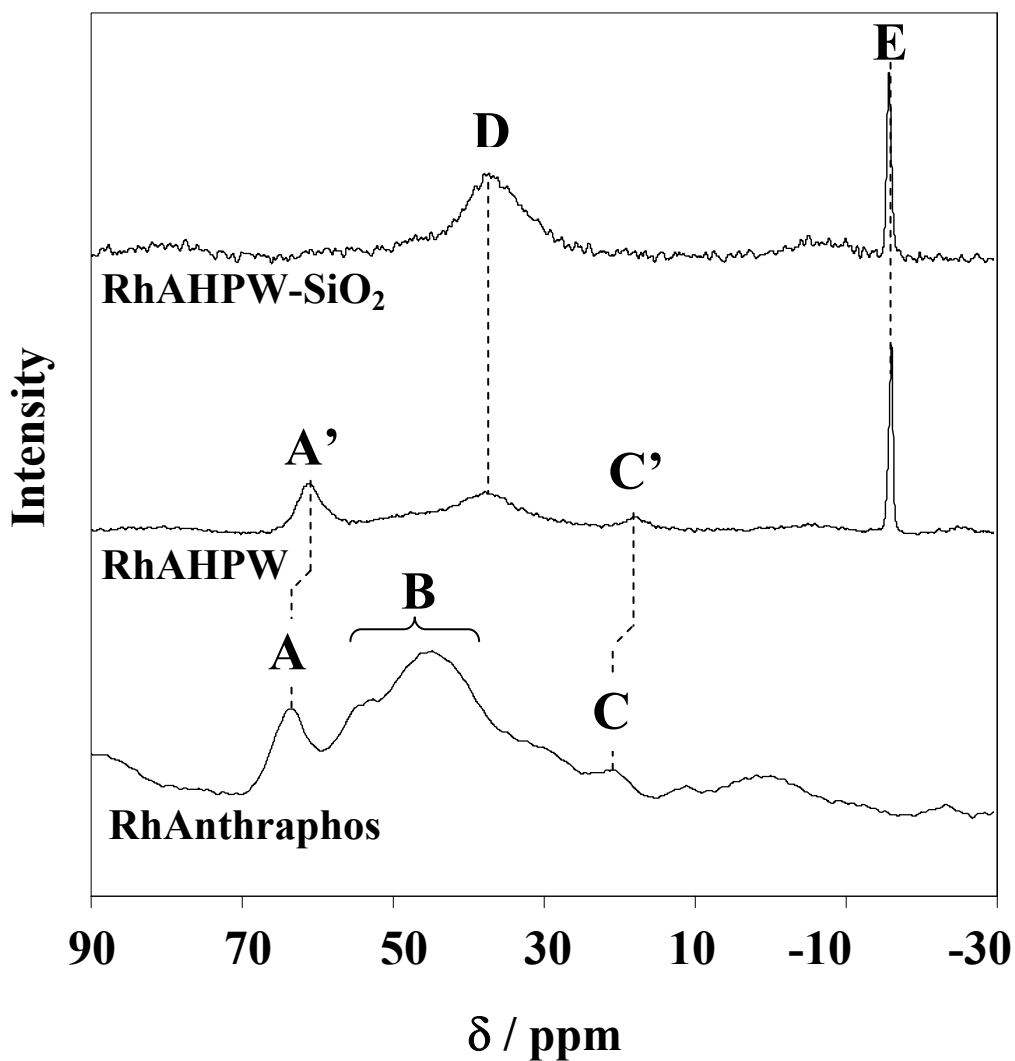


Figure 5.2.3: Solid state $^{31}\text{P}\{^1\text{H}\}$ MAS-NMR spectra of **RhAnthrphos**, **RhAHPW** and **RhAHPW-SiO₂** showing loss of Rh bound phosphine signal **A**, **B** and **C** and **D** on incorporation of HPW (peak **E**).

environment **B** (δ 37 – 53 ppm) is lost in **RhAHPW** in accordance with loss of the parent IR bands from DRIFTS analysis.

Further evidence for the perturbation of Rh environments, observed in $^{31}\text{P}\{^1\text{H}\}$ MAS-NMR is shown from close inspection of W 4f XP high resolution spectra (**Figure 5.3.4**), where a shift of 0.5 eV to lower energy, from 36.8 to 36.4 eV is observed, in accordance with the same effect seen for the **RhXHPW** case (Chapter 4). This implies an ionic interaction of the complex by the non-coordinating, doubly protonated $\text{H}_3\text{PW}_{12}\text{O}_{40}$ anion following crystallisation with **RhAnthraphos** consistent with the greater electropositive character of a Rh-Anthraphos transition metal complex compared to H_5O_2^+ and thus greater initial tungsten charge.

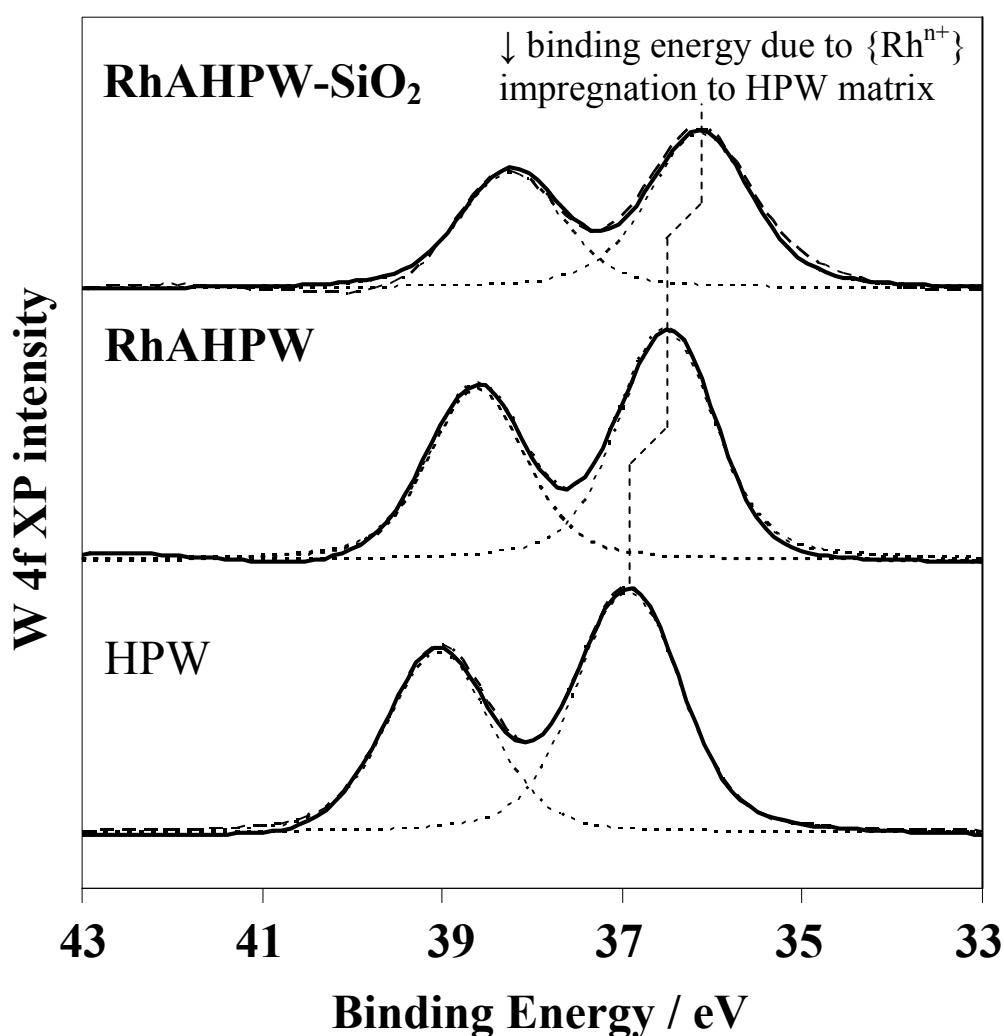


Figure 5.2.4: W 4f XP spectra of **RhAHPW**, **RhAHPW-SiO₂** and bulk **HPW** showing decrease in binding energy due to impregnation of cationic organorhodium into HPW matrix.

The **RhAHPW** was supported on Davisil silica in light of testing its catalytic potential towards methanol carbonylation. The resulting supported analogue was prepared by supporting the HPW on silica in degassed THF followed by introduction of the **RhAnthraphos** complex and stirred in an inert atmosphere for 15 mins. The resulting tan coloured powder was isolated by removal of the solvent in *vacuo*. The isolated compound, again provided good yield and the correct 1 : 3: 12 ratio of Rh : P : W in accordance with 1 : 1 Rh : HPW ratio in **RhAHPW**. DRIFTS analysis showed retention of the HPW and Anthraphos components however complete loss of the two CO bands observed in both **RhAnthraphos** and **RhAHPW** at 2003 cm⁻¹ and 2079 cm⁻¹ was observed with a single carbonyl at 2098 cm⁻¹. This is consistent with loss of peaks **A** and **C** in the ³¹P{¹H} MAS-NMR affording only the broad phosphine peak **D** (δ 36.3 ppm) in addition to the polyoxometallate peak at δ -15.2 ppm. An additional 0.4 eV shift in binding energy to 36 eV in the W 4f XP spectrum shown in **Figure 5.2.4**, compared to that of the **RhAHPW** case, suggests that the Rh functionality attains a higher degree of embedding into the HPW matrix. Rh 3d XP spectra of **RhAnthraphos**, bulk and supported **RhAHPW** are compared in **Figure 5.2.5**. Inspection of the **RhAnthraphos** spectrum shows a Rh binding energy of 308.8 eV consistent with Rh(I) character observed in the **RhXantphos** case. However introduction of HPW notes the formation of a new Rh(III) environment (**Figure 5.2.5**). The Rh(I) (**Figure 5.2.5**) environment shifts to 309.0 eV, a shift of 0.2 eV consistent with that observed for the **RhXHPW** case where an increase in binding energy was observed attributed to a change in the Madelung potential and final state screening upon embedding the organorhodium species within an ionic framework, suggesting similar bulk structural properties. **RhAHPW-SiO₂** shows a greater quantity of Rh(III) formation of 20 % over 10 % in the bulk **RhAHPW** which is consistent with a higher degree of W 4f shift away from pure HPW.

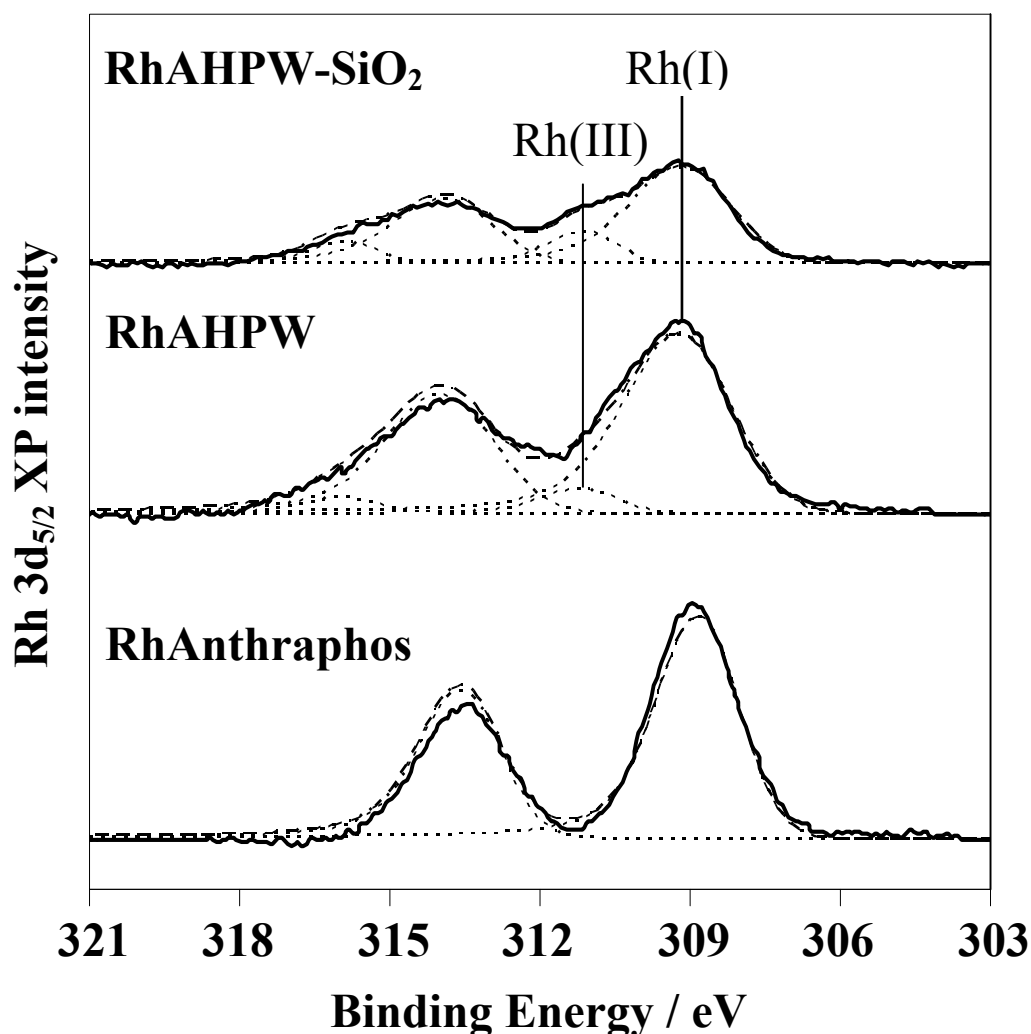


Figure 5.2.5: Rh 3d XP spectra of **RhAnthraphos**, bulk **RhAHPW** and silica supported **RhAHPW-SiO₂** showing a decrease in Rh(I) and increase in Rh(III) character on incorporation of HPW.

The synthesis of a Rh-doped HPW system with Anthraphos PCP backbone proved to yield a mixture of Rh species with common Rh-Anthraphos functionality due to the nature of the [Rh(Anthraphos)(CO)] exhibiting degradation of the starting complex to other unknown Rh-Anthraphos derived complexes believed to be a combination of rhodium-hydride species. Incorporation of HPW showed an increase in Rh(III) character observed in surface XPS studies. This occurs to a higher degree in the silica-supported analogue which is consistent with a greater degree of exposure of organorhodium to HPW acid sites. Further study is necessary to optimise the synthesis of these doped species which will require a more stable pure starting Rh-Anthraphos complex.

5.3 - Thermal stability of RhAHPW-SiO₂

The thermal stability of the **RhAHPW** system was assessed using a combination of TGA and temperature programmed DRIFTS. TGA analysis of **RhAnthraphos** shows an initial loss of 10 % at 150 °C is considered to be adsorbed on breakdown of the crystalline phase and loss of solvent. Decomposition of ligand structure occurs between 270 and 410 °C where a 25 % loss in mass is observed. An additional mass loss at > 420 °C of 31 % is consistent with breakdown of the Anthraphos backbone. These mass losses are observed in the bulk and supported **RhAHPW** consistent with a 5 and 2 % mass between ~ 280 and 420 °C for complex decomposition, followed by a further 15 and 6 % respectively attributed to decomposition of Anthraphos as well as Keggin oxide cage after ~ 650 °C.

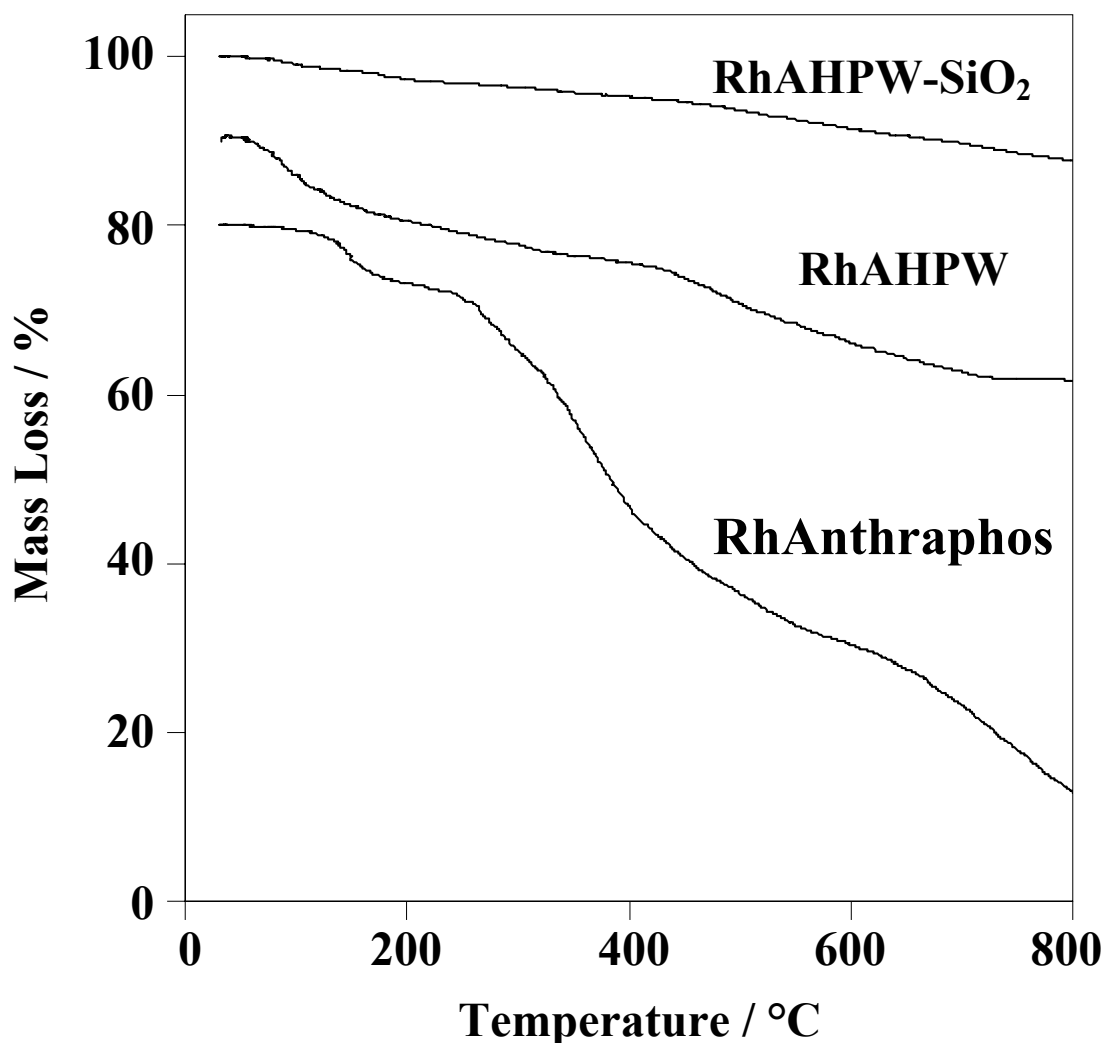


Figure 5.3.1: TGA of **RhAnthraphos**, **RhAHPW** and **RhAHPW-SiO₂** Showing decomposition of the parent complex > 270 °C and >280 °C in the HPW derivatives.

DRIFTS analysis of the thermal evolution of **RhAHPW-SiO₂** agrees with TGA measurements showing loss in Rh-CO carbonyl band at 2098 cm⁻¹ intensity from ~ 225 °C with complete decomposition observed at 350 °C. This is accompanied by decomposition of Anthraphos with loss in intensity of characteristic bands at 1434 and 1483 cm⁻¹. It can be noted that loss of the carbonyl band associated with decomposition of the complex occurs before complete decomposition of Anthraphos consistent with the stability of the PCP backbone.

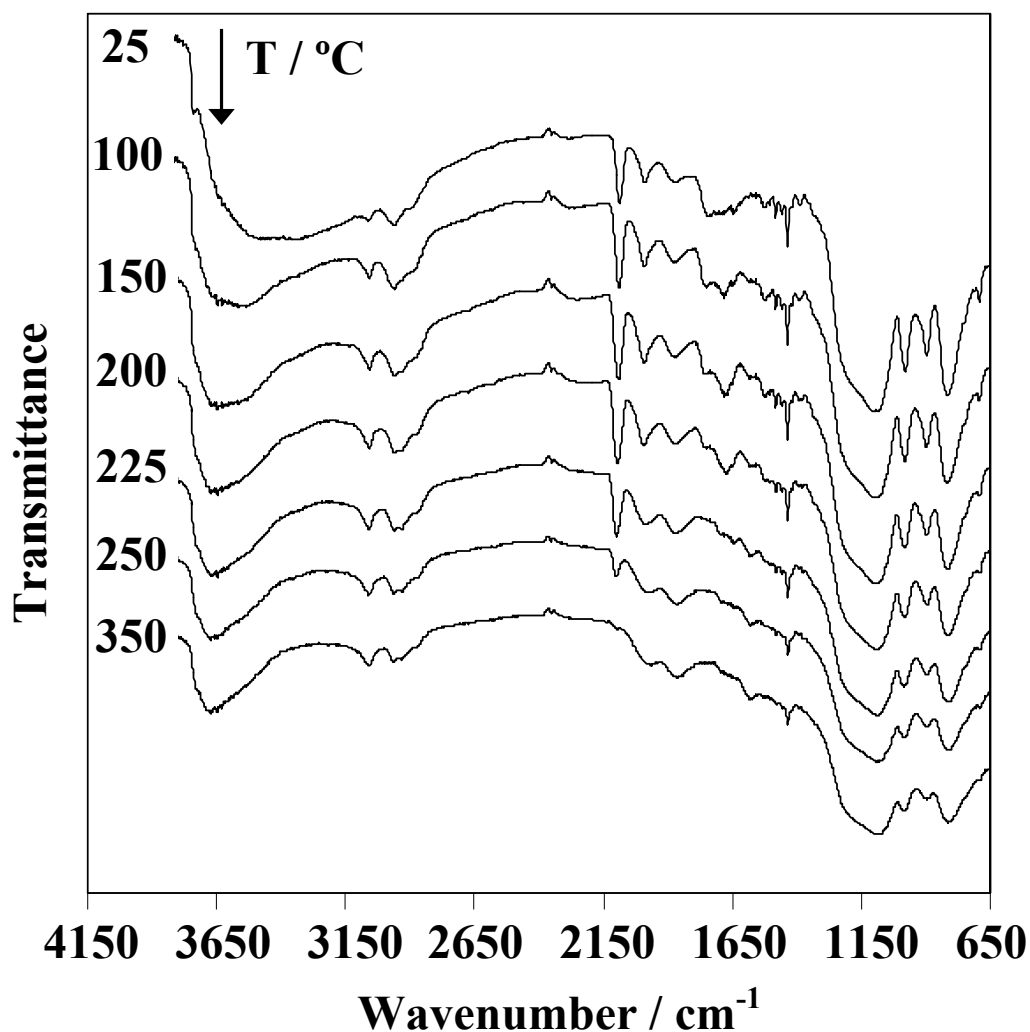


Figure 5.3.2: *In-situ* temperature programmed DRIFTS analysis of **RhAHPW-SiO₂** between 25 and 350 °C showing thermal degradation at temperature.

Consideration of the above thermal measurements shows no improvement in overall stability of the system over analogous **RhXHPW**. However this does not rule out other more stable catalytically active organorhodium species generated

in-situ during exposure to methanol carbonylation conditions. With this in mind, catalyst studies are discussed in the proceeding section.

5.4 - Catalytic application of RhAHPW in methanol carbonylation

Although thermal treatment showed no improvement in thermal stability over analogous **RhXHPW** systems, the *in-situ* generation of more stable catalytic intermediates under methanol carbonylation conditions could not be ruled out. RhAHPW-SiO₂ was subject to the same methanol carbonylation study as that employed in the study of supported **RhXHPW** activity. **Figure 5.4.1** shows the reaction profile of **RhAHPW-SiO₂** as a catalyst for methanol carbonylation over 5 hours. The **RhAHPW-SiO₂** catalyses the carbonylation of methanol under the same conditions as that of analogous **RhXHPW1:1-SiO₂**, also showing the same

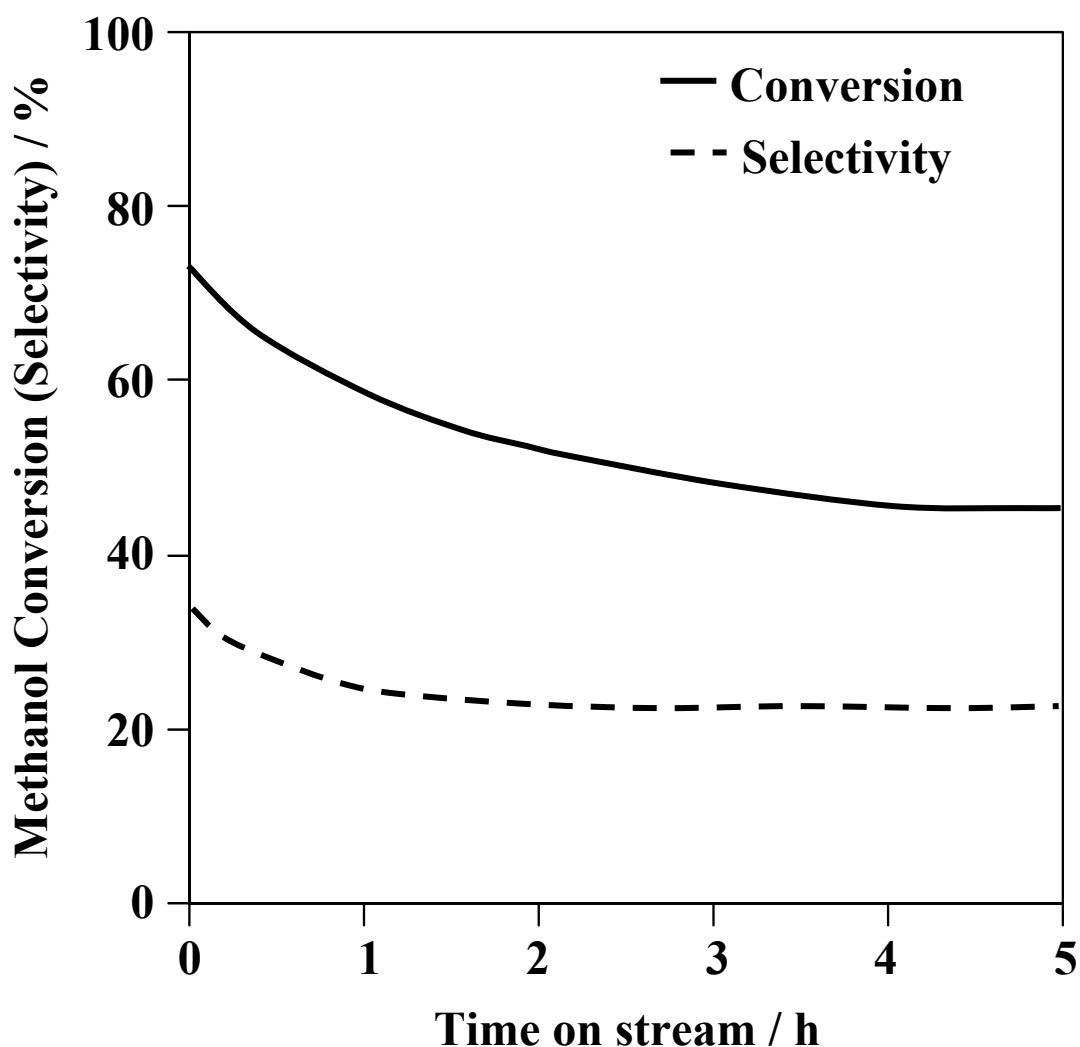


Figure 5.4.1: Methanol conversion and acetyl selectivity of **RhAHPW-SiO₂** during continuous operation at 200 °C under standard carbonylation conditions.

reaction profile features suggesting the same mode of catalytic action. Initial methanol conversion is 73 % showing a steady loss over the first 4 hours reaching steady state at ca. 47 %. An initial selectivity of 34 % toward acetyls, where methyl acetate is the only acetyl product, dropped to 24 % in the first hour reaching steady state for the remaining 4 hours of study. The overall acetyl yield observed was poorer than that of **RhXHPW1:1-SiO₂** where a steady state acetyl yield of 0.95 mmolh⁻¹ was achieved for a catalysts sample containing 5 mg of rhodium. (*c.f.* maximum steady state acetyl yield 1.2 mmolh⁻¹ for 1 : 1 Rh : HPW ratio system).

The key objective of incorporating Anthraphos PCP ligand over the analogous Xantphos, where a weaker Rh-O interaction is employed, was to achieve a more robust Rh functionality for activating CO. At 250 °C, **RhXHPW-SiO₂** shows loss in acetyl selectivity during methanol carbonylation, where Rh reduction is more prevalent. **RhAHPW-SiO₂** was treated under the same conditions to investigate whether the substitution of an Anthraphos backbone can afford sustained acetyl selectivity at higher temperatures. **RhAHPW-SiO₂** was treated at 200 °C for 2 hours where steady state in acetyls was achieved. The sample was then heated to 250 °C at 5 °C per minute and held at temperature for ~ 1 hour. **Figure 5.4.2** shows the acetyl and DME yield with time on stream. An increase in acetyl and DME production is observed where acetyls reach a maximum at 3.0 mmolh⁻¹. DME reaches a sustained yield of ~ 5 mmolh⁻¹. This shows the stability of the HPW acidity for performing methanol condensation. However, the acetyl yield experiences a sharp drop in the first 20 minutes followed by slow loss on stream. This loss in performance and overall selectivity of acetyls over DME at 250 °C suggests that **RhAnthraphos** may not provide the stability required for sustained operation of Rh doped HPW bifunctional catalysts at greater than 200 °C.

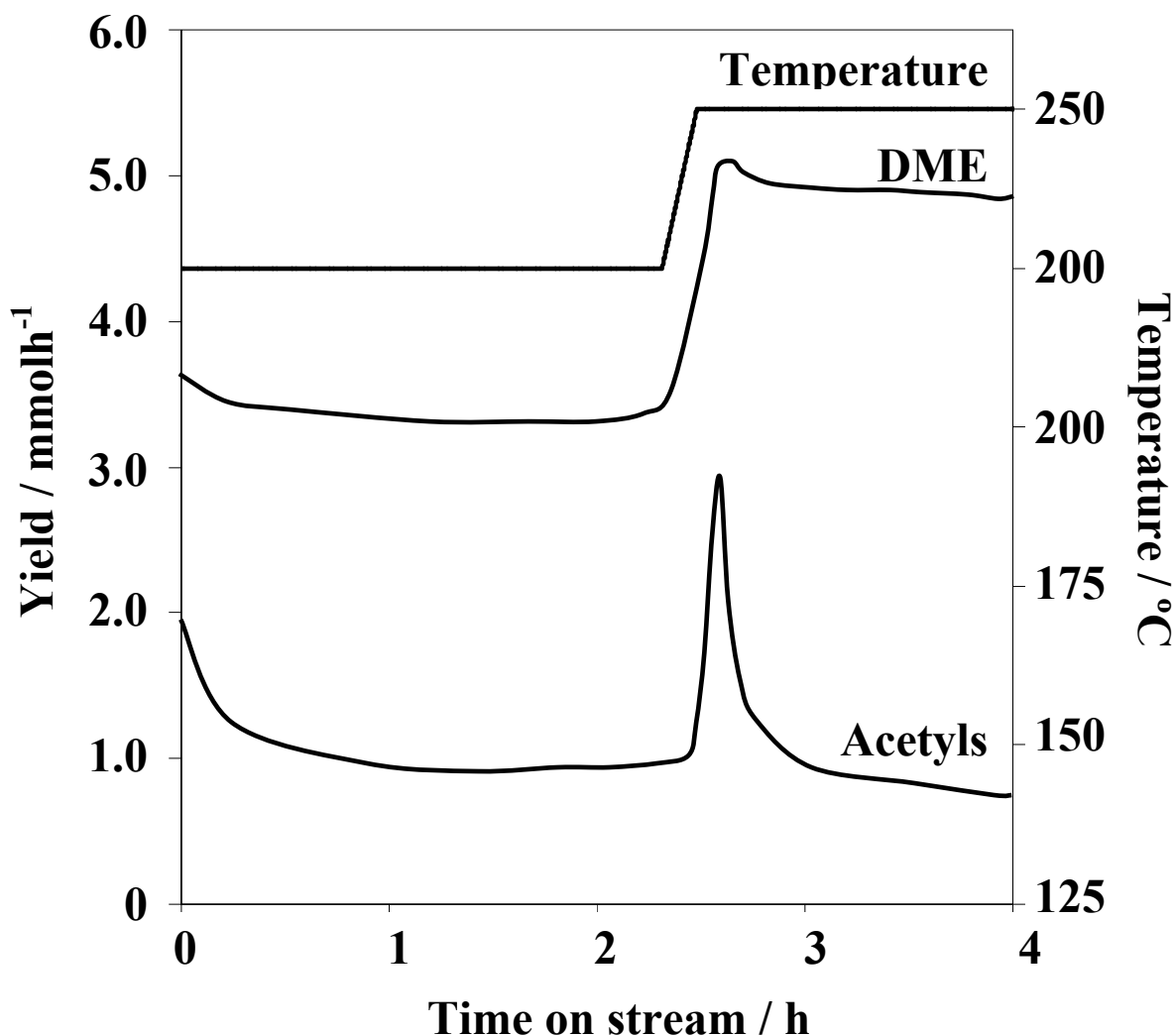


Figure 5.4.2: DME/Acetyl during methanol light-off over **RhAHPW-SiO₂** showing change in product distribution at 200 °C and 250 °C.

5.5 - Conclusions

A Rh-Anthraphos organorhodium doped HPW was synthesised and tested for carbonylation of methanol in light of success of the analogous **RhXHPW** system discussed in Chapter 4. Characterisation of the bulk and silica supported **RhAHPW** material showed a mixture of Rh(I) and Rh(III) within an ionic matrix of Rh and HPW functionalities. The **RhAnthraphos** starting complex shows instability to the formation of other unknown organorhodium species with common Rh-Anthraphos backbone believed to contain hydride ligands. The true nature and origin of these organorhodium species is unclear. Silica supported **RhAHPW** (**RhAHPW-SiO₂**) showed activity in methanol carbonylation,

showing a similar reaction profile to **RhXHPW-SiO₂** indicating the same mode of action where CO is activated by Rh followed by insertion of an activated methyl species from an acidic Keggin and subsequent cleaving of the acyl formed at the Rh centre with methanol to yield methyl acetate. Increasing the temperature of the reactor to 250 °C, after reaching steady state at 200 °C, showed loss in the formation of acetyls and selectivity over DME. No inherent improvement in stability was observed in **RhAHPW-SiO₂** over **RhXHPW-SiO₂** as a catalyst for methanol carbonylation. Further understanding of Rh-Anthrphos-based **RhAHPW** will require the synthesis of a more robust starting material against formation of other [Rh(Anthrphos)(CO)] based analogues, and tuning of the synthesis of subsequent bifunctional Rh-HPW catalyst to be sure of a monotonous organorhodium functionality.

5.6 - References

1. M. Ohff, A. Ohff, M. E. Van der Boom and D. Milstein, *Journal of the American Chemical Society*, 1998, **120**, 3273-3273.
2. A. Vigalok and D. Milstein, *Organometallics*, 2000, **19**, 2061-2064.
3. L. Schwartsburd, E. Poverenov, L. J. W. Shimon and D. Milstein, *Organometallics*, 2007, **26**, 2931-2936.
4. D. Vuzman, E. Poverenov, Y. Diskin-Posner, G. Leitus, L. J. W. Shimon and D. Milstein, *Dalton Transactions*, 2007, 5692-5700.
5. C. M. Frech, L. J. W. Shimon and D. Milstein, *Organometallics*, 2009, **28**, 1900-1908.
6. E. Kossoy, B. Rybtchinski, Y. Diskin-Posner, L. J. W. Shimon, G. Leitus and D. Milstein, *Organometallics*, 2009, **28**, 523-533.
7. M. C. Lipke, R. A. Woloszynek, L. Q. Ma and J. D. Protasiewicz, *Organometallics*, 2009, **28**, 188-196.
8. M. W. Haenel, S. Oevers, K. Angermund, W. C. Kaska, H. J. Fan and M. B. Hall, *Angewandte Chemie-International Edition*, 2001, **40**, 3596-3600.
9. M. W. Haenel, S. Oevers, J. Bruckmann, J. Kuhnigk and C. Kruger, *Synlett*, 1998, 301-303.
10. A. Guijarro, D. J. Ramon and M. Yus, *Tetrahedron*, 1993, **49**, 469-482.
11. M. Yus, R. P. Herrera and A. Guijarro, *Chemistry-a European Journal*, 2002, **8**, 2574-2584.
12. *World Pat.*, 145976, 2008.
13. K. Narasimharao, D. R. Brown, A. F. Lee, A. D. Newman, P. F. Siril, S. J. Tavener and K. Wilson, *Journal of Catalysis*, 2007, **248**, 226-234.

Chapter 6 - Synthesis, characterisation and catalysis of Rh(Terpy)-polyoxometallates

6.1 - Introduction

Chapter 4 and 5 demonstrated the effectiveness of tridentate Rh-Xantphos and Rh-Anthraphos based Rh-HPW systems as successful methanol carbonylation catalysts. This chapter extends the study further to explore other tridentate ligands. Organic nitrogen compounds are well established as nitrogen donor ligands.^{1, 2} Transition metal complexes containing a variety of nitrogen donor species such as amine, imine, pyrrole, pyrrolidine are well established in catalysis³⁻⁵ Terpyridine (**Figure 6.1.1**) is known as a robust multidentate ligand with up to three nitrogen co-ordination sites.⁶⁻⁹ Transition metal complexes of this type have shown activity in a variety of chemistries including C-heteroatom and asymmetric C-C bond forming reactions¹⁰⁻¹³ as well as hydroformylation.¹⁴

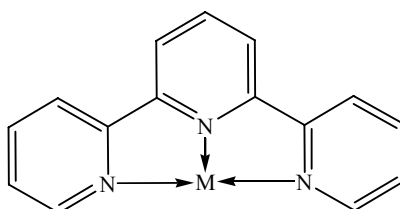


Figure 6.1.1: Terpyridine as a multidentate nitrogen donor ligand where M is a transition metal.

Pyridine and chelating oligopyridines as Rh-ligand species have shown activity as catalysts in homogeneous carbonylation chemistry,^{15, 16} and most recently have demonstrated superior activity to traditional Monsanto catalysts.¹⁷⁻¹⁹ To this end, Terpyridine has been employed to investigate the effects of utilising a tridentate nitrogen ligand to stabilise a Rh centre for bifunctional Rh-HPW methanol carbonylation, analogous to PXP systems discussed in Chapter 4 and 5.

6.2 - Synthesis and characterisation of Rh(η^2 -acac)(CO)₂(Terpyridine) and HPW derivative

One equivalent of Terpyridine was stirred in THF under an inert atmosphere of nitrogen using Rh(η^2 -acac)(CO)₂ as the rhodium source for 15 minutes. The green crystalline rhodium precursor changed colour to a deep red solution upon addition of the colourless Terpyridine powder. The solvent was removed in *vacuo* to yield the deep red micro-crystalline rhodium Terpyridine complex which was washed with hexane.

Elemental analysis of the isolated complex shows an observed Rh : N ratio of 1: 3 consistent with incorporation of Terpyridine. The overall composition was in good agreement with retention of existing ligands suggesting the formation of Rh(η^2 -acac)(CO)₂(Terpy). ESI mass spectrometry shows peaks at 364 and 494 consistent with {Rh(CO)(Terpy)}⁺, and {Rh(acac)(CO)₂(Terpy)-H⁺} respectively with a minor peak at 234 for mono-protonated Terpyridine. It is worth noting here that no higher mass peaks were observed therefore the formation of higher oligopyridine species, which have been observed in the literature and are employed as self assembly materials, can be excluded.^{20, 21} A ¹³C{¹H} solid state MAS-NMR spectrum of the resulting **RhTerpy** complex showed environments for the acetylacetonato, at 27.1 ppm and 188.8 ppm (broad) for the carbonyl carbons, comparable to those at 28.1 for the methyl and 187.0 and 189.3 ppm for carbonyl carbons in Rh(η^2 -acac)(CO)₂ (where the two carbonyl carbon environments are more clearly defined). A peak at 101.5 ppm in the Rh(η^2 -acac)(CO)₂ spectrum associated with the central CH carbon of the acac is not observed in the **RhTerpy** complex, (**Appendix 7**) presumably shifted within the aromatic Carbon region of the Terpyridine carbons. These are in addition to environments at 127.0, 137.6, 149.2 and 155.1 ppm consistent with those for the Terpyridine ligand. ¹H solution NMR (D₆-DMSO) spectroscopy provided supporting evidence for the inclusion of Terpyridine into the rhodium complex, indicated by multiplet peaks at δ 7.6, 8.2, 8.8 and 9.0 with integration of 4 : 3 : 2 : 2 protons respectively, in agreement with that observed in the fingerprint of Terpyridine and a broad environment at δ 1.89 ppm associated with the 6 methyl

protons in the acac ligand and a broad peak at 3.4 ppm for the C-H proton between carbonyl groups. These bands are shifted considerably compared to that expected for η^2 -bound acac ligand protons at 7.7 and 4.7 ppm for the methyl and C-H protons respectively,²² and more like that of η^1 -bound acac with alkyl proton environments. To examine this further DRIFTS analysis (**Figure 6.2.1**) was employed to identify any changes in the acac environment. Examination and comparison of **RhTerpy** with Terpy and Rh(acac)(CO)₂ precursors show characteristic Terpyridine bands at 1423, 1456, 1473, 1564 and 1581 cm⁻¹ as well as bands at 1201, 1277 1381 and 1587 cm⁻¹ consistent with those found in the Rh(acac)(CO)₂ starting complex. A band at 1527 cm⁻¹ appears in **RhTerpy** shifted by 2 cm⁻¹ to lower wavenumber associated with a C-C vibration in the acac ligand. A band at 1672 cm⁻¹ not observed in either of the two starting materials is consistent with carbonyl bands in an η^1 -bound acac ligand bound to the C3 carbon.²³ Two strong bands at 2069 cm⁻¹ and 2010 cm⁻¹ associated with the rhodium-bound carbonyl ligands are both blue shifted by 1 cm⁻¹ from the parent rhodium carbonyl bands. This small change in wavenumber of the rhodium bound CO bands suggests the electronic contribution of the Terpyridine nitrogen donors counteracts the change in contribution of the acac ligand with change in hapticity. This evidence supports the formation of Rh(η^1 -acac)(CO)₂(Terpy) '**RhTerpy**' complex proposed in **Scheme 6.2.1**.

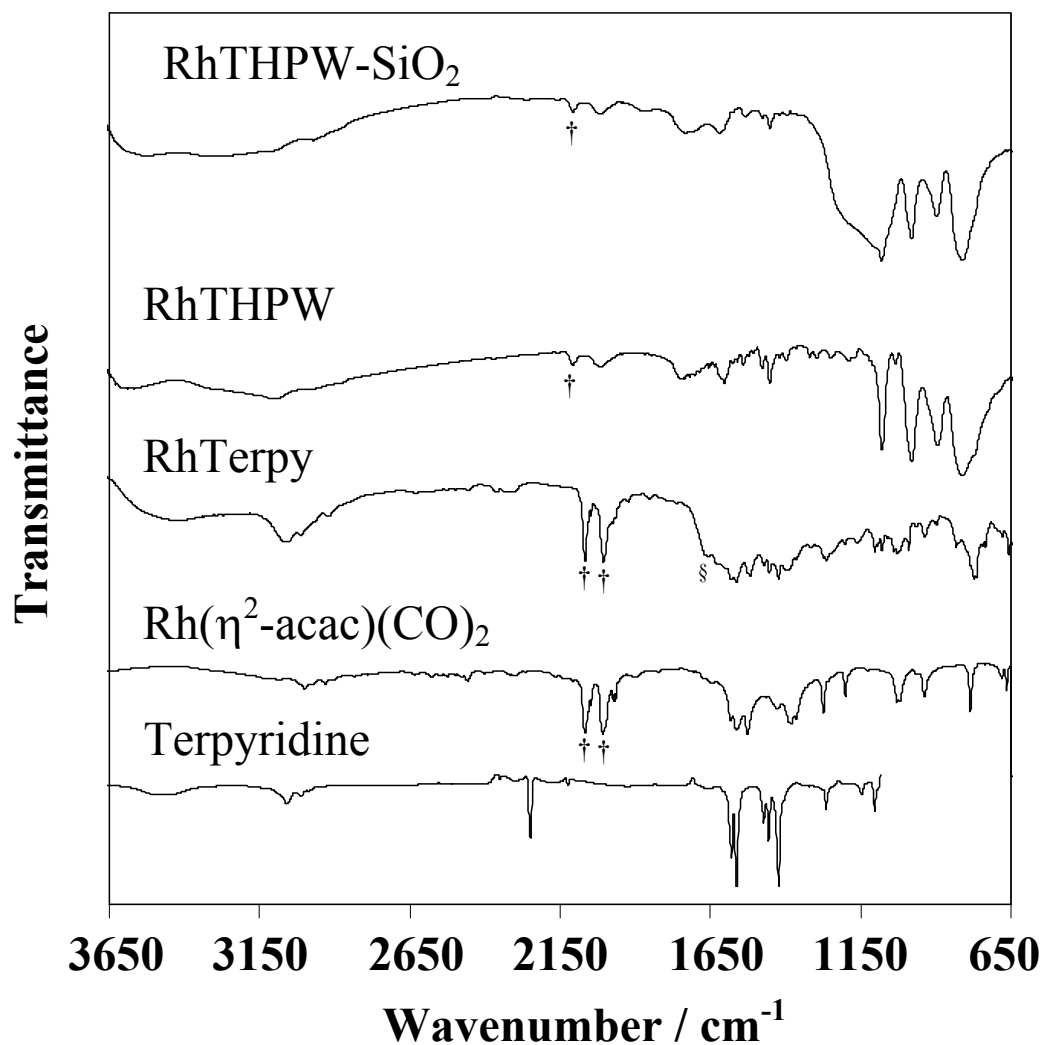
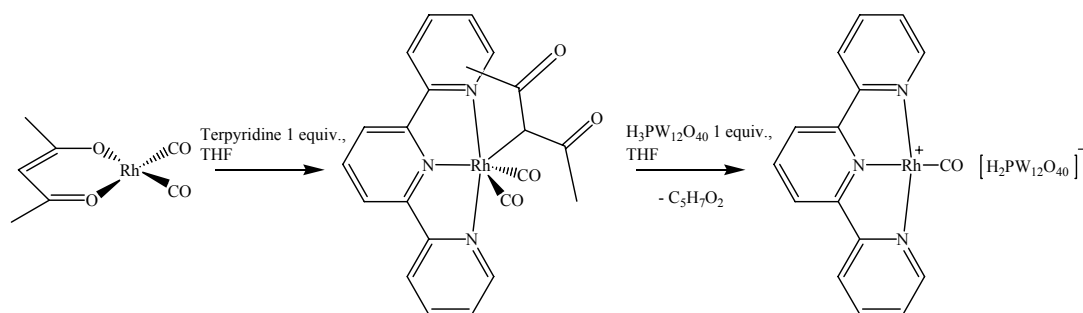


Figure 6.2.1: DRIFTS spectrum of Rh-Terpy series with bulk and supported **RhTHPW** and **RhTHPW-SiO₂** and **RhTerpy** with rhodium carbonyls denoted by † and eta one acac carbonyls denoted by §. Terpyridine and Rh(η²-acac)(CO)₂ precursors for comparison.



Scheme 6.2.1: Proposed synthetic route to Rh(η¹-acac)(CO)₂(Terpy) and bulk and supported rhodium-Terpy doped HPW ‘**RhTHPW**’.

Association of the Terpyridine without dissociation of acac and CO ligands can be rationalised by the lack of steric constraints of the Terpyridine compared with xantphos which contains bulky phenyl groups, demanding the loss of a carbonyl to accommodate the wide bite angle phosphine ligand.

RhTerpy was synthesised according to the method described in Section 2.3.5, and summarised above. In addition, one equivalent of phosphotungstic acid was included (undried) in the preparation to achieve a 1:1 Rh : Keggin ratio for comparison with analogous to that used in **RhXHPW1:1**. After work-up by removal of THF solvent in *vacuo* followed by washing in hexane in an inert atmosphere of nitrogen, a dark red powder was isolated. Elemental analysis provided evidence that the desired 1 : 1 ratio of Rh : Keggin was achieved and 1 : 1 Rh : Terpyridine was conserved with an observed 1 : 3 : 12 Rh : N : W ratio. Solution ESI⁺ (MeOH) showed a mass at m/z 115.1 for suggestive of the presence of $\{(Terpy)(H)_2\}^+$ and m/z 338.4 which would be consistent with $\{Rh(Terpy)(H)\}^+$ indicating Rh-Terpy coordination is conserved, however many low intensity peaks were also observed suggesting degradation and other species present. Solution ¹H {D₆-DMSO} NMR analysis of the isolated product showed a mixture of multiple environments in the aryl-H region between δ 7 and 9 ppm (~15 H approx.). This was unexpected as the free Terpyridine and **RhTerpy** spectra yield a very clean finger print with 8 environments at 7.43, 7.45, 7.98, 8.04, 8.38, 8.40, 8.57, 8.67 integrating to 1, 1, 2, 1, 1, 1, 2 and 2 respectively (**Table 6.2.1**) for the 11 protons on the 3 pyridyl rings. Additionally, ³¹P (D₆-DMSO) NMR spectroscopy was used to identify the nature of the HPW phosphorus. A singlet peak at δ -15.09 ppm is consistent with that observed for an intact Keggin phosphorus species,^{24, 25} This is also consistent with solution ESI⁻ (MeOH) mass spectrometry which shows a peak at 958.6 characteristic of $\{PW_{12}O_{40}\}^{3-}$. This indicates that no decomposition of the polyoxometallate functionality occurs on incorporation of a Rh-Terpyridine species.

To investigate the nature and origin of the multiple ¹H proton environments further, Terpyridine was treated independently with HPW containing 3 protons

and $[\text{NEt}_3\text{H}]^+[\text{PW}_{12}\text{O}_{40}]^{3-}$ (**NEt₃HPW**) which is known from earlier studies discussed in Chapter 3 for having no protons and therefore no Brønsted acidity.

Terpyridine and **NEt₃HPW** were dissolved in D₆-DMSO and analysed by ¹H NMR spectroscopy. No change in chemical shift or splitting was observed in the Terpyridine region. The ethyl protons of the triethyl ammonium cation were observed however the N-H proton which is known for being relatively broad was unresolved. This indicates that the phosphotungstate cage itself does not have an

Table 6.2.1: ^1H NMR chemical environments investigating the effect of Brønsted acidity on the nature of Terpyridine.

Environment (splitting)	δ Shift (ppm) / coupling constant (Hz)				
	integration	Terpyridine	$(\text{NEt}_3)_3\text{HPW}$	Terpyridine + $(\text{NEt}_3)_3\text{PW}_{12}\text{O}_{40}$	Terpyridine + HPW
t	9*	-	1.09	1.08	-
q	6*	-	2.98	2.98	-
2 x dd	2	7.43, 7.45 / 4.8	-	7.43, 7.45 / 4.8	-
dt	2	7.98 / 8, 2	-	7.98 / 8, 2	-
t	1	8.04 / 8	-	8.04 / 8	-
2 x s	2	8.38, 8.40	-	8.38, 8.40	-
dt	2	8.57 / 7.6, 1.2	-	8.57 / 7.6, 1.2	-
dm	2	8.67 / 5.2	-	8.67 / 5.2	-
t	2	-	-	-	8.14 / 6
t	1	-	-	-	8.42 / 8
m	5	-	-	-	8.74
d	2	-	-	-	9.03 / 8
d	2	-	-	-	9.05 / 6.8

effect on the nature of Terpyridine as expected. After dissolving Terpyridine and HPW in deuterated DMSO a colour change was observed from colourless solution to a pale yellow. On analysis by ^1H NMR new proton environments with higher chemical shifts were observed between δ 8.1 and 9.1 ppm. The total integration of all protons in 5 environments provided a ratio of 2 : 1 : 5 : 2 : 2 which would agree with 12 protons with the formation of mono protonated Terpyridinium which is the most common protonated form of Terpyridine observed in the literature where the N atoms take on a preferred *cis-trans* geometry rather than *trans-trans* in the un-protonated case.^{26, 27}

DRIFTS analysis shown in **Figure 6.2.1** indicates the preservation of the Keggin with characteristic bands at 825, 900, 985 and 1085 cm^{-1} discussed in more detail in Chapter 3. The bands at 1672, 2010 and 2069 cm^{-1} associated with η^1 -acac carbonyls and the 2 rhodium carbonyls are not observed. On protonation of Terpyridine characteristic infrared bands are known to indicate the formation of Terpyridinium.²⁸ DRIFTS analysis (**Figure 6.2.2**) was employed to confirm the

formation of Terpyridinium observed using ^1H NMR. Characteristic Terpyridine bands which were retained after coordination to the Rh metal centre at 1423, 1564 and 1581 cm^{-1} were bleached out on introduction of HPW to pure Terpyridine. This phenomenon was also observed in the case of a Rh-Terpy complex incorporation into the HPW matrix in both the bulk and silica supported **RhTHPW**. Bands in the HPW treated systems attributed to Terpyridinium were observed at 1622, 1607, 1584, 1563, 1531 and 1458 consistent with those in the literature.²⁸

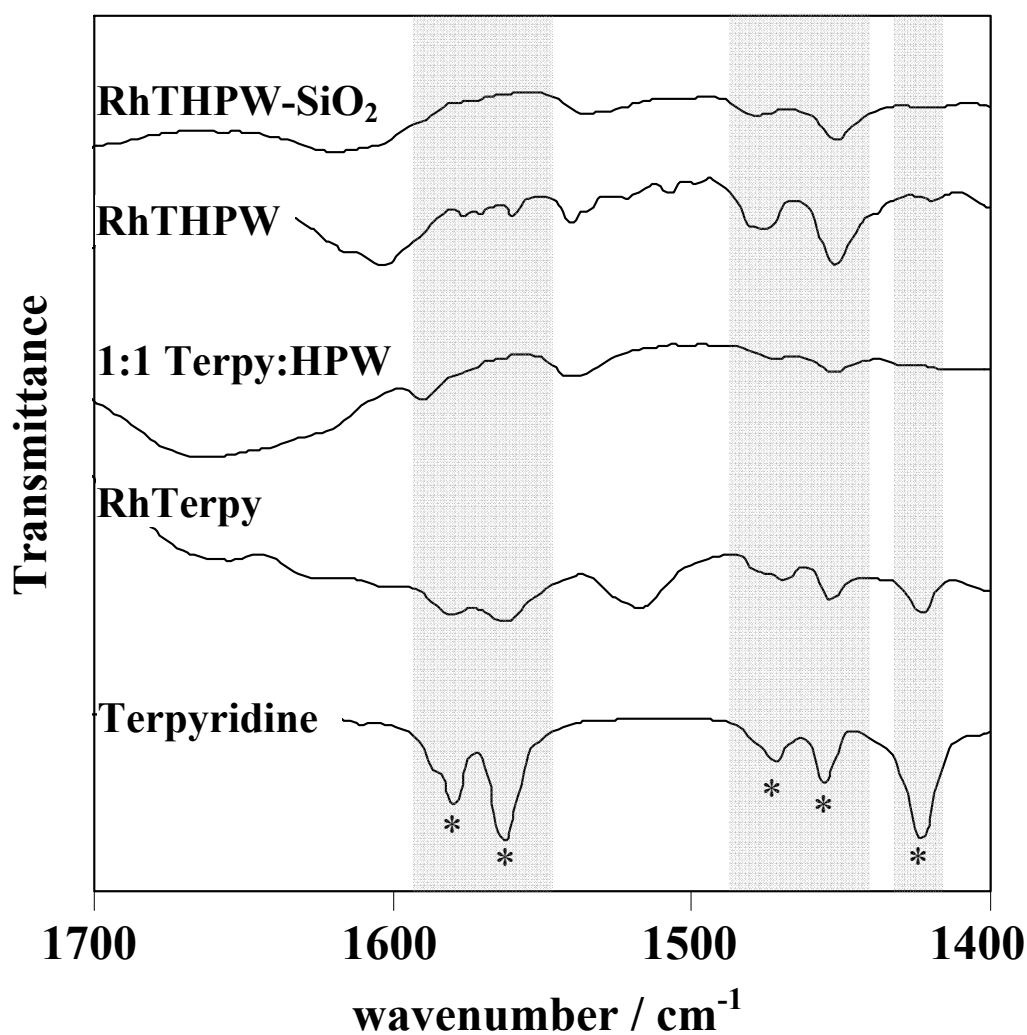


Figure 6.2.2: DRIFTS infrared spectrum of **RhTerpyHPW** (*) indicates characteristic bands for Terpyridine. The light grey regions show bleaching of characteristic Terpyridine bands on incorporation of HPW.

Thermal analysis of **RhTerpy** (**Figure 6.2.3**) shows mass loss between *ca.* 150 and 480 $^{\circ}\text{C}$ of 80 % associated with 388 a.m.u. of the Terpyridine, acac, and

carbonyls on the rhodium. A mass loss between 320 and 600 °C is consistent with the loss of a carbonyl and Terpyridine (~ 261 a.m.u) ~ 10 and 3 % respectively. Mass losses of 2.5 and 1 % between 200 and 230 °C in the bulk and silica supported sample respectively are indicative of HPW crystalline water loss.

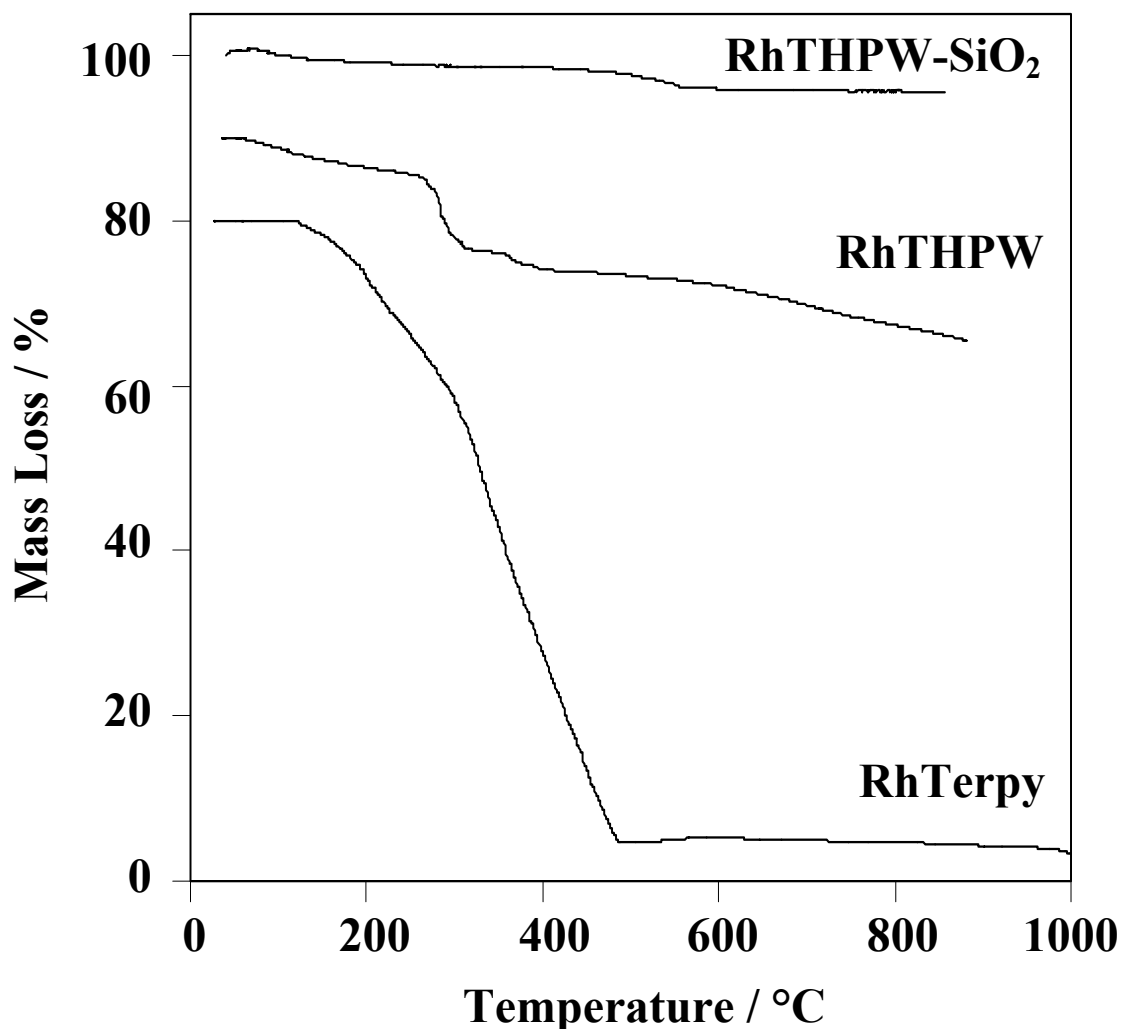


Figure 6.2.3: TGA plot show thermal decomposition profile of **RhTerpy**, **RhTHPW** and **RhTHPW-SiO₂**.

Introduction of a Rh-Terpyridine functionality to HPW shows the formation of a variety of products with a clear indication of the formation of Terpyridinium species. It can be hypothesised that this would have an adverse effect on the catalytic efficiency of the bifunctional Rh-HPW system. **RhTHPW** was investigated in the same manner as the analogous **RhXHPW** system for activity in methanol carbonylation discussed in Section 6.3.

6.3 - Catalytic studies of bulk and silica supported RhTHPW

Treatment of **RhTerpy** complex under the standard conditions employed earlier in the thesis show no activity for methanol carbonylation without HPW functionality. On incorporation of the HPW functionality no production of acetyl species to indicate activity for carbonylation was observed in the bulk material, within the detection limits of the on-line GC analysis ($\sim 0.05 \text{ mmol h}^{-1}$). This could be accounted for by the earlier observation of decomposition of **RhTerpy** in favour of titration of Brønsted acid sites in the bulk **RhTHPW**, forming pyridinium species. However, in the bulk material the DME production observed from condensation chemistry is comparable to that of pure HPW. This suggests that all of the acid sites are not titrated by Terpyridine, which would have occurred if all protons formed pyridinium species with a 1 : 1 N : H⁺ ratio present in the **RhTHPW** case. As it is unclear as to the decomposition mechanism of **RhTerpy** on addition of HPW it is only possible to say that it is likely that the acac ligand is protonated to form acacH and lost to induce the formation of a cationic Rh-Terpyridine monocarbonyl species and that mono, doubly and triply protonated Terpyridinium species are possibly present in the final material quenching some acidity. Impregnation of HPW on silica has shown beneficial effects in increasing the exposed acid sites increasing acid catalysed chemistry. **Figure 6.3.1** shows the methanol conversion and selectivity to acetyls observed in the SiO₂ supported **RhTHPW** with 1 : 1 Rh : Keggin ratio, (**RhTHPW1:1-SiO₂**) at 200 °C for 5 hours. In this case, like the analogous Xantphos catalyst only condensation and carbonylation of methanol chemistries are observed, with a good mass balance of $\sim 99 \%$. However the majority of the methanol is converted to DME *via* methanol condensation *ca.* 98 % at steady state. This selectivity is greatly reduced from that observed for the analogous **RhXHPW1:1-SiO₂** case where observed selectivities are typically an order of magnitude higher (24 compared to 2 % in Terpy case). This is consistent with decomposition of the Rh complex due to loss of Terpyridine and subsequent loss of CO activation ability. However high conversions to DME suggest a reservoir of activated methyl groups is present and a steady state acetyl yield of 0.23 mmol h^{-1} almost a fifth of that observed in the Xantphos case (1.2 mmol h^{-1} for the equivalent 1 : 1 Rh : HPW ratio). The conversion to DME is $\sim 88 \%$ which is lower than that of pure HPW-

SiO₂ where it is possible to achieve $\geq 95\%$ this indicates a slight loss in catalytic acid properties but shows that the retention of some acidity of the HPW retains an efficient working HPW functionality for methanol activation.

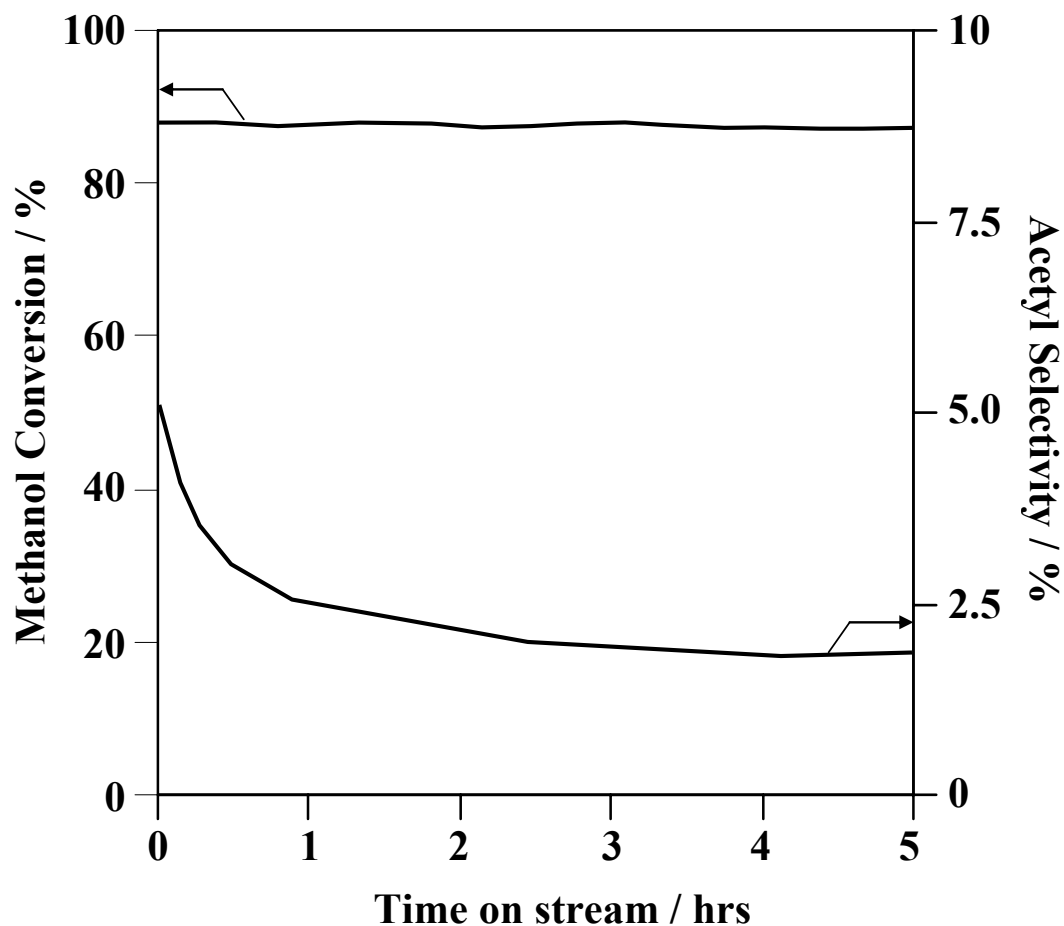


Figure 6.3.1: Methanol conversion and selectivity to acetyls at 200 °C under CO/MeOH conditions.

6.4 - Conclusions

Terpyridine functionalised Rh shows poor activity in activating CO for carbonylation of methanol, which suggests Terpyridine is not a practical candidate for stabilising Rh for bifunctional RhHPW catalysis. The study of this system indicates that the super-acidic Brønsted acid character of the heteropolyacid is too potent for the Rh-Terpyridine interaction causing decomposition of the resulting complex and deactivation toward carbonylation. Molybdic or silicilic

polyoxometallate based acids could be used in future studies, as they are less acidic^{24, 29} and could lead to more stable bifunctional systems.

6.5 - References

1. E. C. Constable, *Tetrahedron*, 1992, **48**, 10013-10059.
2. A. Togni and L. M. Venanzi, *Angewandte Chemie-International Edition in English*, 1994, **33**, 497-526.
3. C. A. Caputo and N. D. Jones, *Dalton Transactions*, 2007, 4627-4640.
4. M. Shi and G. X. Lei, *Appl. Organometallic Chemistry*, 2002, **16**, 55-60.
5. G. Malaise, J. B. Sortais, L. Barloy, M. Pfeffer and N. Kyritsakas, *Polyhedron*, 2006, **25**, 3349-3365.
6. S. D. Cummings, *Coordination Chemistry Reviews*, 2009, **253**, 449-478.
7. R. A. Fallahpour, *Synthesis-Stuttgart*, 2003, 155-184.
8. M. Heller and U. S. Schubert, *European Journal of Organic Chemistry*, 2003, 947-961.
9. F. P. Pruchnik, F. Robert, Y. Jeannin and S. Jeannin, *Inorganic Chemistry*, 1996, **35**, 4261-4266.
10. G. Chelucci, S. Gladiali, M. G. Sanna and H. Brunner, *Tetrahedron-Asymmetry*, 2000, **11**, 3419-3426.
11. G. Chelucci, A. Saba, F. Soccolini and D. Vignola, *Journal of Molecular Catalysis A: Chemical*, 2002, **178**, 27-33.
12. F. T. Esmadi and A. J. Alhamid, *Transition Metal Chemistry*, 1994, **19**, 571-574.
13. H. L. Kwong, H. L. Yeung, C. T. Yeung, W. S. Lee, C. S. Lee and W. L. Wong, *Coordination Chemistry Reviews*, 2007, **251**, 2188-2222.
14. M. Beller, B. Cornils, C. D. Frohning and C. W. Kohlpaintner, *Journal of Molecular Catalysis A: Chemical*, 1995, **104**, 17-85.
15. S. Cenini, F. Ragaini, M. Pizzotti, F. Porta, G. Mestroni and E. Alessio, *Journal of Molecular Catalysis*, 1991, **64**, 179-190.
16. M. Sharma, B. J. Sarmah, P. Bhattacharyya, R. C. Deka and D. K. Dutta, *Applied Organometallic Chemistry*, 2007, **21**, 255-263.
17. B. Sarmah, B. J. Borah, B. Deb and D. K. Dutta, *Journal of Molecular Catalysis A: Chemical*, 2008, **289**, 95-99.
18. B. J. Borah, B. Deb, P. P. Sarmah and D. K. Dutta, *Journal of Molecular Catalysis A: Chemical*, 2010, **319**, 66-70.
19. A. J. Pardey and C. Longo, *Coordination Chemistry Reviews*, 2010, **254**, 254-272.
20. E. C. Constable, *Advances in Inorganic Chemistry*, 1986, **30**, 69-121.
21. S. C. Yuan, H. B. Chen and H. C. Wang, *Progress in Chemistry*, 2009, **21**, 2132-2152.
22. F. Bonati and G. Wilkinson, *Journal of the Chemical Society*, 1964, 3156.
23. D. Gibson, *Coordination Chemistry Reviews*, 1969, **4**, 225-240.
24. I. V. Kozhevnikov, *Chemical Reviews*, 1998, **98**, 171-198.
25. W. H. Knoth and R. D. Farlee, *Inorganic Chemistry*, 1984, **23**, 4765-4766.
26. A. Hergold-Brundic, Z. Popovic and D. Matkovic-Calogovic, *Acta Cryst.*, 1996, **C52**, 3154-3157.
27. A. Kochel, *Acta Cryst.*, 2006, **E62**, 37-38.

28. A. Hugot-Le Goff, S. S. Joiret, P. P. Falaras, M. Graezel, P. Pechy, N. Vlachopoulos and M. Zakeeruddin, in *Optical Materials Technology for Energy Efficiency and Solar Energy Conversion XIV*, Editon edn., 1995, pp. 220-227.
29. G. I. Kapustin, T. R. Brueva, A. L. Klyachko, M. N. Timofeeva, S. M. Kulikov and I. V. Kozhevnikov, *Kinetics and Catalysis*, 1990, **31**, 896-898.

Conclusions and Future Work

Bifunctional systems with heteropolyacid and organometallic functionalities were successfully synthesised with the intention of offering alternative heterogeneous catalysts for methanol carbonylation. These materials were characterised using a variety of surface and bulk analytical techniques. DRIFTS infrared spectroscopy, ESI mass spectrometry as well as solution state ^1H and ^{31}P NMR and solid state MAS-NMR proved to be the most valuable for identifying and confirming the two key functional fragments remain intact. A combination of XPS, XANES spectroscopies were able to confirm the oxidation of Ru and Rh in the organometallic functionality. EXAFS spectroscopy was able to provide structural information of the local coordination environment of the organo-metal centre, thus providing an insight into the nature of interactions between the organometallic centre and the polyoxometallate of the heteropolyacid.

The materials studied in this doctoral thesis can be categorised in two main subgroups, Ru-polyoxometallate and Rh-polyoxometallate systems. The structural interaction between the ruthenium organometallic functionality and polyoxometallate functionality proved difficult to fully clarify with some evidence for a covalent Ru-O=W interaction with the polyoxometallate centre after loss of chloride from the precursor Ru complex. Although a structure is proposed for such a covalent system, further evidence is required to identify whether there is a covalent interaction or an ionic interaction with five-coordinate cationic organometallic Ru and anionic polyoxometallate. Either of these structures requires some proton exchange on the polyoxometallate. Studies of the **RuHPW** and **RudppeHPW** systems discussed in Chapter 3 showed complete loss of all protons. This was found to be due to the formation of triethylammonium when using triethylamine to abstract chloride from the Ru metal centre. Further studies to eliminate the need for triethylamine should be explored, such as, substitution with a weaker or non-nucleophilic base such as DBU or DABCO, rather than using NEt_3 which may limit the loss of acidity of the Keggin and offer the ability to tune organoruthenium incorporation in HPW. Alternatively, a metal such as silver could be used to abstract chloride by salt formation. It would be interesting

to synthesise Ru-polyoxometallates with other ligand systems with chloride-free precursors, potentially incorporating CO groups into the backbone more suitable as an activated carbonyl source for activity towards carbonylation.

In-situ infrared studies showed the Ru interaction with the polyoxometallate provide the ability to activate CO at the Ru centre. Catalytic phenylacetylene dimerization studies showed that both Ru-POM systems show good activity and different selectivity to their chloride precursors (in the case of **RuHPW** shifting the selectivity 70 % towards the *E*-dimer.) These studies could be extended to optimise reaction conditions and elucidate the mechanistic action of the catalyst. An effective approach would be to perform a ¹³C labelling study using NMR spectroscopy to identify coordination modes at the ruthenium centre.

After Ru-POM species showed to be inactive in methanol carbonylation a study on alternative Rh-POM species was undertaken where three Rh ligands were compared. Xantphos and Anthraphos (Chapter 4 and 5) contained tridentate 'PXP' backbones with POP and PCP coordination respectively. Terpy (Chapter 6) was used to explore the use of a tridentate nitrogen donor. All Rh-HPW systems showed activity in methanol carbonylation unlike their individual organo-rhodium and HPW precursors. The majority of this study examines the structure-activity relationship and deactivation of the Rh-Xantphos system.

Sequential reaction between $\text{Rh}(\eta^2\text{-acac})(\text{CO})_2$, tridentate Xantphos ligand, and silica-supported phosphotungstic acid, affords a simple route to a new family of robust, ionic $[\text{Rh}(\text{CO})(\text{Xantphos})]_n^+[\text{H}_{3-n}\text{PW}_{12}\text{O}_{40}]^-/\text{SiO}_2$ heterogeneous catalysts suitable for vapour phase methanol carbonylation under mild reaction conditions (1 bar and 200 °C). Their good rates of methyl acetate production, equating to an optimum space-time yield of $350 \text{ gkg}_{\text{cat}}^{-1}\text{h}^{-1}$, reflect the synergy between the (i) solid acid character of the parent $\text{H}_3\text{PW}_{12}\text{O}_{40}$ necessary for low temperature Me^+ generation, (ii) CO affinity of the stable $[\text{Rh}(\text{CO})(\text{Xantphos})]^+$ complex, and (iii) high active site density generated by dispersed HPW monolayers over Davisil silica. A mechanism for the mode of action of this bifunctional system was proposed to illustrate points (i) and (ii) involving Rh(III)

species identified by IR, XPS and EXAFS measurements similar to those widely accepted for typical Monsanto-type chemistries.

Catalyst deactivation was identified and proved problematic, especially at high temperatures, which drive Rh reduction to the metallic state, and simultaneous loss of crystalline water and solid acidity from the Keggin framework. Studies showed that this can be partially prevented by water addition to the reactant stream. Catalyst performance is sensitive to the degree of proton exchange, reflecting an inverse correlation between selectivity to acetyls (favoured by Rh) versus MeOH conversion (favoured by HPW), with the optimum methyl acetate yield achieved for Rh : HPW ratio = 0.5 : 1.

RhAHPW showed comparable carbonylation performance at 200 °C to Xantphos in 1 : 1 Rh : HPW with acetyl yields of 190 and 240 mmolh⁻¹g_{Rh}⁻¹ respectively (**Figure 7.1**) and similar reaction profile with lifetime studies of up to 5 hours on-stream. However steady state selectivity and conversion are almost inversed. Further structural studies on the Anthraphos system are required comparable to those accomplished for Xantphos in order to draw further conclusions about the nature of steady state operation. This was hindered by the complexity of synthesis of **RhAnthraphos** starting material and the nature of the active species. **RhTHPW** showed poor performance when compared with the 'PXP' (2 % selectivity to acetyls, (47 mmolh⁻¹g_{Rh}⁻¹)) systems where results indicated the terpyridine ligand on the rhodium metal centre was unstable under the acidic conditions of the solid acid component, attributed to terpyridinium formation. This suggests that although a tridentate ligand seems to benefit this type of bifunctional system over bidentate acetyls and monodentate chlorides discussed herein, the nature of this system is important to allow stability under reaction and synthetic conditions. It may be prudent to study a variety of other nitrogen donor ligands to verify whether poor performance is inherent across a series of different ligand systems with alternative nitrogen containing groups. Other interesting avenues for study could include increasing CO partial pressures which may improve conversion, where CO can potentially stabilise rhodium towards agglomeration (a key consequence in the decomposition of organo-Rh

ligand framework) and promote carbonylation versus methanol to DME dehydration and MTG chemistry.

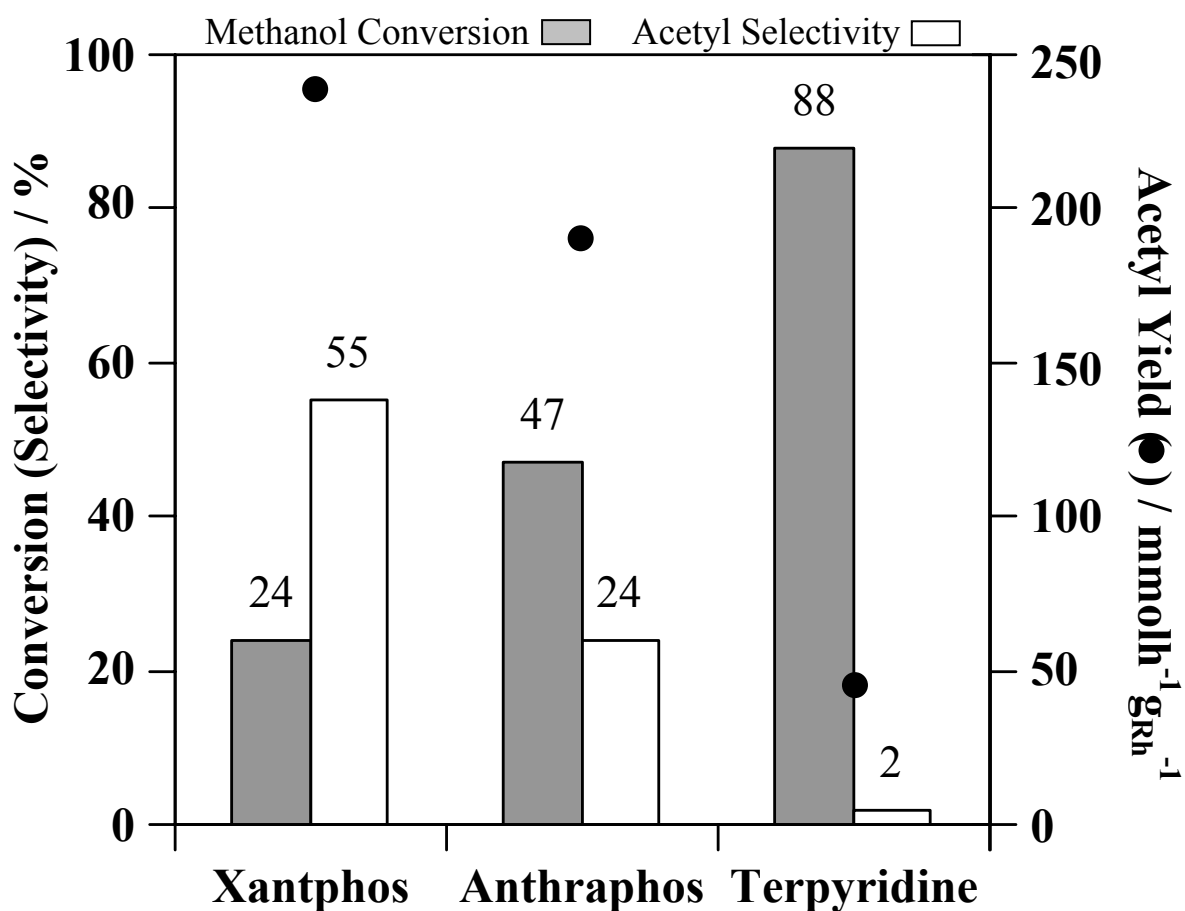


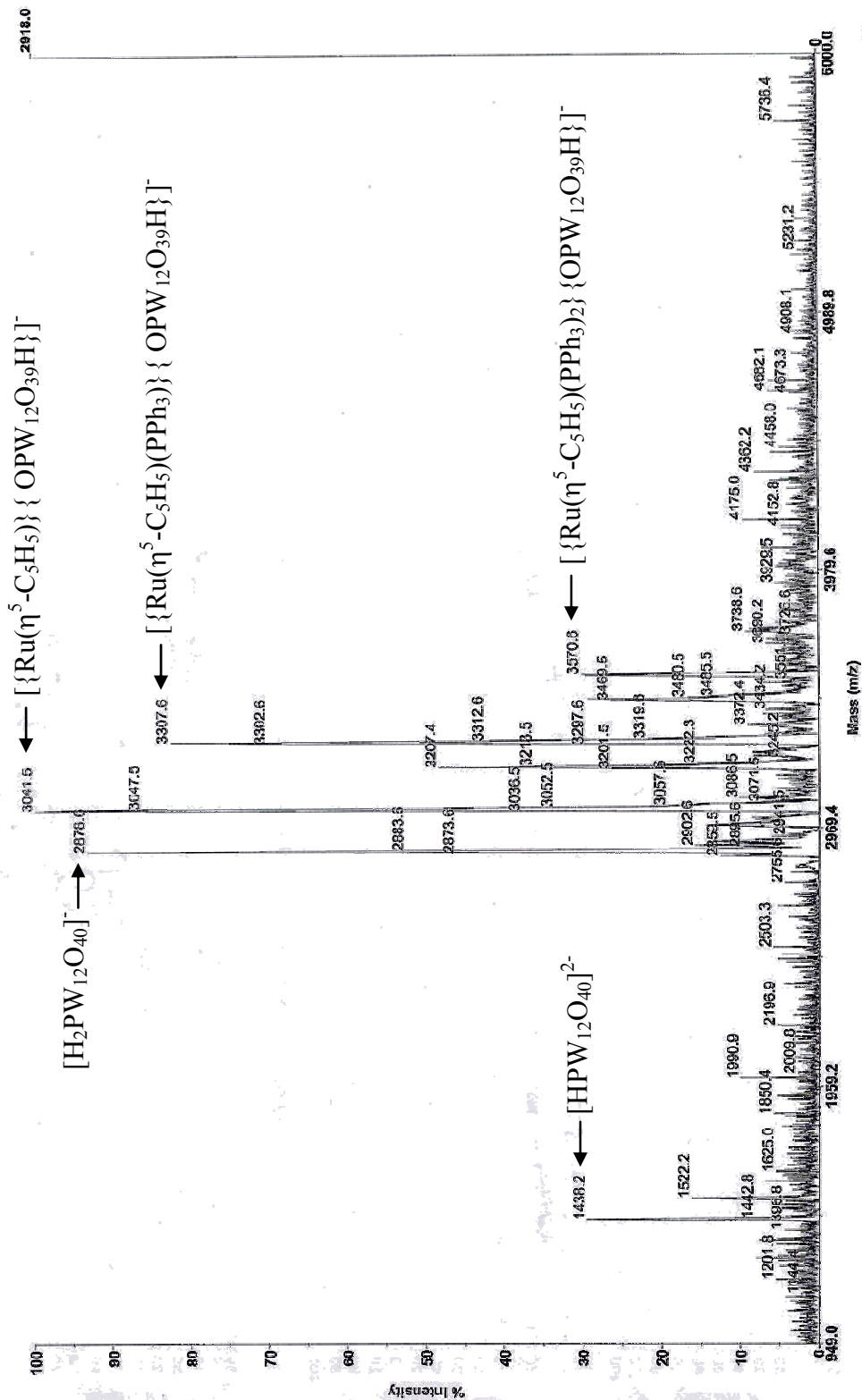
Figure 7.1: Comparison of methanol conversion, selectivity to acetyls and acetyl yield in mmolh⁻¹g_{Rh}⁻¹ of Rh(L)HPW1:1-SiO₂ catalysts in the carbonylation of methanol containing Rh bound to Xantphos, Anthrphos and Terpyridine ligands. All data is quoted for catalysts in steady state at 200 °C with 1 : 1 CO/MeOH feed.

Appendices

Appendix 1: MALDI-TOF MS of RuHPW

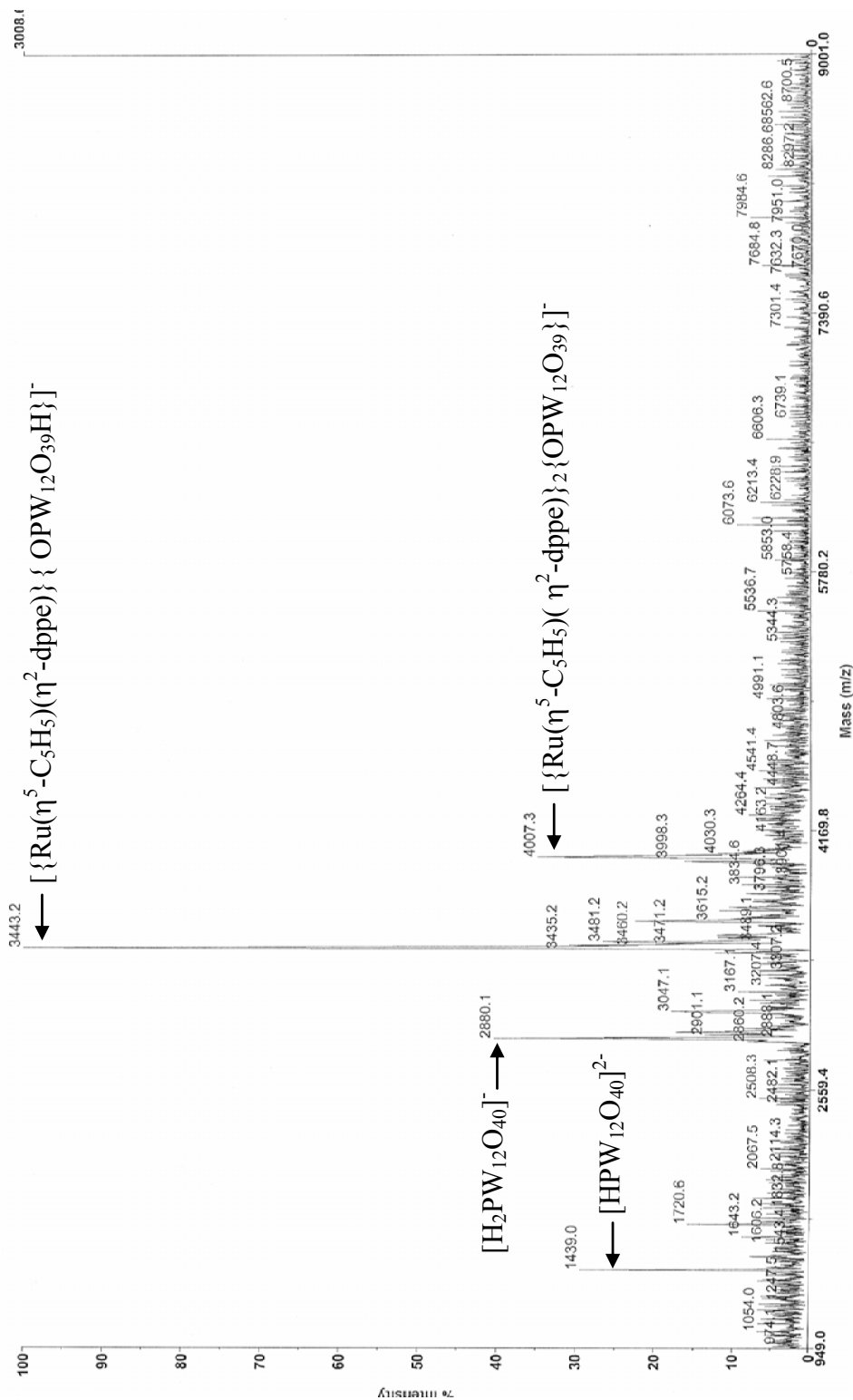
EPSRC National Mass Spectrometry Service Centre (NMSSC), Swansea

<<YOR01LYN-NEG_0001>> Voyager Spec #1=>AdvBC(64,0,5,0.1)=>NF0.7[BP = 3041.5, 2918]



Appendix 2: MALDI-TOF MS of RudppeHPW

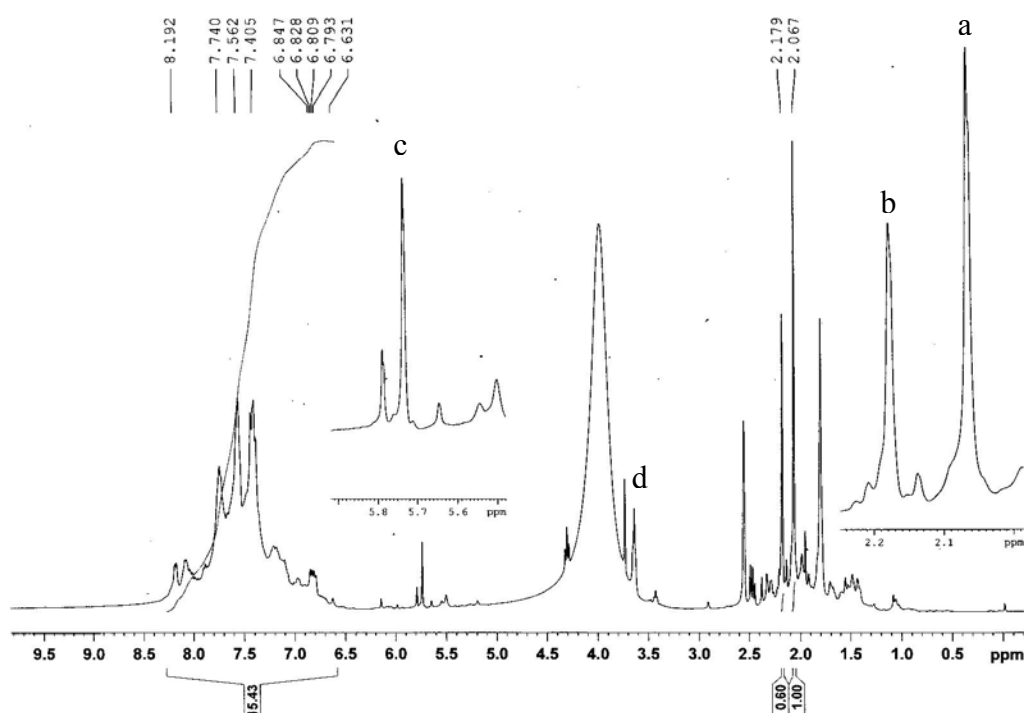
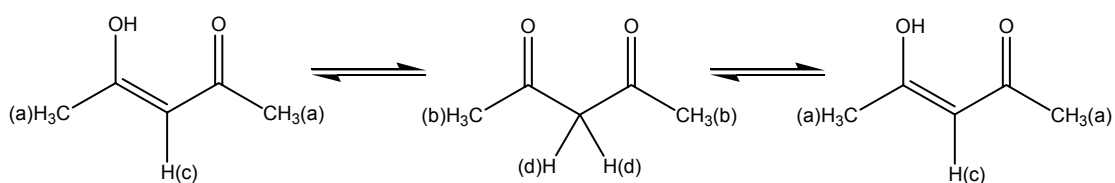
EPSRC National Mass Spectrometry Service Centre (NMSSC), Swansea
 <<YOR02LYN-NEG_0001>> Voyager Spec #1=>AdvBC(64,0.5,0.1)=>NF0.7[BP = 3443.2, 3009]



Acquired: 10:32:00, October 18, 2007
 Inlet: RudppeHPA MW=4298? [0.3mg:10] (DCTB:Glass/CuBB) Neg Ref
 File: \2007\Oct07\YOR02LYN-NEG_0001.dat

Printed: 11:55, October 18, 2007

Appendix 3: ^1H NMR ($\text{D}^6\text{-DMSO}$) spectrum of **RhXHPW1:1** indicating presence of uncoordinated acetylacetonate after reaction of **RhXantphos** with HPW
 Note: integration of CH_3 protons and subsequent calculation of ketone : enol tautomer ratio differ from expected 3 : 1 ratio (ca. 2 : 1) due to solvent impurities.



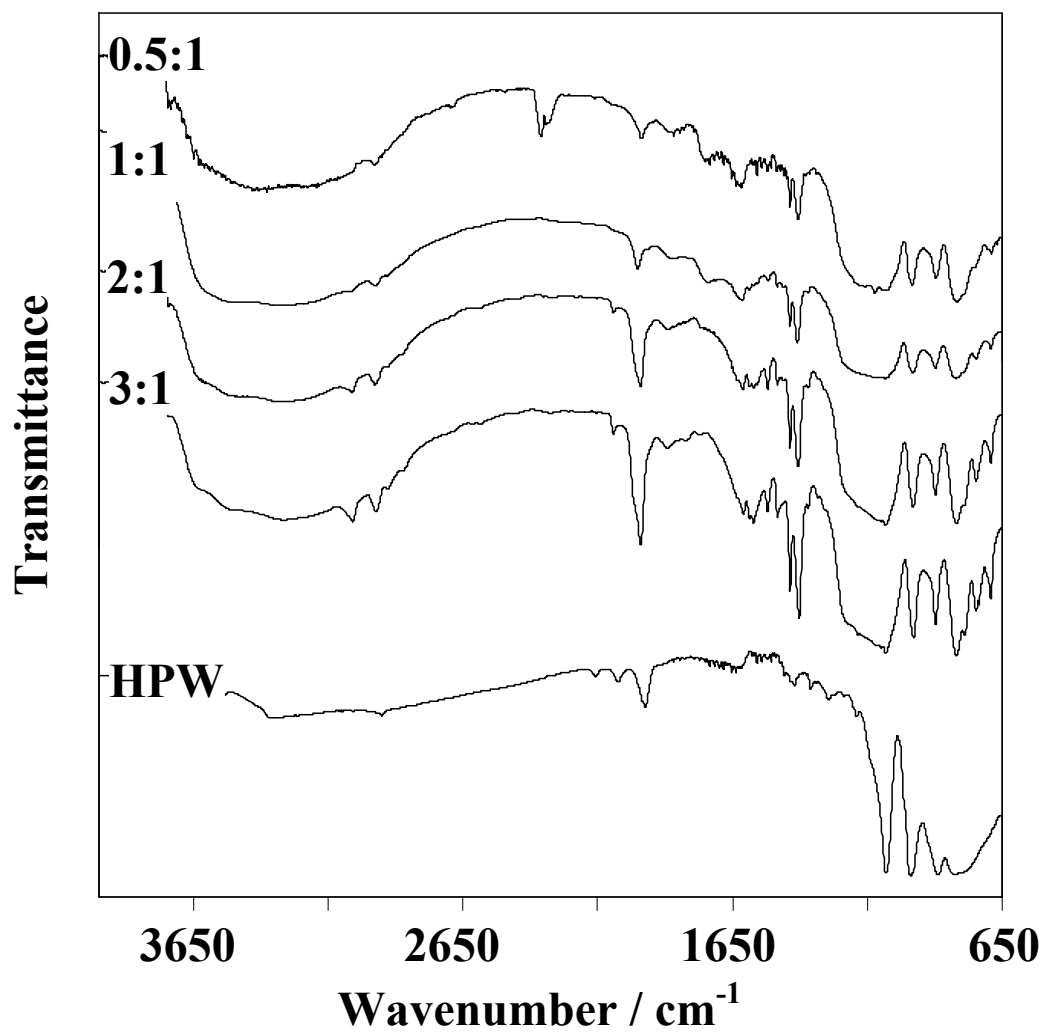
Appendix 4: XPS elemental composition

Element	$\text{Rh}(\eta^2\text{-acac})(\text{CO})_2$	$\text{Rh}(\eta^1\text{-acac})(\text{CO})_2(\text{xantphos})$	RhXHPW
Rh	8.9	1.1	0.8
P	-	1.9	2.3
W	-	-	10.0
O	59.4	24.7	34.4
C	27.7	72.4	52.6

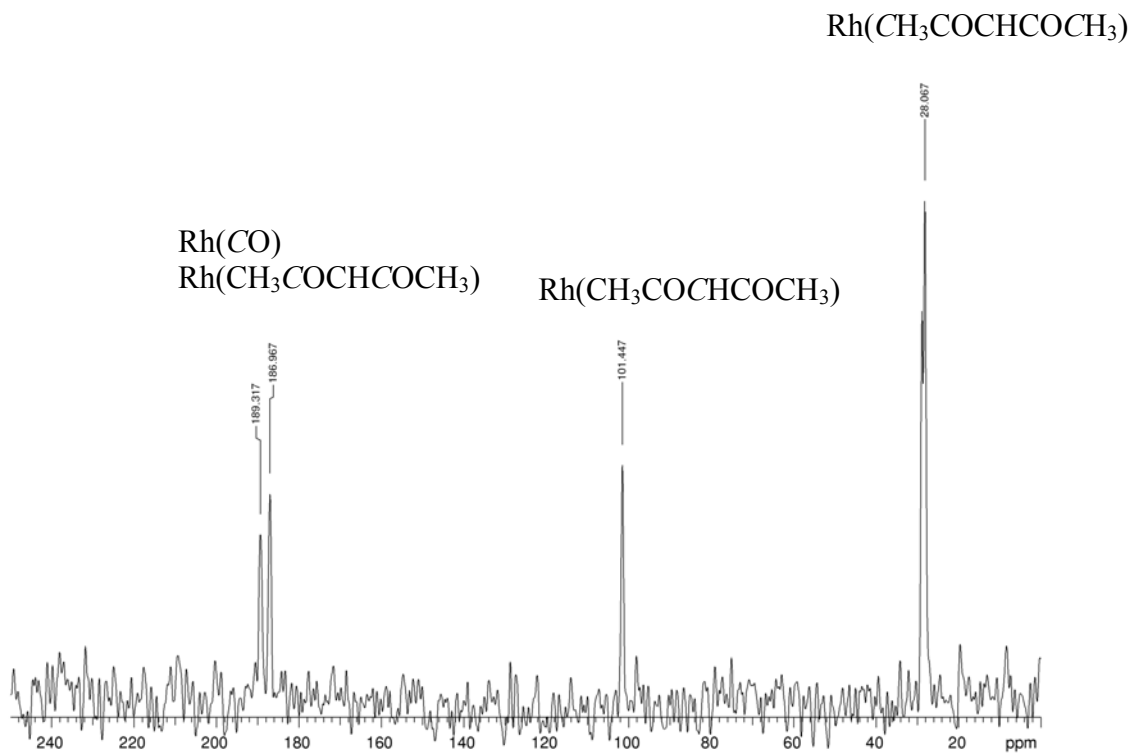
Appendix 5: Calculated BET surface area and BJH pore size from porosimetry measurements of RhXHPW-SiO₂ series and HPW, HPW-SiO₂ standards showing the loss of surface area and pore volume after impregnation.

	Surface area m²g⁻¹	Pore volume cm³g⁻¹	Pore Radius Å
HPW-SiO ₂	110	0.34	65.0
RhXHPWD0.5:1-SiO ₂	109	0.41	65.2
RhXHPWD1:1-SiO ₂	115	0.30	65.0
RhXHPWD2:1-SiO ₂	113	0.31	64.2
RhXHPWD3:1-SiO ₂	109	0.30	64.6
Davisil SiO ₂	324	1.18	65.2

Appendix 6: DRIFTS spectra of RhXHPW_n:1-SiO₂ series (n = 0.5, 1, 2, 3) denoted '*n:1*' showing characteristic bands for [Rh(CO)(Xantphos)]⁺ and HPW functionalities.



Appendix 7: (top) $^{13}\text{C}\{^1\text{H}\}$ MAS-NMR spectrum of $\text{Rh}(\eta^2\text{-acac})(\text{CO})_2$.
(bottom) $^{13}\text{C}\{^1\text{H}\}$ MAS-NMR spectrum of $\text{Rh}(\eta^1\text{-acac})(\text{CO})(\text{terpyridine})$.



$\text{Rh}(\text{Terpyridine}) - \text{Ar-C}$

